NASA/TM-1999-206587

Inlet Flow Characteristics During Rapid Maneuvers for an F/A-18A Airplane

William G. Steenken and John G. Williams
GE Aircraft Engines
Cincinnati, Ohio

Kevin R. Walsh
Dryden Flight Research Center
Edwards, California

NASA Contract NAS3-26617

October 1999

The NASA STI Program Office...in Profile

Since its founding, NASA has been dedicated to the advancement of aeronautics and space science. The NASA Scientific and Technical Information (STI) Program Office plays a key part in helping NASA maintain this important role.

The NASA STI Program Office is operated by Langley Research Center, the lead center for NASA's scientific and technical information. The NASA STI Program Office provides access to the NASA STI Database, the largest collection of aeronautical and space science STI in the world. The Program Office is also NASA's institutional mechanism for disseminating the results of its research and development activities. These results are published by NASA in the NASA STI Report Series, which includes the following report types:

- TECHNICAL PUBLICATION. Reports of completed research or a major significant phase of research that present the results of NASA programs and include extensive data or theoretical analysis. Includes compilations of significant scientific and technical data and information deemed to be of continuing reference value. NASA's counterpart of peer-reviewed formal professional papers but has less stringent limitations on manuscript length and extent of graphic presentations.

- TECHNICAL MEMORANDUM. Scientific and technical findings that are preliminary or of specialized interest, e.g., quick release reports, working papers, and bibliographies that contain minimal annotation. Does not contain extensive analysis.

- CONTRACTOR REPORT. Scientific and technical findings by NASA-sponsored contractors and grantees.

- CONFERENCE PUBLICATION. Collected papers from scientific and technical conferences, symposia, seminars, or other meetings sponsored or cosponsored by NASA.

- SPECIAL PUBLICATION. Scientific, technical, or historical information from NASA programs, projects, and mission, often concerned with subjects having substantial public interest.

- TECHNICAL TRANSLATION. English-language translations of foreign scientific and technical material pertinent to NASA's mission.

Specialized services that complement the STI Program Office's diverse offerings include creating custom thesauri, building customized databases, organizing and publishing research results...even providing videos.

For more information about the NASA STI Program Office, see the following:

- Access the NASA STI Program Home Page at ***http://www.sti.nasa.gov***

- E-mail your question via the Internet to help@sti.nasa.gov

- Fax your question to the NASA Access Help Desk at (301) 621-0134

- Telephone the NASA Access Help Desk at (301) 621-0390

- Write to:
  NASA Access Help Desk
  NASA Center for AeroSpace Information
  7121 Standard Drive
  Hanover, MD 21076-1320

NASA/TM-1999-206587

Inlet Flow Characteristics During Rapid Maneuvers for an F/A-18A Airplane

William G. Steenken and John G. Williams
GE Aircraft Engines
Cincinnati, Ohio

Kevin R. Walsh
Dryden Flight Research Center
Edwards, California

Prepared for
NASA Dryden Flight Research Center
Edwards, California
NASA Contract NAS3-26617

National Aeronautics and
Space Administration

Dryden Flight Research Center
Edwards, California 93523-0273

October 1999

NOTICE

Use of trade names or names of manufacturers in this document does not constitute an official endorsement of such products or manufacturers, either expressed or implied, by the National Aeronautics and Space Administration.

Available from the following:

NASA Center for AeroSpace Information (CASI)
7121 Standard Drive
Hanover, MD 21076-1320
(301) 621-0390

National Technical Information Service (NTIS)
5285 Port Royal Road
Springfield, VA 22161-2171
(703) 487-4650

TABLE OF CONTENTS

	Page
List of Figures	vi
List of Tables	viii
Nomenclature	ix
Abstract	1
1.0 Introduction	2
2.0 Test Hardware, Data Acquisition, and Data Reduction System Descriptions	3
2.1 HARV Aircraft Description	3
2.2 F404-GE-400 Engine Description and Instrumentation	3
2.3 Aircraft Instrumentation	6
2.3.1 Inlet Airflow and Distortion Instrumentation	6
2.3.2 Aircraft Aerodynamic Position Instrumentation	6
2.3.3 Trajectory Reconstruction of Aircraft Attitude During Rapid Maneuvers	8
2.4 Flight Test Data Acquisition System	8
2.5 Flight Test Data Reduction	9
2.5.1 Calibration	9
2.5.2 Data Reduction and Analysis	10
3.0 Approach	11
4.0 Modeling of Stabilized Maneuver Inlet Characteristics	14
4.1 Data Base and Modeling	14
4.2 Peak Dynamic Distortion Representations	17
4.3 Inlet Recovery Representation	17
5.0 Discussion of Results	36
5.1 Data Format	36
5.2 Data Consistency	40
5.3 Inlet Recovery	40
5.4 Peak Dynamic Circumferential Distortion	40
5.5 Peak Dynamic Radial Distortion	41
6.0 Conclusions	46
References	47
Appendix A: Inlet Flow Descriptor Definitions	49

TABLE OF CONTENTS (Continued)

	Page
Appendix B: M = 0.3 Rapid Maneuvers	50
Low-to-High Angle of Attack	50
Flight 212, Test Point 6b3	51
Flight 230, Test Point 2b2	54
Flight 230, Test Point 0b1	57
Flight 230, Test Point 0b2	60
Flight 230, Test Point 0b3	63
Flight 236, Test Point 22b	66
Flight 236, Test Point 22c	69
Flight 236, Test Point 23b	72
High-to-Low Angle of Attack	75
Flight 212, Test Point 07b	76
Flight 231, Test Point 04c	79
Flight 232, Test Point 05c	82
Flight 233, Test Point 05c	85
Flight 242, Test Point 16c	88
Flight 242, Test Point 17b	91
Flight 243, Test Point 16c	94
Flight 243, Test Point 29d	97
Flight 247, Test Point 6b4	100
Mid-to-High Angle of Attack	103
Flight 213, Test Point 12b	104
Flight 230, Test Point 15b	107
Flight 241, Test Point 19b	110
Flight 241, Test Point 19c	113
Mid-to-Low-to-High Angle of Attack	116
Flight 213, Test Point 11b	117
Mid-to-Low-to-Mid Angle of Attack	120
Flight 230, Test Point 14b	121
Flight 236, Test Point 18b	124
Flight 236, Test Point 18c	127
Appendix C: M = 0.4 Rapid Maneuvers	130
Low-to-High Angle of Attack	130
Flight 214, Test Point 04b	131
Flight 215, Test Point 07b	134
Flight 230, Test Point 13b	137
Flight 230, Test Point 18b	140
Flight 230, Test Point 22b	143
Flight 236, Test Point 4b1	146
Flight 236, Test Point 4b2	149
Flight 236, Test Point 24c	152
Flight 242, Test Point 21b	155
Flight 242, Test Point 21c	158

TABLE OF CONTENTS (Concluded)

	Page
High-to-Low Angle of Attack	161
Flight 233, Test Point 4c1	162
Flight 235, Test Point 09b	165
Flight 235, Test Point 9b1	168
Flight 245, Test Point 03b	171
Flight 245, Test Point 03c	174
Flight 245, Test Point 04b	177
Flight 245, Test Point 04c	180
Mid-to-High Angle of Attack	183
Flight 241, Test Point 0d1	184
Flight 241, Test Point 0d2	187
Flight 243, Test Point 25b	190
Flight 243, Test Point 25c	193
Mid-to-Low-to-High Angle of Attack	196
Flight 215, Test Point 06b	197
Flight 230, Test Point 17b	200
Flight 242, Test Point 20b	203
Flight 242, Test Point 20c	206

LIST OF FIGURES

	Page
1. High Alpha Research Vehicle (HARV) and F/A-18 Inlet System	4
2. AIP Pressure Sensing Locations	7
3. M = 0.3 HARV Stabilized Maneuver Database	15
4. M = 0.4 HARV Stabilized Maneuver Database	16
5. Representation of M = 0.3 Peak Dynamic Circumferential Distortion as a Function of Angle of Sideslip	20
6. Representation of M = 0.3 Peak Dynamic Circumferential Distortion as a Function of Angle of Attack	21
7. Representation of M = 0.4 Peak Dynamic Circumferential Distortion as a Function of Angle of Sideslip	22
8. Representation of M = 0.4 Peak Dynamic Circumferential Distortion as a Function of Angle of Attack	23
9. Comparison of Measured and Modeled Peak Dynamic Circumferential Distortion	24
10. Representation of M = 0.3 Peak Dynamic Radial Distortion as a Function of Angle of Sideslip	25
11. Representation of M = 0.3 Peak Dynamic Radial Distortion as a Function of Angle of Attack	26
12. Representation of M = 0.4 Peak Dynamic Radial Distortion as a Function of Angle of Sideslip	27
13. Representation of M = 0.4 Peak Dynamic Radial Distortion as a Function of Angle of Attack	28
14. Comparison of Measured and Modeled Peak Dynamic Radial Distortion	29
15. Representation of M = 0.3 Inlet Recovery as a Function of Angle of Sideslip	31
16. Representation of M = 0.3 Inlet Recovery as a Function of Angle of Attack	32
17. Representation of M = 0.4 Inlet Recovery as a Function of Angle of Attack	33
18. Representation of M = 0.4 Inlet Recovery as a Function of Angle of Sideslip	34
19. Comparison of Measured and Modeled Inlet Recovery	35
20. Time History of Angle of Attack, Angle of Sideslip, Mach Number, and Inlet Recovery (Measured and Estimated) - Flight 236, Test Point 22b	37
21. Time History of Peak Inlet Dynamic Circumferential and Radial Distortion (Measured and Estimated) - Flight 236, Test Point 22b	38

LIST OF FIGURES (Concluded)

	Page
22. Angle of Attack/Angle of Sideslip Trajectory During Maneuver and Measured versus Estimated Recovery - Flight 236, Test Point 22b	39
23. Time History of Angle of Attack, Angle of Sideslip, Mach Number, and Inlet Recovery (Measured and Estimated) - Flight 213, Test Point 11b	42
24. Time History of Peak Inlet Dynamic Circumferential and Radial Distortion (Measured and Estimated) Flight 213, Test Point 11b	43
25. Angle of Attack/Angle of Sideslip Trajectory During Maneuver and Measured versus Estimated Recovery - Flight 213, Test Point 11b	44

LIST OF TABLES

	Page
1. ESN 310-051 (Right-Hand-Side) Ground and Flight Test Instrumentation	5
2. M = 0.3 Rapid Maneuvers	12
3. M = 0.4 Rapid Maneuvers	13
4. Peak Dynamic Circumferential Distortion Representation	18
5. Peak Dynamic Radial Distortion Representation	19
6. Inlet Recovery Representation	30

NOMENCLATURE

AIP	Aerodynamic Interface Plane
ALF	Aft Looking Forward
AOA	Angle of Attack, deg
AOATJ	Angle of Attack Calculated from Trajectory Reconstruction, deg
AOSS	Angle of Sideslip, deg
AOSSTJ	Angle of Sideslip Calculated from Trajectory Reconstruction, deg
ARP	Aerospace Recommended Practice
DAMP	Dynamic Aircraft Maneuver Program
DP/PC	Circumferential Distortion Descriptor (See Appendix A)
DP/PR	Radial Distortion Descriptor (See Appendix A)
EERAM	Inlet Recovery from Slow Response Transducers
ERAMB	Inlet Recovery from High-Response Transducers
ESN	Engine Serial Number
GEAE	General Electric Aircraft Engines
HARV	High Alpha Research Vehicle
HAP	HARV Analysis Program
IRP	Intermediate Rated Power
INS	Inertial Navigation System
LEX	Leading Edge Extension
M	Mach number
NACA	National Advisory Committee for Aeronautics
PCM	Pulse Code Modulation
PLA	Power Lever Angle, deg
QCP	Quality Check Program
RMS	Root Mean Square
ZDCPCF	Dynamic Circumferential Distortion
ZDCPCFST	Peak Dynamic Circumferential Distortion Based on Computer Model
ZERAMST	Inlet Recover Based on Computer Model
ZIDR	Dynamic Radial Distortion
ZIDRST	Peak Dynamic Radial Distortion Based on Computer Model
Hz	Hertz
lbf	Pounds force
lbm	Pounds mass
psi	Pounds per square inch
sec	Seconds
sps	Samples per Second
°	Degree

ABSTRACT

The F404-GE-400 engine powered F/A-18A High Alpha Research Vehicle (HARV) was used to examine the characteristics of inlet airflow during rapid aircraft maneuvers. A study of the degree of similarity between inlet data obtained during rapid aircraft maneuvers and inlet data obtained at steady aerodynamic attitudes was conducted at the maximum engine airflow of approximately 145 lbm/sec using a computer model that was generated from inlet data obtained during steady aerodynamic maneuvers. Results show that rapid-maneuver inlet recoveries agreed very well with recoveries obtained at equivalent stabilized angle-of-attack conditions. The peak dynamic circumferential distortion values obtained during rapid maneuvers agreed within 0.01 units of distortion over the 10 - 38 degree angle of attack range with the values obtained during steady aerodynamic maneuvers while similar agreement was found for the peak dynamic radial distortion values up to 29 degrees angle-of-attack. Exceedences of the rapid-maneuver peak dynamic circumferential distortion values relative to the peak distortion model values at steady attitudes occurred only at low or negative angles of attack and were inconsequential from an engine-stability assessment point of view. The results of this study validate the current industry practice of testing at steady aerodynamic conditions to characterize inlet recovery and peak dynamic distortion levels.

1.0 INTRODUCTION

Most inlet testing accomplished for the purposes of obtaining recovery and distortion data is done at fixed combinations of angle of attack and sideslip, and constant Mach number and inlet corrected airflow. Inlet-engine compatibility practitioners have often questioned whether the recovery and distortion data acquired at fixed conditions is equivalent to the inlet recovery and distortion obtained during rapid aircraft maneuvers, that is, during conditions when the Mach number and airflow are held constant and the inlet angle of attack is varied as a function of time while trying to hold angle of sideslip constant. The two most often raised questions are:

1. Do the inlet recovery and distortion obtained during rapid changes in angle of attack (termed a rapid maneuver) differ from the inlet recovery and distortion obtained during fixed attitude testing accomplished in wind tunnels at corresponding angles of attack?

2. Does interpolating between points obtained during wind-tunnel fixed-attitude testing adequately represent the characteristics of the flow or are there significant characteristics of the flow that can be missed that occur between the fixed attitude data points?

The NASA High Alpha Research Vehicle (HARV) F/A18-A aircraft flown at NASA Dryden Flight Research Center provided an excellent test vehicle for such studies since it was configured, in part, for propulsion research. That is, the aircraft had thrust vectoring capability which allowed rapid maneuvers to high angles of attack to be accomplished and had the complement of inlet instrumentation, aircraft attitude instrumentation, and engine instrumentation that could readily provide the data needed to accomplish the appropriate studies. Thus, the rapid maneuver investigations could be conducted as part of the HARV propulsion system research program (Reference 1).

HARV Program inlet propulsion results that have been previously reported can be found in References 2 - 9. Reference 4 provides a summary of all the inlet research efforts that were conducted on the HARV aircraft. Discussion of the inlet characteristics during stabilized maneuvers can be found in References 2 and 3 while discussion of the inlet characteristics during maneuvers with rapidly changing angles of attack can be found in References 5 and 6. References 7 and 8 provide discussions of the inlet characteristics during high angle-of-attack departures. Discussion of the study to estimate engine airflow under clean and distorted flight conditions is presented in Reference 9.

The following sections of this report provide a description of the HARV aircraft, the instrumentation, the types of analyses conducted, the approach for conducting the rapid maneuvers, a discussion of the results, and conclusions. The types of analyses conducted during the rapid maneuver investigation will be illustrated for a few typical and/or key dynamic maneuvers in an effort to maintain a degree of conciseness to this report. However, data figures similar to those presented in the text are presented in the appendix for all other rapid maneuvers.

2.0 TEST HARDWARE, DATA ACQUISITION, AND DATA REDUCTION SYSTEM DESCRIPTIONS

The HARV aircraft, specifically configured to accomplish high angle-of-attack research, was highly instrumented and possessed modern data acquisition and data reduction systems as described below.

2.1 HARV Aircraft Description

The HARV is a single-seat F/A-18A aircraft (pre-production aircraft Number 6) powered by two afterburning turbofan F404-GE-400 engines. The high angle-of-attack capability is obtained by thrust vectoring, in this case, by removing the divergent nozzle flaps from the convergent-divergent exhaust nozzle and deflecting the nozzle exit flow by inserting three externally mounted paddles into each exhaust stream in a controlled and coordinated manner to produce the desired thrust vectoring (Reference 1). This thrust-vectoring capability allowed a wide range of stabilized angles of attack and sideslip to be achieved at the desired Mach numbers in the range of 0.3 to 0.4. The wide range of conditions, in terms of inlet distortion to which the inlet was subjected, provided part of the database necessary for conducting the desired rapid maneuvers study.

The F/A-18A aircraft inlets are two-dimensional, external compression inlets with 5-degree compression ramps mounted on the sides of the aircraft fuselage under the aft portion of the LEX (Leading Edge Extension of the wing) approximately 25 feet aft of the aircraft nose. Additional details of the inlet are described in Reference 10. The propulsion research was conducted on the right-hand inlet aft looking forward (ALF).

The HARV aircraft and F/A-18A inlet system are shown in Figure 1.

2.2 F404-GE-400 Engine Description and Instrumentation

The F404-GE-400 engine is a low-bypass, twin-spool, axial-flow turbofan engine with an afterburner. The 3-stage fan (low-pressure compressor) and 7-stage high-pressure compressor are each independently driven by a single-stage turbine. In the fan, the inlet guide vanes and the stators of the first stage are variable. In the high-pressure compressor, the inlet guide vanes and the first two stator stages are variable. These variable inlet guide vanes direct the inlet air at an optimum angle for efficient and stable engine operation. The through-flow annular combustor uses atomizing fuel nozzles. The mixed-flow augmentor burns air from both the bypass and the high-pressure core in the afterburner section. The engine control is an integrated system, using both hydromechanical and electronic control components. The sea-level-static IRP thrust of each engine is approximately 10,700 lbf, and the maximum afterburner thrust is approximately 16,000 lbf. The maximum corrected airflow through the engine is approximately 145 lbm per sec.

Engine Serial Number (ESN) 310-083 was installed on the left-hand side of the aircraft and ESN 310-051 was installed on the right-hand side of the aircraft. Both engines were equipped with an original engine control which placed the IRP flat at 87 degrees PLA.

ESN 310-051 had the standard complement of engine readout parameters as shown in Part A of Table 1. Additionally, flight test instrumentation was installed to provide additional readouts of bill-of-material parameters or additional parameters that were of interest to propulsion research. These parameters are listed in Part B of Table 1.

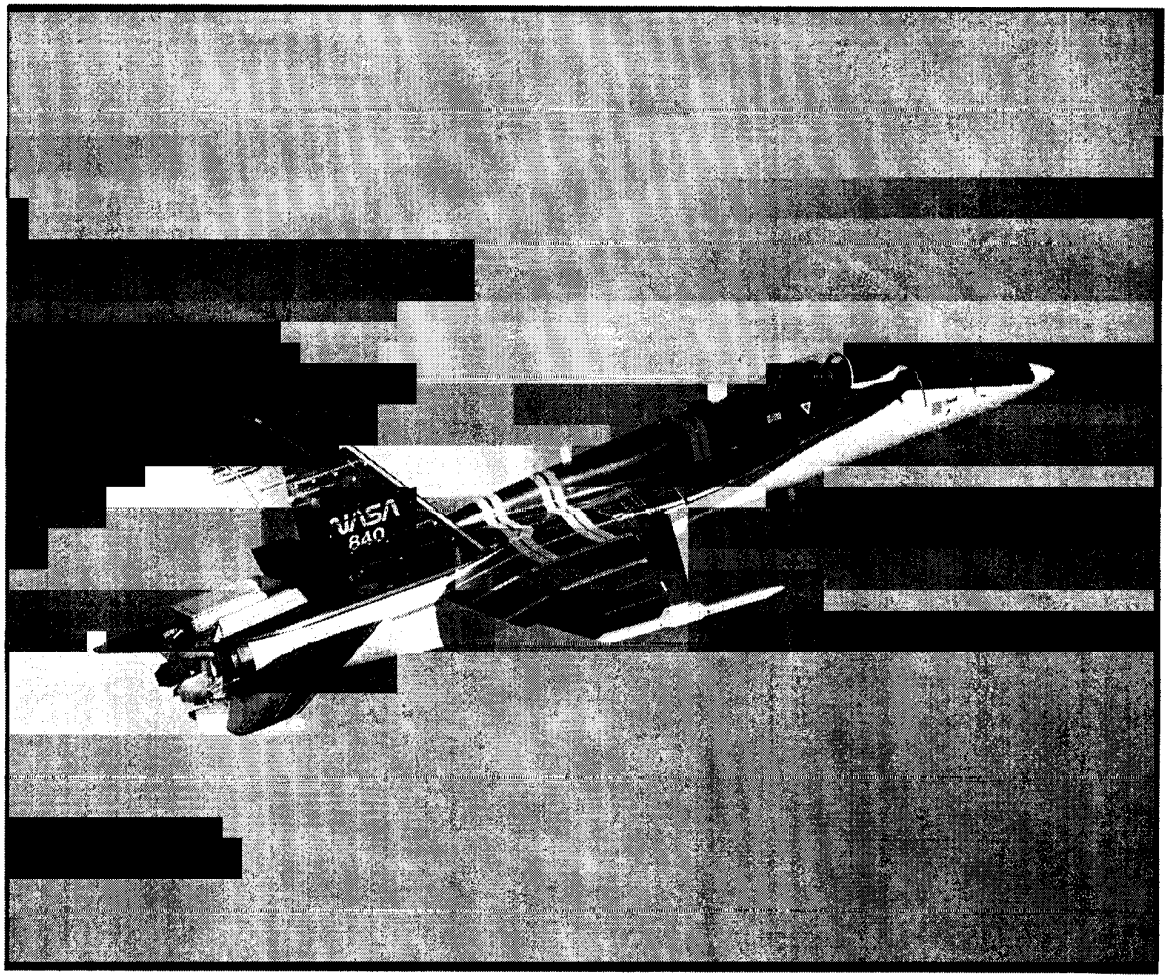

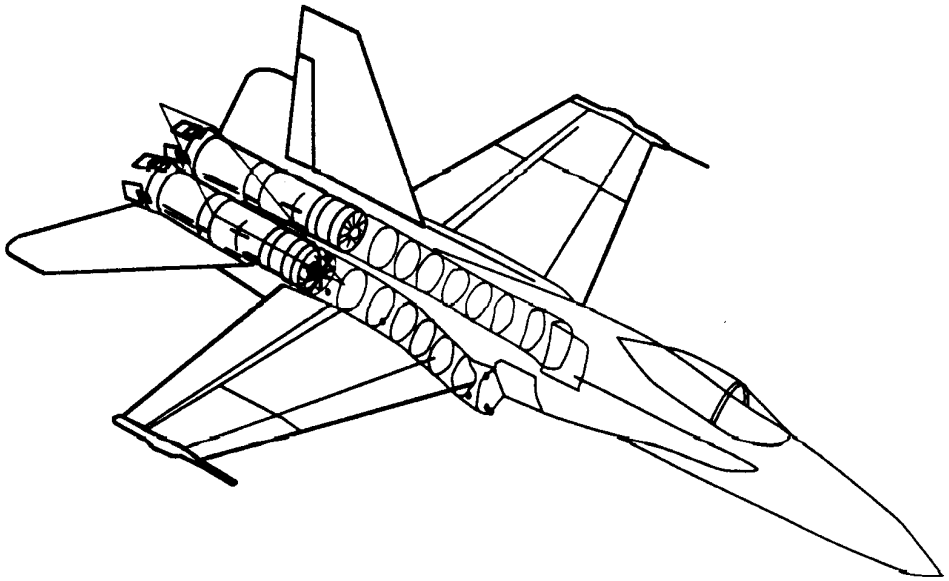

Figure 1. High Alpha Research Vehicle (HARV) and F/A-18 Inlet System.

Table 1. ESN 310-051 (Right-Hand-Side) ground and flight test instrumentation.

Part A - Bill of Material		Part B - Flight Test Instrumentation	
Instrumentation Designation	Instrumentation Description	Instrumentation Designation	Instrumentation Description
PLA*	Power Lever Angle	N1	Physical Fan Speed
TT1*	Engine Inlet Total Temperature	N2	Physical Compressor Speed
N1*	Physical Fan Speed	FGV	Fan Variable Geometry Position
N2*	Physical Compressor Speed	HPVG	Compressor Variable Geometry Position
FIGV	Fan Inlet Guide Vane Position	WFE	Engine Fuel Flow
CIGV	Compressor Inlet Guide Vane Position	WFET	Engine Fuel Temperature
CDP*	Compressor Discharge Pressure	WFABM	Afterburner Main Fuel Flow
WF*	Engine Fuel Flow	WFABMT	Afterburner Main Fuel Temperature
PT56*	Turbine Exhaust Pressure	WFABP	Afterburner Pilot Fuel Flow
EGT*	Exhaust Gas Temperature	PSFUELI	Control Inlet Fuel Pressure
A8*	VEN Position	PSFUELO	Control Outlet Fuel Pressure
		PS211, PS212	Fan Discharge Wall Static Pressures
		PSB1, PSB2	Combustor Wall Static Pressures
		PT56 (20)	Low Pressure Turbine Discharge Total Pressures
		PS6REF	Afterburner Inlet Reference Pressures
		PS6 (3)	Afterburner Inlet Wall Static Pressures
		PS7 (4)	Exhaust Nozzle Wall Static Pressures

*Parameters Also Used in Flight Test

The health of the engine was checked many times during the propulsion research portion of the flight program. The fan corrected speed - compressor corrected speed relationship, fan inlet guide vane as a function of corrected fan speed, compressor inlet guide vane position as a function of compressor corrected speed, exhaust nozzle area as a function of fan corrected speed, and exhaust gas temperature as a function of compressor corrected speed were compared with calibration values acquired during a ground run (Reference 9). No significant changes were noted during the flight test program. The fact that no significant change occurred probably is because the engine was already significantly deteriorated prior to the start of the propulsion research program.

2.3 Aircraft Instrumentation

The aircraft instrumentation that was used to provide data necessary to analyze the rapid maneuver flight data is going to be treated as three separate categories. These are inlet airflow and distortion instrumentation, aircraft aerodynamic position instrumentation, and aircraft attitude position instrumentation. The following paragraphs address each of these types of instrumentation.

2.3.1 Inlet Airflow and Distortion Instrumentation

The inlet airflow and distortion instrumentation was comprised of forty high-response and forty time-averaged (also known as steady-state) total pressures and eight high-response and eight time-averaged wall-static pressures all located at the Aerodynamic Interface Plane (AIP). Figure 2 provides a schematic layout of the AIP total-pressure instrumentation. The AIP was located approximately 4.0 inches forward of the engine bullet nose. This inlet distortion rake, which is described in Reference 11, provides both high-response and low-response (quasi-steady) total-pressure measurements at forty probes located on the centroids of equal areas for a five ring, eight rake array. It should be noted that the probe sensing configuration was designed to be very insensitive to flow angularity, an important criterion when measuring total pressure in distorted flows. Per Reference 11, this configuration allows the sensors to read true pressure levels at yaw angles over the range ±25 degrees and pitch angles from +15 to -25 degrees with positive angles being in the direction of the engine centerline. The flow blockage of the distortion rake structure at the AIP is 0.4 percent. The maximum blockage of the rake, which is less than eight percent, is located 1.5 inches downstream of the AIP.

2.3.2 Aircraft Aerodynamic Position Instrumentation

The aircraft aerodynamic position is specified by two parameters - aircraft angle of attack and aircraft angle of sideslip. The typical noseboom-mounted air data system was not installed during the HARV flight program because at high angle of attack, the noseboom had a significant effect on the forebody aerodynamics and thus, on the stability and control of the aircraft. Instead, specially designed, self-aligning air data probes (also called swivel probes) and NACA angle-of-attack and angle-of-sideslip vanes were mounted on each wing tip (Reference 12). Each swivel probe consisted of a combined pitot-static tube with four fins attached to the end of the probe to aerodynamically align it to the local flow. Hence, because these probes aligned themselves with the local flow, total pressure losses as a result of local angle-of-attack and - sideslip effects were effectively eliminated. The probes swiveled freely for local angles of attack between -15 degrees and +72 degrees and for local angles of sideslip between ±40 degrees. However, the swivel probe static-pressure measurements still were affected by the presence of the aircraft.

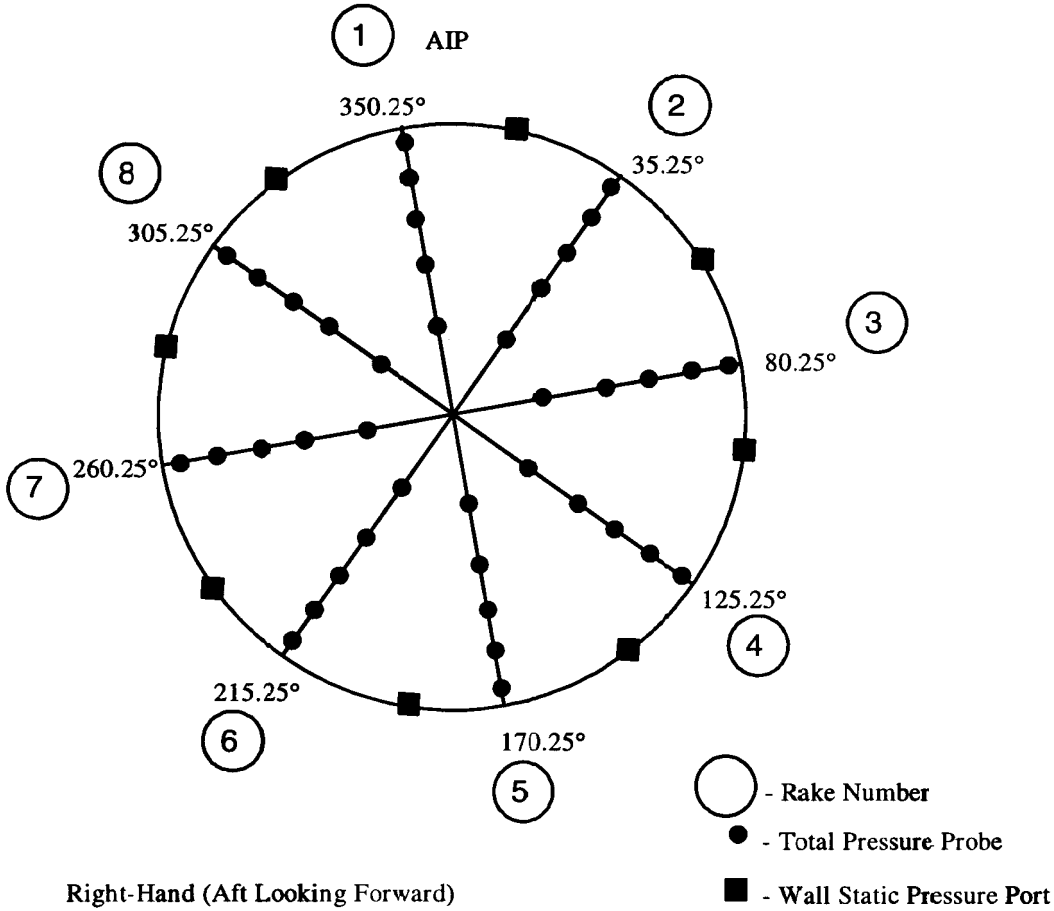

ANGULAR LOCATIONS OF WALL-STATIC PRESSURES		
BETWEEN RAKES	HIGH-RESPONSE	STEADY-STATE
1-2	12.25°	9.25°
2-3	58.75°	55.75°
3-4	97.50°	94.50°
4-5	144.0°	141.0°
5-6	189.0°	186.0°
6-7	234.0°	231.0°
7-8	283.0°	280.0°
8-1	323.0°	320.0°

Figure 2. AIP Pressure Sensing Locations.

Calibrations of the NACA angle of attack and angle of sideslip vanes provided accurate measurements from low-to-high angle of attack during steady aerodynamic conditions. This calibration accounted for aerodynamic effects such as local upwash and sidewash. The various flight test techniques that were used to establish the angle-of-attack and angle-of-sideslip calibrations are described in Reference 12. For the HARV inlet program, angle of attack was obtained from the left wing-tip vane, while angle of sideslip was obtained by averaging the left and right vanes. A total-temperature probe was mounted on the right wing tip without a pitot-static probe. Hence, the right angle-of-attack vane could not have Mach number corrections applied whereas the angle-of-sideslip vanes did not require Mach number corrections.

At high angles of attack, the wing-tip mounted flow angle vanes were subject to the effects of wing bending and torsional frequencies. The bending frequency mode of the wings was between 6 and 8 Hz, whereas the torsional mode frequency was 12 Hz. These frequencies influenced the measurement signal of the vanes. To compensate for these frequencies, a combination 12 Hz low pass and 6-8 Hz notch filter was used to remove the frequency content from the angle-of-attack and angle-of-sideslip signals. To compensate for the time lag associated with the notch filter, a time skew of -0.14 seconds was applied to the filtered angle-of-attack and angle-of-sideslip signals.

2.3.3 Trajectory Reconstruction of Aircraft Attitude During Rapid Maneuvers

The measurements of the angle-of-attack and angle-of-sideslip vanes together with their associated calibrations are accurate only during steady aerodynamic conditions. During rapid dynamic maneuvers, measurement hysteresis associated with angle-of-attack and angle-of-sideslip data results in unreliable and inaccurate measurements. An alternate approach described as "trajectory reconstruction" is employed. This approach uses data from the inertial navigation system (INS) to determine the aircraft orientation and to calculate angle-of-attack and angle-of-sideslip values.

To reconstruct the trajectory of an aircraft, the relationship between aerodynamic positions, aircraft body positions, and atmospheric winds must be defined. The angle of attack and angle of sideslip of an aircraft are defined using the aircraft body axes and the velocity vector. The velocity vector is the combination of the inertial velocity and the wind velocity. Therefore, angle of attack and angle of sideslip can be described as a function of pitch (angle between the longitudinal body axis and the horizon), roll (angle between the lateral body axis and the horizon), yaw (angle of movement about the vertical axis), the inertial velocity vector, and the wind velocity vector.

During steady aerodynamic conditions just before departure, the trajectory reconstruction methodology uses the wing-tip angle-of-attack and angle-of-sideslip measurements and the INS information to obtain a baseline average wind calculation. This average wind is then directly applied to the aircraft attitudes and INS velocity during a departure to calculate angle of attack and angle of sideslip for the departure.

2.4 Flight Test Data Acquisition System

All data during the test program were acquired using three PCM systems. The data acquired using PCM1 and PCM2 were telemetered to a ground station for recording on magnetic tape in a digital format while the data acquired using PCM3 were recorded on-board the aircraft on magnetic tape in a digital format. All PCM systems recorded an embedded time code which was taken from an on-board time code generator and was used in merging the three data streams during the data reduction sequence. The sample rates varied from 10 sps for a reference pressure to 2143 sps for the AIP high-response total pressures used for inlet distortion calculations.

2.5 Flight Test Data Reduction

Each PCM data stream in raw counts was stored on NASA Dryden Flight Research Center computers. The embedded time code in each data stream was used to time tag each data sample. This allowed data from all three PCM systems to be merged into a single data set using the common time source. The raw count data were converted into engineering units using appropriate calibration curves. Then, a merged computer file was created for each test flight condition containing the parameters required for data analysis. This computer file was reduced further by applying the appropriate in-flight calibrations to the pressure transducers. The final reduced computer file was available to all members of the NASA/GEAE Propulsion Research Team.

2.5.1 Calibration

Although significant effort had been expended to assure that the AIP high-response transducers had minimum zero-shift and thermal-sensitivity characteristics, analysis of the in-flight AIP distortion rake data revealed significant differences between the mean pressure values obtained from the low-response pressure transducers and the high-response absolute-pressure transducers, even after accounting for the high-response transducer temperature sensitivity. This possibility had been anticipated and procedures had been incorporated in the data reduction programs to handle this effect. These adjustments were termed "biases" and there were two sets. One set was for the low-response pressure transducers and was derived by applying equal pressure to both sides of the transducer. The second set was for the high-response pressure transducers and was determined from the difference between the means of the high-response pressure transducer outputs and the corresponding mean outputs of the low-response transducers.

Typical magnitudes of the low-response transducers biases were very small, typically less than ± 0.02 psi. However, the high-response transducer biases could be as large as ±0.3 psi. To identify the bias levels to be applied to a given set of data, a short "calibration point" was acquired during straight and level flight prior to the start of a series of maneuver test conditions. During a given flight, five or more such calibration points were acquired. Each of these was associated with a single test or series of test conditions.

The distribution of the high-response transducer bias values was always similar, although the magnitudes could change. The reason for this has not been completely explained. Also, there were indications that the high-response transducers tended to drift with time in flight (there was no evidence of such tendencies during hanger or ground checks). The longer in time that a test point was from a calibration point, the larger the difference in the mean signal level, and therefore, a greater question as to its accuracy. In-flight, the absolute value of the temperature used for high-response transducer compensation was not a big driver at the test conditions of interest - variations of ± 20 °F did not make a big difference (less than 0.05 psi) to the bias levels for a typical flight temperature condition.

The absence of a bias correction to the high-response signals would result in significant differences in the indicated pressure values and consequently, the resulting engine face pressure contours and distortion levels. Also, inlet pressure recovery was in error, but to a lesser extent.

A comparison of the engine face isobaric contours based on the time-averaged pressure values measured by the low-response system and those measured by the time high-response system, corrected only for temperature compensation effects, showed that there were a few similarities in the two patterns. The inclusion of the bias levels in the data reduction procedures forced the time-averaged high-response pressure-transducer pattern to mimic the low-response pressure-transducer pattern at the flight calibration condition.

2.5.2 Data Reduction and Analysis

Digital data files containing the aircraft, inlet, and engine measured parameters were produced by NASA Dryden Flight Research Center. The in-flight calibration bias had been applied to these data. The sampling rate was 2143 sps.

The initial step in the process of data reduction was to validate the data. This function was provided by the Quality Check Program (QCP). This program compared the raw data values to user-established limits and to relative change from the previous time-step values. Data substitution techniques were established for handling invalid or missing data.

The output from the QCP was fed into the HARV Analysis Program (HAP). This program filtered the data to the critical response time of the engine, evaluated the AIP total-pressure time-variant distortion descriptors according to GEAE and ARP 1420 (Reference 13) definitions, and generated isobaric-contour patterns. Also, the HAP provided mean and RMS levels for the inlet measurements, inlet airflow, and recovery values.

3.0 APPROACH

The procedure that was employed to determine if the inlet distortion and recovery data obtained during flight test dynamic maneuvers produced the same magnitudes as the inlet distortion and recovery data obtained during stabilized maneuver conditions (References 2 - 4) is described in this section.

This procedure involved flying a range of maneuver conditions at M = 0.3 and M = 0.4 and comparing the resulting inlet distortion and recovery levels with those obtained by interpolating or extrapolating from a model constructed from the data obtained at the stabilized maneuver conditions. The manner in which the model of the stabilized maneuver inlet distortion and recovery characteristics was constructed from the flight data is described in detail in Section 4.0.

The dynamic maneuver flight data, that were to be compared to the stabilized maneuver data, were obtained during fifteen flights conducted over a two month period from mid-March to mid-May 1994 at the NASA Dryden Flight Research Center. The fifty dynamic maneuvers that constitute the database for this portion of the HARV propulsion flight research program are described in greater detail in Tables 2 and 3 for Mach numbers of 0.3 and 0.4, respectively. These maneuvers were segregated into five angle-of-attack categories: 1) "low-to-high" with the angle of attack starting at approximately +10 degrees and increasing beyond approximately +50 degrees, 2) "high-to-low" with the initial angle of attack in excess of +40 degrees and decreasing to usually less than +10 degrees, 3) "mid-to-high" starting at angles of attack in excess of approximately +30 degrees and increasing to in excess of +50 degrees, 4) "mid-to-low-to-high" starting at approximately +15 degrees angle of attack and decreasing to +9 degrees or less followed by an increase to greater than approximately +50 degrees of angle of attack, and 5) "mid-to-low-to-mid" which was initiated at approximately +30 degrees angle of attack and was followed by a decrease to less than +4 degrees and then by an increase to more than +9 degrees angle of attack.

Examination of the tables shows descriptive characteristics for each of the dynamic maneuvers that were performed in terms of the category of the maneuver; the flight on which it was accomplished and the test point designation; angle-of-attack information in terms of the initial angle of attack at the start of the maneuver, the angle of attack at the end of the maneuver, and the minimum angle of attack achieved in the cases of the dynamic maneuvers which were not monotonically increasing or decreasing with time; and the range of the angle of sideslip that occurred while the angle of attack dynamic maneuver was being performed. While it was the pilot's intent to hold the angle of sideslip constant during an angle-of-attack maneuver, the flight characteristics of the aircraft often prevented the attainment of this objective.

The flight data obtained during the dynamic maneuvers as well as the comparisons with the stabilized flight maneuver database are presented in Section 5.

Table 2. M=0.3 Rapid Maneuvers.

ANGLE OF ATTACK CATEGORY	FLIGHT	TEST POINT	ANGLE OF ATTACK, deg INITIAL	MIN	END	ANGLE OF SIDESLIP, deg RANGE
Low-to-High	212	6b3	9	-	71	+0.2 - +2.3
	230	2b2	9	-	60	+0.1 - +1.1
	230	0b1	11	-	56	-0.3 - +0.8
	230	0b2	9	-	63	-0.1 - +1.1
	230	0b3	9	-	62	+0.5 - +0.9
	236	22b	9	-	62	+0.2 - +1.4
	236	22c	9	-	60	-4.0 - +6.0
	236	23b	11	-	68	-6.0 - +6.0
High-To-Low	212	07b	58	-	-1	+1.0 - +5.2
	231	04c	58	-	17	-1.2 - +3.6
	232	05c	59	-	3	-0.5 - +3.7
	233	05c	60	-	4	-0.3 - +2.3
	242	16c	59	-	6	+0.6 - +4.1
	242	17b	59	-	17	+0.3 - +2.7
	243	16c	59	-	8	-0.5 - +2.9
	243	29d	59	-3	1	-3.0 - +8.0
	247	6b4	62	-	13	-4.7 - -0.5
Mid-To-High	213	12b	30	-	70	+0.1 - +2.9
	230	15b	25	-	71	+0.2 - +2.7
	241	19b	26	-	71	+3.4 - +5.6
	241	19c	28	-	67	-6.8 - -3.1
Mid-To-Low-To-High	213	11b	30	-8	68	-0.6 - +5.0
Mid-To-Low-To-Mid	230	14b	32	-11	9	+0.1 - +4.6
	236	18b	28	4	24	-2.8 - +5.5
	236	18c	28	0	23	-6.0 - +6.5

Table 3. M=0.4 Rapid Maneuvers.

ANGLE OF ATTACK CATEGORY	FLIGHT	TEST POINT	ANGLE OF ATTACK, deg INITIAL	MIN	END	ANGLE OF SIDESLIP, deg RANGE
Low-To-High	214	04b	10	-	53	-0.1 - +1.0
	215	07b	14	-	58	+0.5 - +2.3
	230	13b	10	-	57	-0.3 - +2.6
	230	18b	13	-	57	+0.3 - +1.9
	230	22b	9	-	55	+0.1 - +0.8
	236	4b1	8	-	52	+0.4 - +3.2
	236	4b2	9	-	51	+5.0 - -7.0
	236	24c	10	-	44	-4.0 - +3.2
	242	21b	14	-	55	+4.3 - -6.5
	242	21c	13	-	51	-5.0 - +8.0
High-to-Low	233	4c1	40	-7	-4	-0.3 - +2.7
	235	09b	39	-	-7	+0.5 - +3.5
	235	9b1	39	-	-5	-0.8 - +1.3
	245	03b	39	-	-7	+2.2 - +4.7
	245	03c	41	-	-5	-5.5 - +8.0
	245	04b	40	-	-6	+1.1 - +4.5
	245	04c	40	-	-8	-4.4 - +3.7
Mid-To-High	241	0d1	40	-	63	-3.0 - -5.0
	241	0d2	39	-	63	+2.0 - -6.0
	243	25b	38	-	58	+4.0 - +6.0
	243	25c	40	-	59	-2.0 - -6.0
Mid-To-Low-To-High	215	06b	14	6	59	+0.2 - +1.0
	230	17b	13	2	50	0.0 - +0.6
	242	20b	13	9	49	+7.0 - -4.2
	242	20c	14	9	55	-5.0 - +11.0

4.0 MODELING OF STABILIZED MANEUVER INLET CHARACTERISTICS

A key requirement for assessing the degree of similarity between inlet data obtained at fixed aerodynamic attitude test conditions and inlet data obtained during rapid aircraft maneuvers is to have an automated procedure that allows estimating the inlet characteristics such as the peak dynamic distortions and recovery at Mach numbers, and angles of attack and sideslip of interest. The method for doing this is to build a computer model of the stabilized maneuver data base that permits estimating the peak distortion and recovery levels at flight conditions of interest with the test points that comprise the stabilized maneuver data base. The computer model that was constructed is described in the following paragraphs.

4.1 Data Base and Modeling

The basis for the inlet distortion and recovery representations were the peak circumferential and radial dynamic distortion values and the inlet recovery values obtained from the high-response total-pressure measurements at the AIP distortion rake during the stabilized maneuver flights (References 2 - 4). The HARV stabilized maneuver database is comprised of 80 cases at Mach numbers of approximately 0.3 and 0.4 as shown in Figures 3 and 4. Specifically:

- 54 conditions at $M \cong 0.3$; AOA range from -8.6 to +60.0° and AOSS range from -8.3 to +10.8°
- 26 conditions at $M \cong 0.4$; AOA range from -10.3 to +39.8° and AOSS range from -7.6 to +7.5°

Trends were established to describe the inlet distortion and recovery characteristics from the data at the above flight Mach number, angle of attack, and angle of sideslip conditions. Special attention was paid to preserve consistent trends from the various measured flight speed/attitude conditions. These established trends were then extrapolated to encompass the more extreme attitude conditions of the rapid maneuver flights.

From these descriptions, it was possible to construct numerical models in the form of tabular values to describe the peak dynamic circumferential and radial distortion and recovery values as functions of Mach number and attitude. The construction of all the models was similar. They were comprised of a set of values at a base value of Mach 0.3 and a set of Mach number derivatives, each set being a function of angle of attack and angle of sideslip. This format was selected on the basis of being easily incorporated in a computer representation to facilitate comparisons with measured results from the rapid maneuver flights. The procedure to derive a predicted value for a given Mach number and attitude was to: 1) establish the magnitude at the base value (at Mach 0.3) at the given attitude using linear interpolation within the tabulated range of angle-of-attack and angle-of-sideslip values, 2) similarly establish the magnitude of the derivative value at the given attitude within the tabulated range of angle-of-attack and angle-of-sideslip values, and 3) sum the base value magnitude and product of the derivative value magnitude multiplied by the difference in the given Mach number from 0.3.

The tabular values encompassed the following range of maneuver conditions:

- AOA range from -10.3 to +70.0°
- AOSS range from -10.0 to +10.0°

The relative magnitudes of the "rapid maneuver" and the "stabilized maneuver" envelopes are shown in Figures 3 and 4 for M = 0.3 and 0.4, respectively, with the angle of attack and angle of sideslip combinations from which the computer model was derived superposed. The stabilized maneuver envelope represents the limit to which the computer model could be expected to represent adequately the stabilized maneuver data in the NASA Dryden Dynamic Aircraft Maneuver Program (DAMP). The stabilized envelope encompasses approximately 85 percent of the rapid maneuver envelope at M = 0.3 and 62 percent at M = 0.4.

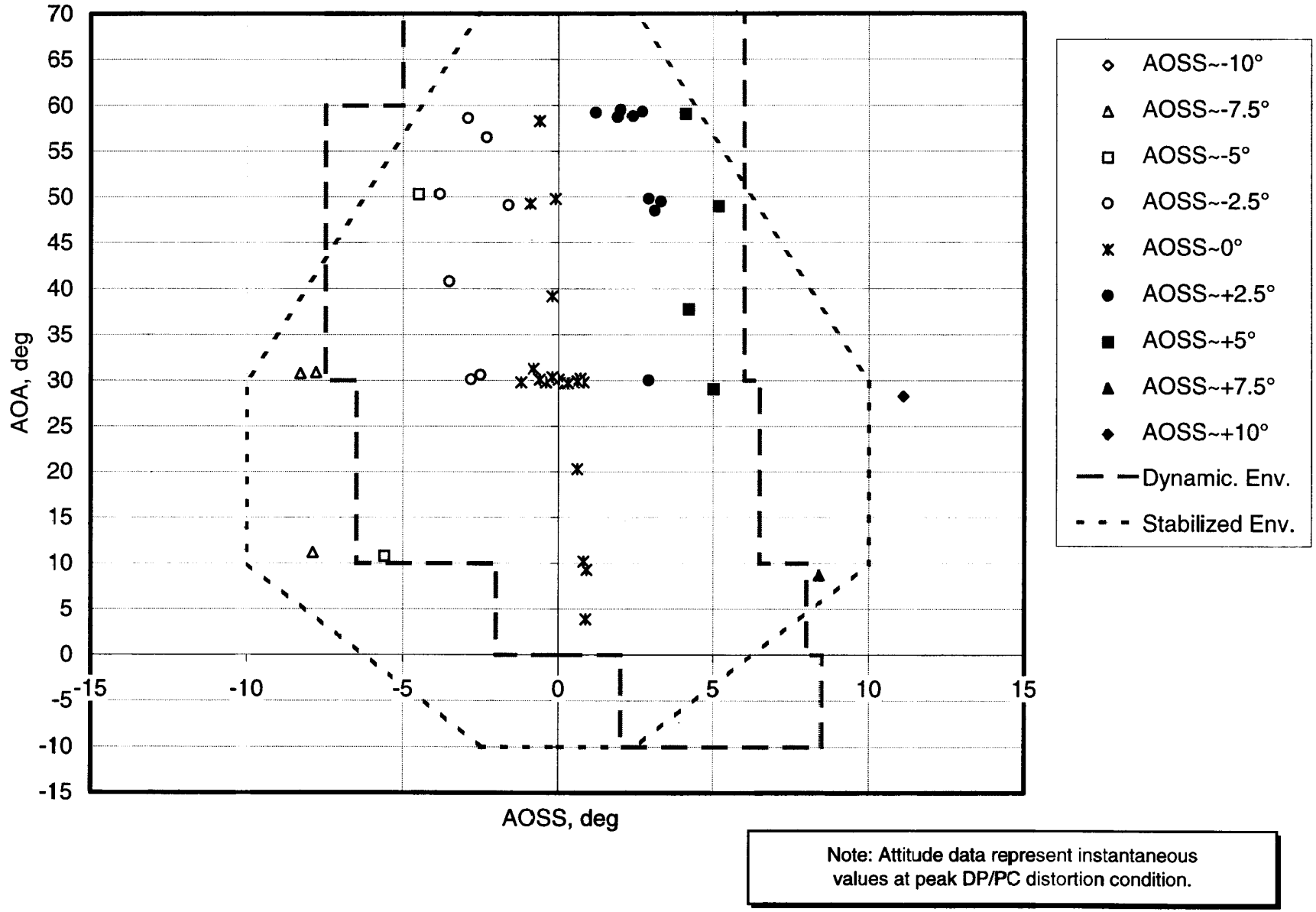

Figure 3. M=0.3 HARV Stabilized Maneuver Database.

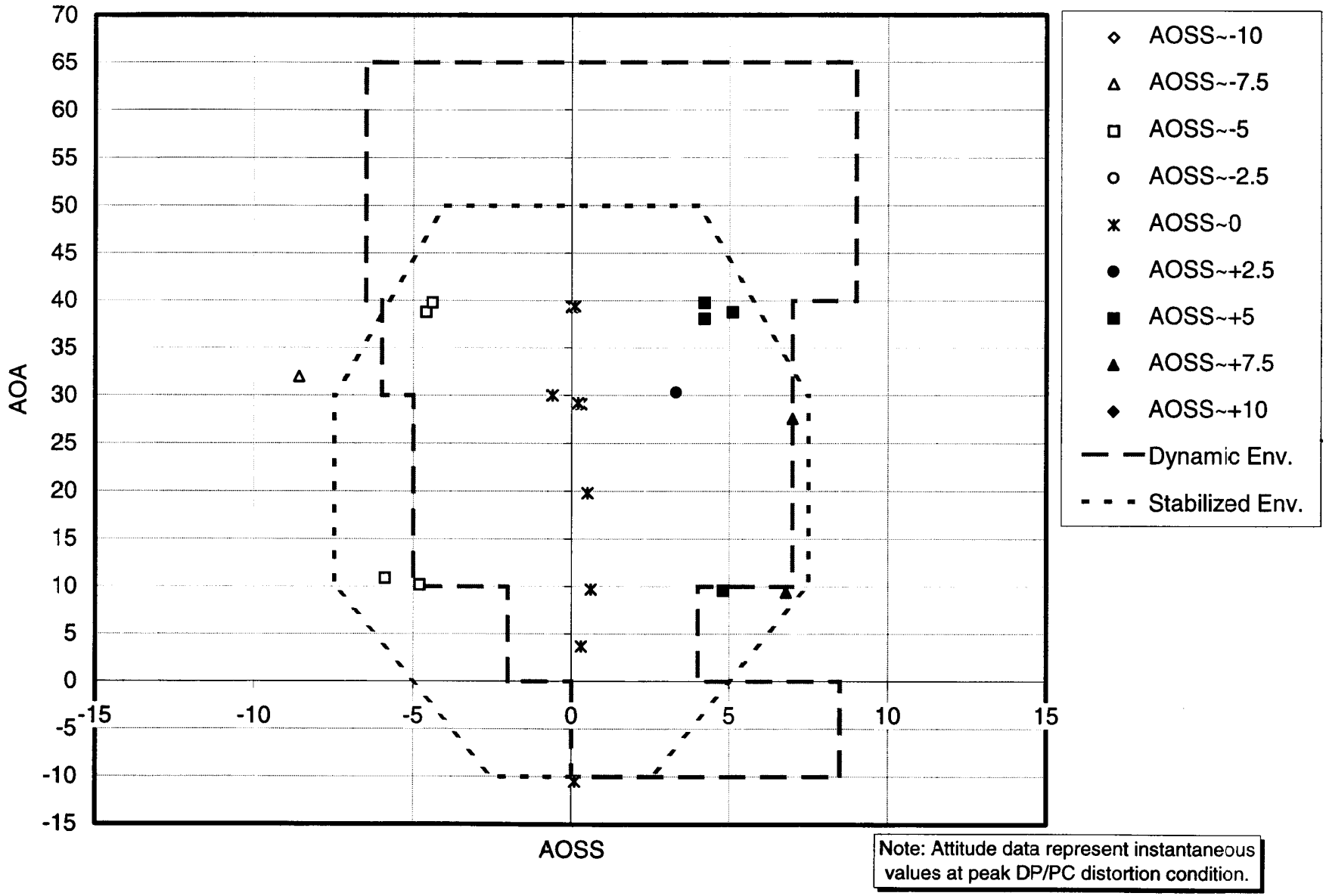

Figure 4. M=0.4 HARV Stabilized Maneuver Database.

4.2 Peak Dynamic Distortion Representations

Data tables were formulated describing the trends in HARV peak circumferential and radial dynamic distortion levels as functions of angle-of-attack and sideslip during high power operation in the Mach = 0.3 to 0.4 flight regime for incorporation into the DAMP. Details are provided in Tables 4 and 5. The trends used the instantaneous values for aircraft Mach number and aerodynamic attitude at the peak dynamic circumferential distortion index condition.

The procedure to define the trends of the peak dynamic distortion data was as follows: boundary lines were established that encompassed the highest peak dynamic distortion values. By definition, these lines represented the highest dynamic distortion levels encountered as a function of instantaneous angle-of-sideslip and angle-of-attack obtained during steady aerodynamic maneuvers. These levels are then compared with values measured during dynamic maneuver testing. The boundary lines were used to establish the tabulations, extrapolations, and cross-plots in terms of angle-of-sideslip and angle-of-attack. The process was iterated to provide continuous data trends as a function of the vehicle aerodynamic attitude.

Descriptions of the measured results and established trends of the peak dynamic circumferential distortion index (DP/PC max) as a function of vehicle Mach number and attitude are provided in Figures 5 - 8. The relative magnitudes of the measured and modeled levels for the peak dynamic distortion are illustrated in Figure 9. The correspondence is good. Contained in this figure are the mean, maximum, minimum, and standard deviation values for the difference (error) of the model from the measured level. By intent, the measured values tend not to exceed the modeled values.

Similar descriptions of the measured results and established trends of the peak dynamic radial distortion index (DP/PR max) are provided in Figures 10 - 13. The relative magnitudes of the measured and modeled levels for this peak dynamic distortion index are illustrated in Figure 14.

4.3 Inlet Recovery Representation

In a similar manner to the peak dynamic distortion levels, data tables were formulated describing the trends in HARV inlet recovery as a function of angle-of-attack and sideslip during high power operation in the Mach = 0.3 to 0.4 flight regime for incorporation into the DAMP. Details are provided in Table 6.

The data matching procedure was as follows: trend curves were generated for the measured data. These trends were used as the basis for the tabulations, extrapolations, and cross-plots in terms of angle-of-sideslip and angle-of-attack to the actual data. The process was iterated to provide smooth and continuous data trends as a function of the vehicle aerodynamic attitude(s).

Descriptions of the measured results and established trends of inlet recovery as functions of vehicle Mach number and attitude are provided in Figures 15 - 18.

The relative magnitudes of the measured and modeled levels for inlet recovery are illustrated in Figure 19. The correspondence is good. Contained in this figure are the mean, maximum, minimum, and standard deviation values for the difference (error) of the model from the measured level. The largest differences occur at conditions where there were variations between several measured-data values.

Table 4. Peak Dynamic Circumferential Distortion Representation.

Base (@M=0.3)		AOSS, deg						
		-10.0	-5.0	-2.5	0.0	2.5	5.0	10.0
AOA, deg	-10.3	0.108	0.104	0.103	0.095	0.079	0.075	0.080
	-8.6	0.104	0.100	0.098	0.090	0.075	0.071	0.075
	3.6	0.075	0.072	0.064	0.055	0.046	0.043	0.040
	10.0	0.089	0.085	0.080	0.070	0.059	0.055	0.050
	20.1	0.075	0.072	0.064	0.055	0.046	0.043	0.040
	30.0	0.104	0.100	0.098	0.090	0.075	0.071	0.075
	39.2	0.129	0.124	0.122	0.113	0.105	0.101	0.101
	49.4	0.163	0.156	0.152	0.139	0.132	0.125	0.125
	56.6	0.189	0.182	0.179	0.167	0.156	0.150	0.150
	59.2	0.198	0.192	0.189	0.177	0.164	0.159	0.159
	70.0	0.236	0.232	0.230	0.215	0.199	0.196	0.196

Mach Number Derivative		AOSS, deg						
		-10.0	-5.0	-2.5	0.0	2.5	5.0	10.0
AOA, deg	-10.3	0.560	0.360	0.260	0.180	0.320	0.350	0.300
	3.7	0.150	-0.030	-0.090	-0.100	-0.030	0.020	0.000
	10.5	0.200	0.050	-0.020	-0.010	0.030	0.020	0.000
	19.7	0.230	0.050	0.010	0.000	0.050	0.080	0.050
	29.4	0.260	0.060	-0.060	-0.130	-0.070	-0.090	-0.170
	39.1	0.350	0.160	0.070	0.000	0.060	0.090	0.090
	70.0	0.350	0.160	0.070	0.000	0.060	0.090	0.090

Table 5. Peak Dynamic Radial Distortion Representation.

Base (@M=0.3)		AOSS, deg						
		-10.0	-5.0	-2.5	0.0	2.5	5.0	10.0
AOA, deg	-10.3	0.045	0.045	0.046	0.047	0.051	0.055	0.055
	-8.6	0.045	0.045	0.046	0.047	0.051	0.055	0.055
	3.6	0.050	0.050	0.053	0.057	0.057	0.057	0.057
	10.0	0.050	0.050	0.053	0.057	0.057	0.057	0.057
	20.1	0.044	0.044	0.045	0.046	0.050	0.054	0.054
	30.0	0.046	0.046	0.047	0.048	0.052	0.056	0.056
	39.2	0.052	0.052	0.055	0.059	0.059	0.059	0.059
	49.4	0.083	0.083	0.079	0.074	0.069	0.069	0.069
	56.6	0.096	0.096	0.095	0.093	0.087	0.080	0.080
	59.2	0.102	0.102	0.102	0.102	0.094	0.084	0.084
	70.0	0.121	0.121	0.121	0.121	0.113	0.103	0.103

Mach Number Derivative		AOSS, deg						
		-10.0	-5.0	-2.5	0.0	2.5	5.0	10.0
AOA, deg	-10.3	-0.160	-0.160	-0.170	-0.180	-0.220	-0.260	-0.260
	3.7	0.050	0.050	0.020	-0.020	-0.020	-0.020	-0.020
	10.5	0.050	0.050	0.020	-0.020	-0.020	-0.020	-0.020
	19.7	0.130	0.130	0.100	0.060	0.020	-0.020	-0.020
	29.4	0.110	0.110	0.080	0.040	0.000	-0.040	-0.040
	39.1	0.090	0.090	0.060	0.010	0.000	0.000	0.000
	70.0	0.090	0.090	0.060	0.010	0.000	0.000	0.000

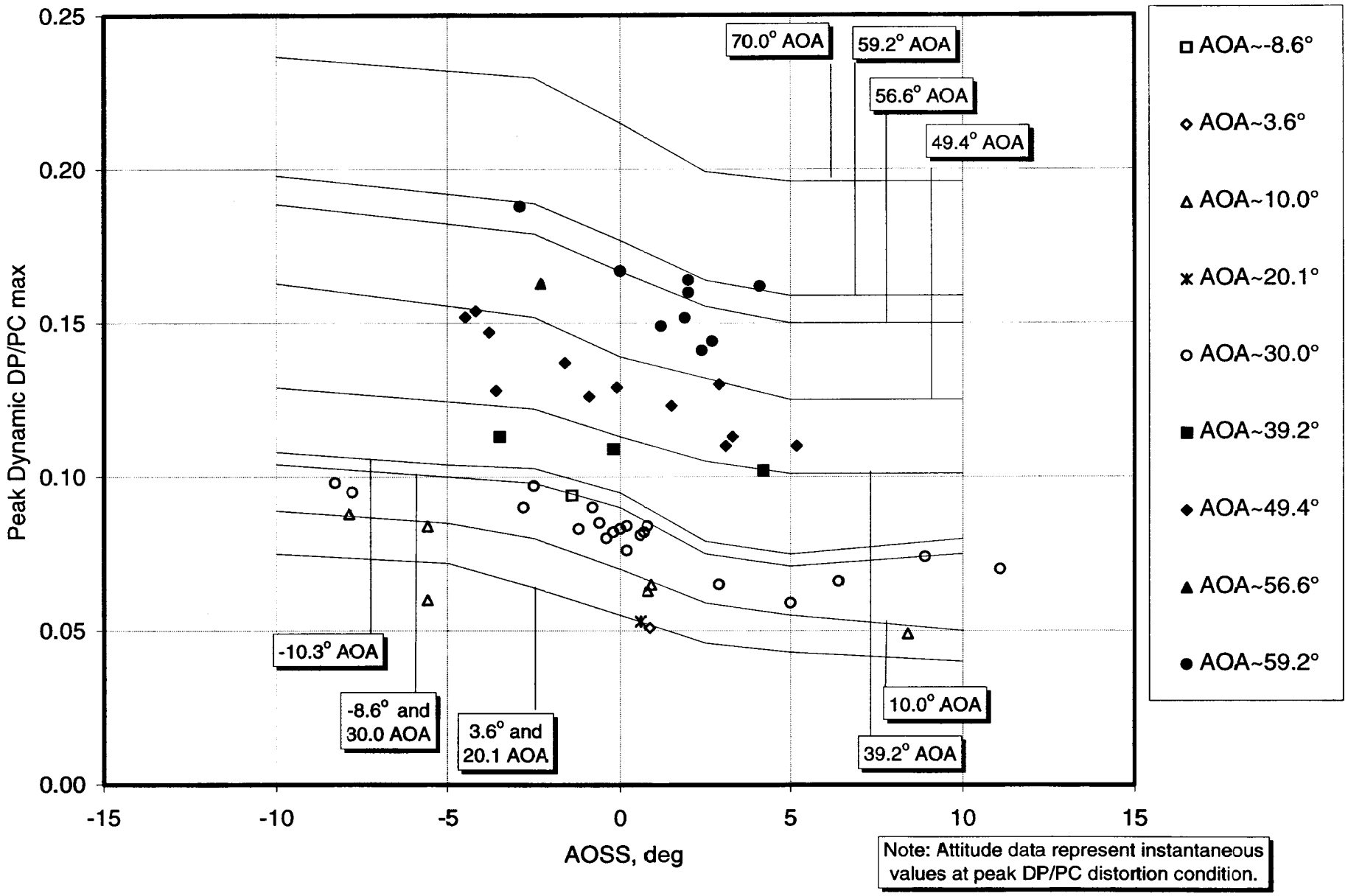

Figure 5. Representation of M=0.3 Peak Dynamic Circumferential Distortion as a Function of Angle of Sideslip.

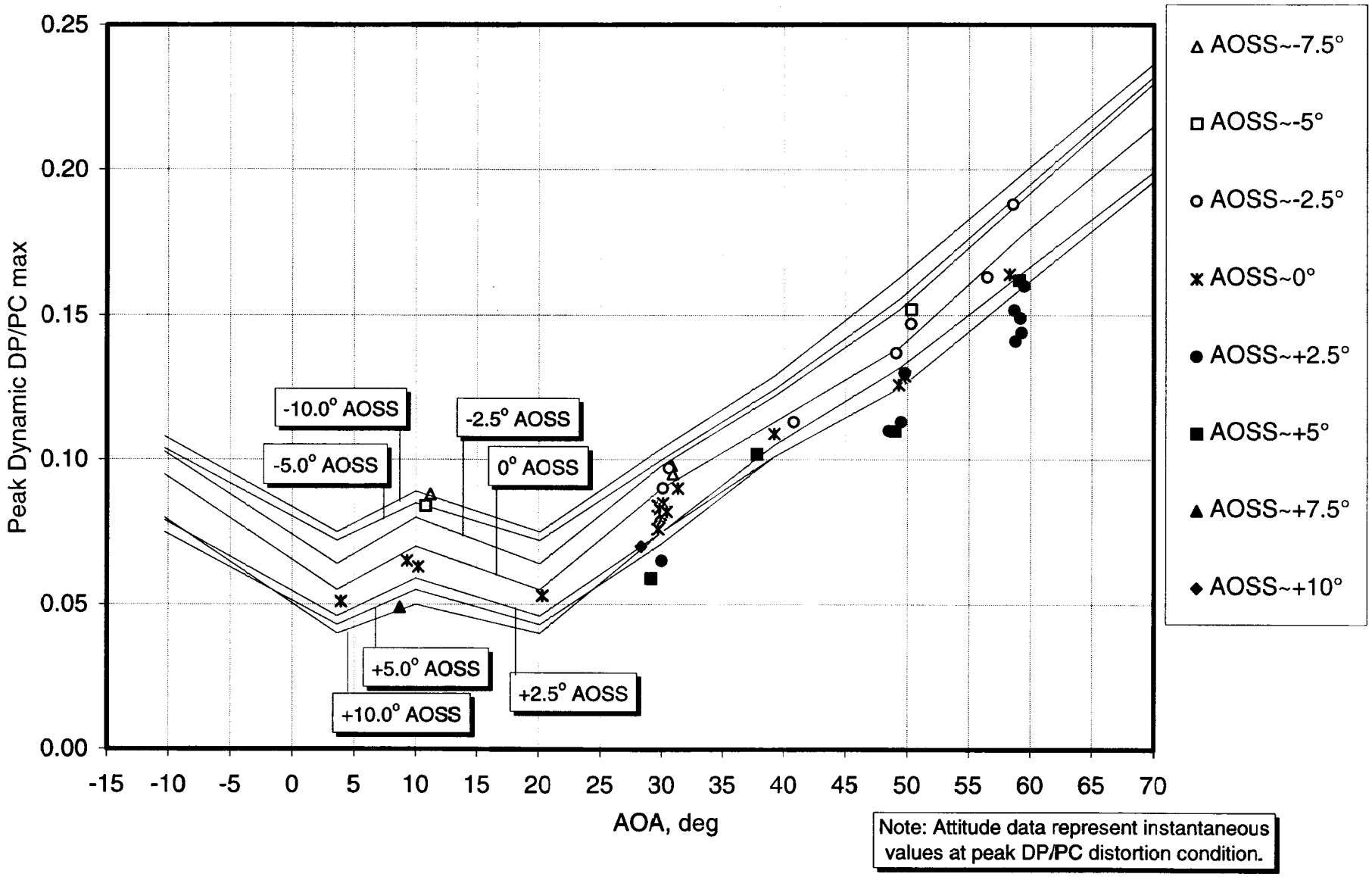

Figure 6. Representation of M=0.3 Peak Dynamic Circumferential Distortion as a Function of Angle of Attack.

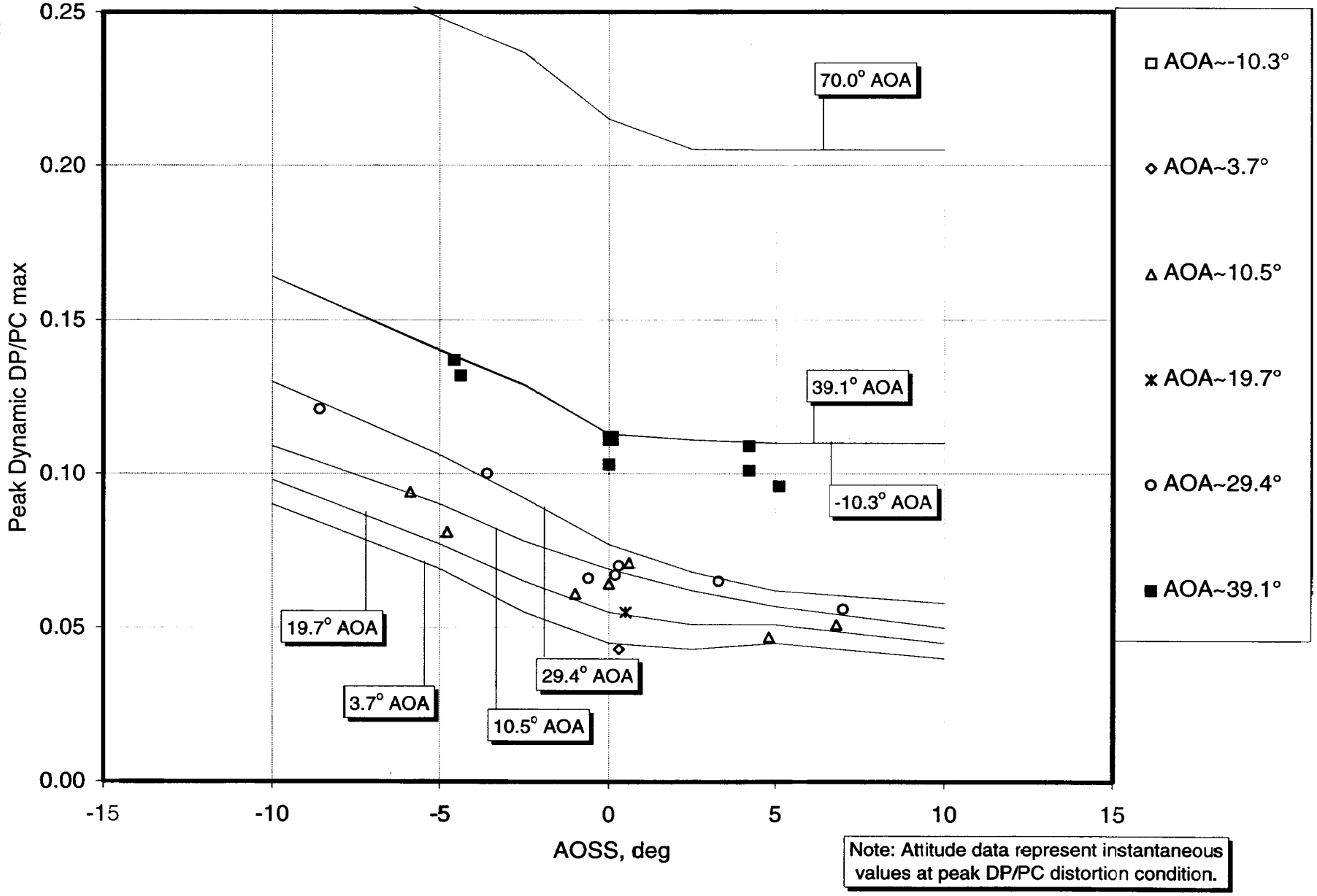

Figure 7. Representation of M=0.4 Peak Dynamic Circumferential Distortion as a Function of Angle of Sideslip.

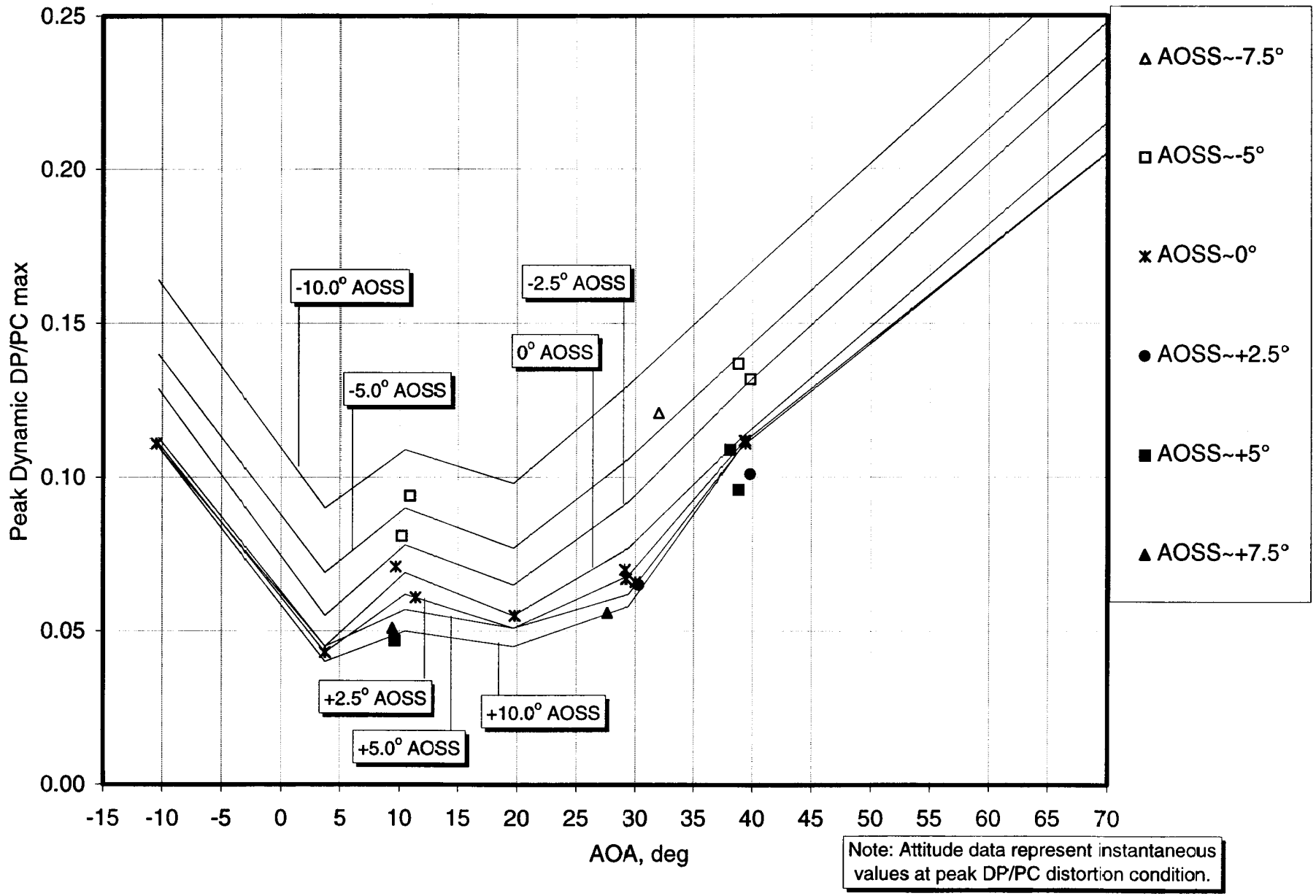

Figure 8. Representation of M=0.4 Peak Dynamic Circumferential Distortion as a Function of Angle of Attack.

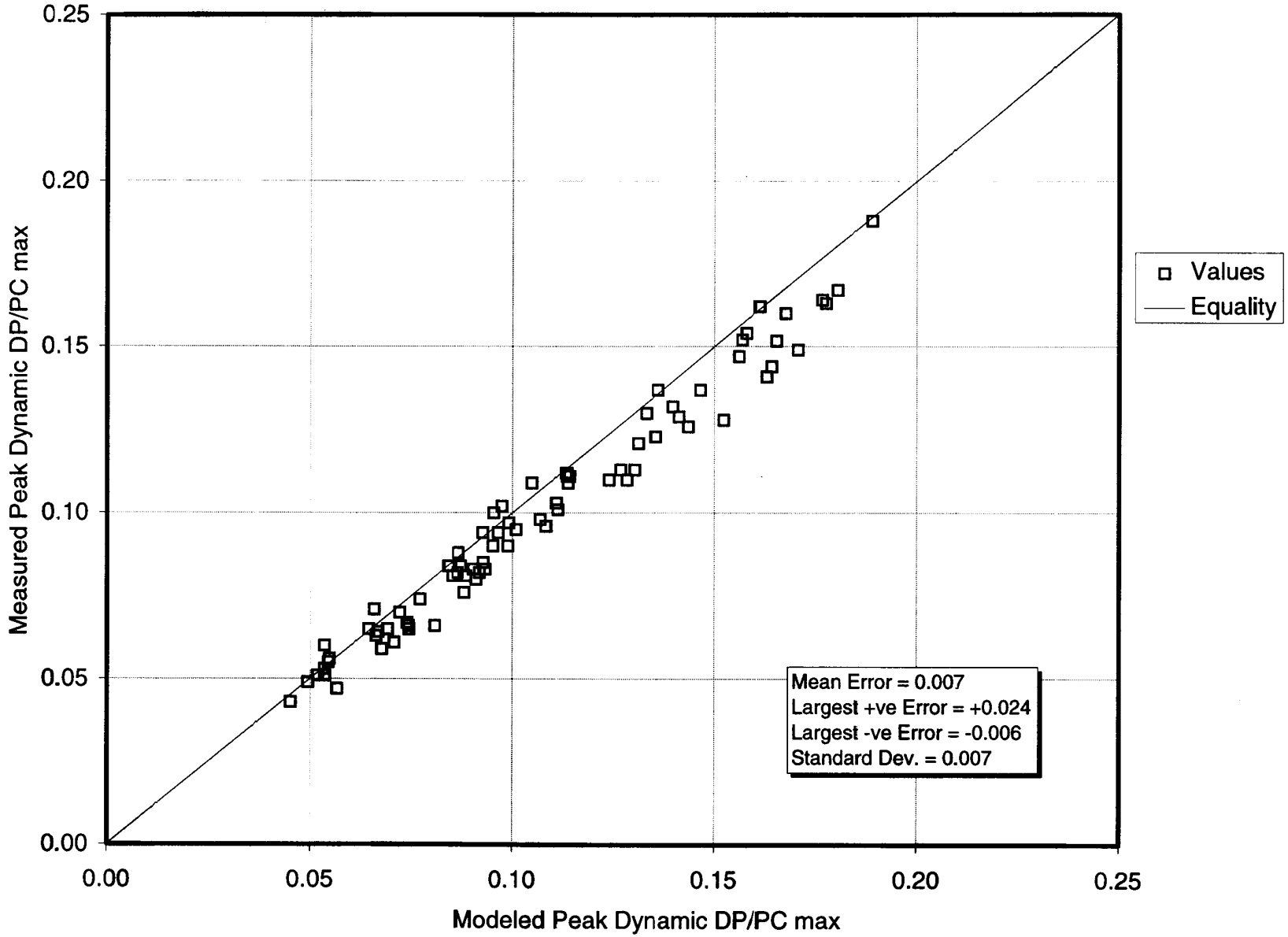

Figure 9. Comparison of Measured and Modeled Peak Dynamic Circumferential Distortion.

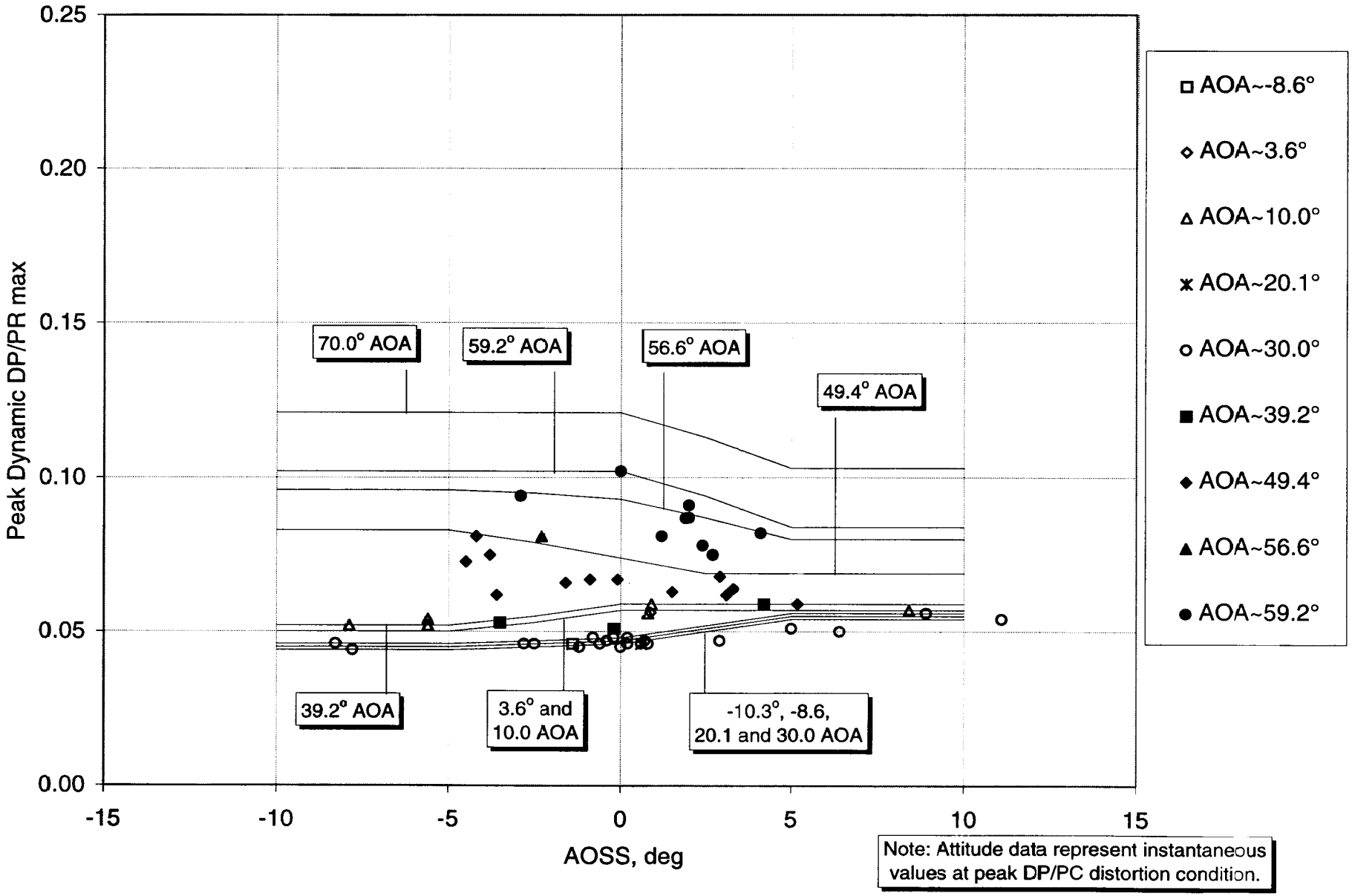

Figure 10. Representation of M=0.3 Peak Dynamic Radial Distortion as a Function of Angle of Sideslip.

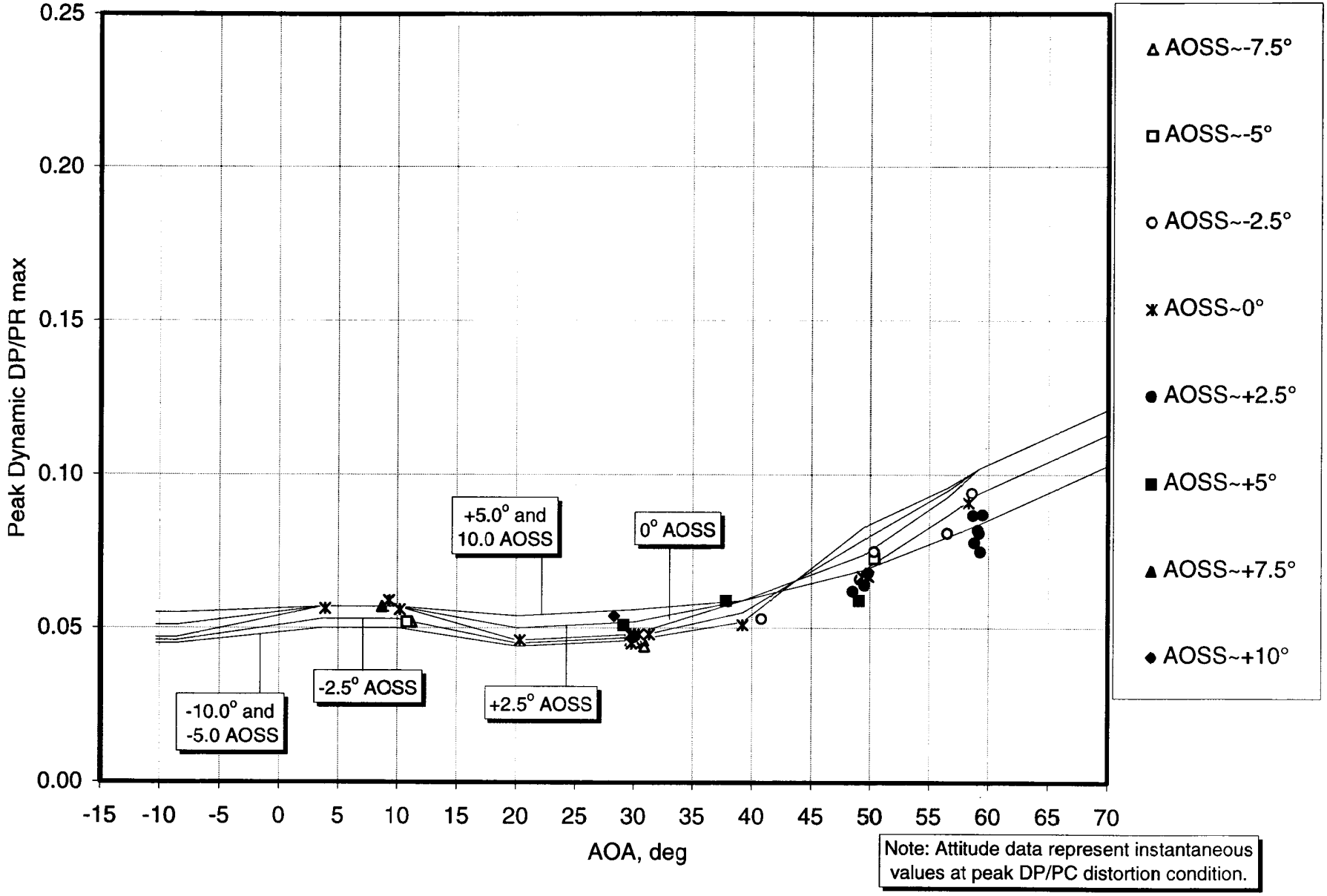

Figure 11. Representation of M=0.3 Peak Dynamic Radial Distortion as a Function of Angle of Attack.

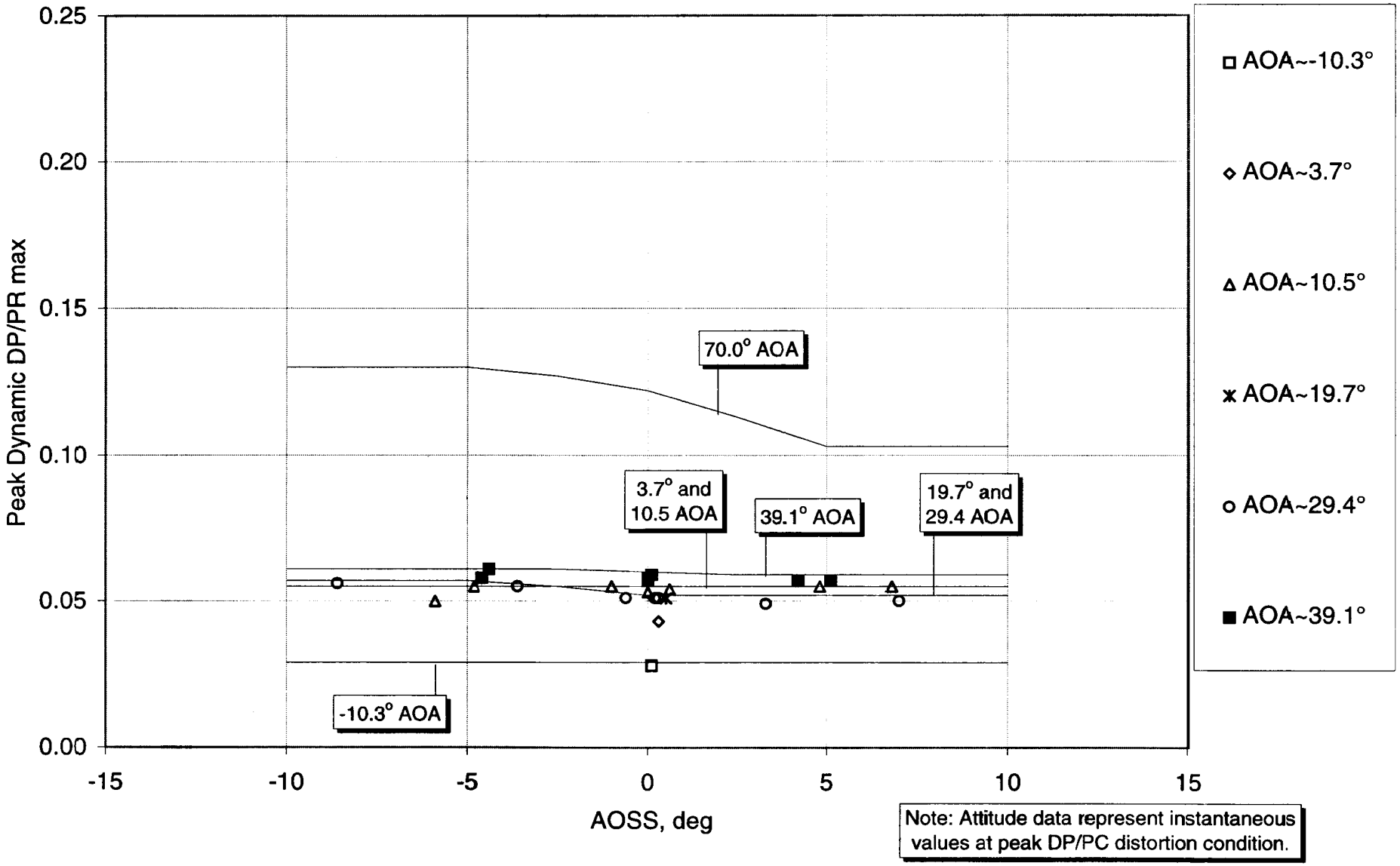

Figure 12. Representation of M=0.4 Peak Dynamic Radial Distortion as a Function of Angle of Sideslip.

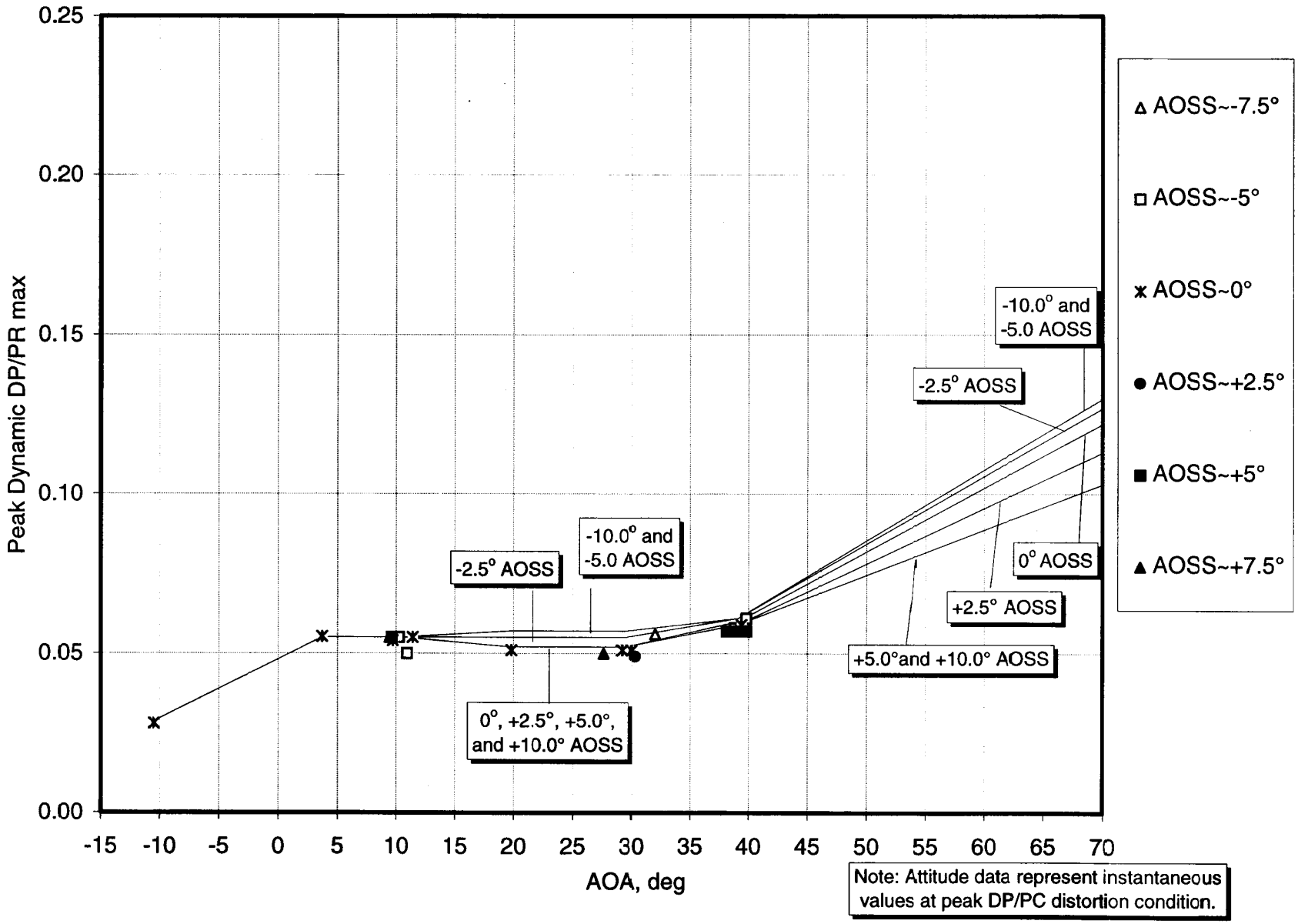

Figure 13. Representation of M=0.4 Peak Dynamic Radial Distortion as a Function of Angle of Attack.

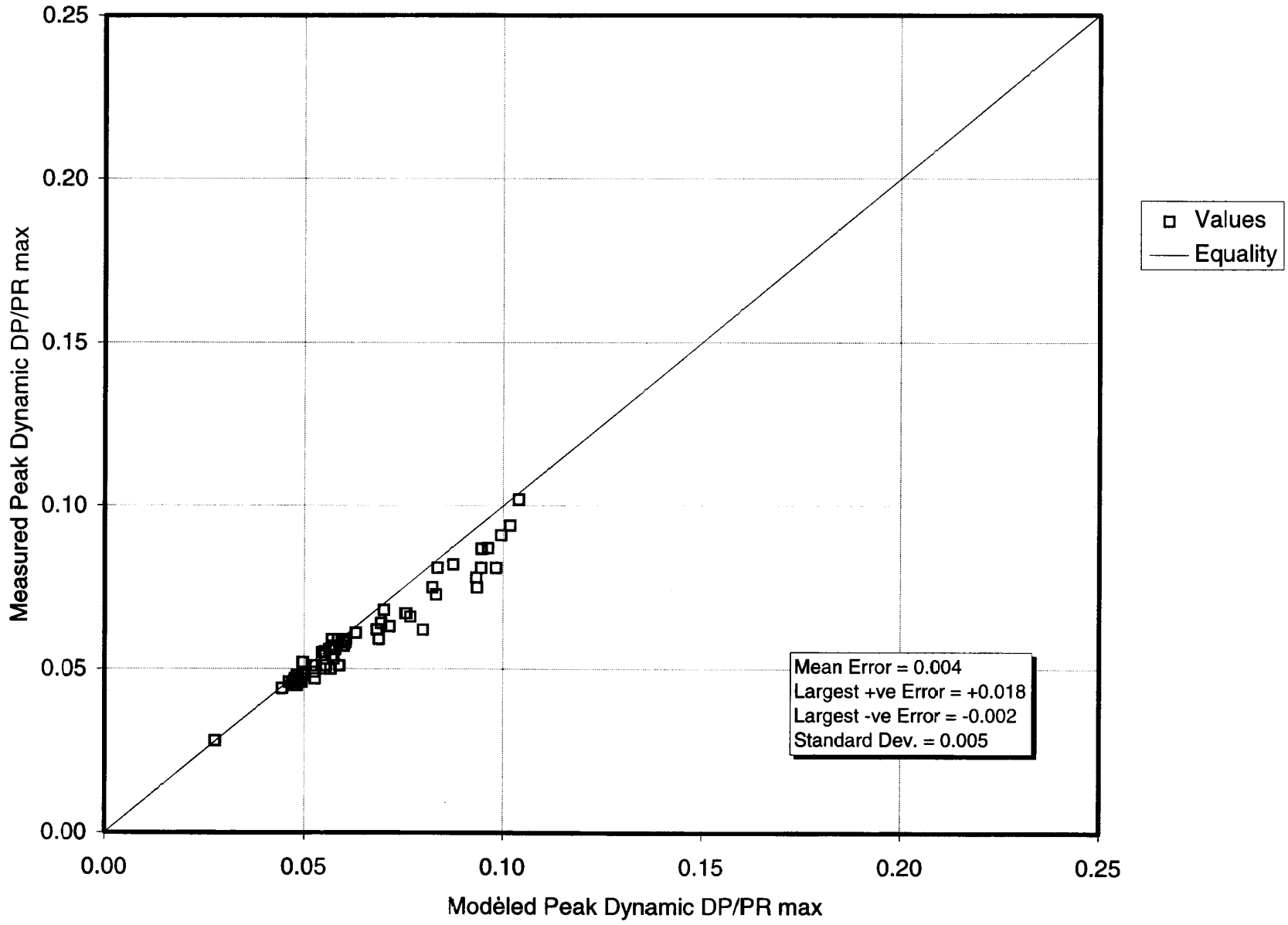

Figure 14. Comparison of Measured and Modeled Peak Dynamic Radial Distortion.

Table 6. Inlet Recovery Representation.

Base (@M=0.3)		AOSS, deg						
		-15.0	-10.0	-5.0	0.0	5.0	10.0	15.0
AOA, deg	-10.3	0.9364	0.9474	0.9564	0.9610	0.9619	0.9604	0.9589
	-8.6	0.9380	0.9490	0.9580	0.9626	0.9635	0.9620	0.9605
	3.6	0.9558	0.9633	0.9685	0.9725	0.9733	0.9708	0.9683
	10.0	0.9575	0.9650	0.9702	0.9742	0.9750	0.9725	0.9700
	20.1	0.9595	0.9670	0.9722	0.9762	0.9770	0.9745	0.9720
	30.0	0.9505	0.9590	0.9660	0.9701	0.9710	0.9690	0.9670
	39.2	0.9335	0.9455	0.9550	0.9597	0.9610	0.9615	0.9615
	49.4	0.9070	0.9180	0.9285	0.9397	0.9500	0.9530	0.9540
	56.6	0.8820	0.8930	0.9035	0.9150	0.9310	0.9375	0.9400
	59.2	0.8715	0.8825	0.8935	0.9044	0.9200	0.9275	0.9300
	70.0	0.8271	0.8381	0.8491	0.8600	0.8756	0.8831	0.8856

Mach Number Derivative		AOSS, deg						
		-15.0	-10.0	-5.0	0.0	5.0	10.0	15.0
AOA deg	-10.3	-0.1365	-0.0990	-0.0615	-0.0240	0.0005	0.0005	0.0005
	3.7	-0.1125	-0.0750	0.0035	0.0410	0.0655	0.0800	0.0800
	10.5	-0.1125	-0.0750	0.0035	0.0410	0.0655	0.0800	0.0800
	19.7	-0.1325	-0.0950	-0.0165	0.0210	0.0455	0.0600	0.0600
	29.4	-0.1620	-0.1080	-0.0170	0.0370	0.0730	0.0800	0.0800
	39.1	-0.1590	-0.1060	-0.0180	0.0350	0.0720	0.0720	0.0720
	70.0	-0.1590	-0.1060	-0.0180	0.0350	0.0720	0.0720	0.0720

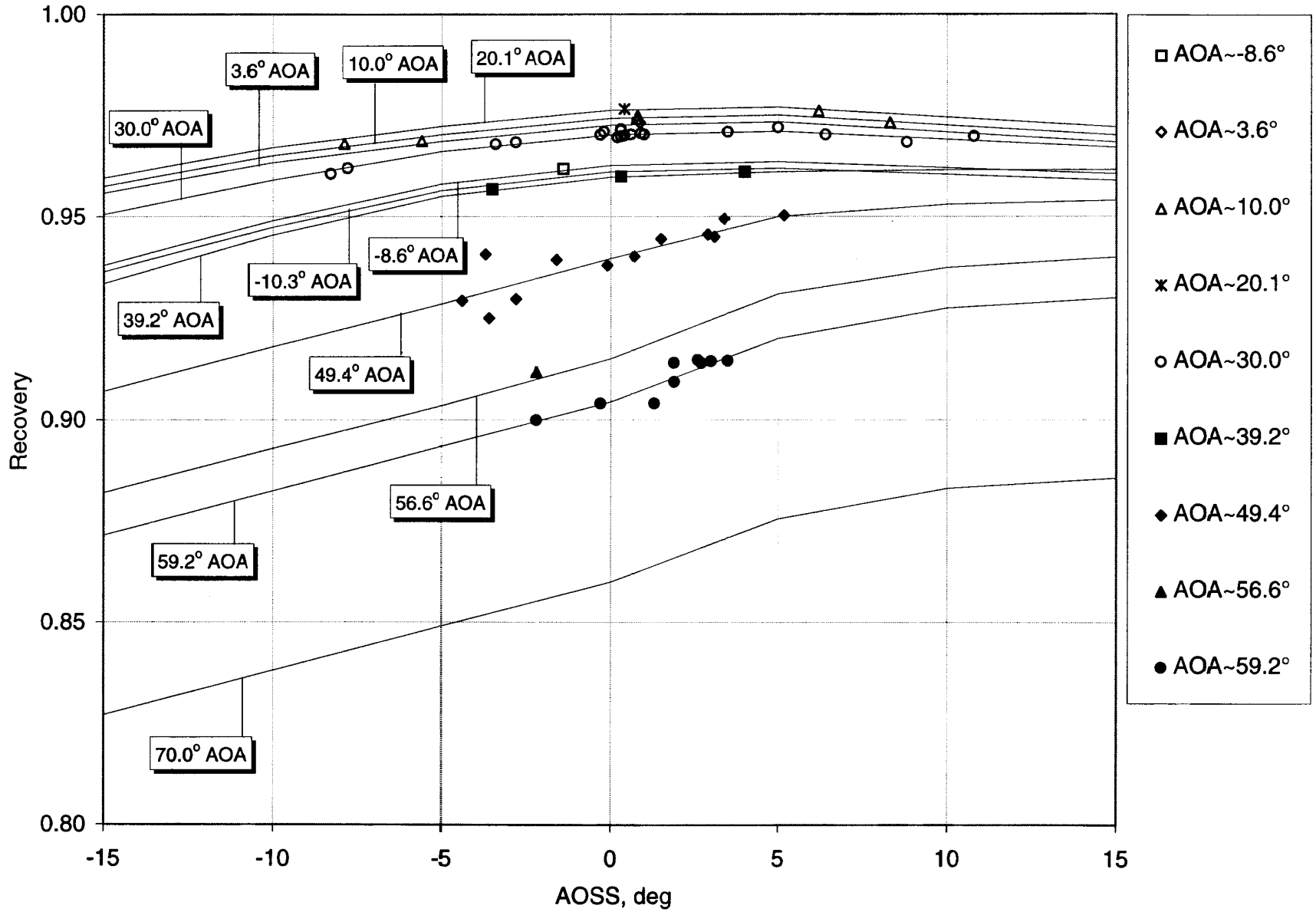

Figure 15. Representation of M=0.3 Inlet Recovery as a Function of Angle of Sideslip.

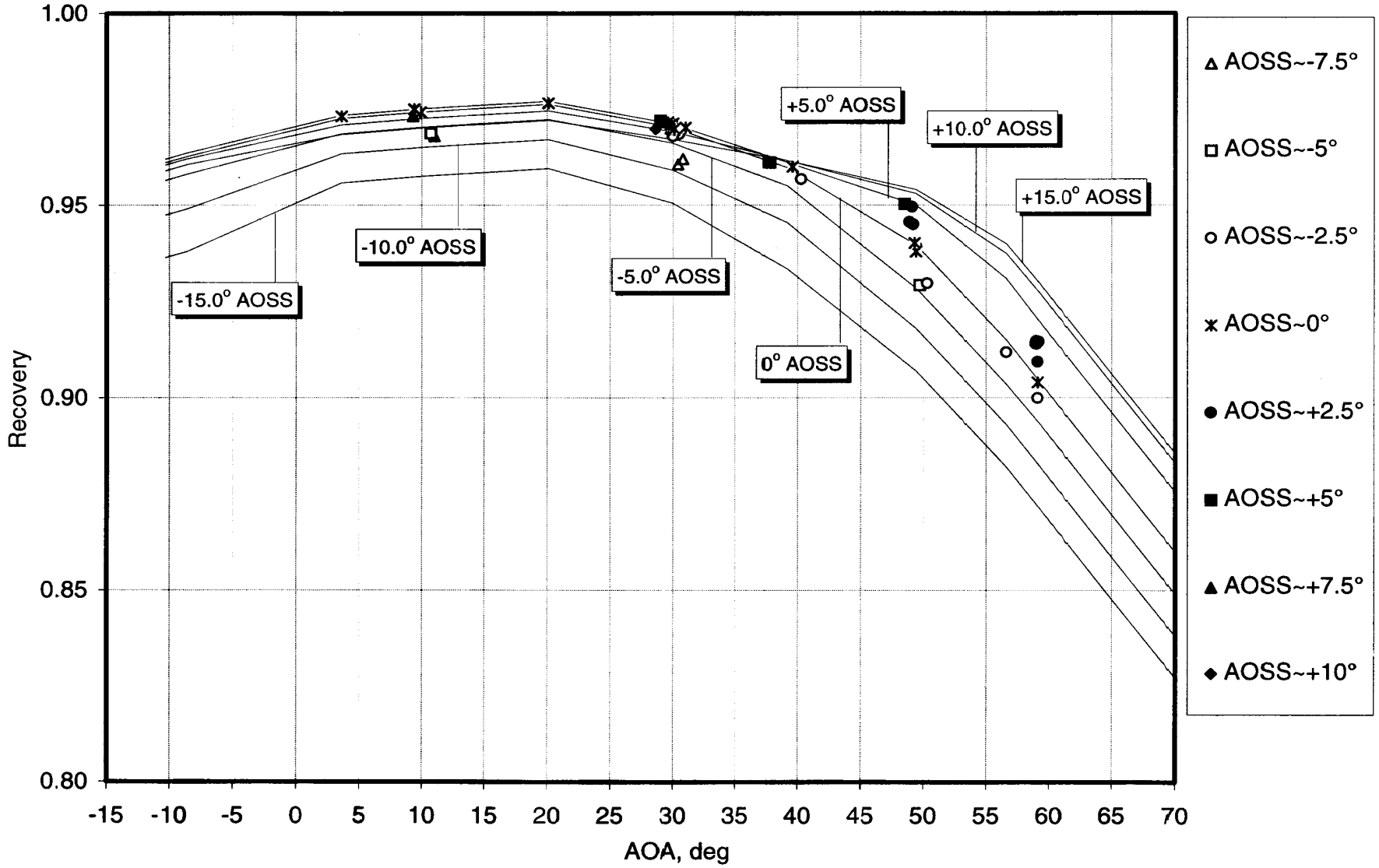

Figure 16. Representation of M=0.3 Inlet Recovery as a Function of Angle of Attack.

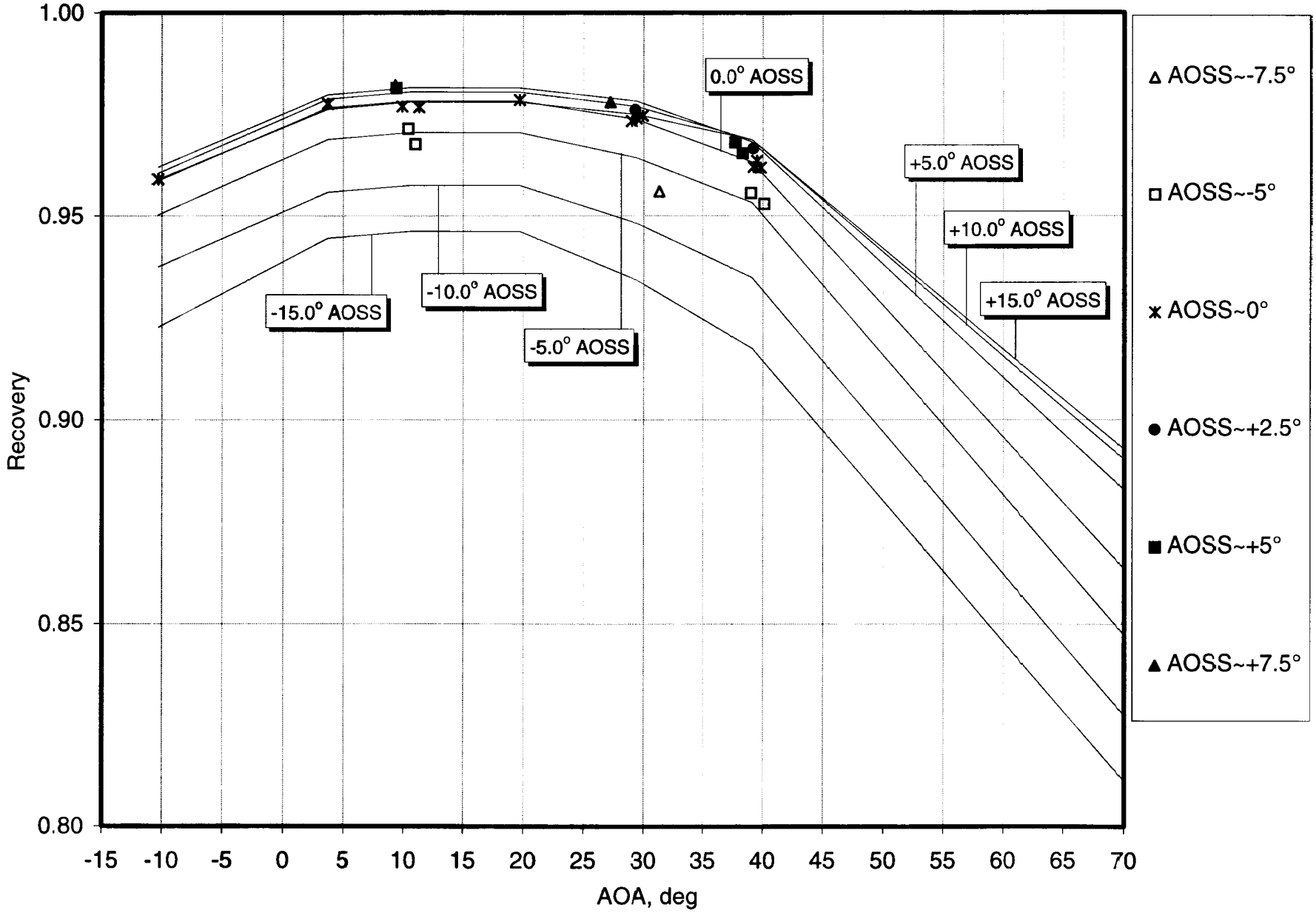

Figure 17. Representation of M=0.4 Inlet Recovery as a Function of Angle of Attack.

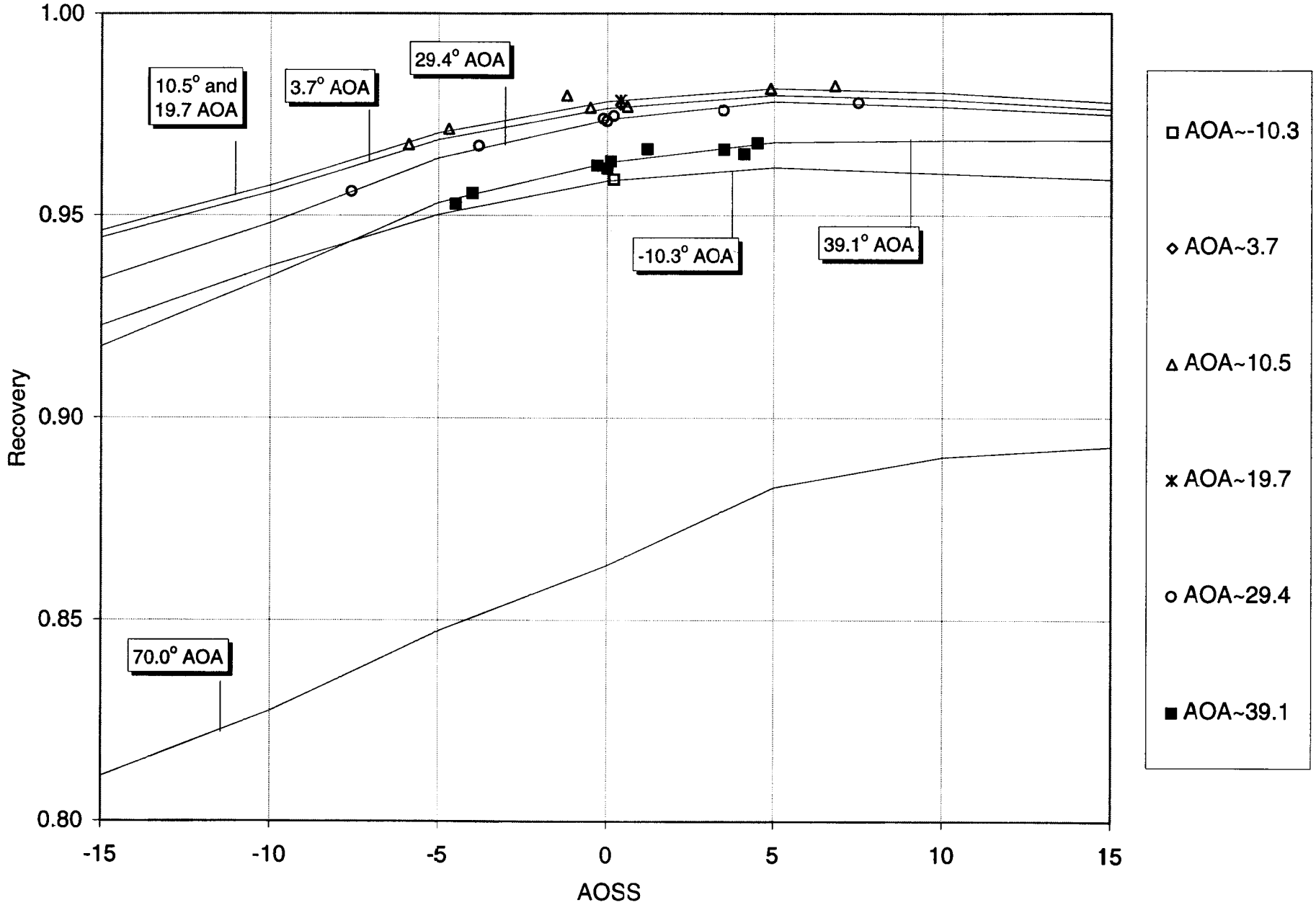

Figure 18. Representation of M=0.4 Inlet Recovery as a Function of Angle of Sideslip.

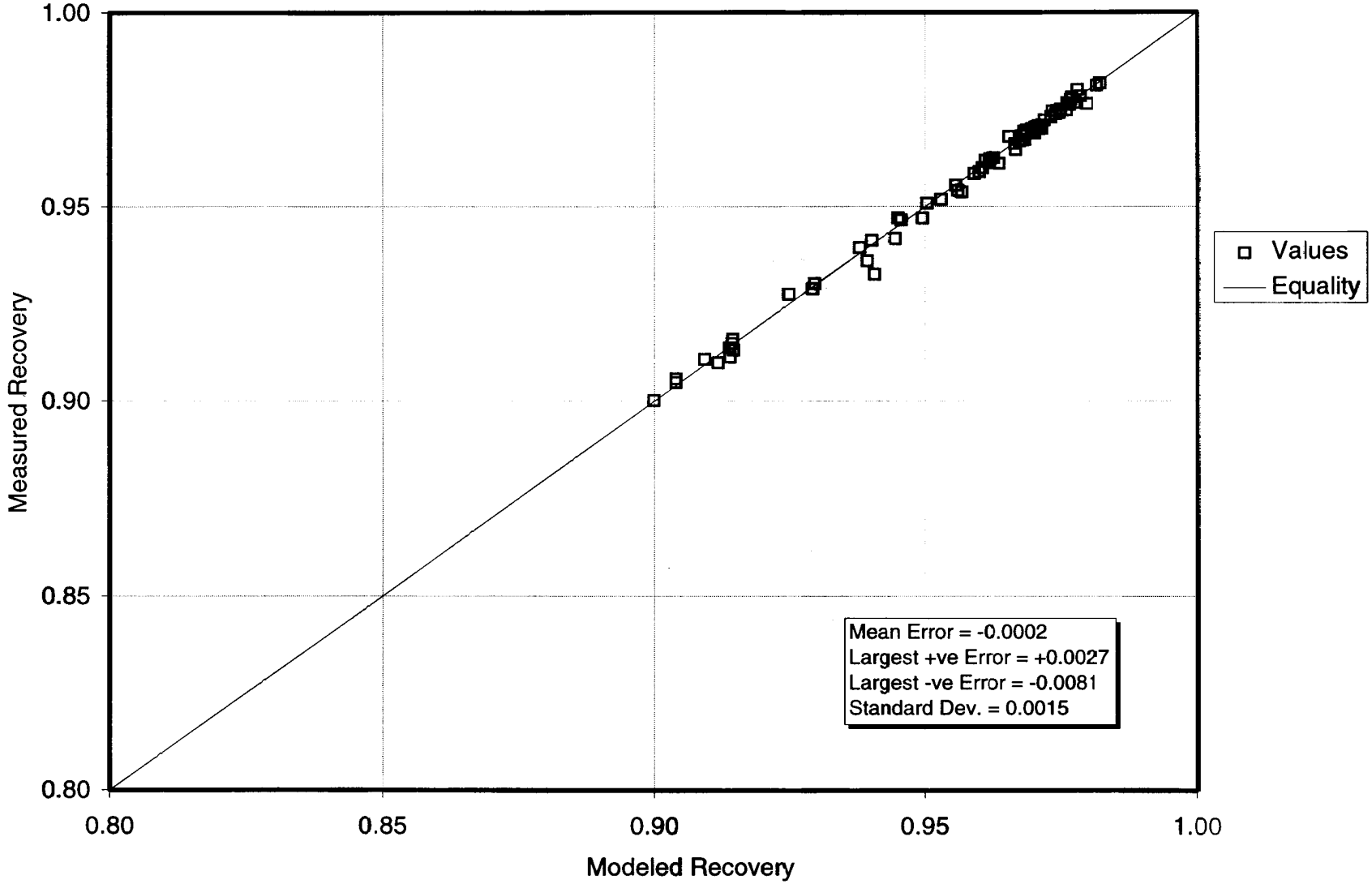

Figure 19. Comparison of Measured and Modeled Inlet Recovery.

5.0 DISCUSSION OF RESULTS

In an effort to illustrate the data format employed in this report and to help maintain conciseness, the analysis discussion will be based on the data from selected, though typical test points. The majority of the discussion will be illustrated by the results obtained from Flight 236, Test Point 22b, a low-to-high angle of attack rapid maneuver (see Table 2, page 12). The data for all 50 rapid maneuver conditions are contained in Appendices B (M = 0.3 results) and C (M = 0.4 results), and are presented in the same format as discussed in the next paragraph.

5.1 Data Format

The Flight 236, Test Point 22b data are presented in a three-figure format as illustrated by Figures 20 - 22. The time duration of all plots has been selected to be 6 seconds so that the "initial conditions" prior to the rapid maneuver can be viewed. The monotonically increasing or decreasing angle-of-attack maneuvers were generally accomplished within 2 - 3 seconds while the more complex rapid maneuvers (e.g., mid-to-low-to-high) generally took about five seconds to accomplish. The first figure of the set (Figure 20) shows time histories of aircraft angle of attack (AOATJ) and sideslip (AOSSTJ), calculated using trajectory reconstruction, in the upper window; aircraft Mach number in the middle window; and inlet recovery obtained in three ways in the bottom window. The three recoveries represent the following:

- The dynamic recovery obtained from the high-response transducers at the AIP (ERAMB),
- The recovery obtained from the slow-response (steady-state) transducers (EERAM), and
- The recovery estimate obtained from the computer model based on the stabilized maneuver data (ZERAMST).

The second figure in the set (Figure 21) presents the dynamic circumferential (ZDCPCF) and radial (ZIDR) distortion values obtained during the rapid maneuver as functions of time with the peak dynamic circumferential (ZDCPCFST) and radial (ZIDRST) distortion values, as obtained from the computer model, superposed for comparison.

The recovery, circumferential distortion, and radial distortion estimates from the computer model all show evidence of the linear fit between data points showing discontinuities in slope where none exist and possibly missing nuances seen in the data due to the finite separation of test data points.

The top window of third figure of the set (Figure 22) shows the angle of attack/angle of sideslip trajectory during the rapid maneuver to provide a graphical picture of the manner in which the angle of sideslip behaves during the maneuver. The bottom window is a plot of the measured recovery (ERAMB) versus the computer model recovery (ZERAMST), thus providing at a glance, an insight relative to the degree of correspondence between the two. The straight lines represent an agreement band of ± 0.01 points of recovery around the data.

These three figures contain the basic set of data for each rapid maneuver and provide the data necessary for conducting analyses and drawing conclusions. The data for all 50 rapid maneuver flight test points are contained in Appendices B and C, and are presented in the same three figure format. The maneuvers in the appendices are further organized by angle-of attack category: low-to-high, high-to-low, mid-to-high, mid-to-low-to-high, and mid-to-low-to-mid.

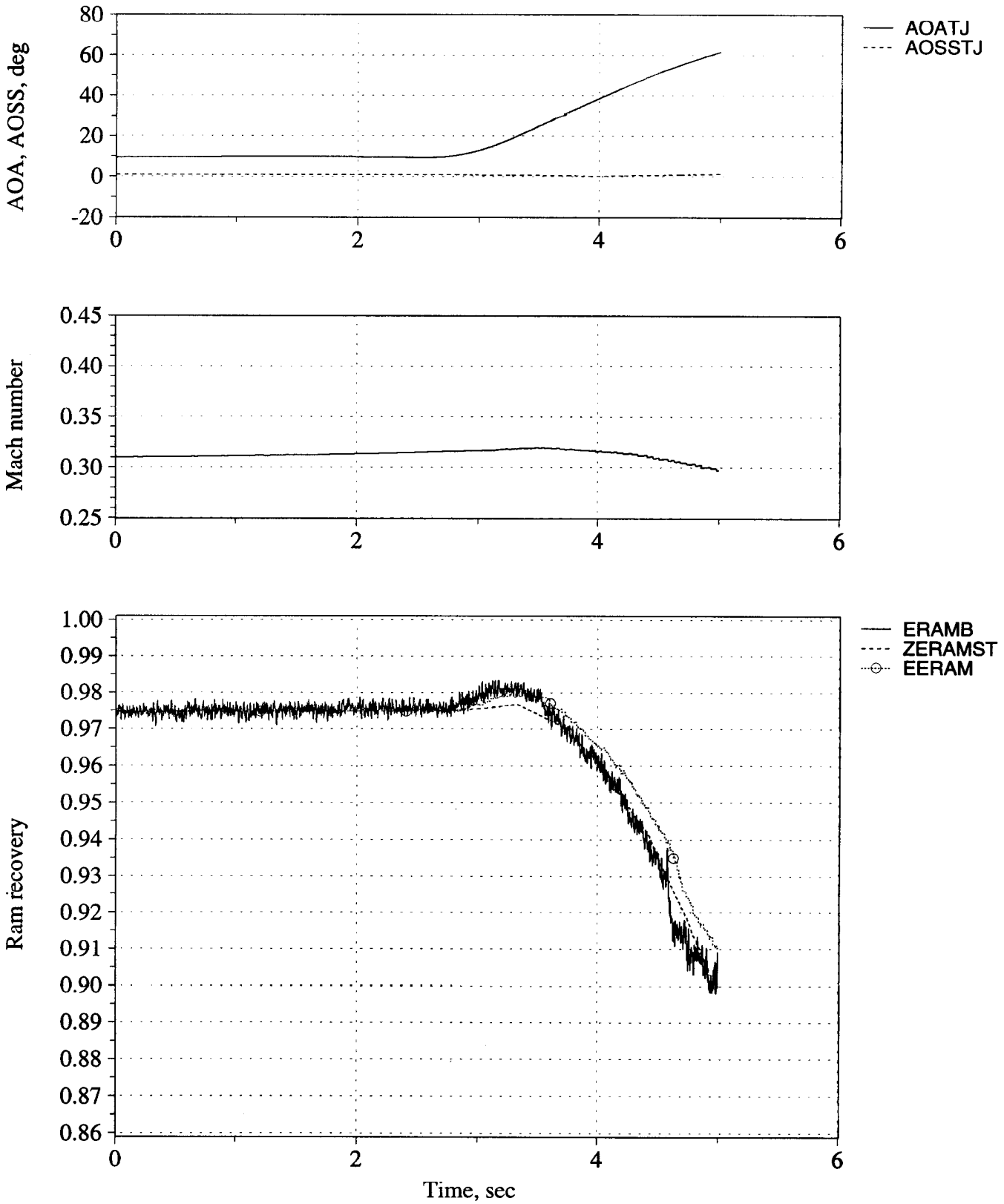

Figure 20. Time history of angle of attack, angle of sideslip, Mach number, and inlet recovery (measured and estimated) - Flight 236, Test point 22b.

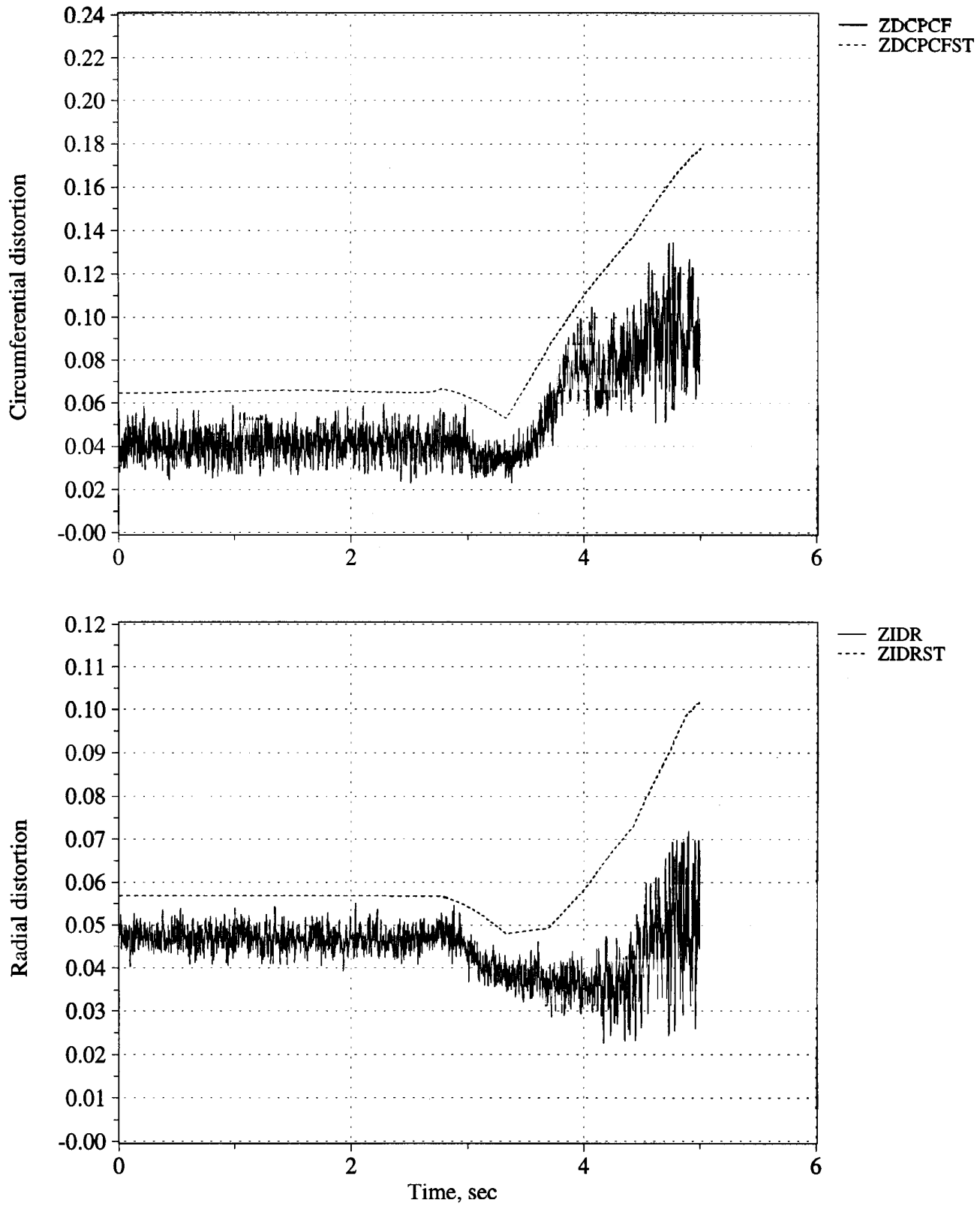

Figure 21. Time history of peak inlet dynamic circumferential and radial distortion (measured and estimated) - Flight 236, Test point 22b.

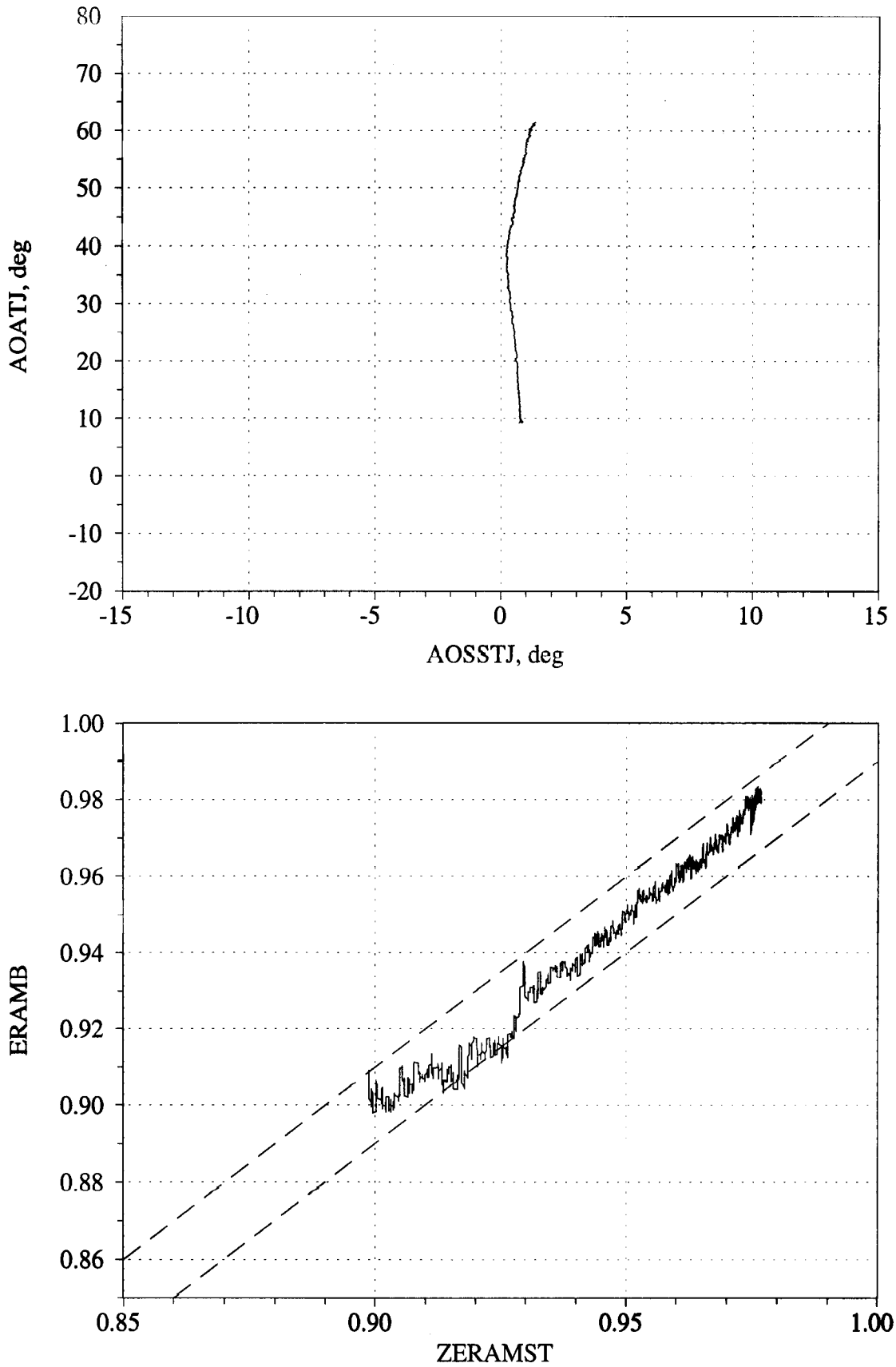

Figure 22. Angle of attack/angle of sideslip trajectory during maneuver; and measured versus estimated recovery - Flight 236, Test point 22b.

5.2 Data Consistency

Significant effort was expended during the flight test program to control some key parameters, namely Mach number and angle of sideslip during the rapid maneuvers. The degree to which Mach number was controlled can be ascertained by careful examination of the middle window of Figure 20 or its equivalent in the appendices. The degree to which angle of sideslip was controlled can be ascertained by examination of the top window of Figure 20 and the top window of Figure 22 or the equivalents in the appendices.

In addition, data repeatability was addressed. Several rapid maneuver test points were flown that were near repeats of each other, e. g., Flight 230, Test Point 0b2 and Flight 230, Test Point 0b3 (see Appendix B). One can practically overlay the recovery, the circumferential distortion, and the radial distortion plots from one test point over the other. Similarly, there is good correspondence among inlet data when data are compared for the same Mach number, angle of attack, and angle of sideslip conditions, but taken as part of different test points.

5.3 Inlet Recovery

A review of the inlet recovery data shows that the dynamic recovery (ERAMB) follows the trends in all respects of the computer model recovery derived from the stabilized maneuver data. In general, the dynamic recovery data track the computer model recoveries within ±0.01 recovery units. The bottom window of Figure 22 shows an example of the data used to support these findings.

Detailed analysis of the Mach = 0.3 dynamic recovery data consistently indicate a significant change in the dynamic character of the recovery waveform as a function of time as the aircraft increases through approximately 52° angle of attack. Data of the type contained in the bottom window of Figure 20 illustrate this behavior. Also, it is in the angle of attack range of 52 - 62° that the recovery will be lower than the computer model values by more that 0.01 recovery units. This change in character appears to be planar since the time-dependent spatial distortion descriptors do not exhibit a similar behavior. Unfortunately, no data were acquired where the initial angle of attack was in the 52 - 62° range or greater during the high-to-low angle of attack maneuvers. If such data had been obtained, more insight as to the nature or cause of the behavior might have been gained. Lack of stabilized maneuver data upon which to base the computer model is not an obvious part of the explanation since, per Figure 15, data were available at 49.4, 56.6, and 59.2° angle of attack. However, close examination of Figure 15 for the approximately 1° angle of sideslip data at 59.2 degrees of angle of attack shows a spread which may be indicative of the dynamic activity noted.

Also of interest is to note that the computer model of the stabilized recovery data provides a good representation of the interplay between angle of attack and angle of sideslip. Flight 236, Test Point 18c (see Appendix B, Figures B73 - B75) is a good example of such data.

Analysis of the Mach = 0.4 dynamic recovery data showed similar results except that the angle of attack at which the dynamic character change was noted was approximately 48° and greater, the range of deviation being greater than -0.01.

5.4 Peak Dynamic Circumferential Distortion

The dynamic circumferential distortion was calculated according to the algorithm in Appendix A at each time step after each inlet total pressure was recalculated via a rolling average to give a filtered frequency content equivalent to approximately the one-per-rev frequency of the engine (≈107 Hz and see Paragraph 2.5.2). Typical results are displayed in the upper window of Figure 21 for a Mach = 0.3 case.

The dynamic circumferential distortion (ZDCPCF) is plotted as a function of time in a manner similar to the parameters of Figure 20. The dynamic distortion data follow the trend of the estimated peak dynamic distortion values (ZDCPCFST) as calculated from the model based on the data obtained from the stabilized maneuver data until the angle of attack exceeds approximately 38 degrees at which point the time-varying distortion data produce maximum values that are considerably less than those obtained from the stabilized maneuvers. Further, it is noted that the measured dynamic distortion data peaks generally fall within .01 units until the angle of attack exceeds the previously mentioned 38 degrees. The trends, repeatability, and correspondence between the measured data and the estimated peak values holds for the data of Table 2 until approximately 38 degrees angle of attack for all instances where the angle of attack is increasing in low-to-high and mid-to-high angle of attack rapid maneuvers.

From a stability assessment point of view, there is a need to be sure that the distortion values obtained during rapid maneuvers do not exceed those obtained during stabilized maneuver (or wind tunnel) testing. In no case did the peak distortion values obtained during dynamic maneuver testing exceed the estimated stabilized peak distortion values at high angles of attack where stability margin predictions are of prime concern. At low angles of attack, there were some minor exceedences (≤ 0.01). But because the distortion values are relatively low, they are of no consequence. However, there were cases where the distortion values exceeded the estimated distortion values by more than 0.01 based on the stabilized data base. Flight 213, Test Point 11b provides a good illustration of these types of cases and the data are shown in Figures 23 - 25. Consistently, when the angle of attack drops below approximately 10 degrees and especially when it is negative (Figure 23), the distortion values exceed the values obtained from the model (Figure 24) in the cases of high-to-low, mid-to-low-to-high, and mid-to-low-to-mid rapid maneuvers. In general, these exceedences occur in between the points for which stabilized data were obtained. It is believed that flow field disturbances generated outside the inlet such as vortices emanating from the LEX and being ingested by the inlet give rise to these exceedences, that is, stabilized testing was conducted at angles of attack where these flow field disturbances would not be ingested. But again, these are relatively low values of distortion and would not give rise to engine stability concerns.

Returning to the data in the top window of Figure 21 associated with high angle of attack, an effort has been made to assess why the time-varying distortion levels do not rise to the levels anticipated by the predictions of the model based on the stabilized maneuver data. It has been established that it is not an instrumentation problem for such levels of distortion are indicated by the initiation points of the high-to-low rapid maneuvers of Table 2. Interrogation of inlet-lip wall-static pressures at high angles of attack suggests that the mode of flow separation is changing. It may be that it takes a finite time for the separated flow to fully develop as would occur for the stabilized maneuver points and this time is longer than one second.

All the above findings are supported by the M = 0.4 data in all respects. One of the data sets at this Mach number (Flight 242, Test Point 21c - Figures C28 to C30 of Appendix C) illustrates the excellent degree to which the peak dynamic circumferential distortion data trends and magnitudes are represented by the model based on the stabilized maneuver data base for a case where there is significant interplay between angle of attack and angle of sideslip.

5.5 Peak Dynamic Radial Distortion

The dynamic radial distortion was calculated according to the algorithm in Appendix A at each time step in a manner similar to the procedure employed for the dynamic circumferential distortion as described in the previous paragraph. Typical data are displayed in the bottom window of Figure 21 for a Mach = 0.3 case. The dynamic radial distortion (ZIDR) is plotted as a function time in a manner similar to the parameters of Figure 20. The peak dynamic radial distortion estimated from the computer model based on the stabilized maneuver database is plotted as ZIDRST. In general, the measured dynamic radial distortion follows the trend of the peak dynamic radial distortion estimated by the computer model for M = 0.3 up to angles of

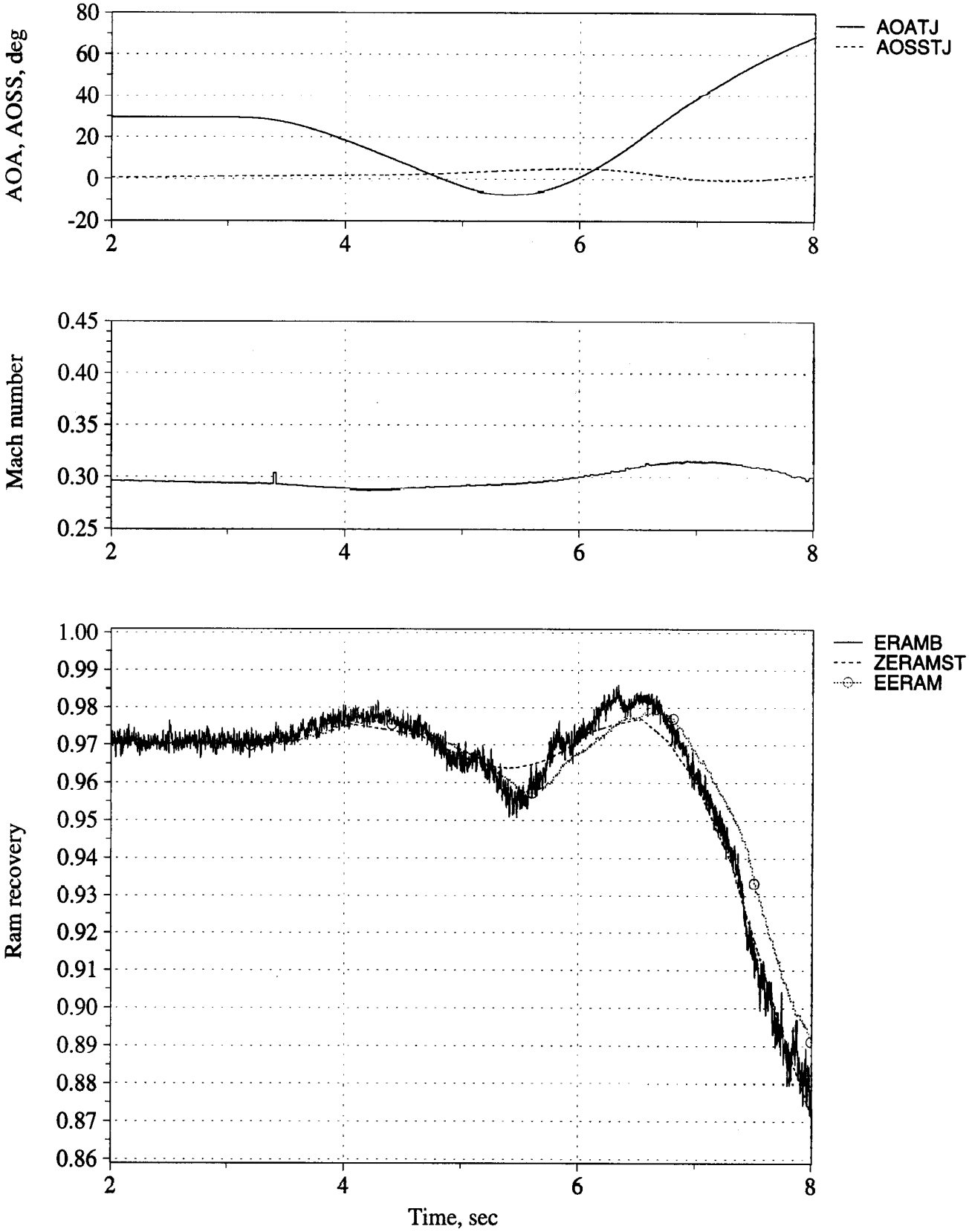

Figure 23. Time history of angle of attack, angle of sideslip, Mach number, and inlet recovery (measured and estimated) - Flight 213, Test point 11b.

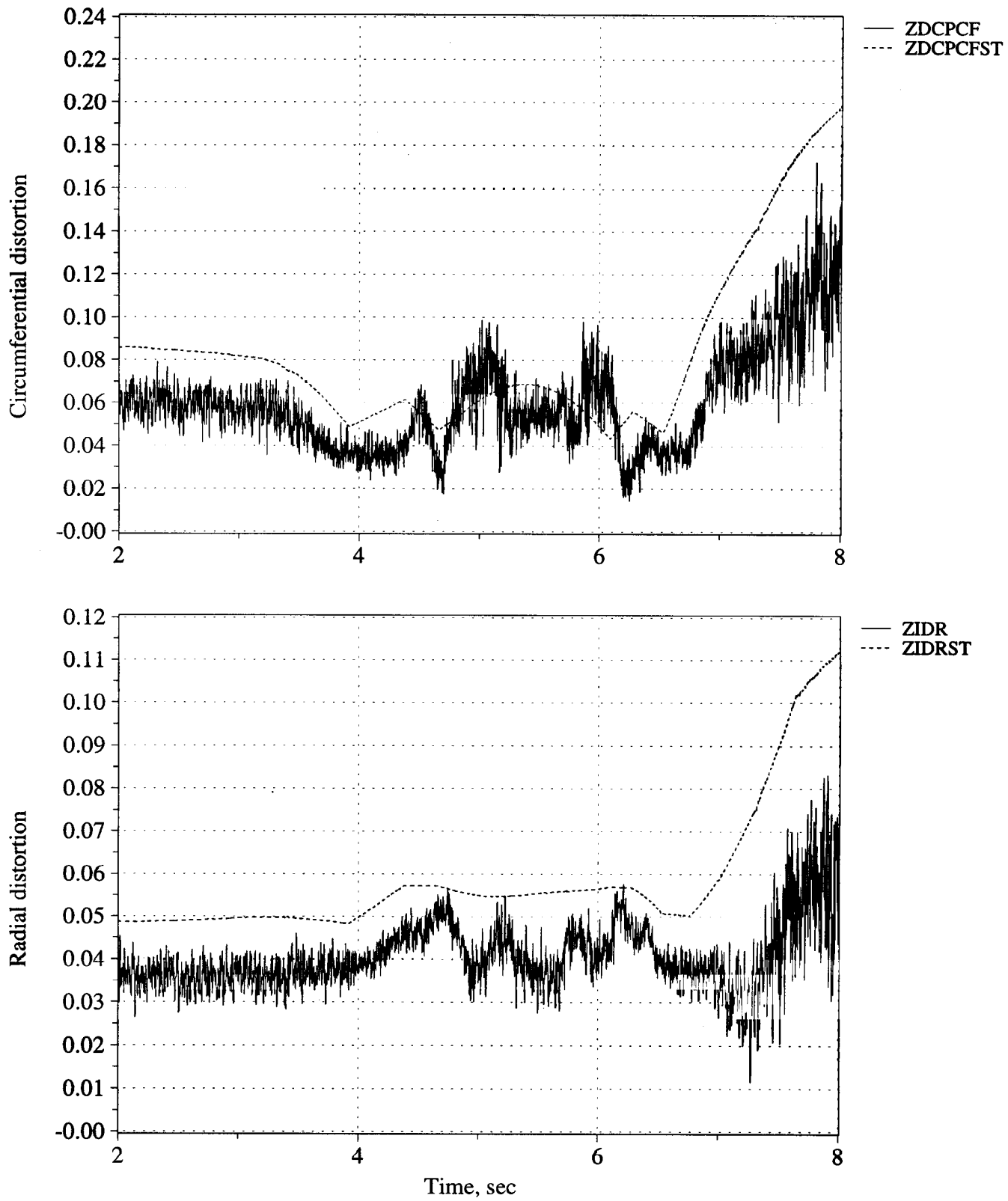

Figure 24. Time history of peak inlet dynamic circumferential and radial distortion (measured and estimated) - Flight 213, Test point 11b.

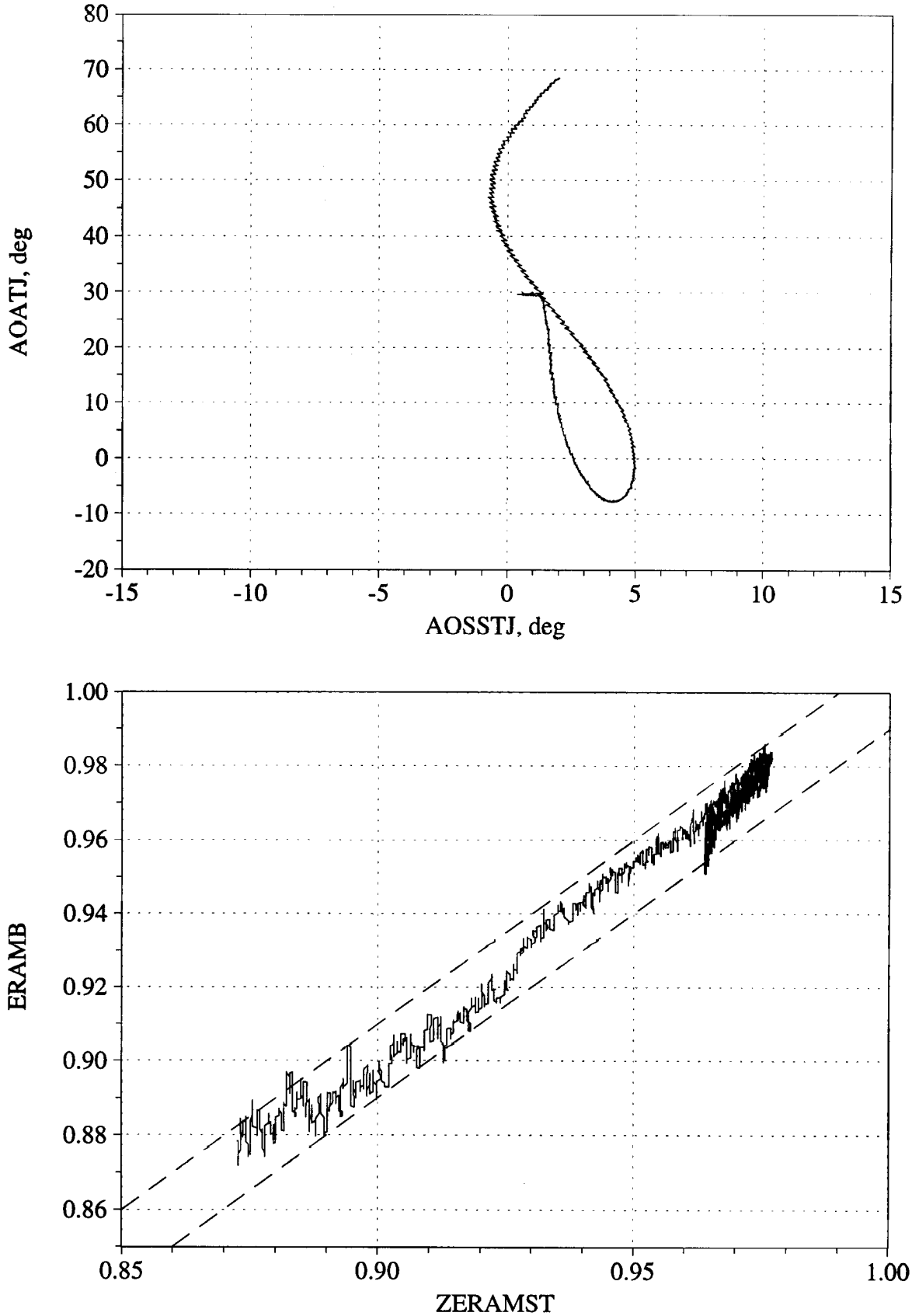

Figure 25. Angle of attack/angle of sideslip trajectory during maneuver; and measured versus estimated recovery - Flight 213, Test point 11b.

attack approximately equal to 29 degrees and at M = 0.4, up to approximately 35 degrees. Thus, the peak dynamic radial distortion tends to deviate from the model predicted values at lower angles of attack than the peak dynamic circumferential distortion values. The reason for this difference is unknown, but since the F/A-18 A/B/C/D inlet duct is relatively long and will produce a significant wall boundary layer, it is possible that the radial characteristics of the duct flow are transiently changed in a manner that temporarily reduces the peak dynamic radial distortion.

In the few test points where the flight-obtained peak dynamic radial distortion exceeds the estimated peak dynamic radial distortion obtained from the model, it occurs at angles of attack of ten degrees or less. This result is similar to the finding for peak dynamic circumferential distortion and probably occurs for the same reason, that is, the ingestion of some disturbance external to the inlet. These exceedences are relatively small and do not significantly raise the absolute levels of the peak dynamic radial distortion.

6.0 CONCLUSIONS

Analysis of the data from the rapid maneuvers produced several key findings as follows:

1. In general, the inlet recovery obtained during the rapid flight maneuvers agreed within ± 0.01 recovery units over the range of angle of attack until the angle of attack exceeded approximately 50 degrees. That the recovery obtained during rapid maneuvers was significantly less than the values obtained during stabilized maneuvers above approximately 50 degrees was associated with a change in the dynamic character of the flow and may be attributable to a change in location of the separating region in the inlet.

2. For conditions judged to be important to engine stability assessments, there were no cases where either the peak dynamic circumferential or radial distortion values obtained during rapid flight maneuvers exceeded the values of peak dynamic circumferential or radial distortion obtained during stabilized maneuvers. This finding supports the rationale for obtaining inlet model data at fixed angle-of-attack and angle-of-sideslip attitudes during wind tunnel tests.

3. At low or negative angles of attack where the distortion values were relatively low, there were cases where the values of peak dynamic circumferential and radial distortion exceeded those of the stabilized maneuver database. While these cases are not important from a stability assessment point of view, they did illustrate that inlets under some conditions may ingest disturbances that are produced external to the inlet and which may fall in between the angle-of-attack and angle-of-sideslip grid test points chosen for a wind tunnel test matrix.

4. For angles of attack increasing beyond the 30 to 40 degree range, the trend for both the flight measured peak dynamic circumferential and radial distortion values does not increase as rapidly as suggested by the values obtained during stabilized maneuver testing. At this point in time, the lower rate of increase of peak dynamic distortion values obtained during rapid maneuver testing is being attributed to the time for a separated flow to fully develop.

5. The measured peak values of dynamic circumferential distortion during a rapid maneuver generally fall within 0.01 distortion units of the peak dynamic values obtained during stabilized maneuvers in the approximately 10 - 38 degree angle of attack range. Above 38 degrees angle of attack, the measured peak dynamic values obtained during a rapid maneuver begin to increasingly deviate on the low side from the peak dynamic circumferential distortion levels obtained during stabilized maneuvers. At less than 10 degrees, there are instances where the measured peak dynamic circumferential distortion exceeds the stabilized maneuver obtained values apparently due to the ingesting of an external flow field disturbance.

6. The measured peak values of dynamic radial distortion during a rapid maneuver generally fall within 0.01 distortion units of the peak dynamic values obtained during stabilized maneuvers over the angle of attack range from negative angles of attack to approximately 29 degrees angle of attack at M = 0.3 and to 35 degrees angle of attack at M = 0.4. Above this angle of attack, the peak dynamic radial distortion increasingly deviated on the low side from the values obtained during stabilized maneuver testing.

The rapid maneuver tests performed with the HARV aircraft provided inlet data and insight to transient inlet flows during aircraft rapid maneuvers that are invaluable to the practicing inlet-engine compatibility engineer and heretofore have been unavailable.

REFERENCES

1. Regenie, V., Gatlin, D., Kempel, R., and Matheny, N., "The F-18 High Alpha Research Vehicle: A High-Angle-of-Attack Testbed Aircraft," National Aeronautics and Space Administration Report TM 104253, September 1992.

2. Walsh, K. R., Yuhas, A. J., Williams, J. G., and Steenken, W. G., "Inlet Distortion for an F/A-18A Aircraft During Stabilized Maneuvers up to 60° Angle of Attack," National Aeronautics and Space Administration Report TM-104329, April 1997.

3. Walsh, K. R., Yuhas, A. J., Williams, J. G., and Steenken, W. G., "Inlet Distortion for an F/A-18A Aircraft During Stabilized Maneuvers up to 60° Angle of Attack," High-Angle-of-Attack Technology Report NASA/CP-1998-207676/PT3 compiled by Chambers, J. R., Burley, J. R., II, and Meyer, R. R., Jr., June 1998, pp. 1083 - 1126.

4. Walsh, K.R., Steenken, W.G., and Williams, J.G., "Summary of Inlet Characteristics of the F/A-18A High Alpha Research Vehicle," AIAA Paper 98-3713, 1998.

5. Yuhas, A.J., Steenken, W.G., Williams, J.G., and Walsh, K.R., "F/A-18A Inlet Flow Characteristics During Maneuvers with Rapidly Changing Angle of Attack," National Aeronautics and Space Administration Technical Memorandum 104327, 1997.

6. Yuhas, A.J., Steenken, W.G., Williams, J.G., and Walsh, K.R., "F/A-18A Inlet Flow Characteristics During Maneuvers with Rapidly Changing Angle of Attack," High-Angle-of-Attack Technology Report NASA/CP-1998-207676/PT3 compiled by Chambers, J. R., Burley, J. R., II, and Meyer, R. R., Jr., June 1998, pp. 1205 - 1224.

7. Steenken, W. G., Williams, J. G., Yuhas, A. J., and Walsh, K. R., "An Inlet Distortion Assessment During Aircraft Departures at High Angle of Attack for an F/A-18A Aircraft," High-Angle-of-Attack Technology Report NASA/CP-1998-207676/PT3 compiled by Chambers, J. R., Burley, J. R., II, and Meyer, R. R., Jr., June 1998, pp. 1051 - 1081.

8. Steenken, W.G., Williams, J.G., Yuhas, A.J., and Walsh, K.R., "Factors Affecting Inlet-Engine Compatibility During Aircraft Departures at High Angle of Attack for an F/A-18A Aircraft," National Aeronautics and Space Administration Technical Memorandum NASA/TM-1999-206572, February 1999.

9. Williams, J. G., Steenken, W. G., and Yuhas, A. J., "Estimating Engine Airflow in Gas-Turbine Powered Aircraft with Clean and Distorted Inlet Flows," National Aeronautics and Space Administration Contractor Report 198052, September 1996 and High-Angle-of-Attack Technology Report NASA/CP-1998-207676/PT3 compiled by Chambers, J. R., Burley, J. R., II, and Meyer, R. R., Jr., June 1998, pp. 1127 - 1203.

10. Amin, N. F. and Hollweger, D. J., "F/A-18A Inlet/Engine Compatibility Flight Test Results," AIAA Paper No. AIAA-81-1393, July 1981.

11. Yuhas, A. J., Ray, R. J., Burley, R. R., Steenken, W. G., Lechtenberg, L., and Thornton, D., "Design and Development of an F/A-18 Inlet Distortion Rake: A Cost and Time Saving Solution," American Institute of Aeronautics and Astronautics Paper No. AIAA-94-2132, June 1994.

12. Moes, T. R. and Whitmore, S. A., "A Preliminary Look at Techniques Used to Obtain Airdata from Flight at High Angles of Attack," National Aeronautics and Space Administration Report TM 101729, December 1990.

REFERENCES (Concluded)

13. Society of Automotive Engineers, "Gas Turbine Engine Inlet Flow Distortion Guidelines," Aerospace Recommended Practice ARP 1420, March 1978.

APPENDIX A - INLET FLOW DESCRIPTOR DEFINITIONS

For a given pattern of 40 total-pressure measurements (8 rakes, 5 rings), the total-pressure distortion descriptors are defined as follows:

Maximum Circumferential Distortion Descriptor - DP/PC max

This circumferential ring pressure distortion index is based on the calculation of $DP/PC_{ring\ i}$,

where the subscript "ring i" refers to any of the five pressure rings.

The rings are counted in ascending order, innermost to outermost.

$$DP/PC_{ring\ i} = \{[\ PAV_{ring\ i} - PMIN_{ring\ i}\ ] / PAV\} \quad \text{for rings } i=1,5$$

where:

1. $PAV_{ring\ i}$ = area-averaged total pressure of ring i
2. $PMIN_{ring\ i}$ = minimum total pressure in the largest low pressure region in ring i
3. PAV = area-averaged total pressure over the complete face

DP/PC max is defined as the largest of:

$$0.5 \cdot [DP/PC_{ring\ i} + DP/PC_{ring\ i+1}] \qquad \text{for } i=1,4 \qquad \text{(A1)}$$

Maximum Radial Distortion Descriptor - DP/PR max

Similar to DP/PC, DP/PR is calculated for each of the five rings as follows:

$$DP/PR_{ring\ i} = [\ PAV - PAV_{ring\ i}\ ] / PAV \quad \text{for rings } i=1,5 \qquad \text{(A2)}$$

where:

1. PAV = area-averaged total pressure over the complete face
2. $PAV_{ring\ i}$ = area-averaged total pressure of ring i

If a DP/PR_{ring} value is negative, it is assumed to be zero.

DP/PR max is defined as the larger of $DP/PR_{ring\ 1}$ or $DP/PR_{ring\ 5}$

If DP/PR max is located in ring 1, the distortion is hub radial.

If DP/PR max is located in ring 5, the distortion is tip radial.

APPENDIX B: M = 0.3 RAPID MANEUVERS

- Low-to-High Angle of Attack -

Figures B1 - B3, Flight 212, Test Point 6b3
Figures B4 - B6, Flight 230, Test Point 2b2
Figures B7 - B9, Flight 230, Test Point 0b1
Figures B10 - B12, Flight 230, Test Point 0b2
Figures B13 - B15, Flight 230, Test Point 0b3
Figures B16 - B18, Flight 236, Test Point 22b
Figures B19 - B21, Flight 236, Test Point 22c
Figures B22 - B24, Flight 236, Test Point 23b

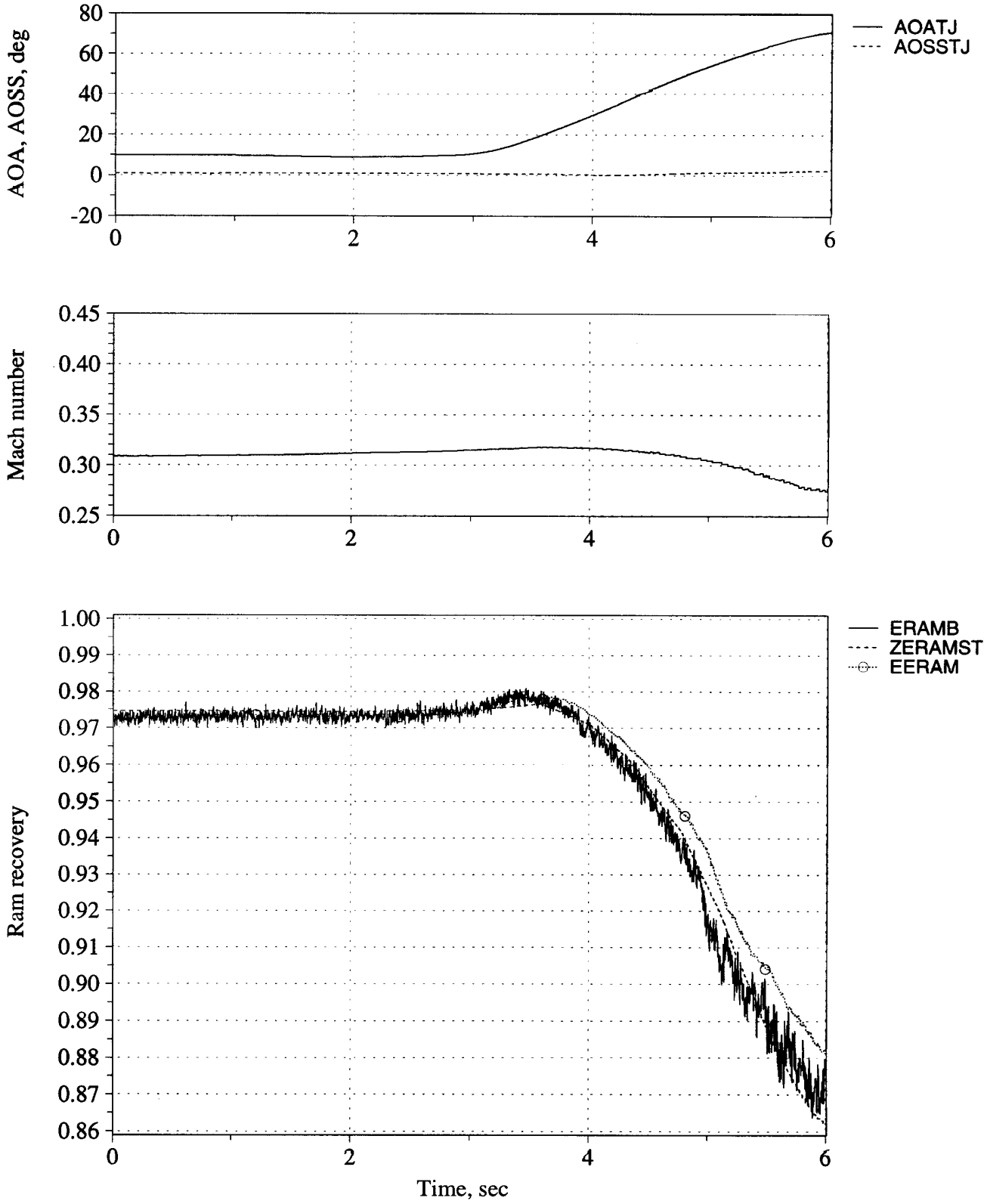

Figure B1. Time history of angle of attack, angle of sideslip, Mach number, and inlet recovery (measured and estimated) - Flight 212, Test point 6b3.

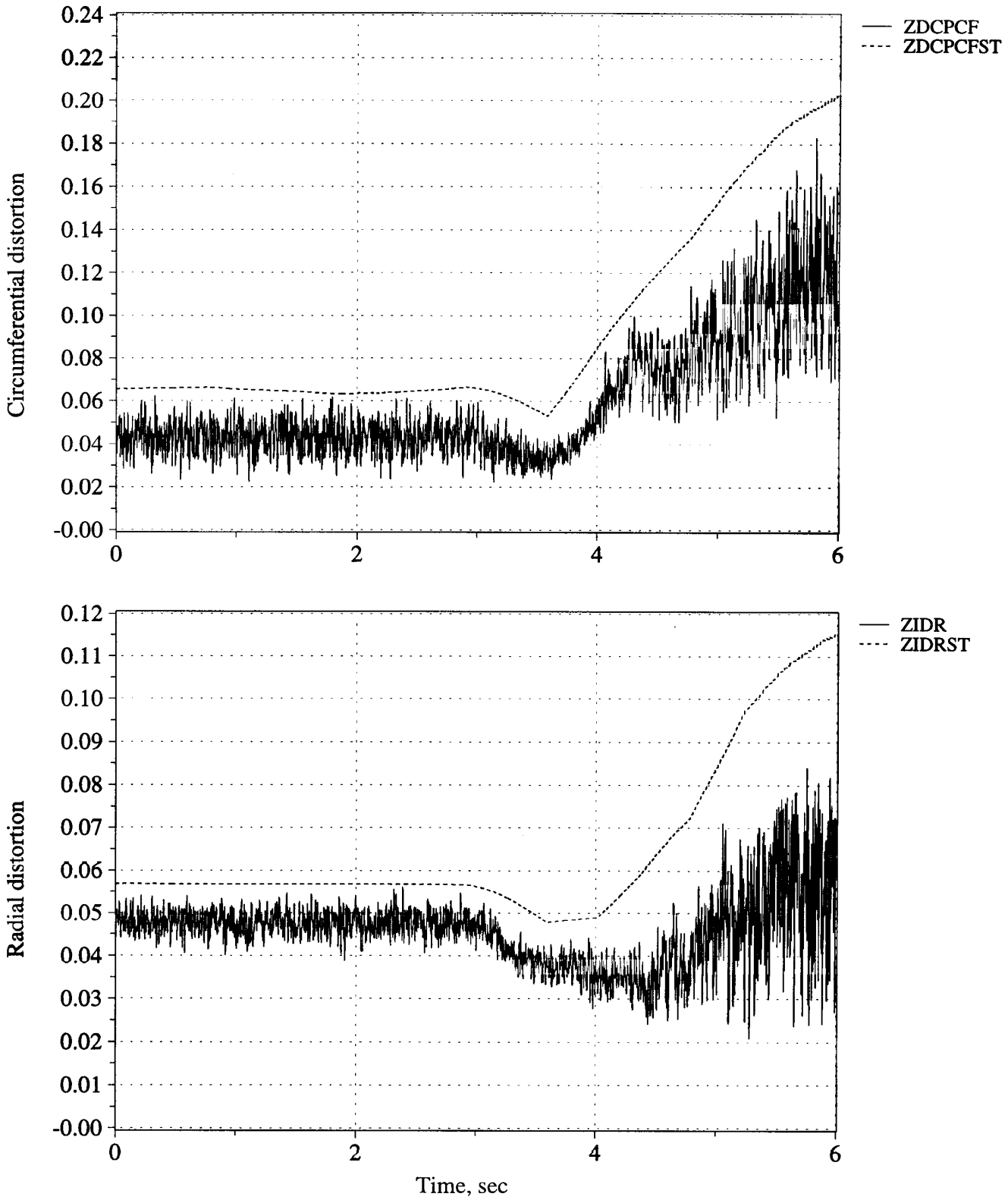

Figure B2. Time history of peak inlet dynamic circumferential and radial distortion (measured and estimated) - Flight 212, Test point 6b3.

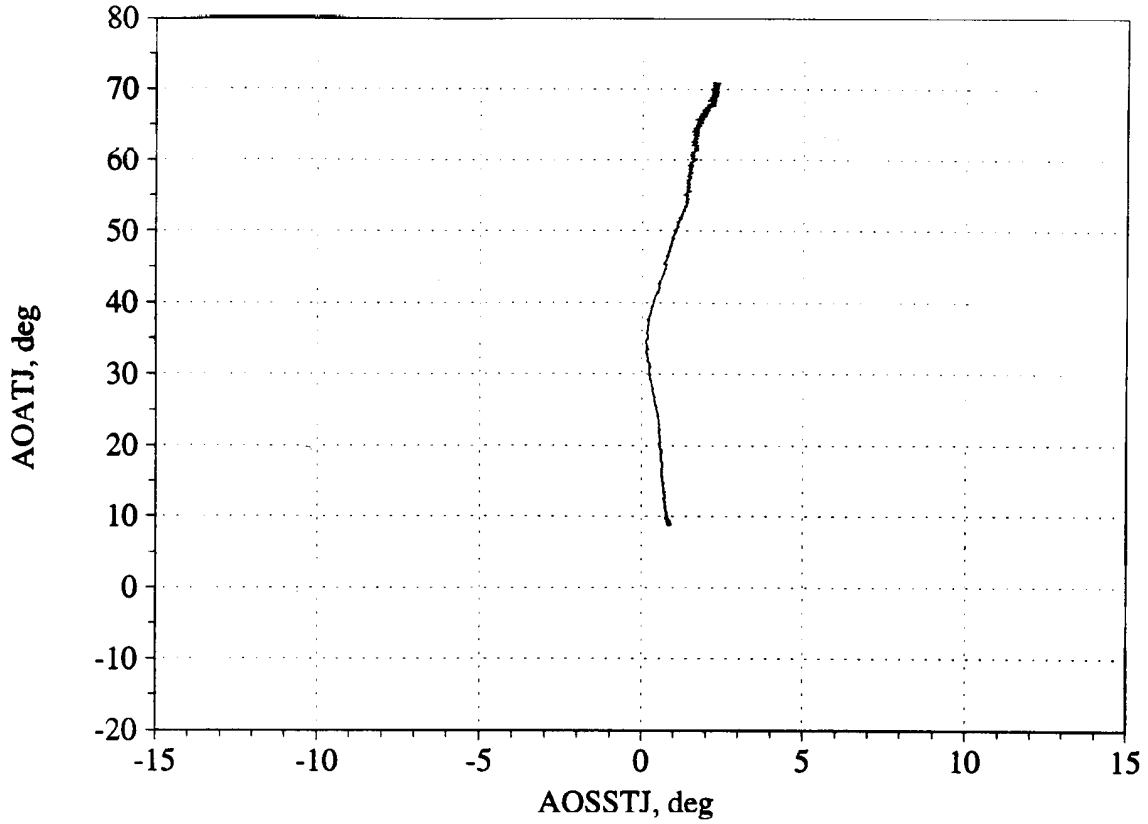

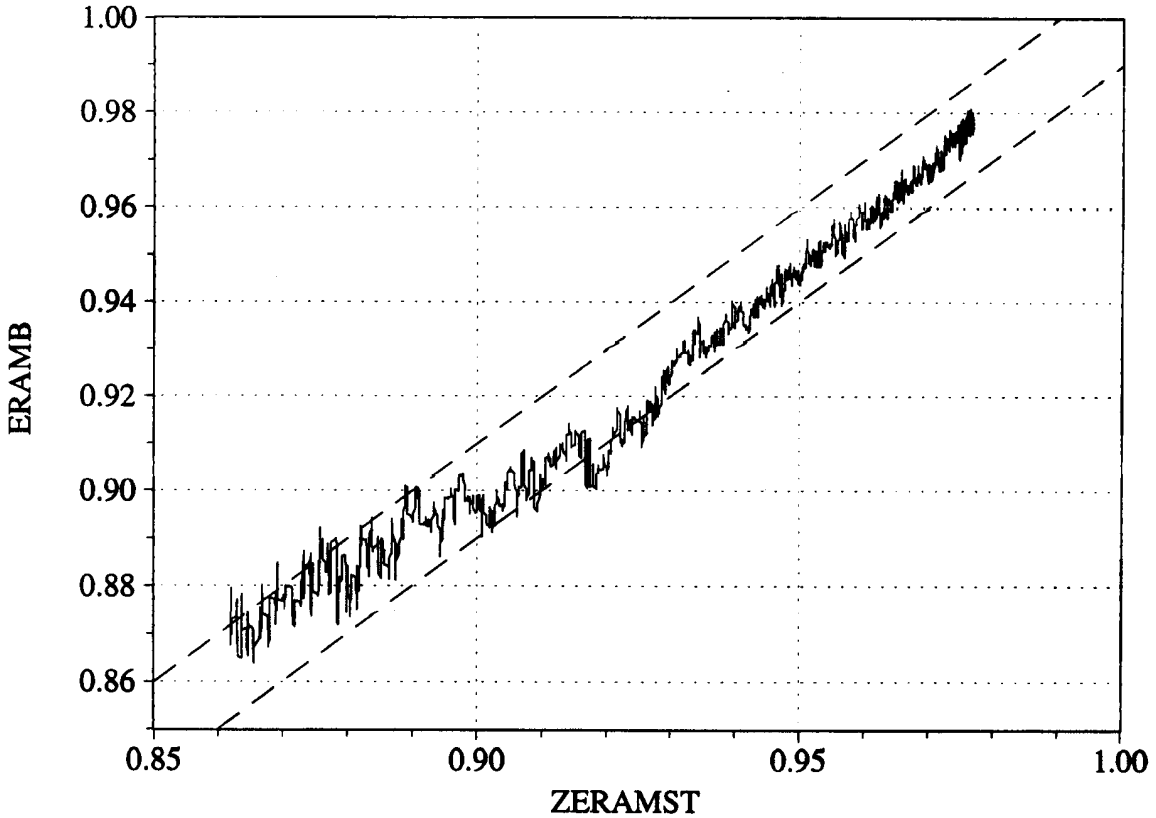

Figure B3. Angle of attack/angle of sideslip trajectory during maneuver; and measured versus estimated recovery - Flight 212, Test point 6b3.

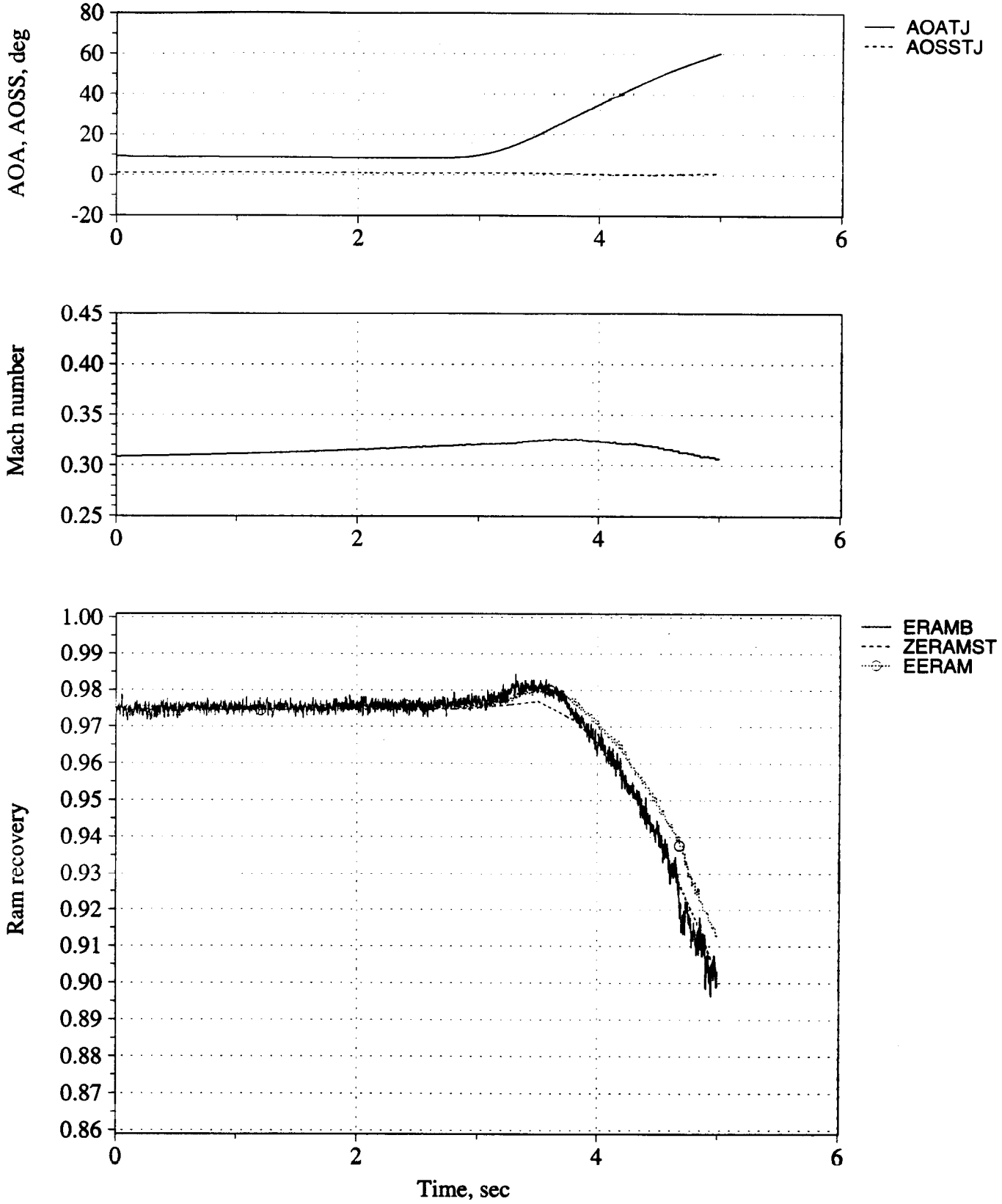

Figure B4. Time history of angle of attack, angle of sideslip, Mach number, and inlet recovery (measured and estimated) - Flight 230, Test point 2b2.

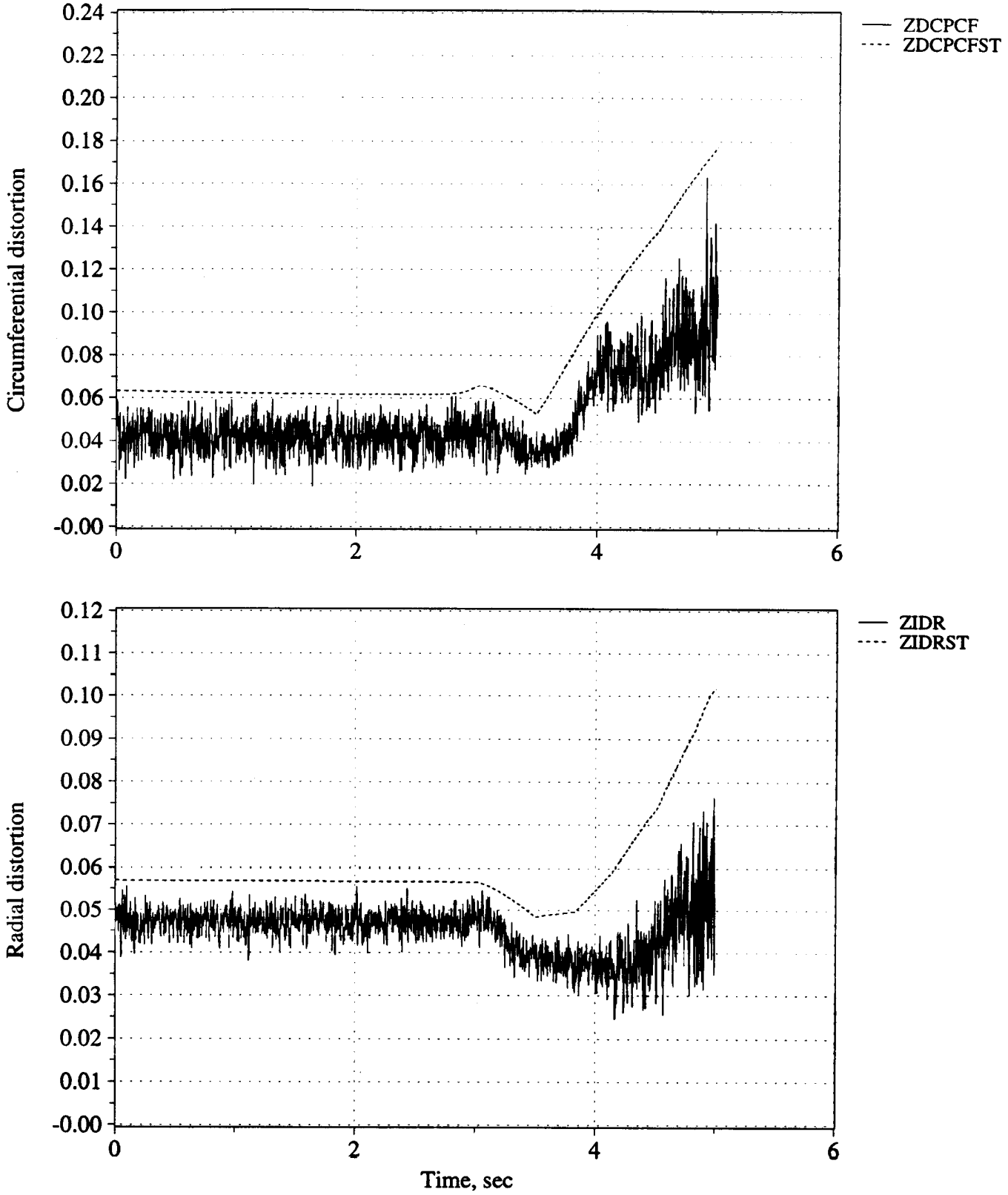

Figure B5. Time history of peak inlet dynamic circumferential and radial distortion (measured and estimated) - Flight 230, Test point 2b2.

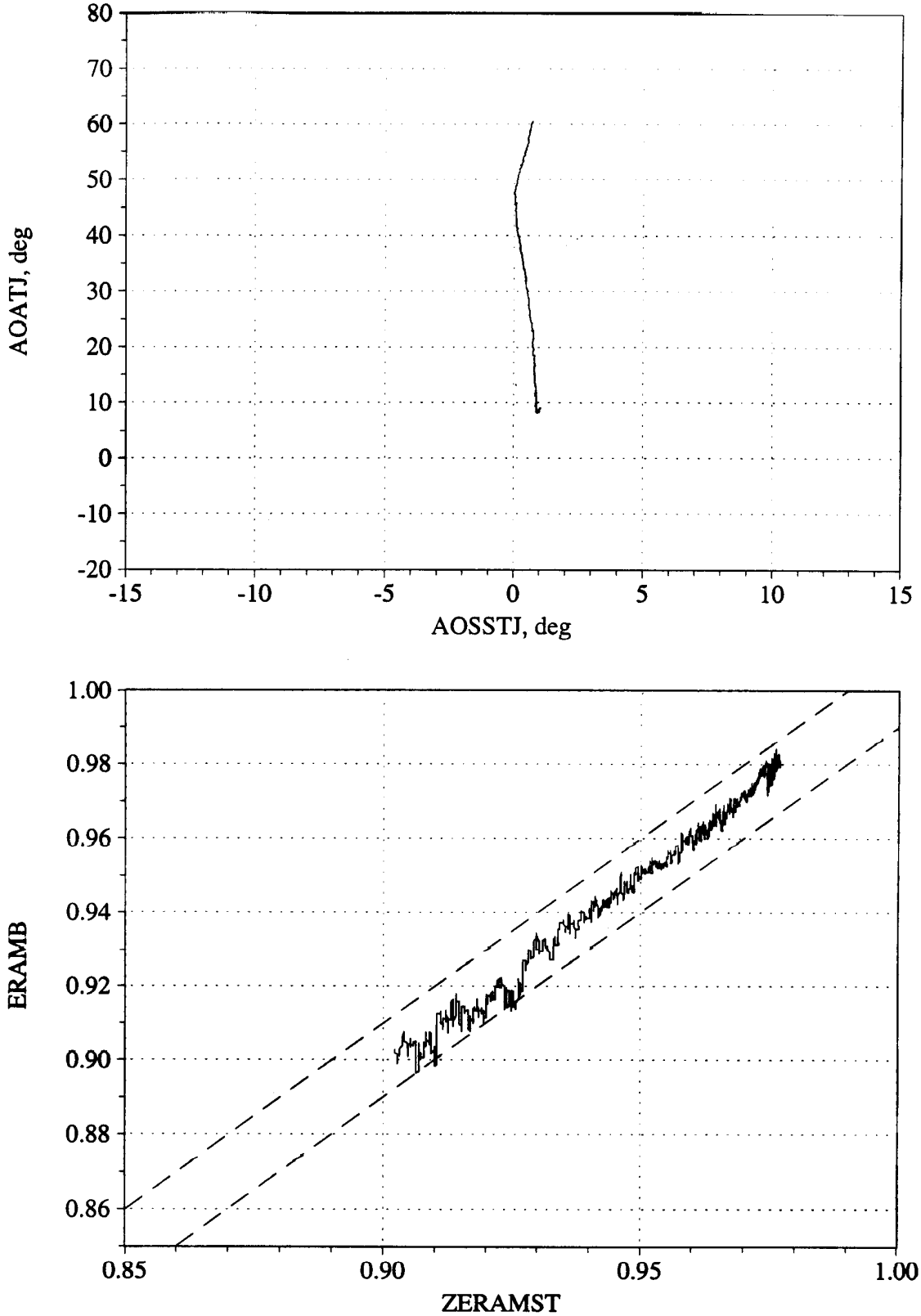

Figure B6. Angle of attack/angle of sideslip trajectory during maneuver; and measured versus estimated recovery - Flight 230, Test point 2b2.

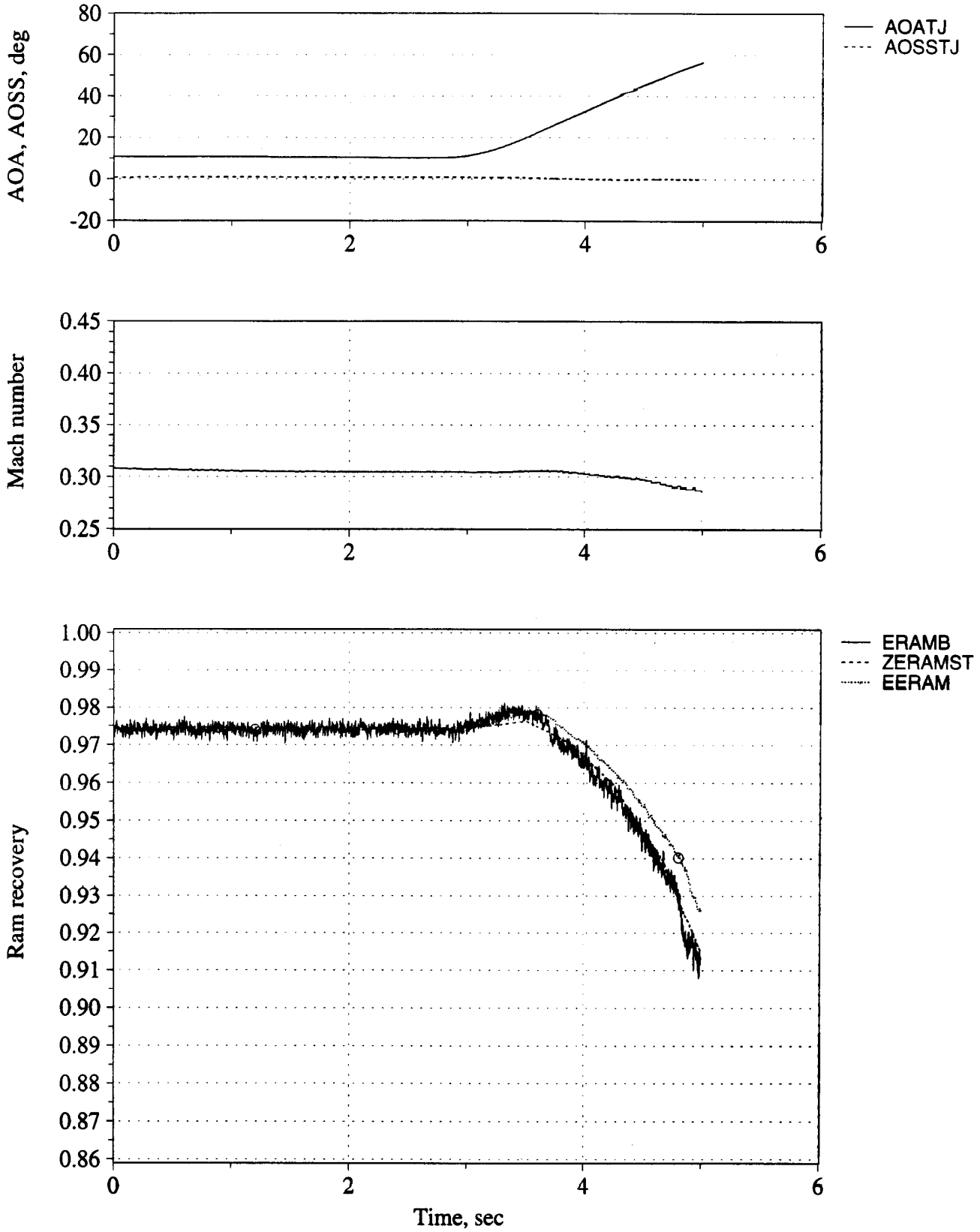

Figure B7. Time history of angle of attack, angle of sideslip, Mach number, and inlet recovery (measured and estimated) - Flight 230, Test point 0b1.

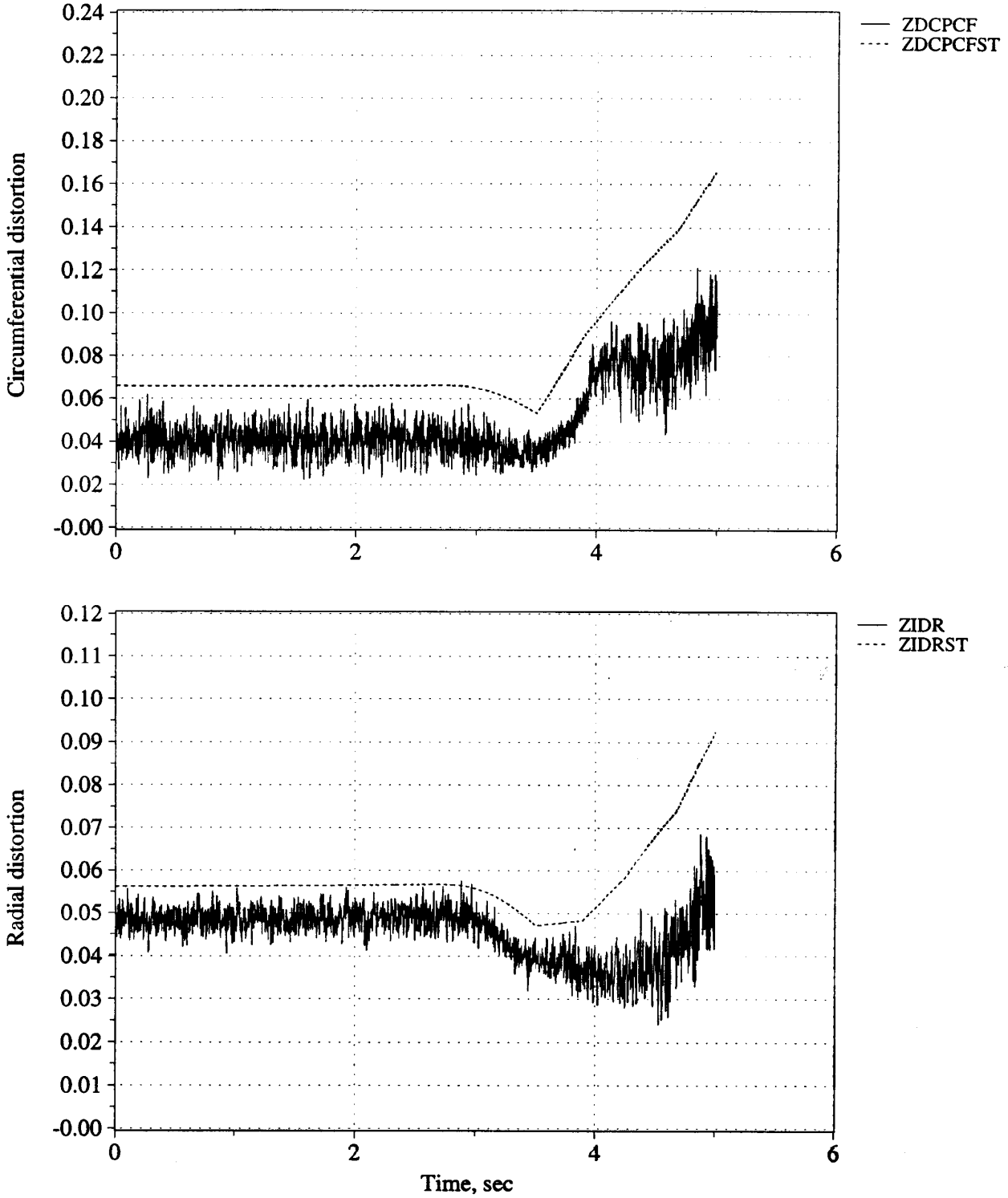

Figure B8. Time history of peak inlet dynamic circumferential and radial distortion (measured and estimated) - Flight 230, Test point 0b1.

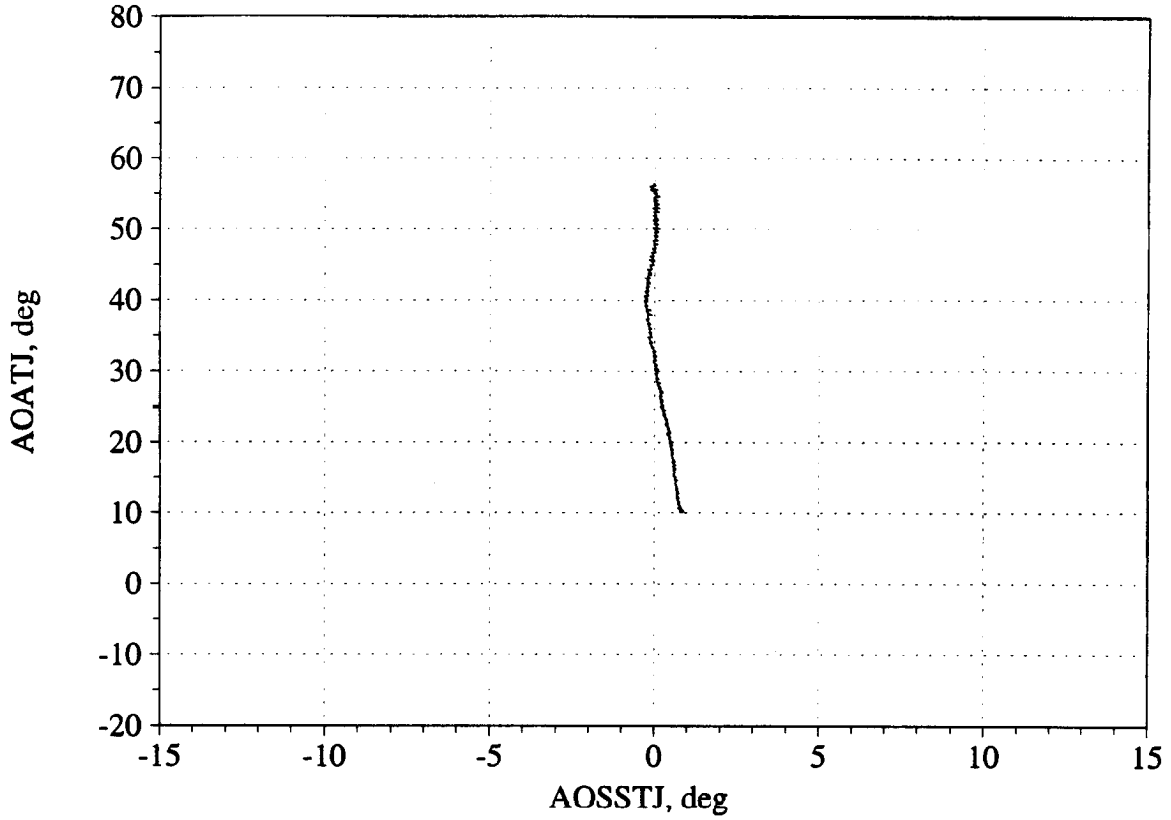

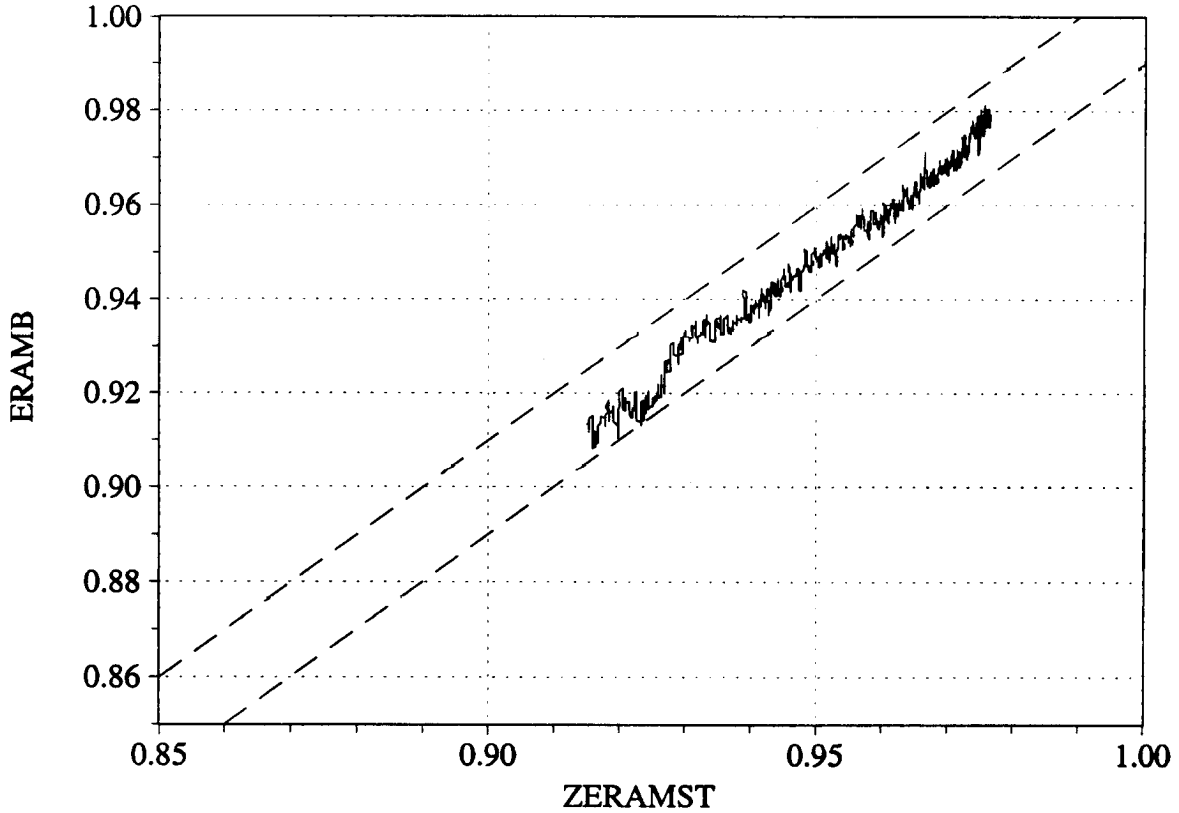

Figure B9. Angle of attack/angle of sideslip trajectory during maneuver; and measured versus estimated recovery - Flight 230, Test point 0b1.

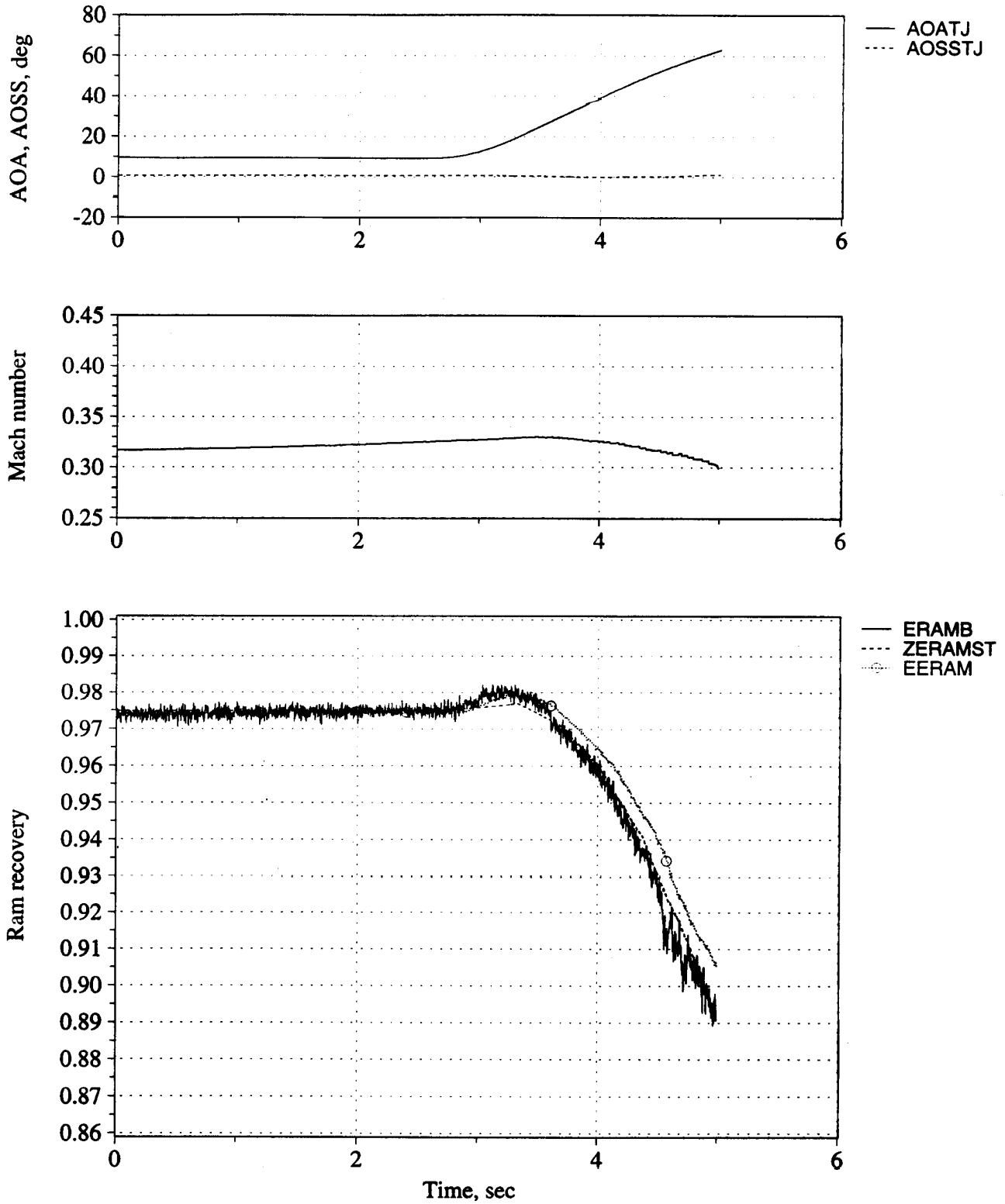

Figure B10. Time history of angle of attack, angle of sideslip, Mach number, and inlet recovery (measured and estimated) - Flight 230, Test point 0b2.

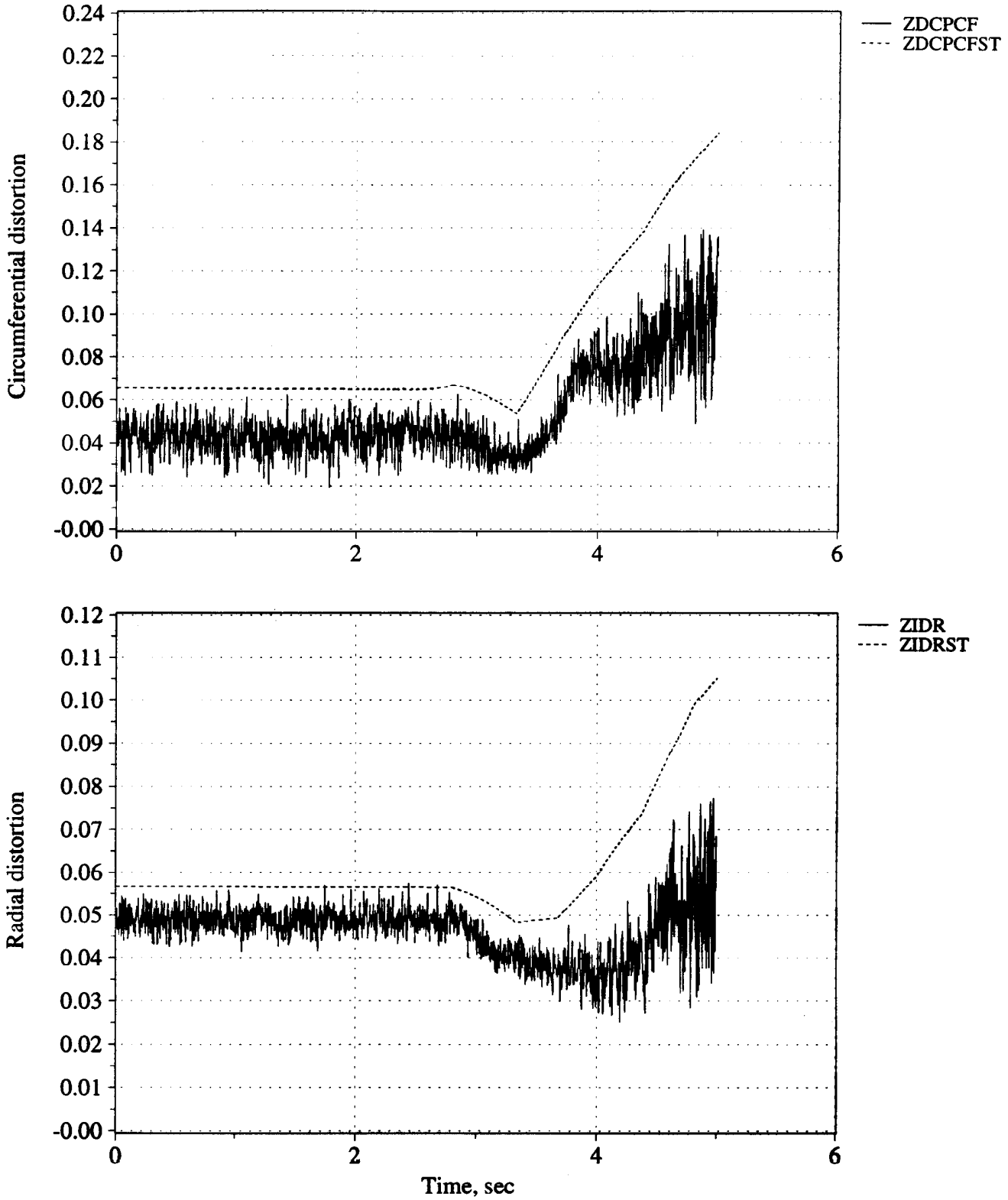

Figure B11. Time history of peak inlet dynamic circumferential and radial distortion (measured and estimated) - Flight 230, Test point 0b2.

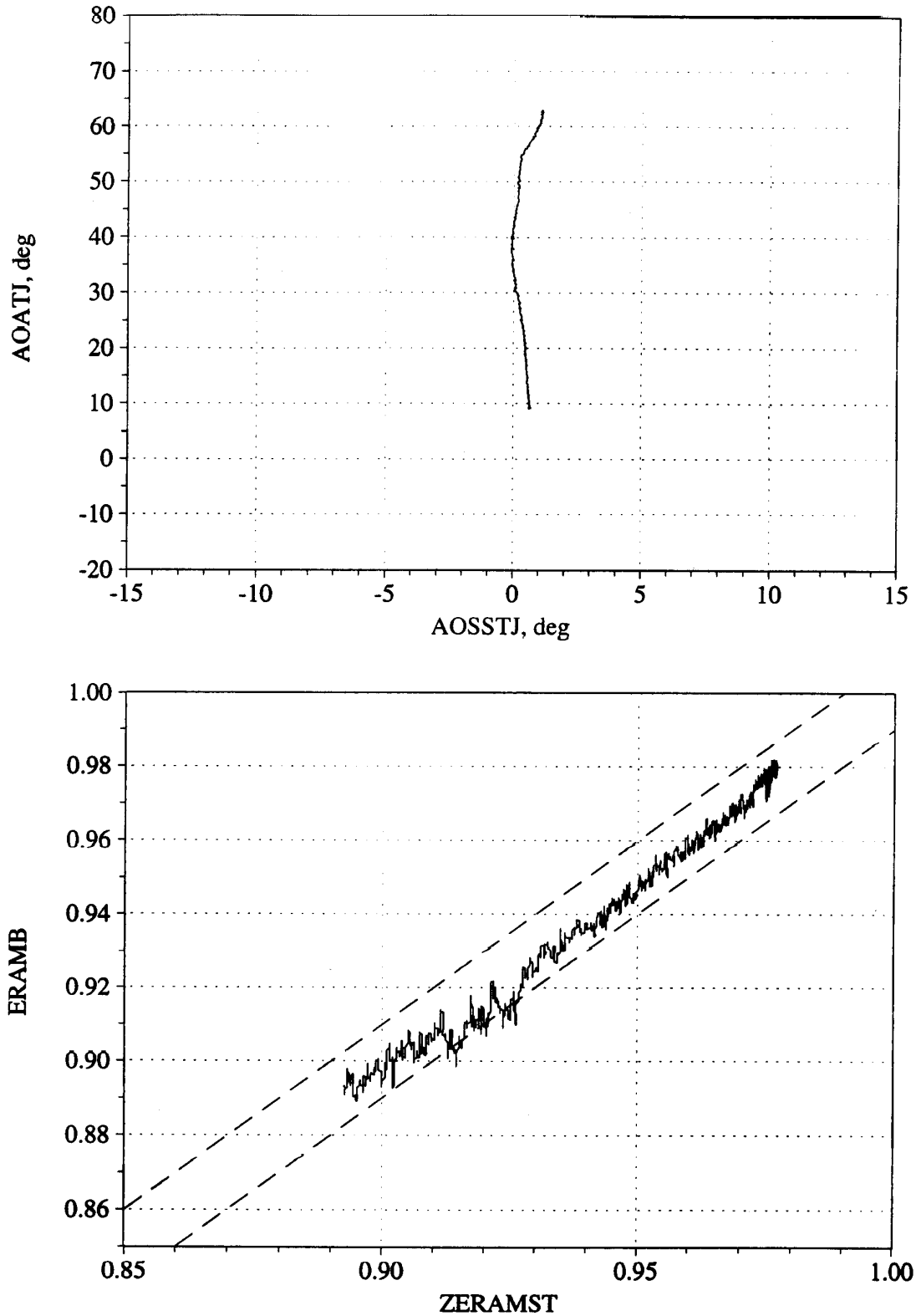

Figure B12. Angle of attack/angle of sideslip trajectory during maneuver; and measured versus estimated recovery - Flight 230, Test point 0b2.

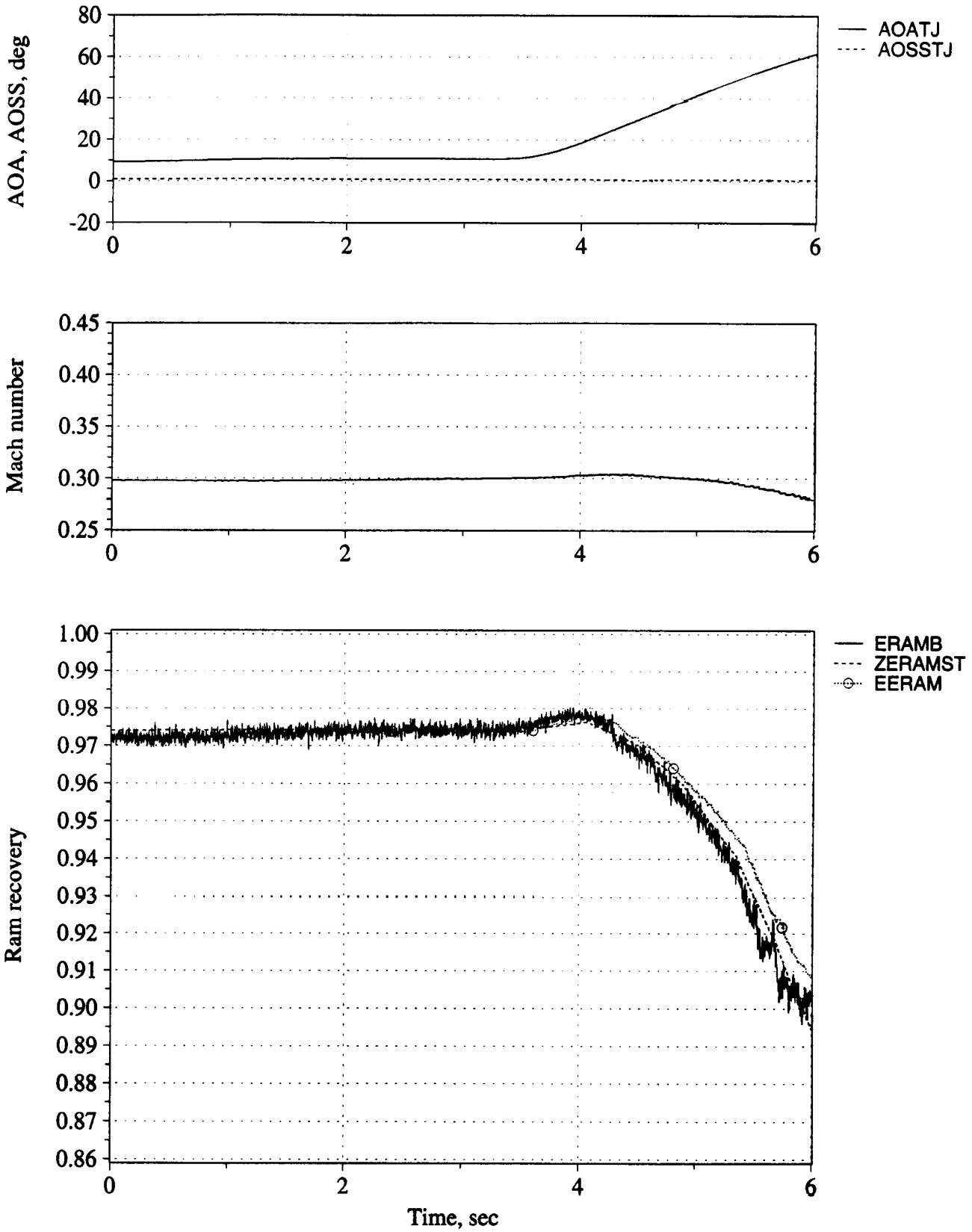

Figure B13. Time history of angle of attack, angle of sideslip, Mach number, and inlet recovery (measured and estimated) - Flight 230, Test point 0b3.

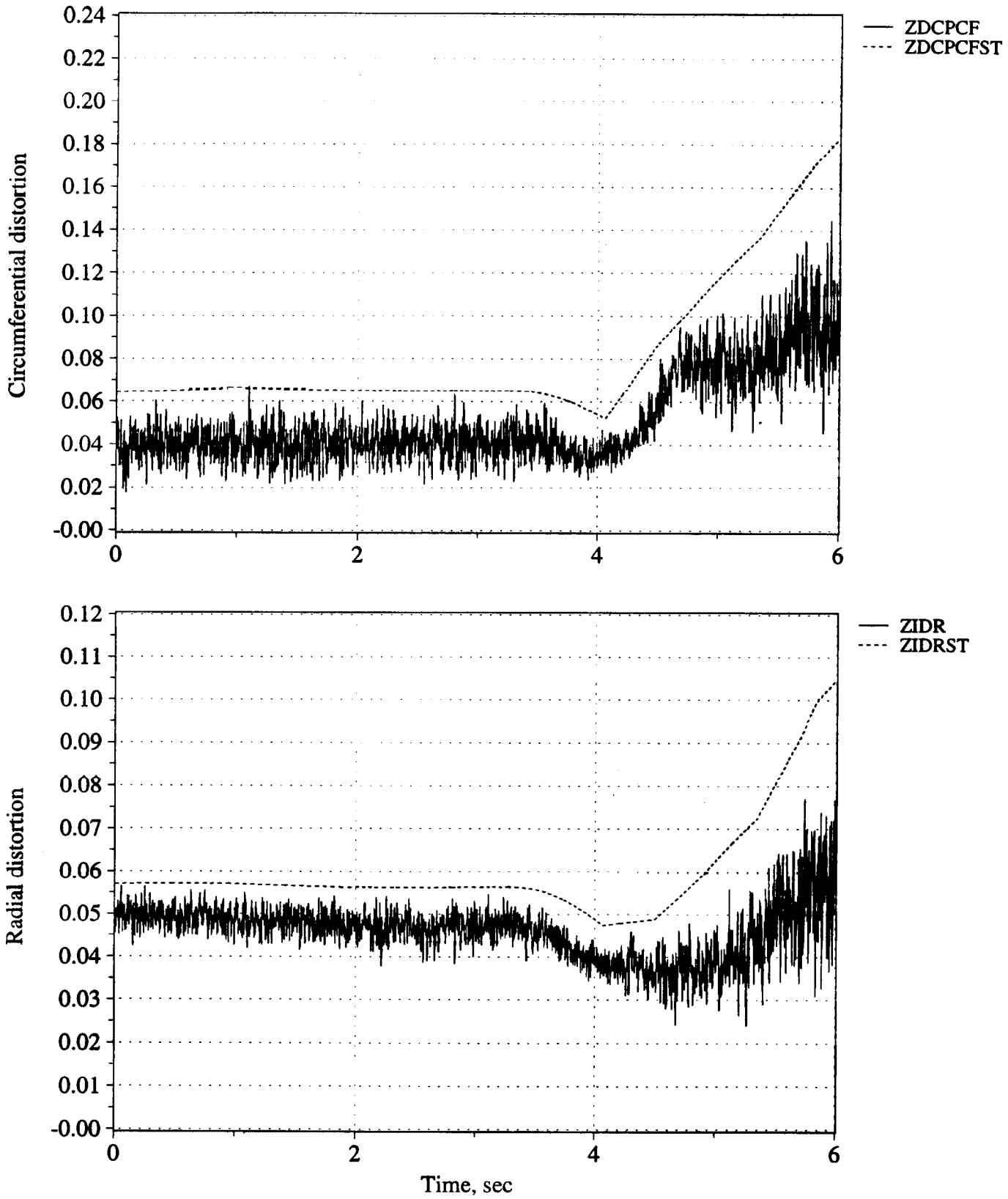

Figure B14. Time history of peak inlet dynamic circumferential and radial distortion (measured and estimated) - Flight 230, Test point 0b3.

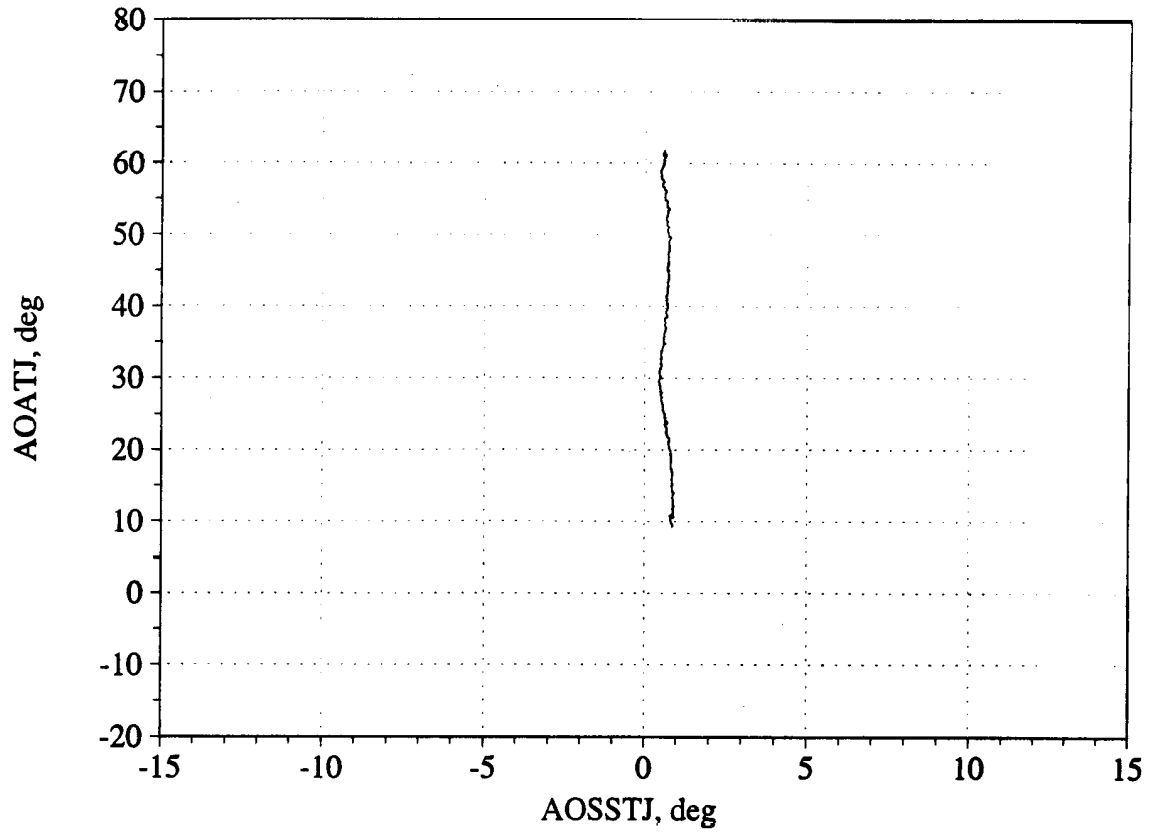

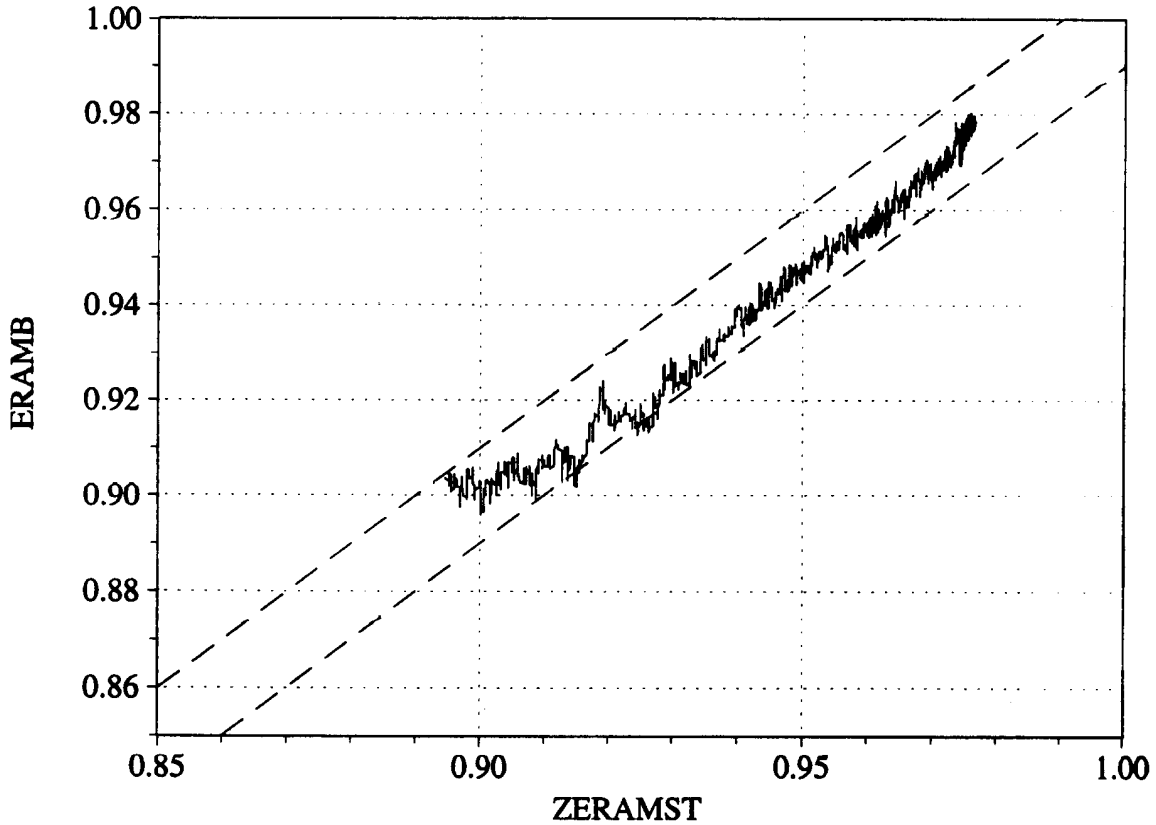

Figure B15. Angle of attack/angle of sideslip trajectory during maneuver; and measured versus estimated recovery - Flight 230, Test point 0b3.

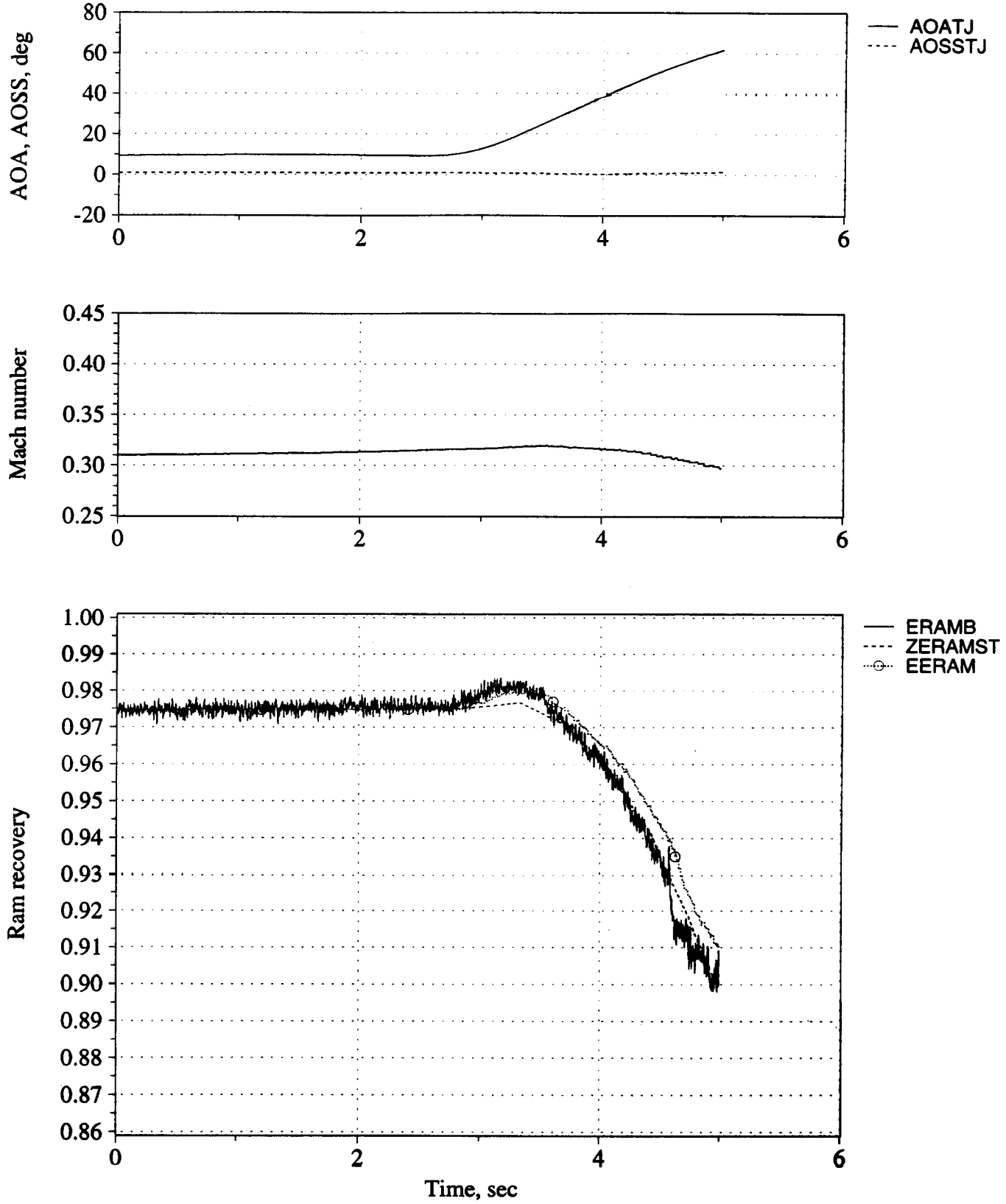

Figure B16. Time history of angle of attack, angle of sideslip, Mach number, and inlet recovery (measured and estimated) - Flight 236, Test point 22b.

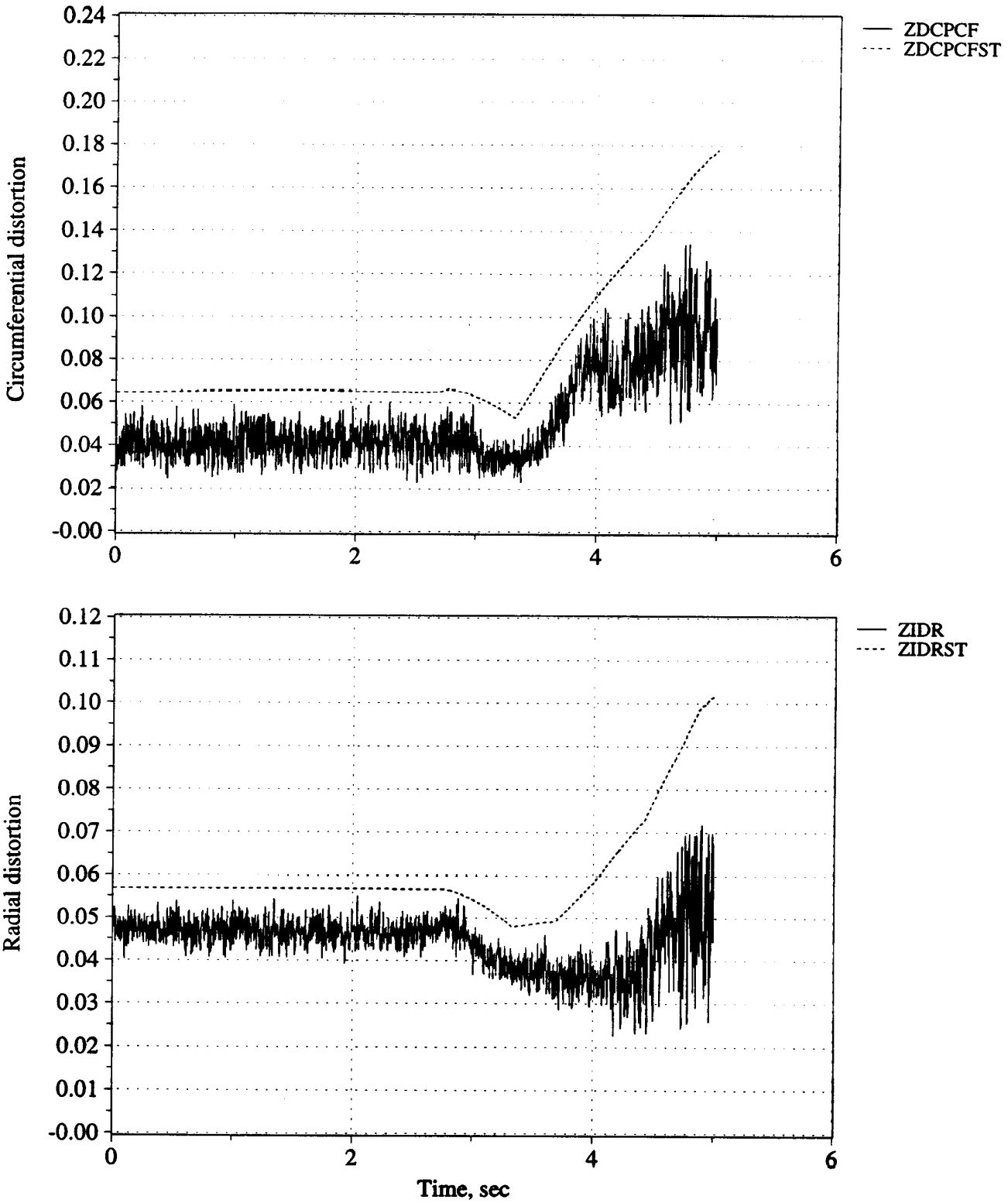

Figure B17. Time history of peak inlet dynamic circumferential and radial distortion (measured and estimated) - Flight 236, Test point 22b.

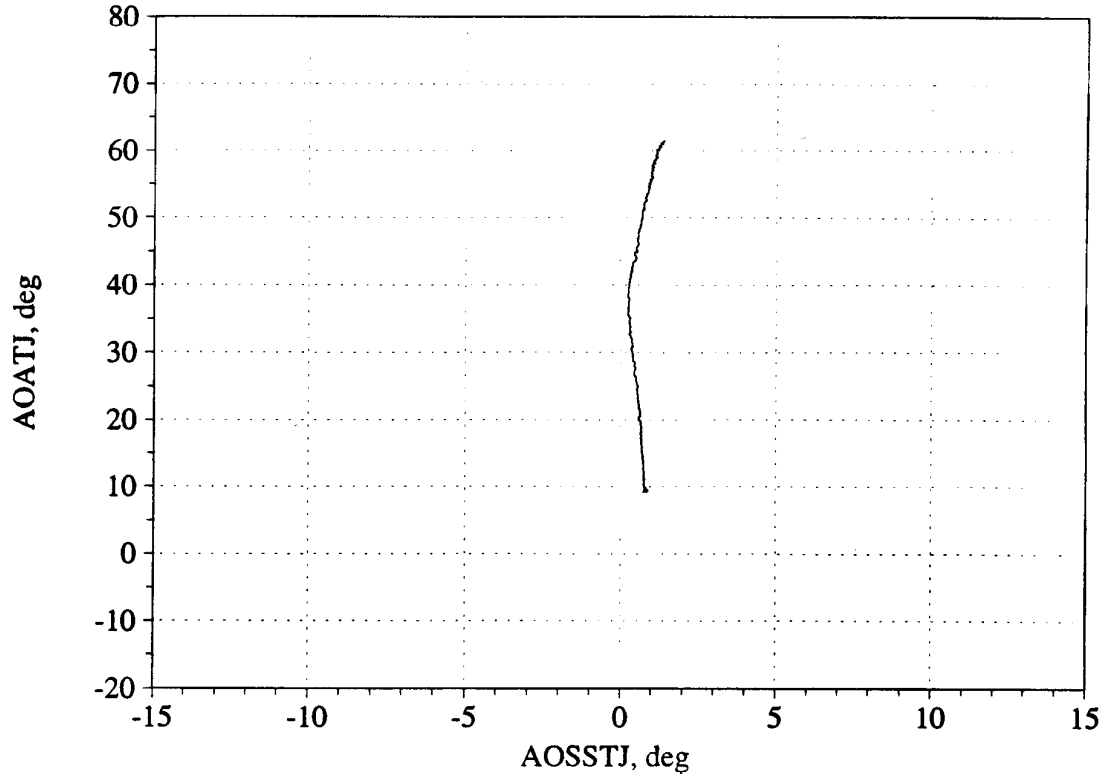

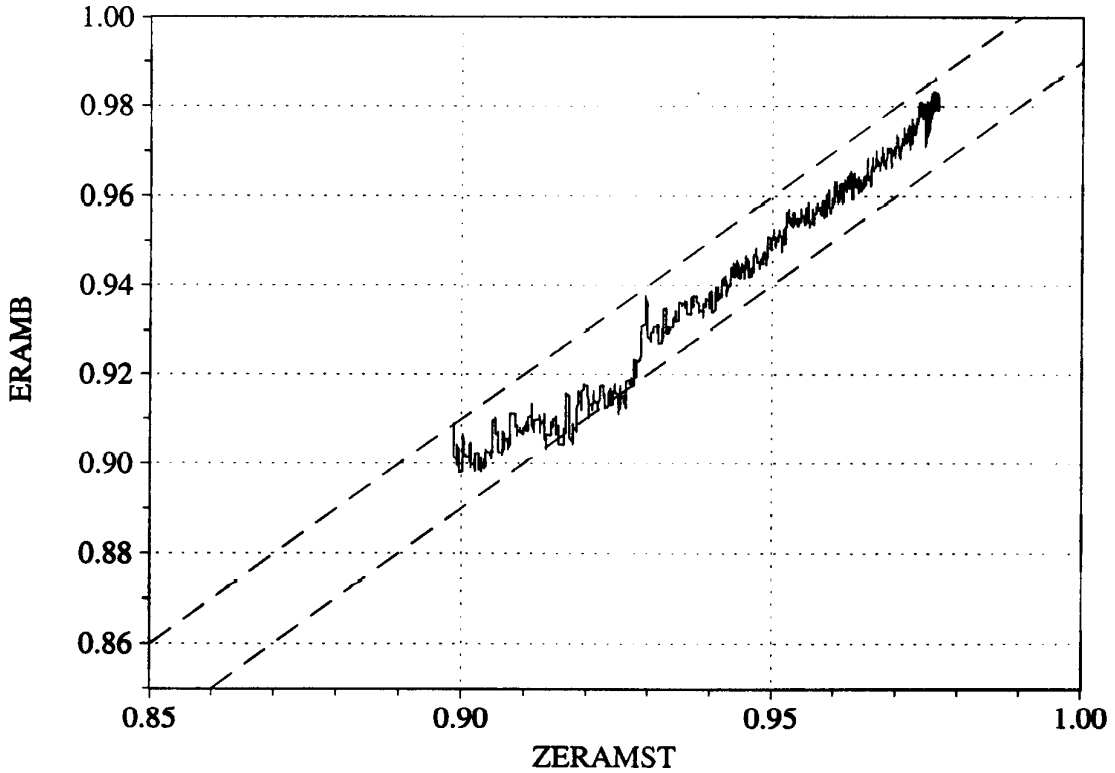

Figure B18. Angle of attack/angle of sideslip trajectory during maneuver; and measured versus estimated recovery - Flight 236, Test point 22b.

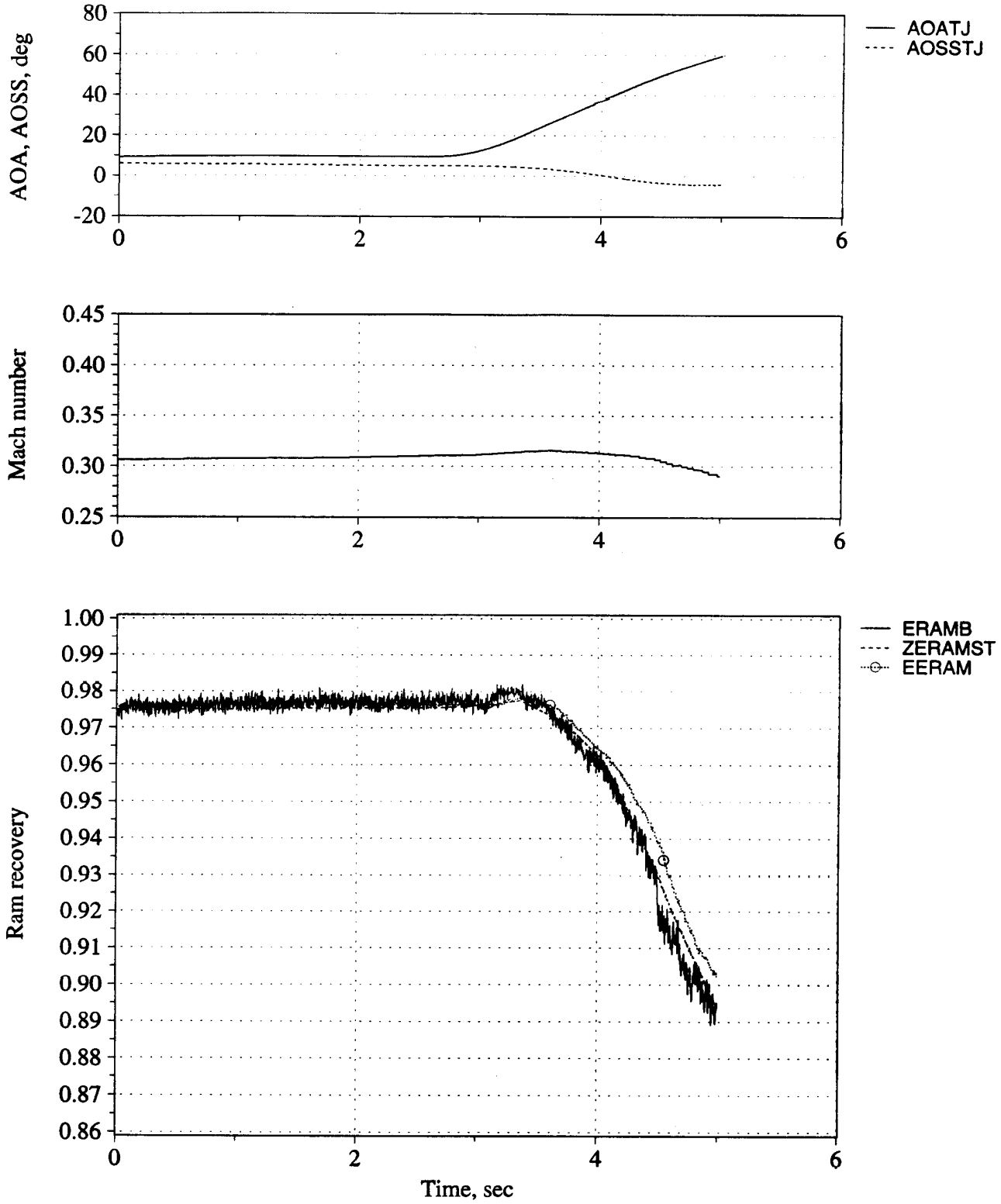

Figure B19. Time history of angle of attack, angle of sideslip, Mach number, and inlet recovery (measured and estimated) - Flight 236, Test point 22c.

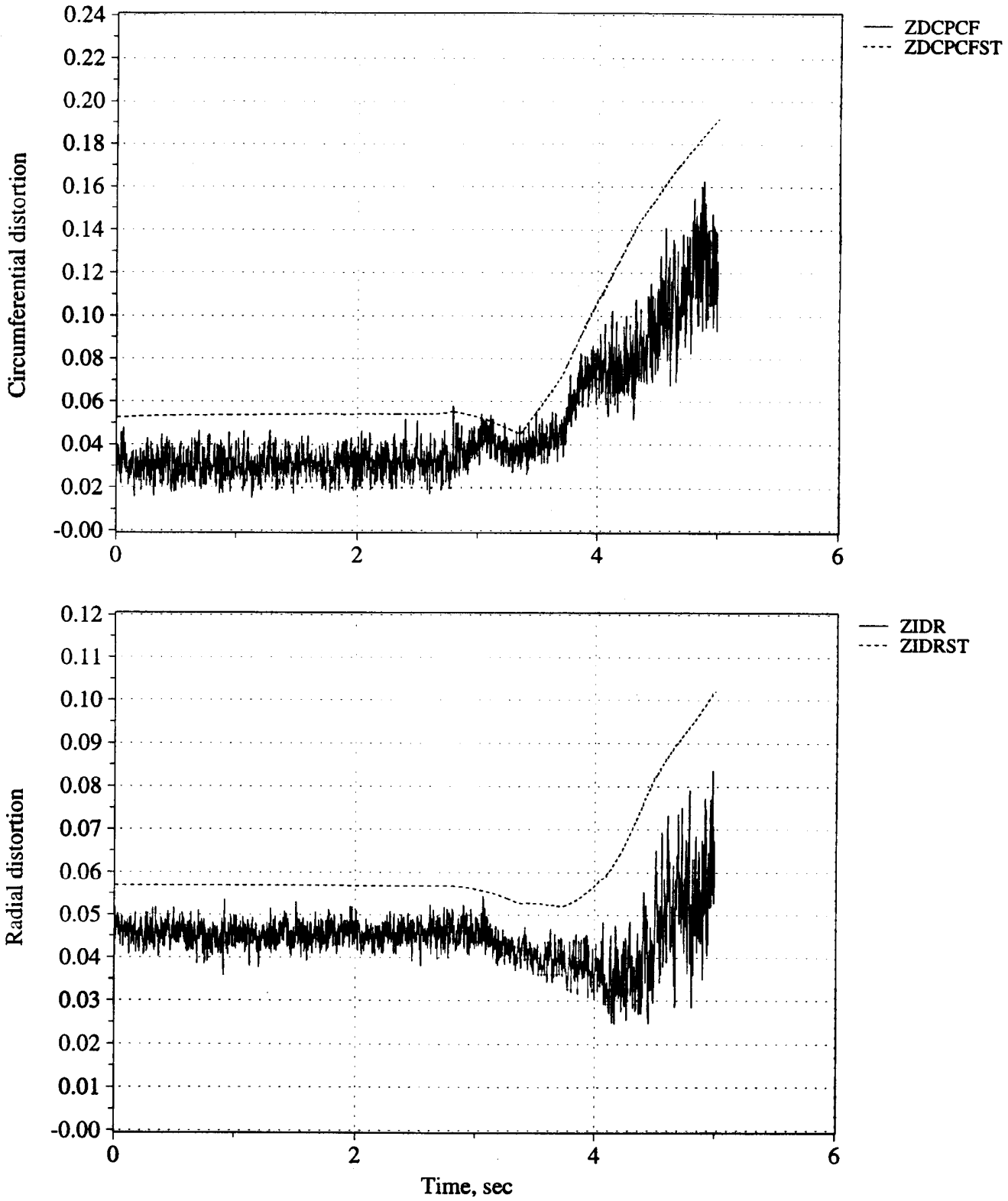

Figure B20. Time history of peak inlet dynamic circumferential and radial distortion (measured and estimated) - Flight 236, Test point 22c.

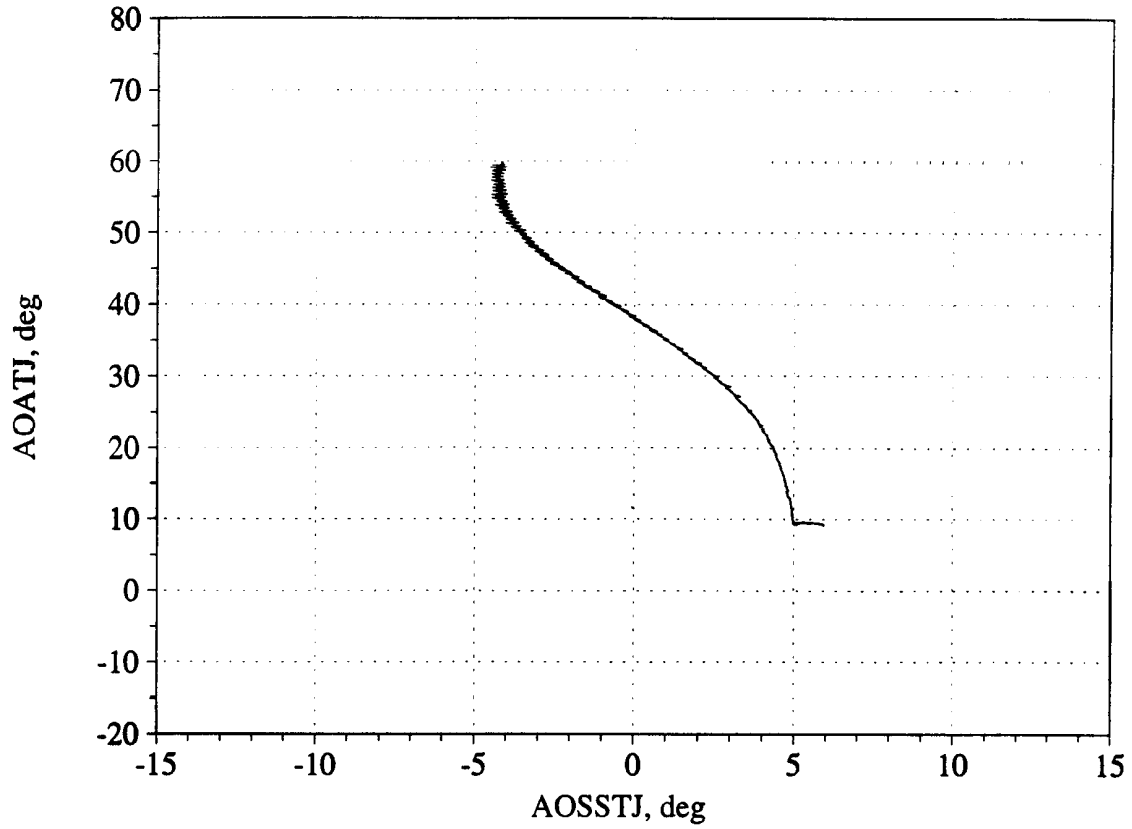

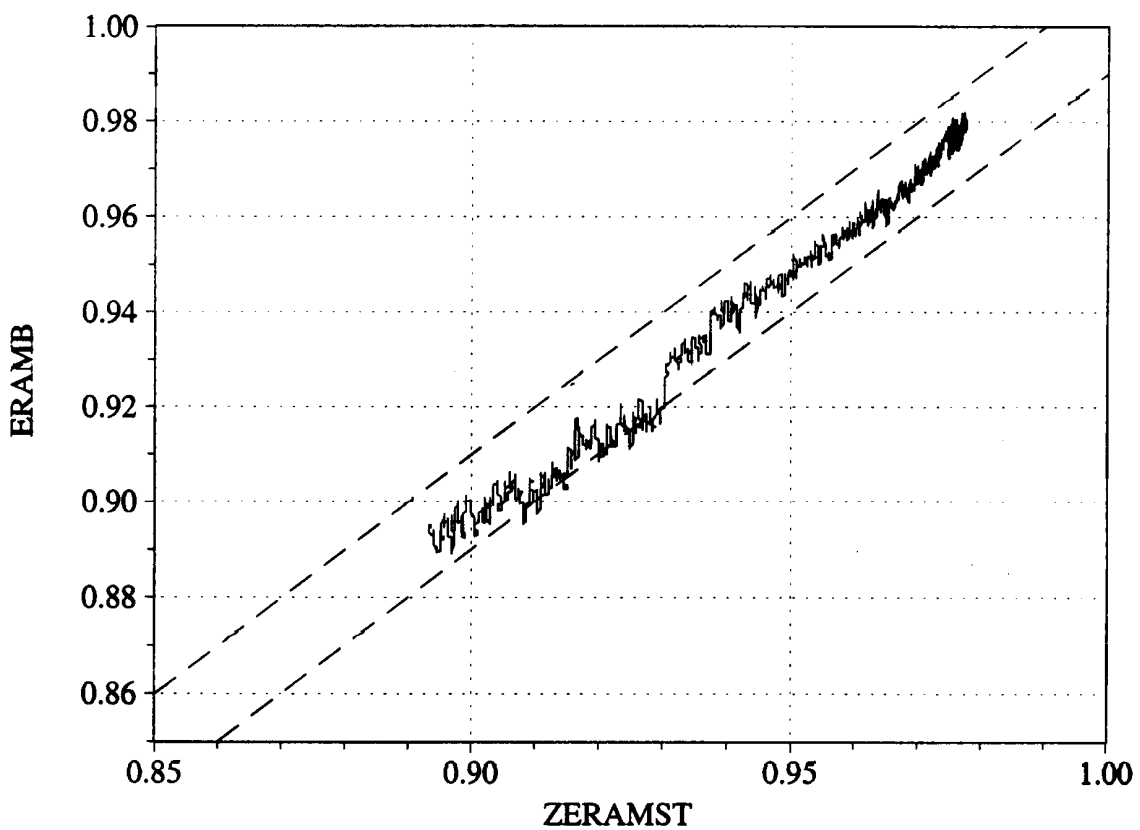

Figure B21. Angle of attack/angle of sideslip trajectory during maneuver; and measured versus estimated recovery - Flight 236, Test point 22c.

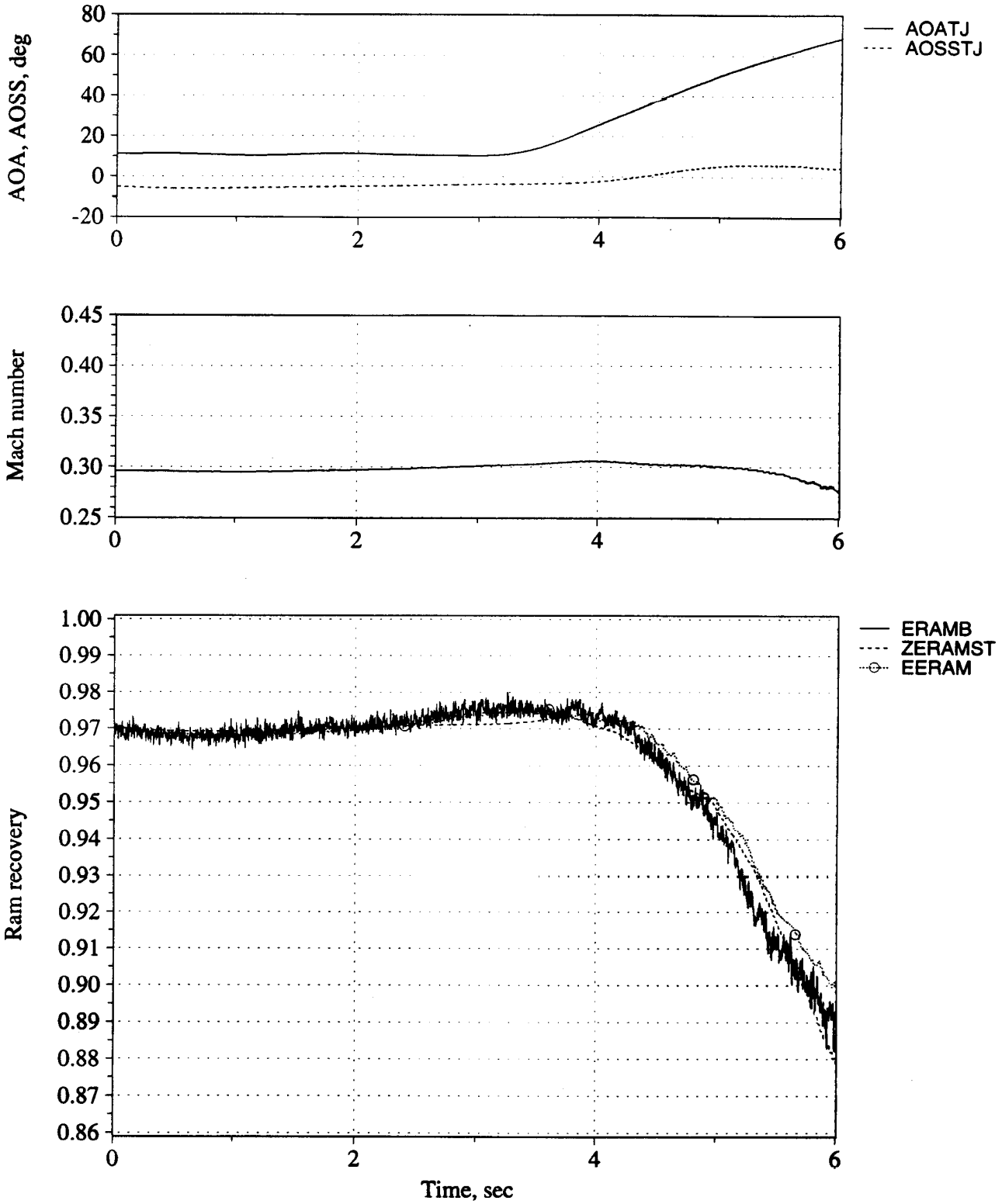

Figure B22. Time history of angle of attack, angle of sideslip, Mach number, and inlet recovery (measured and estimated) - Flight 236, Test point 23b.

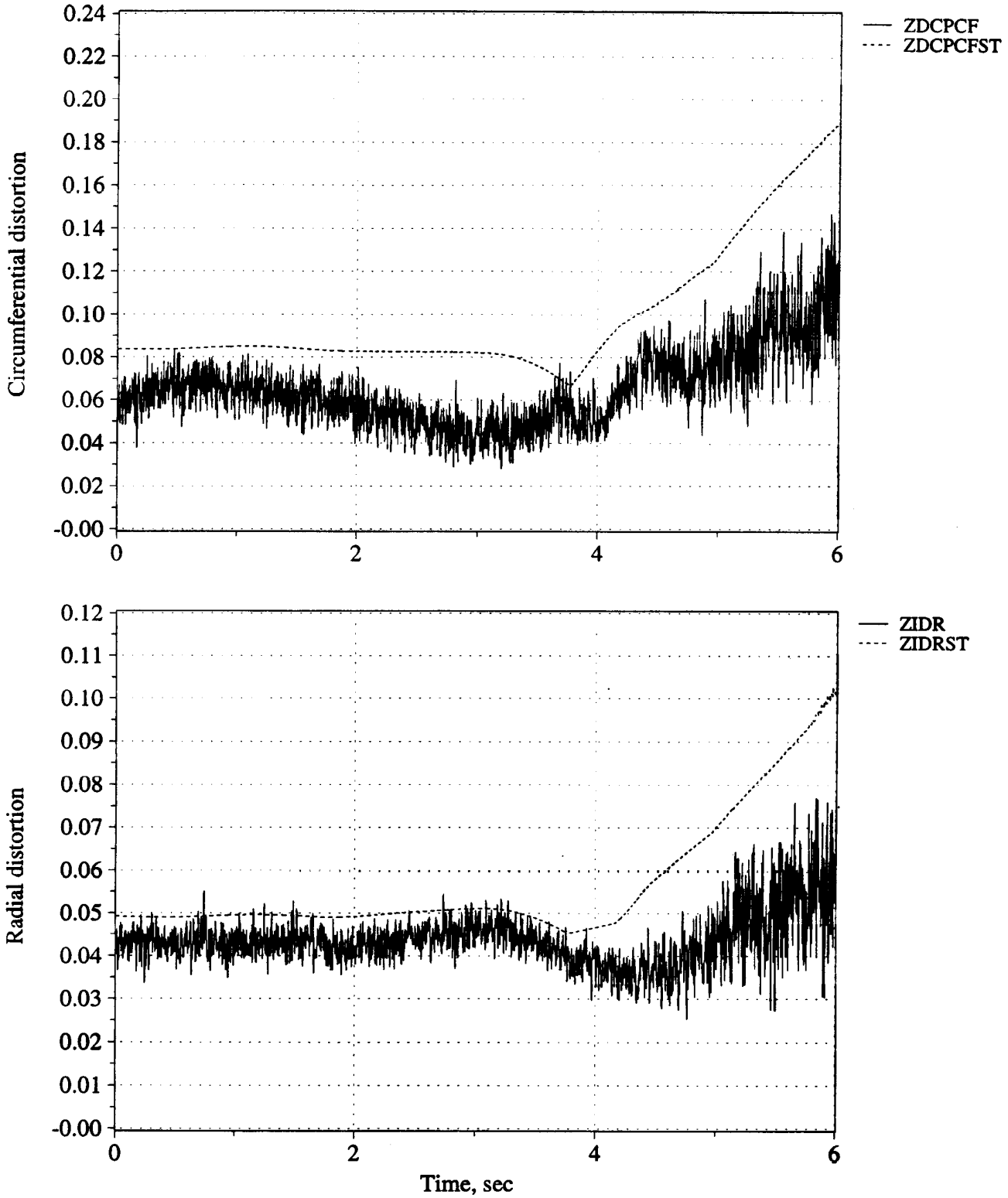

Figure B23. Time history of peak inlet dynamic circumferential and radial distortion (measured and estimated) - Flight 236, Test point 23b.

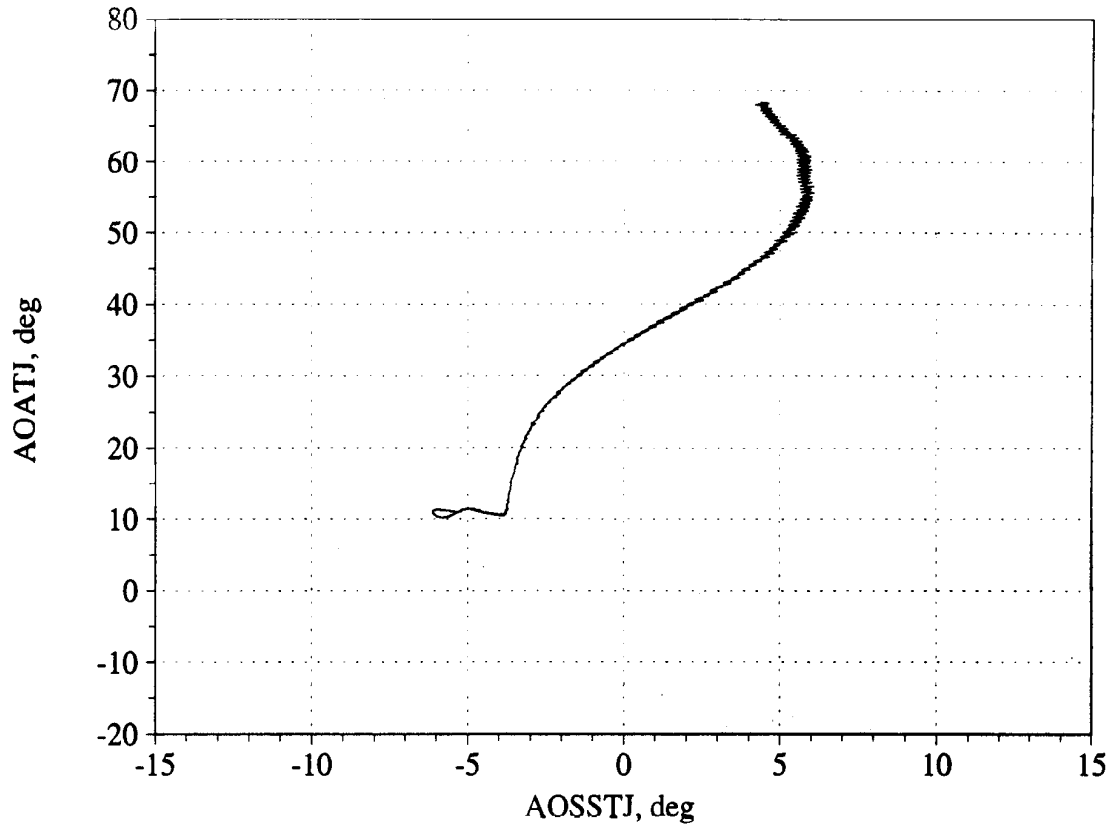

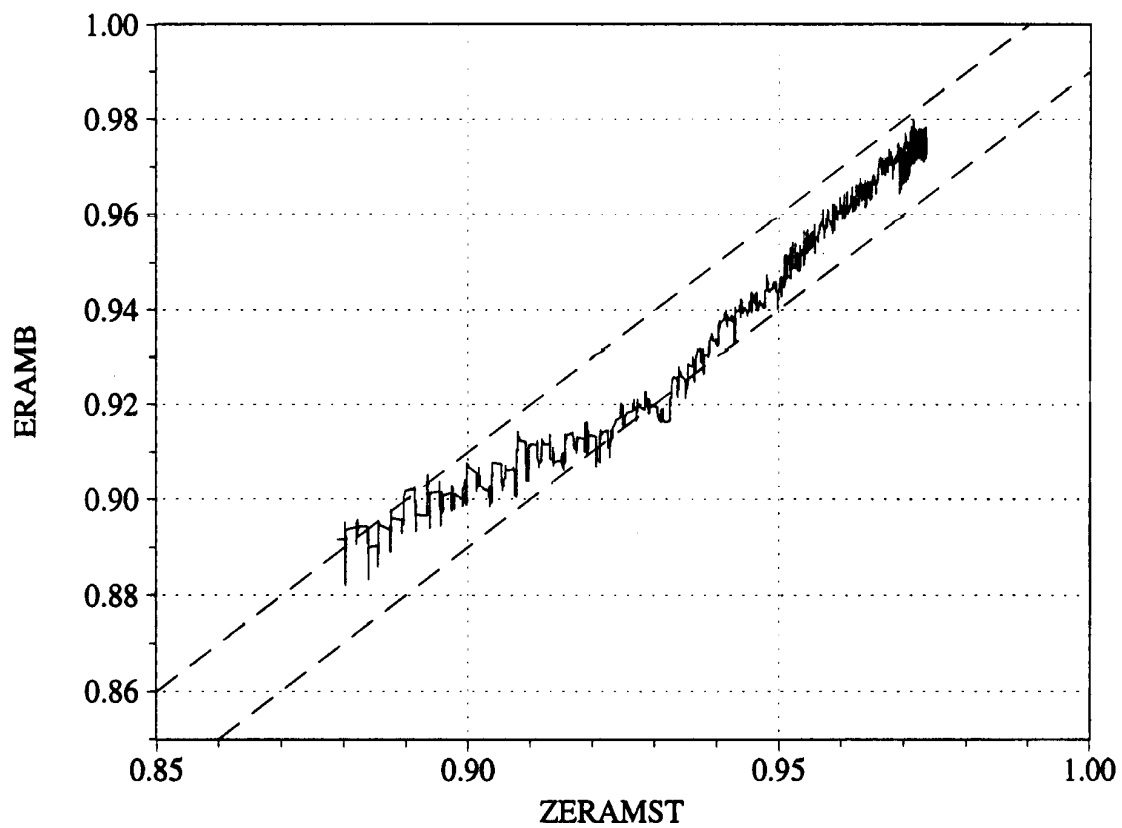

Figure B24. Angle of attack/angle of sideslip trajectory during maneuver; and measured versus estimated recovery - Flight 236, Test point 23b.

- High-to-Low Angle of Attack -

Figures B25 - B27, Flight 212, Test Point 07b
Figures B28 - B30, Flight 231, Test Point 04c
Figures B31 - B33, Flight 232, Test Point 05c
Figures B34 - B36, Flight 233, Test Point 05c
Figures B37 - B39, Flight 242, Test Point 16c
Figures B40 - B42, Flight 242, Test Point 17b
Figures B43 - B45, Flight 243, Test Point 16c
Figures B46 - B48, Flight 243, Test Point 29d
Figures B49 - B51, Flight 247, Test Point 6b4

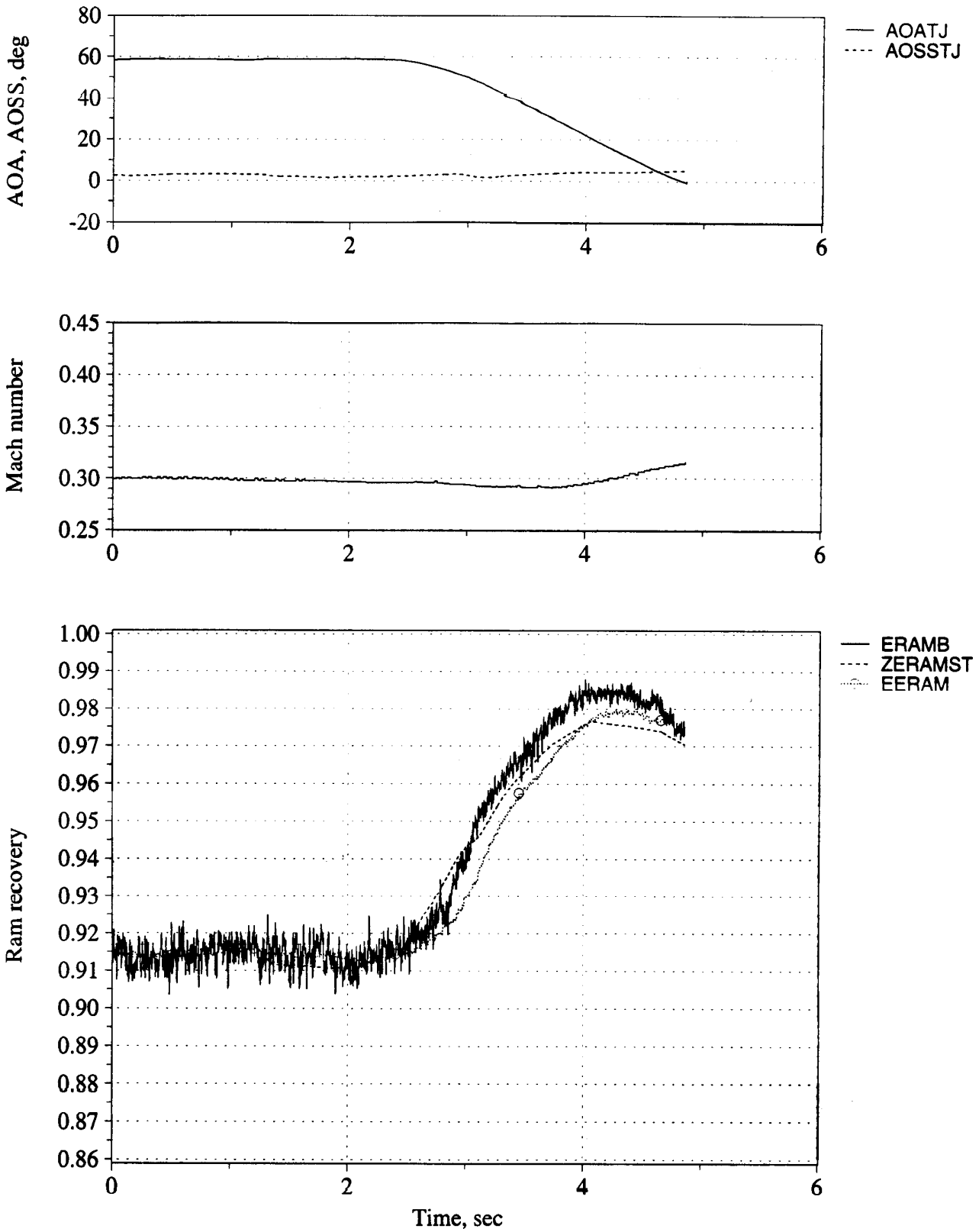

Figure B25. Time history of angle of attack, angle of sideslip, Mach number, and inlet recovery (measured and estimated) - Flight 212, Test point 07b.

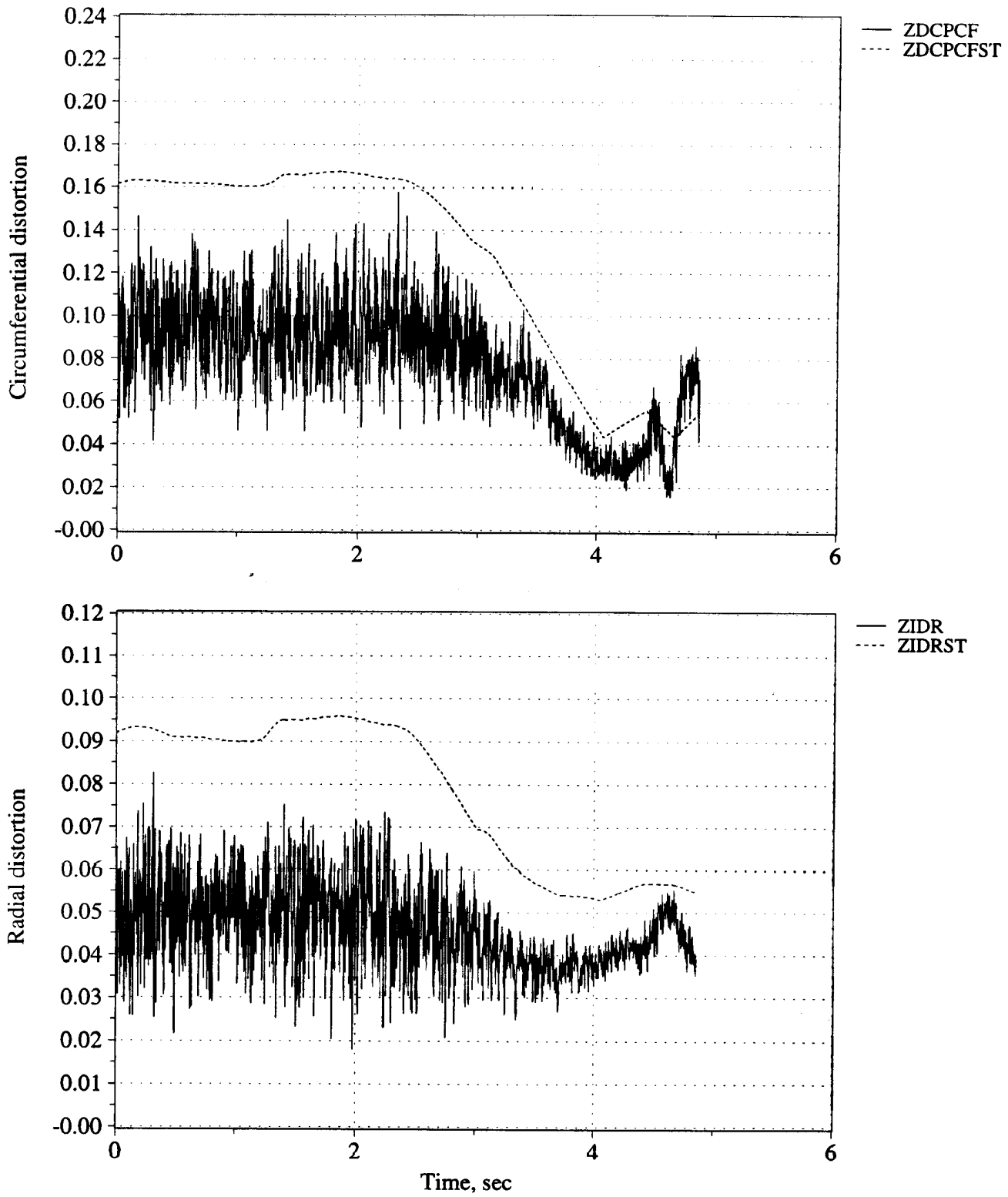

Figure B26. Time history of peak inlet dynamic circumferential and radial distortion (measured and estimated) - Flight 212, Test point 07b.

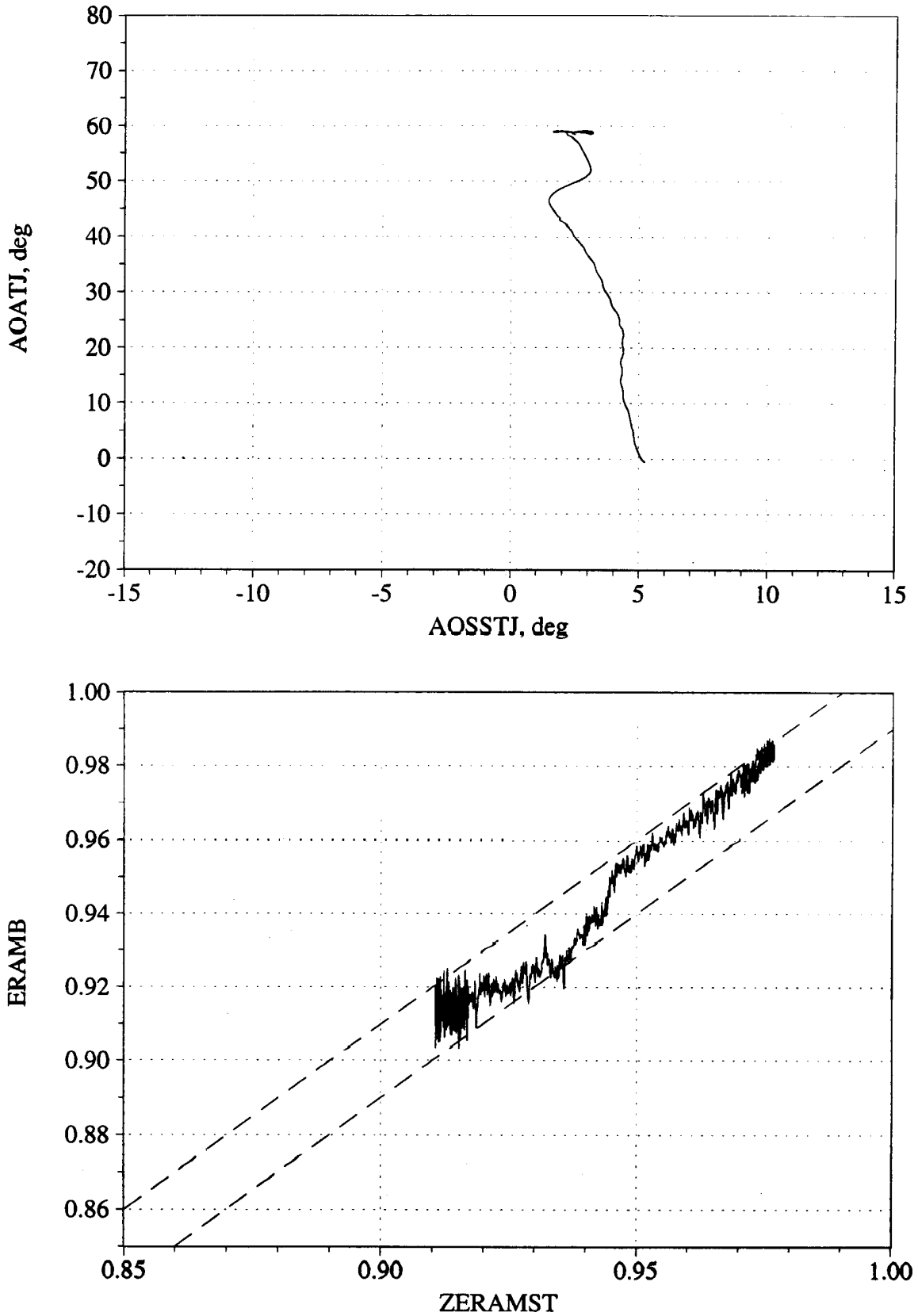

Figure B27. Angle of attack/angle of sideslip trajectory during maneuver; and measured versus estimated recovery - Flight 212, Test point 07b.

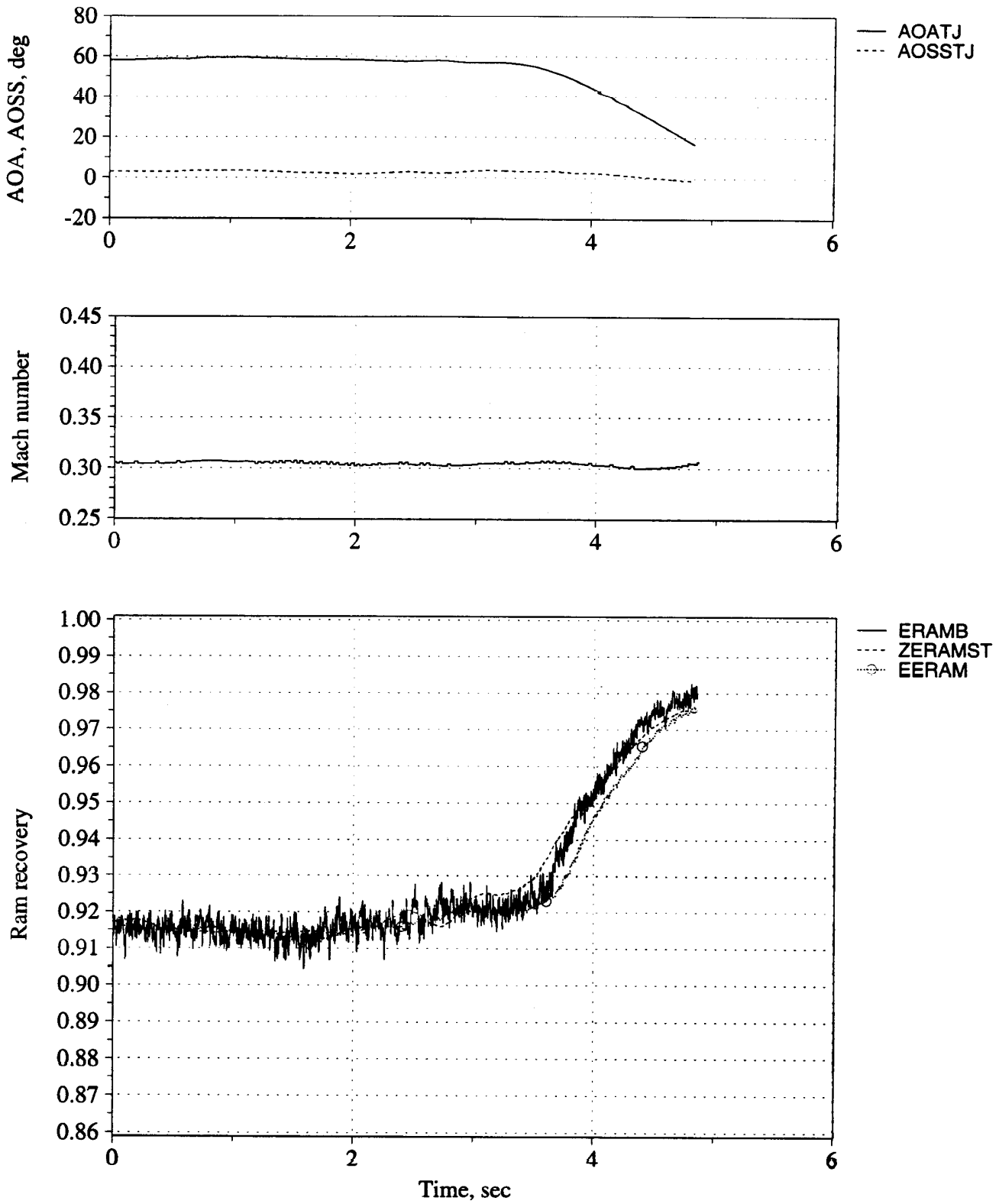

Figure B28. Time history of angle of attack, angle of sideslip, Mach number, and inlet recovery (measured and estimated) - Flight 231, Test point 04c.

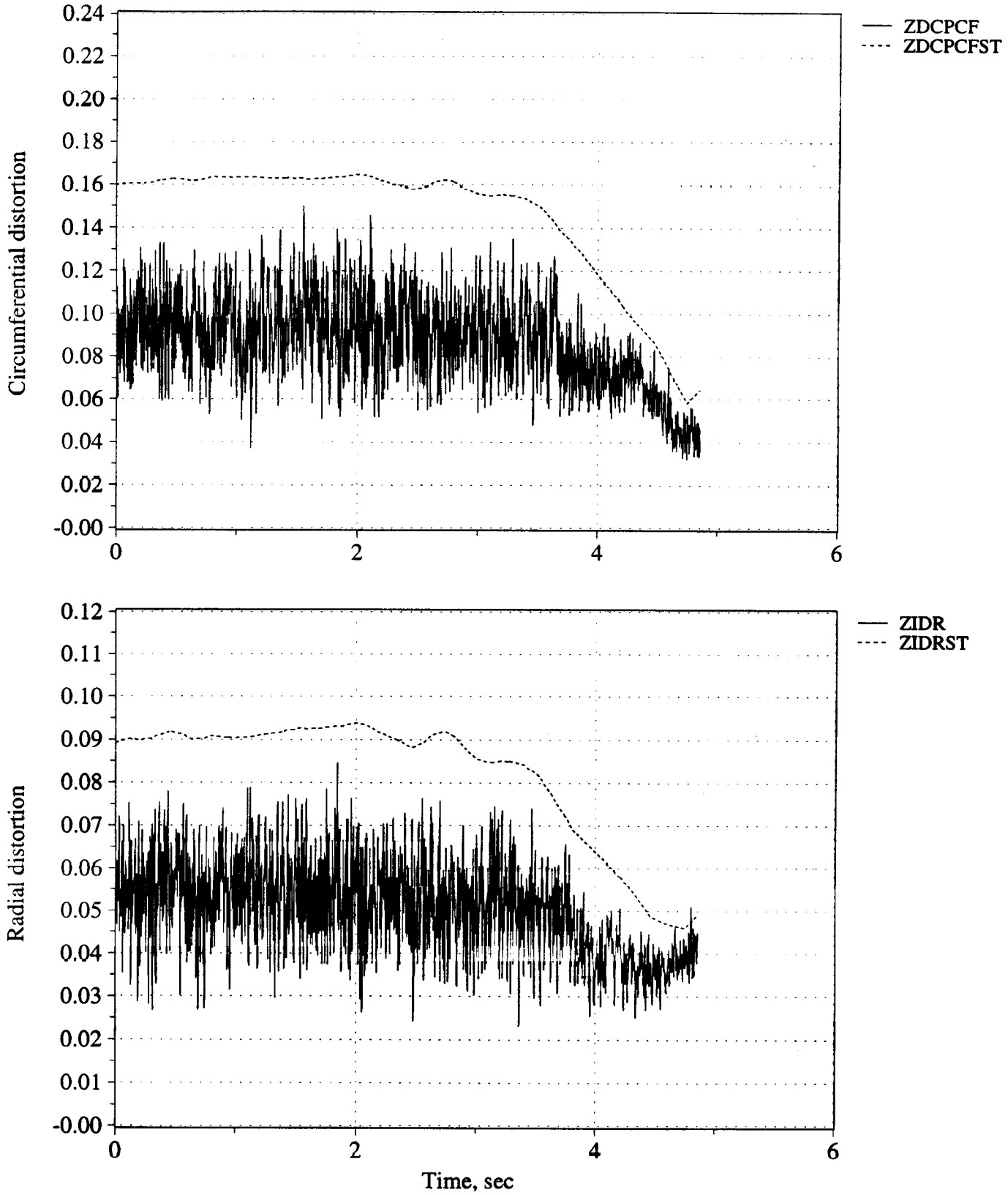

Figure B29. Time history of peak inlet dynamic circumferential and radial distortion (measured and estimated) - Flight 231, Test point 04c.

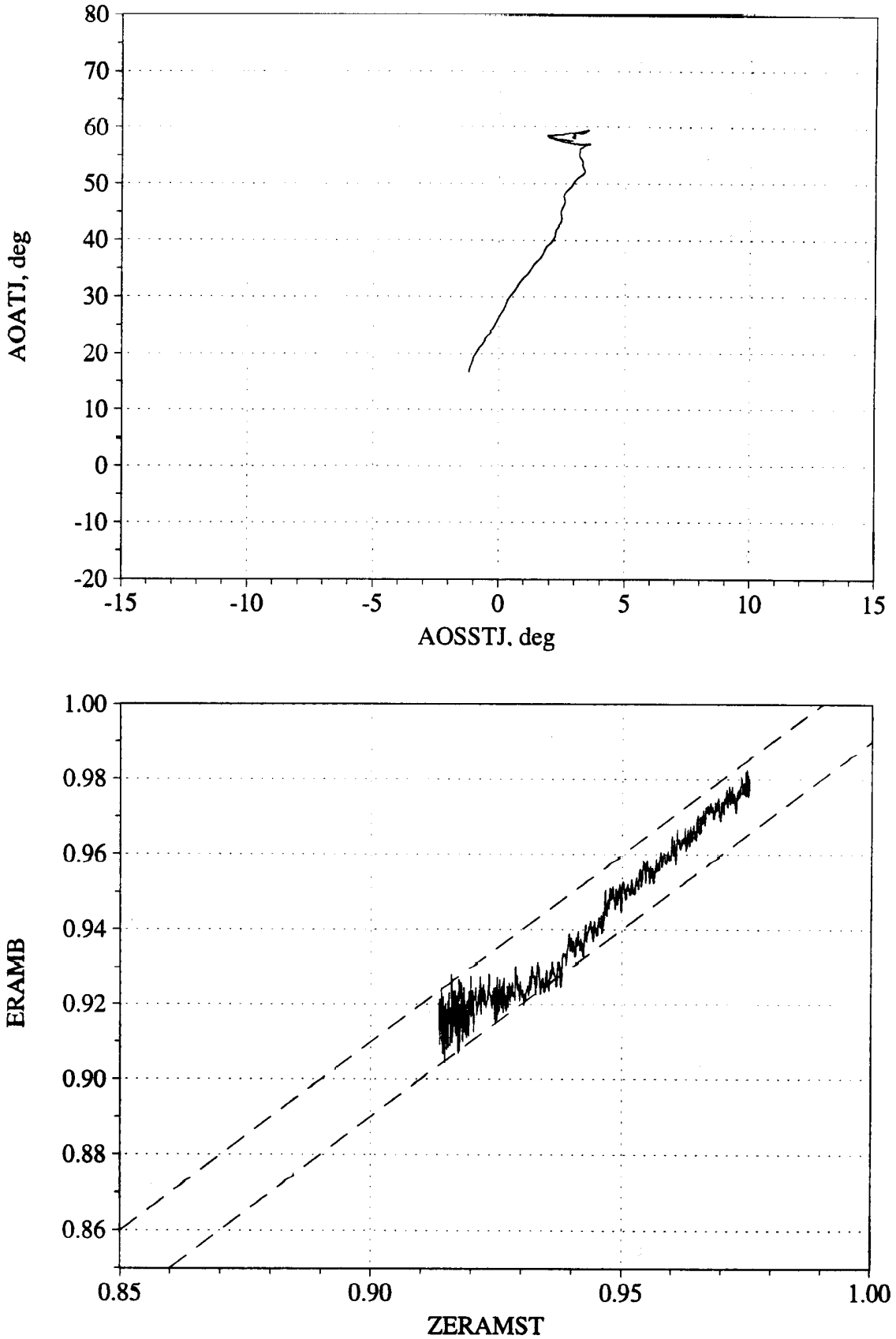

Figure B30. Angle of attack/angle of sideslip trajectory during maneuver; and measured versus estimated recovery - Flight 231, Test point 04c.

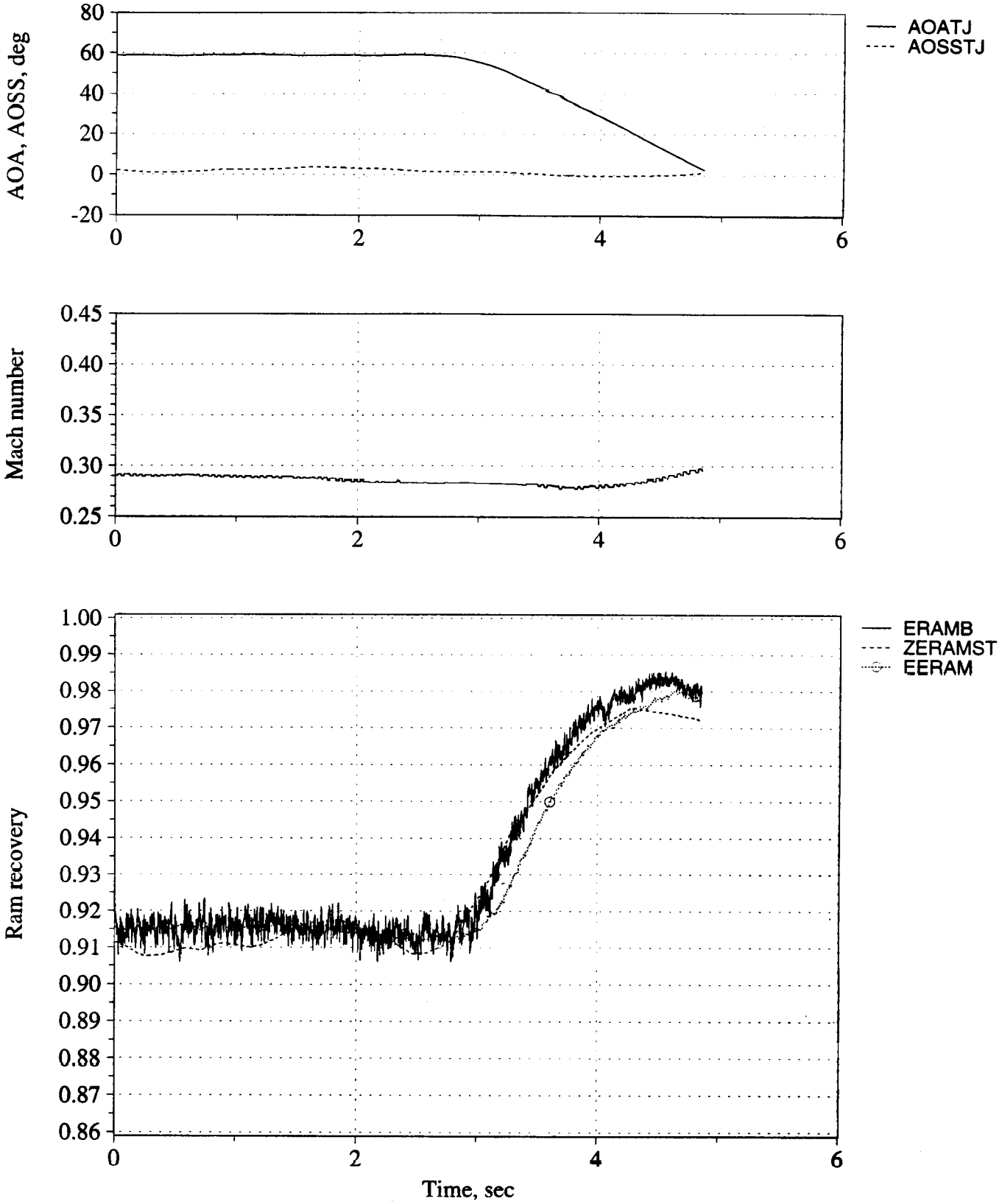

Figure B31. Time history of angle of attack, angle of sideslip, Mach number, and inlet recovery (measured and estimated) - Flight 232, Test point 05c.

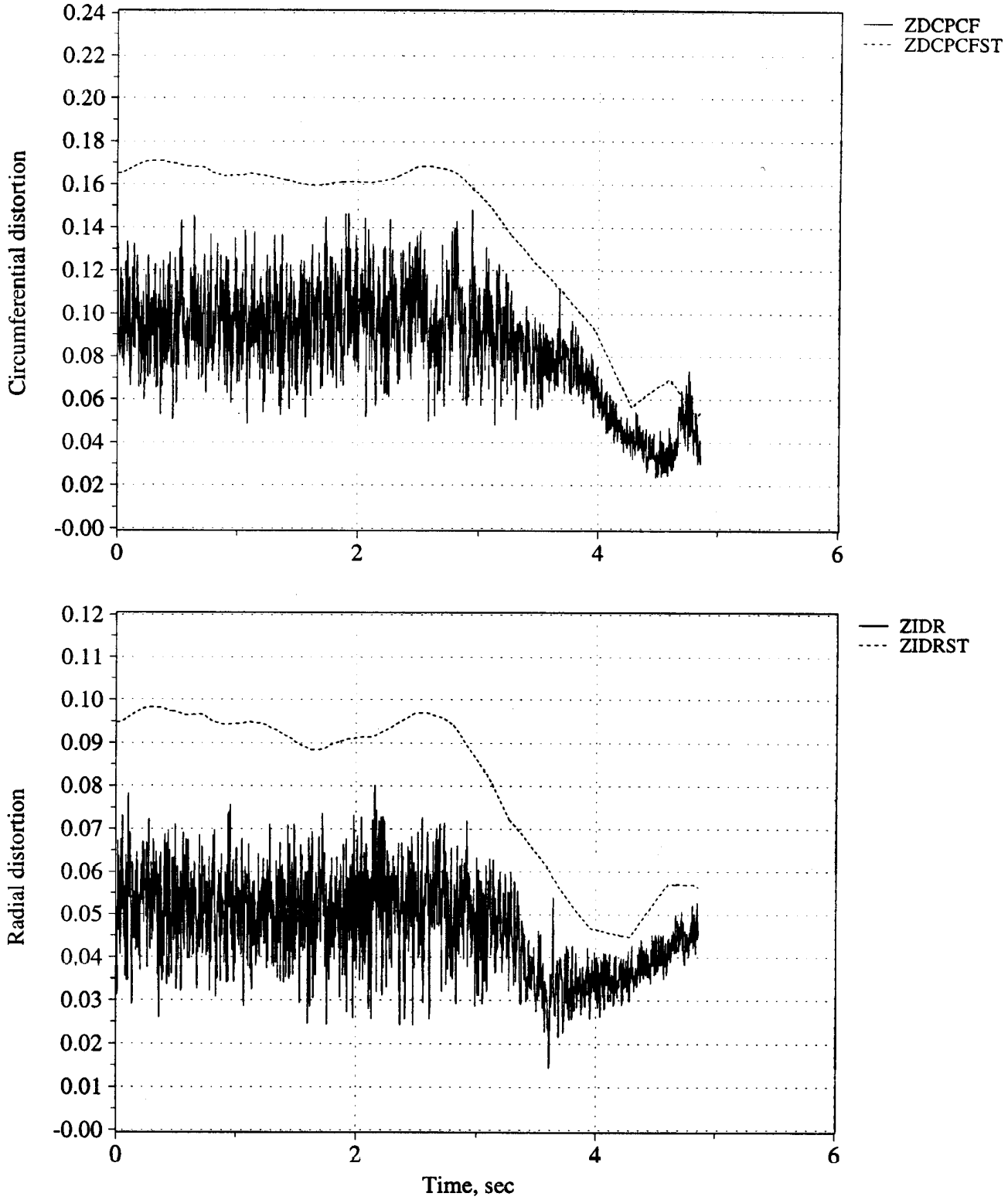

Figure B32. Time history of peak inlet dynamic circumferential and radial distortion (measured and estimated) - Flight 232, Test point 05c.

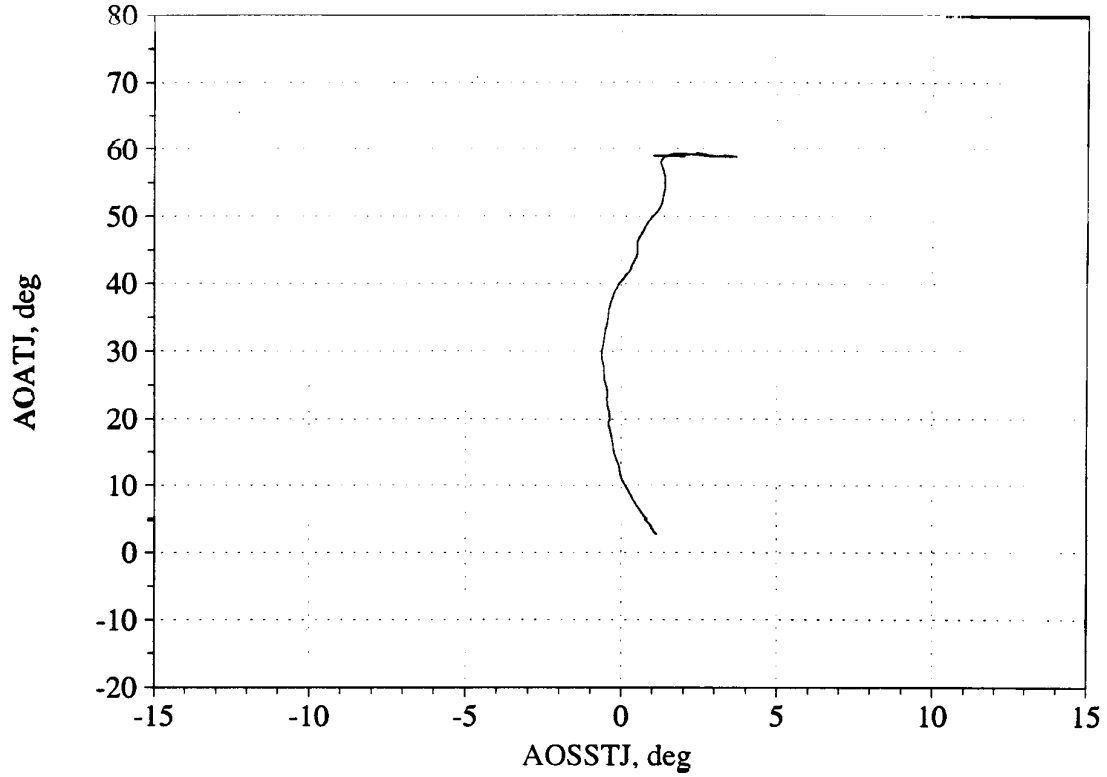

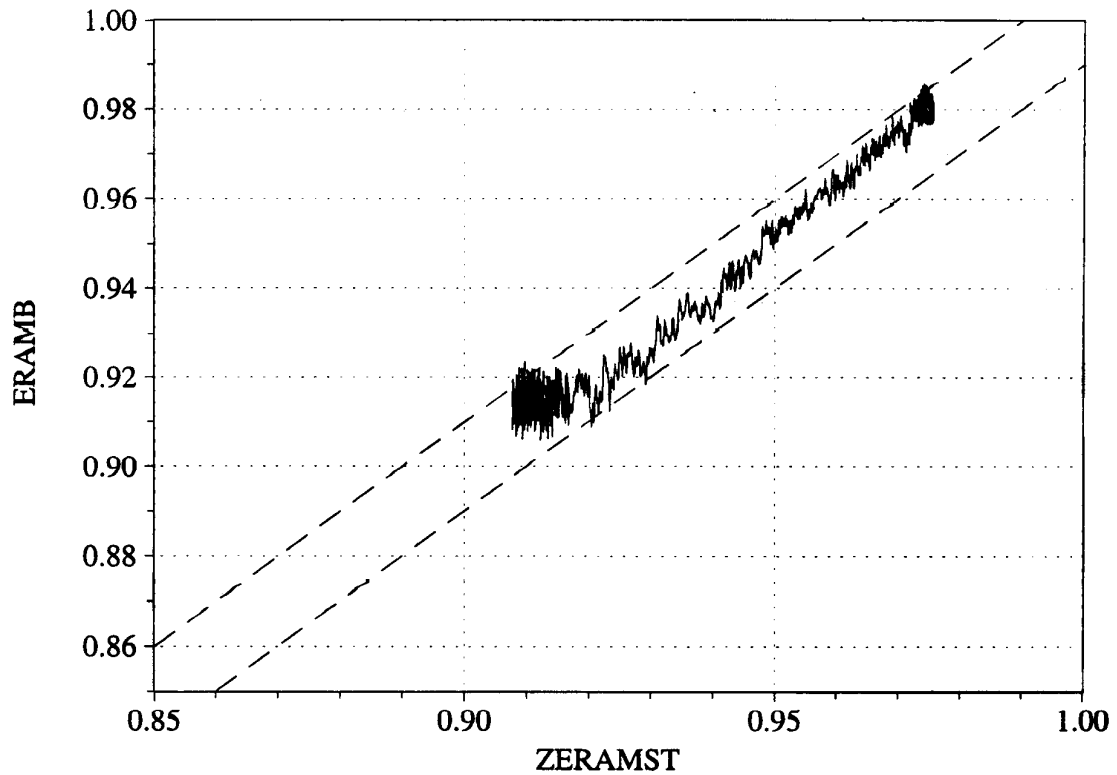

Figure B33. Angle of attack/angle of sideslip trajectory during maneuver; and measured versus estimated recovery - Flight 232, Test point 05c.

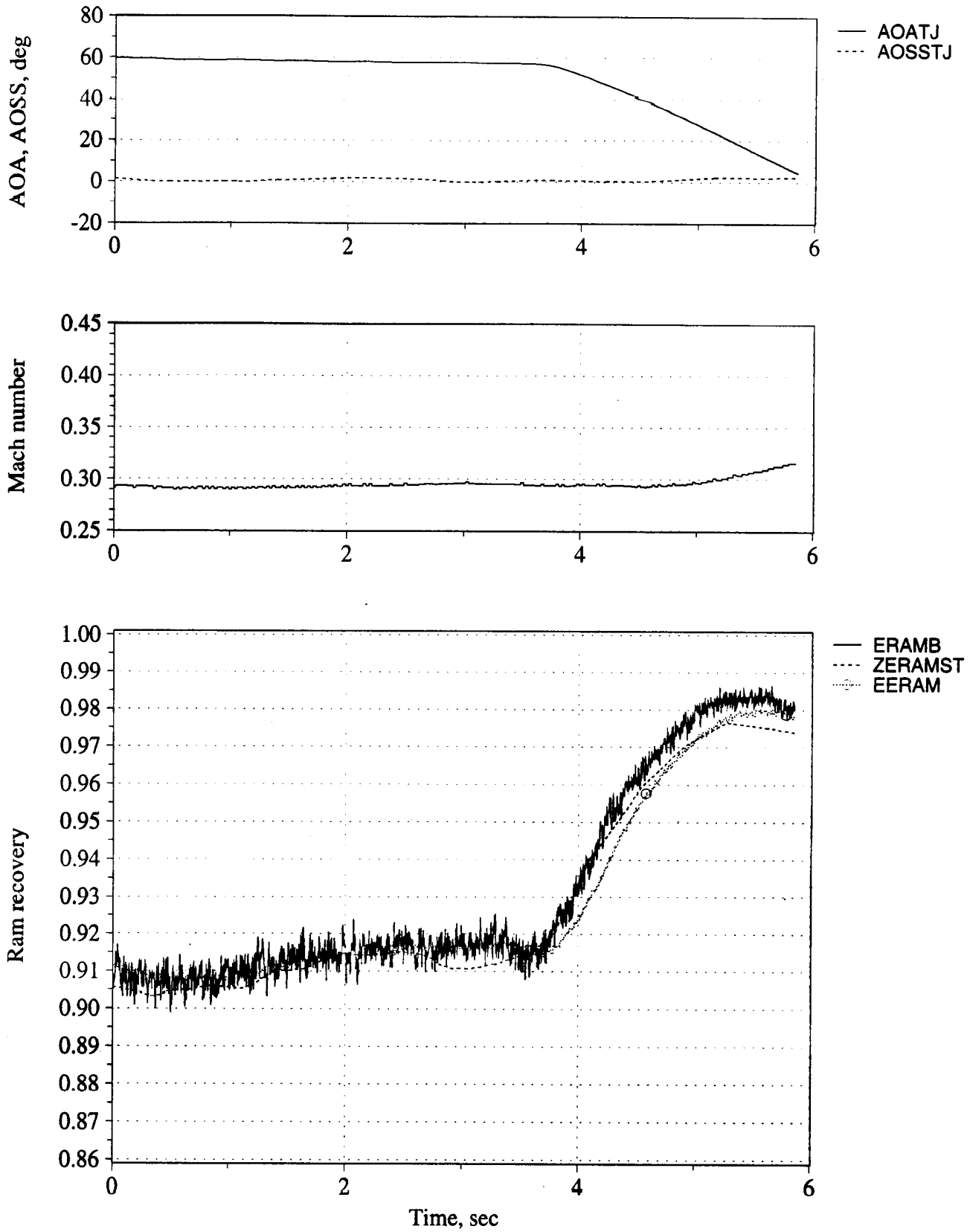

Figure B34. Time history of angle of attack, angle of sideslip, Mach number, and inlet recovery (measured and estimated) - Flight 233, Test point 05c.

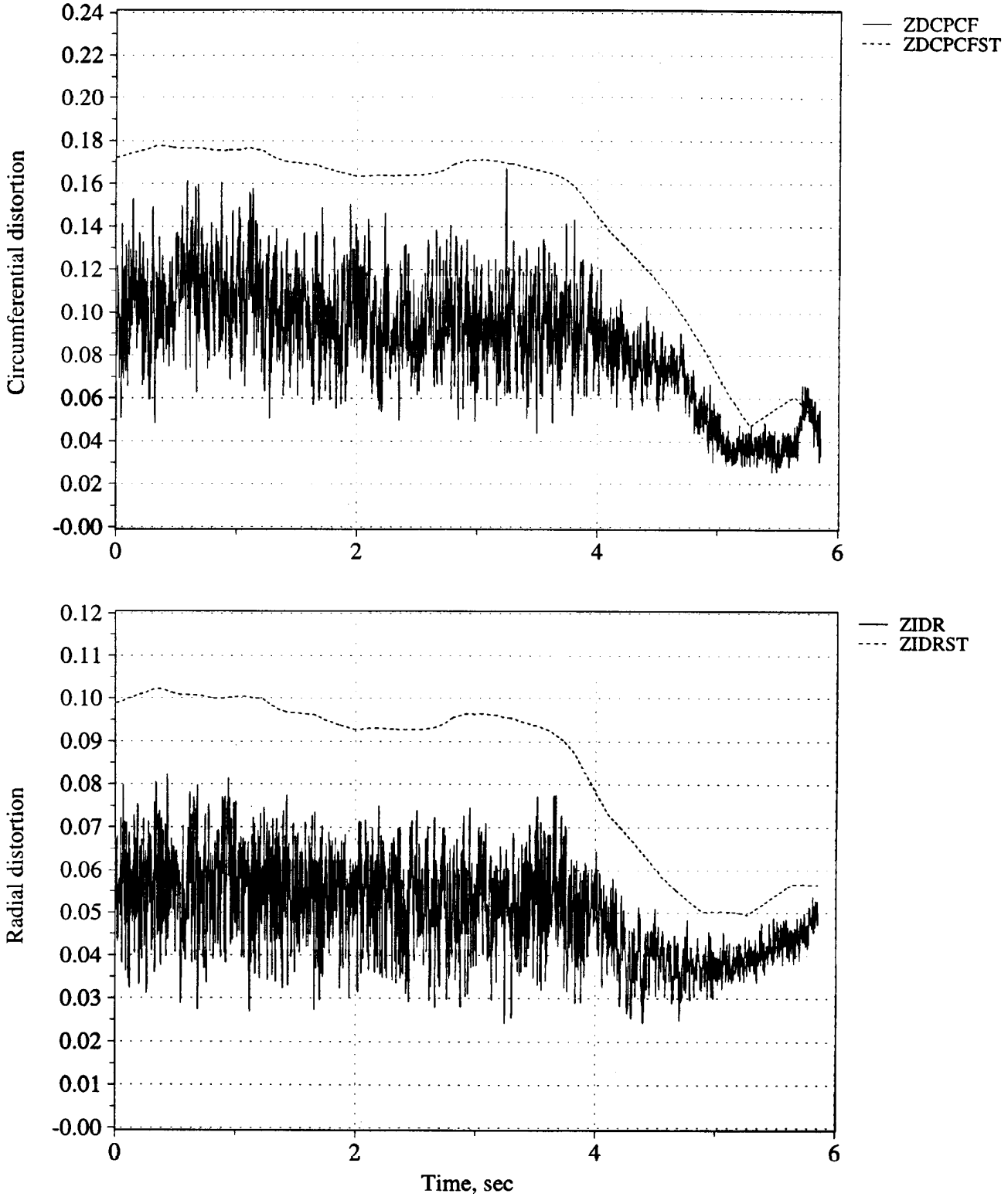

Figure B35. Time history of peak inlet dynamic circumferential and radial distortion (measured and estimated) - Flight 233, Test point 05c.

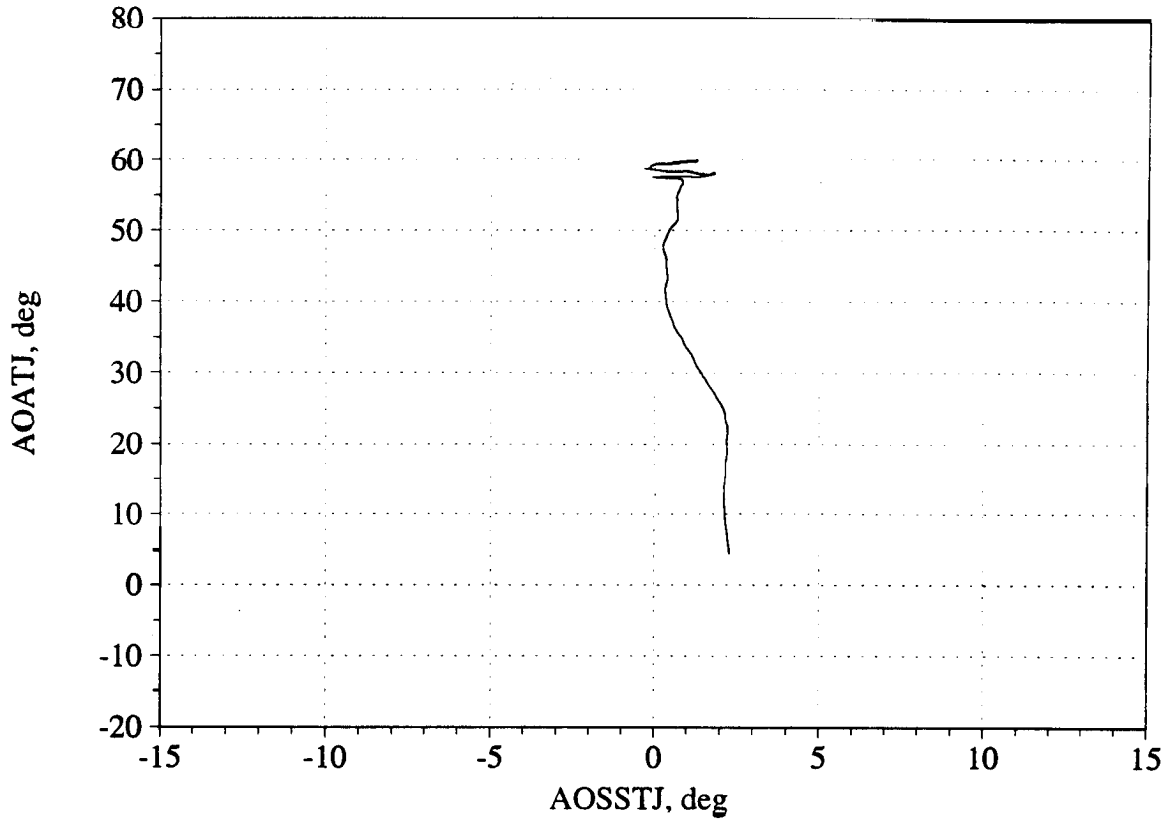

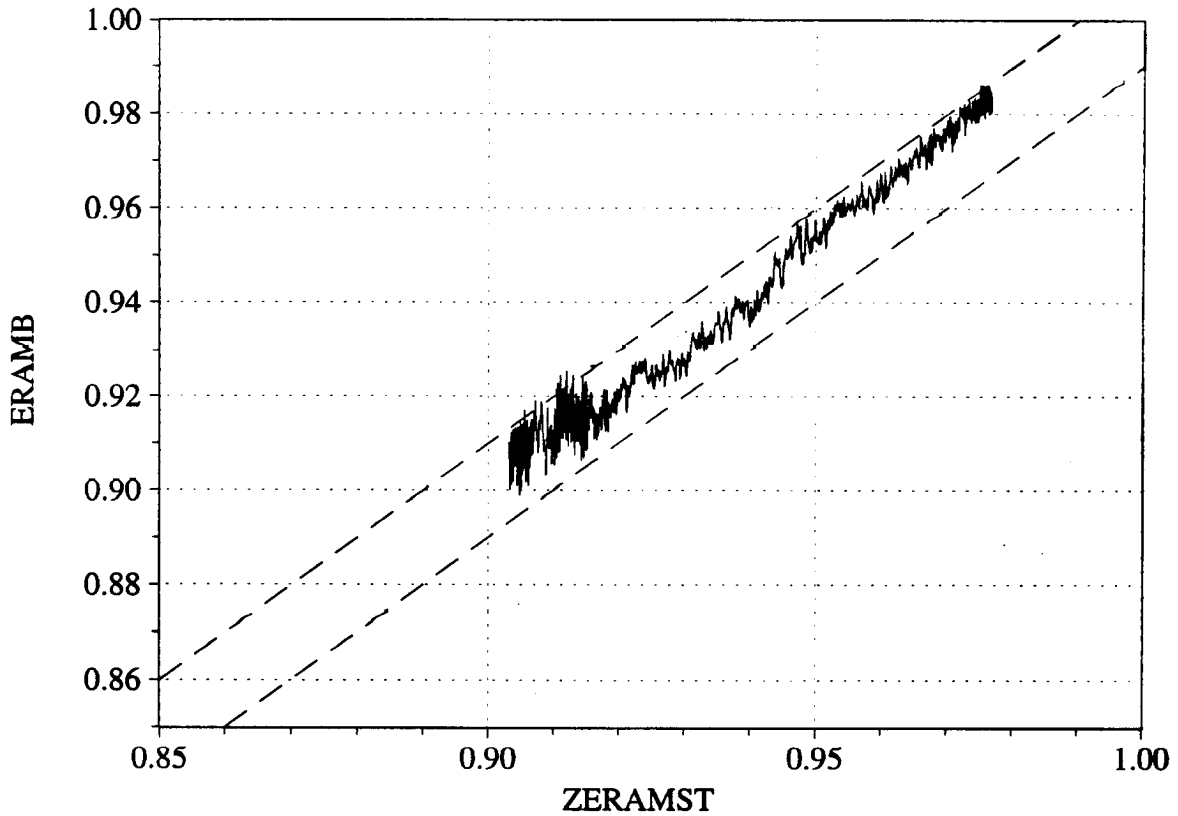

Figure B36. Angle of attack/angle of sideslip trajectory during maneuver; and measured versus estimated recovery - Flight 233, Test point 05c.

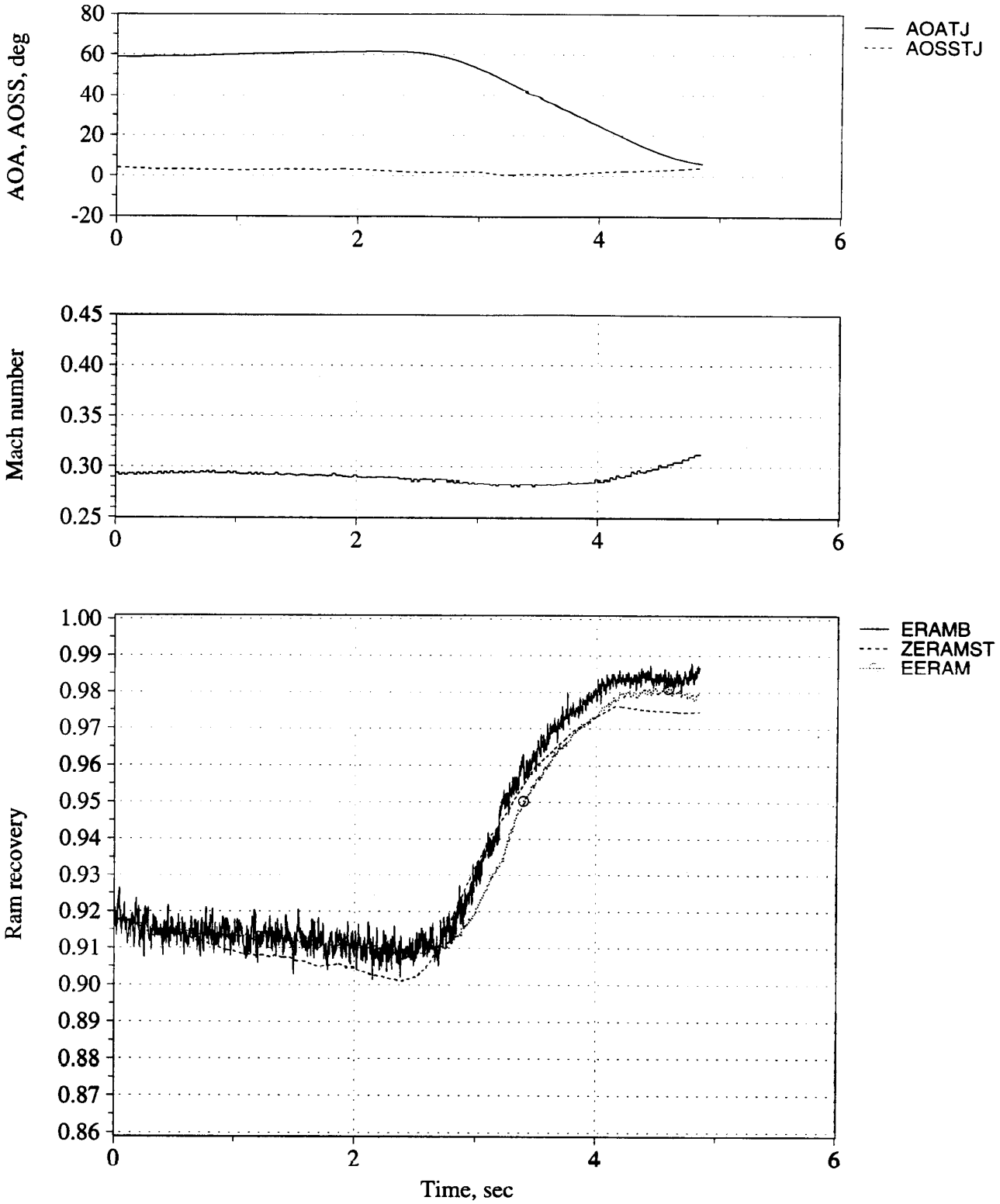

Figure B37. Time history of angle of attack, angle of sideslip, Mach number, and inlet recovery (measured and estimated) - Flight 242, Test point 16c.

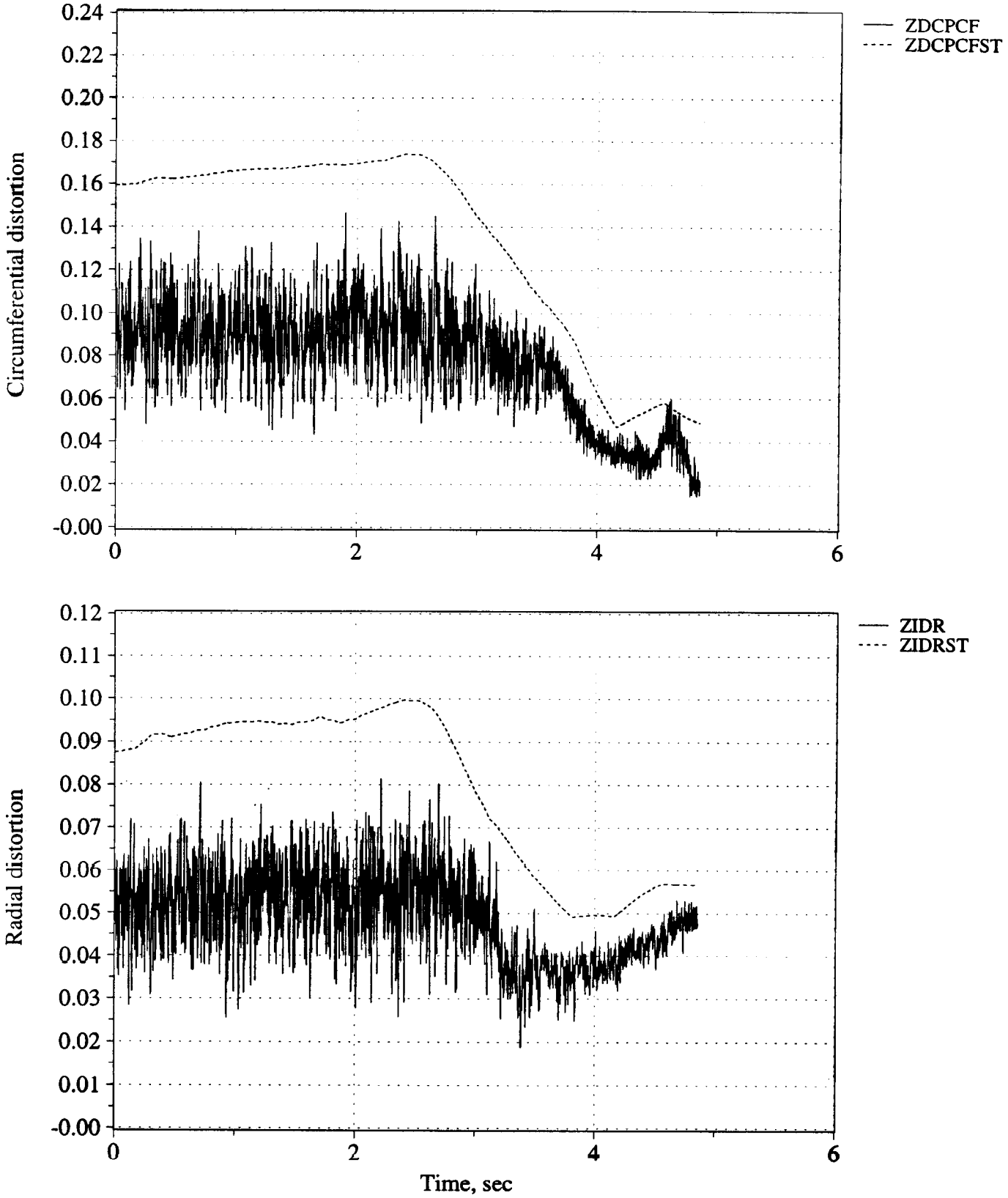

Figure B38. Time history of peak inlet dynamic circumferential and radial distortion (measured and estimated) - Flight 242, Test point 16c.

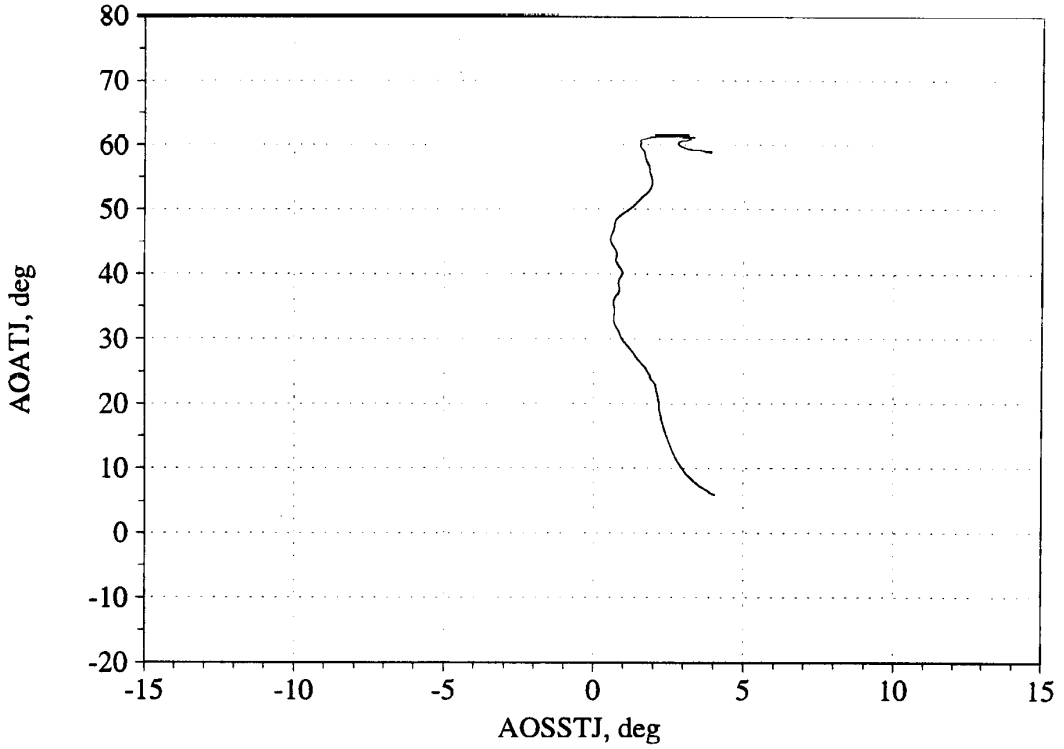

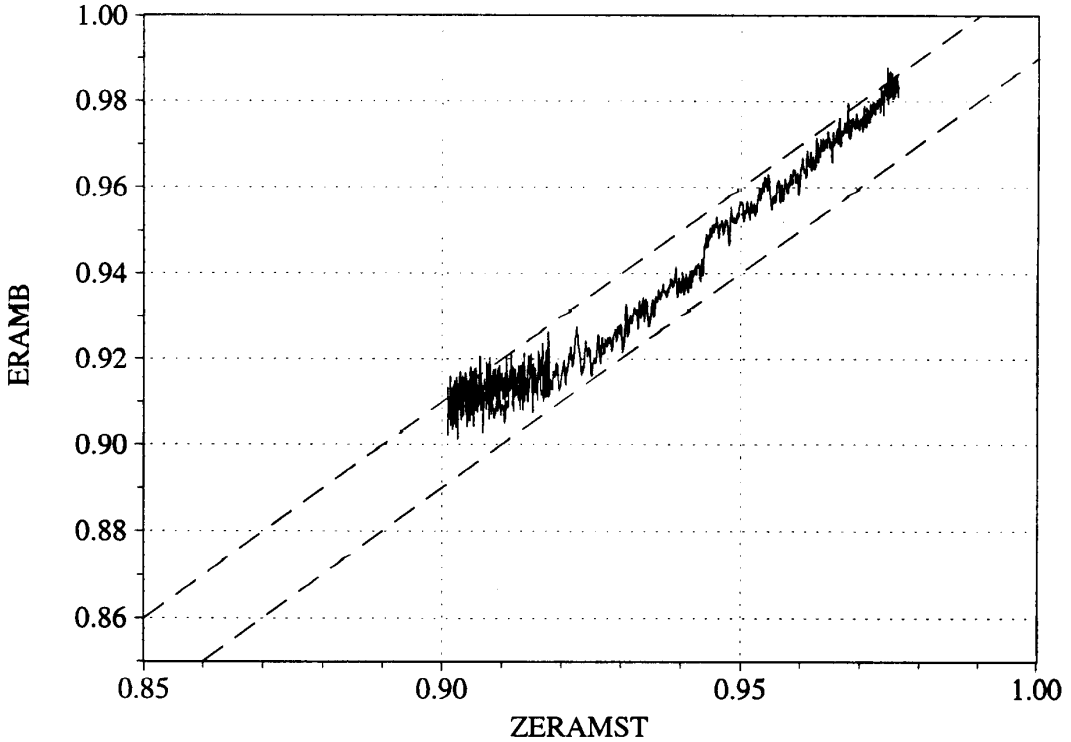

Figure B39. Angle of attack/angle of sideslip trajectory during maneuver; and measured versus estimated recovery - Flight 242, Test point 16c.

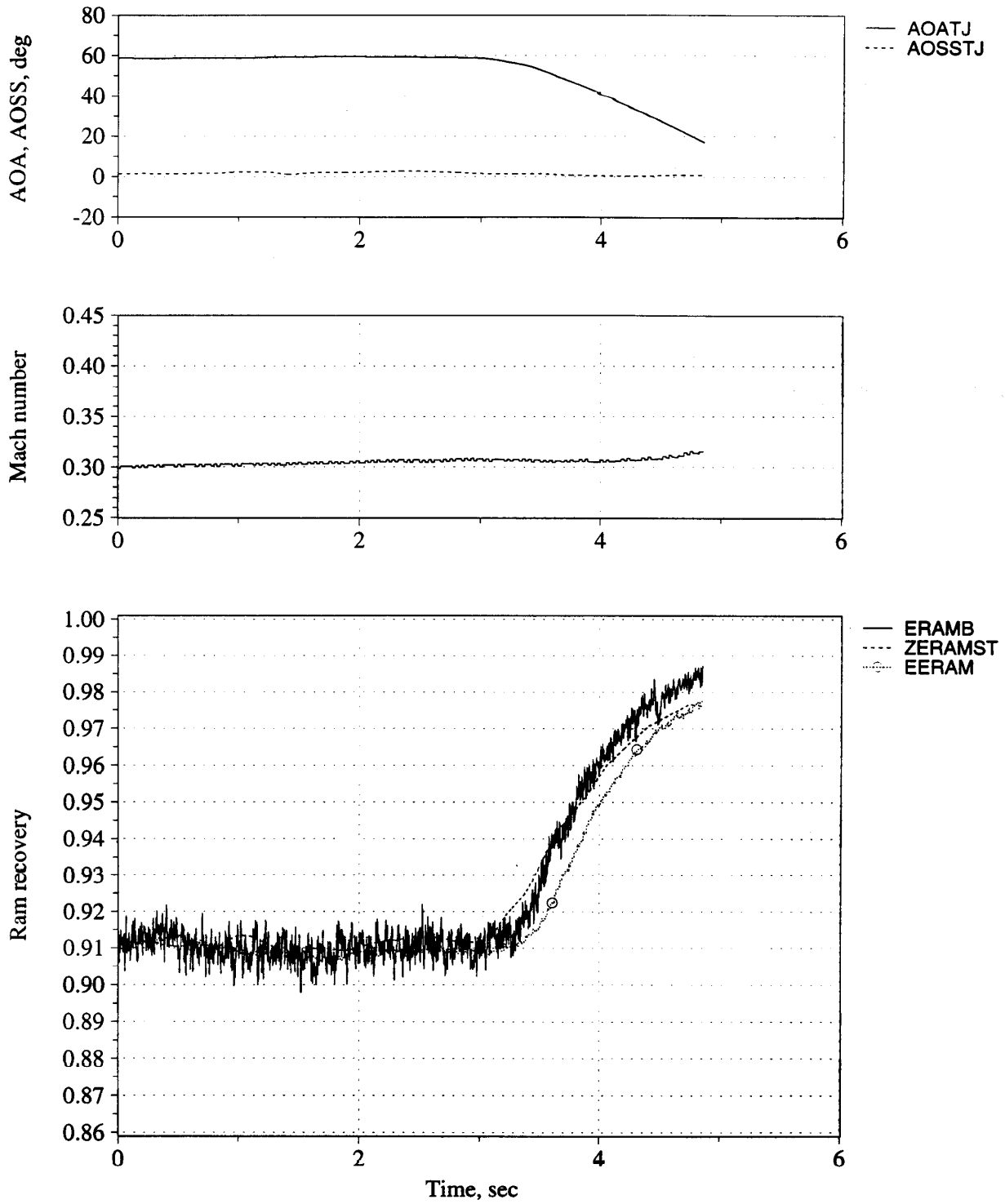

Figure B40. Time history of angle of attack, angle of sideslip, Mach number, and inlet recovery (measured and estimated) - Flight 242, Test point 17b.

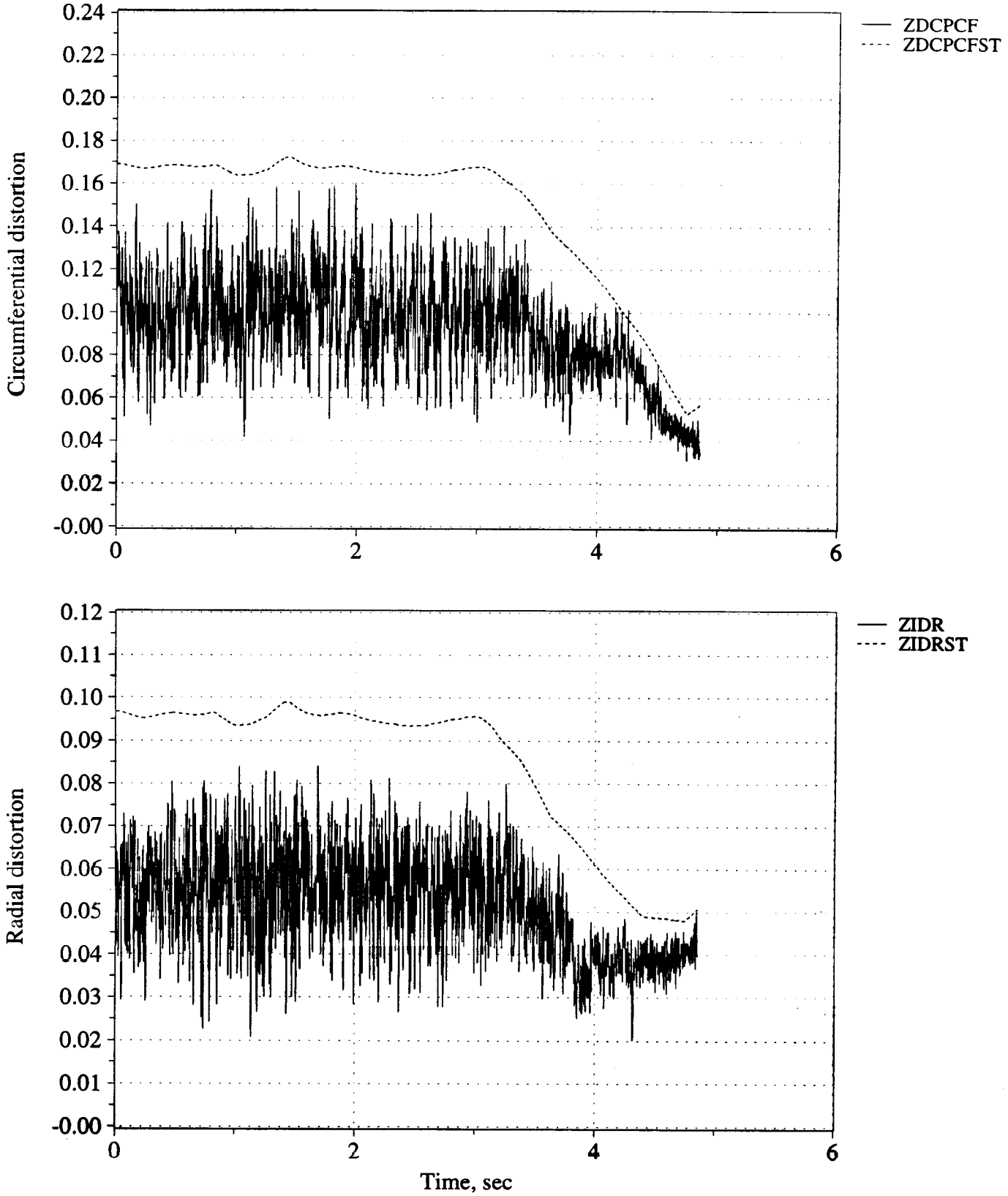

Figure B41. Time history of peak inlet dynamic circumferential and radial distortion (measured and estimated) - Flight 242, Test point 17b.

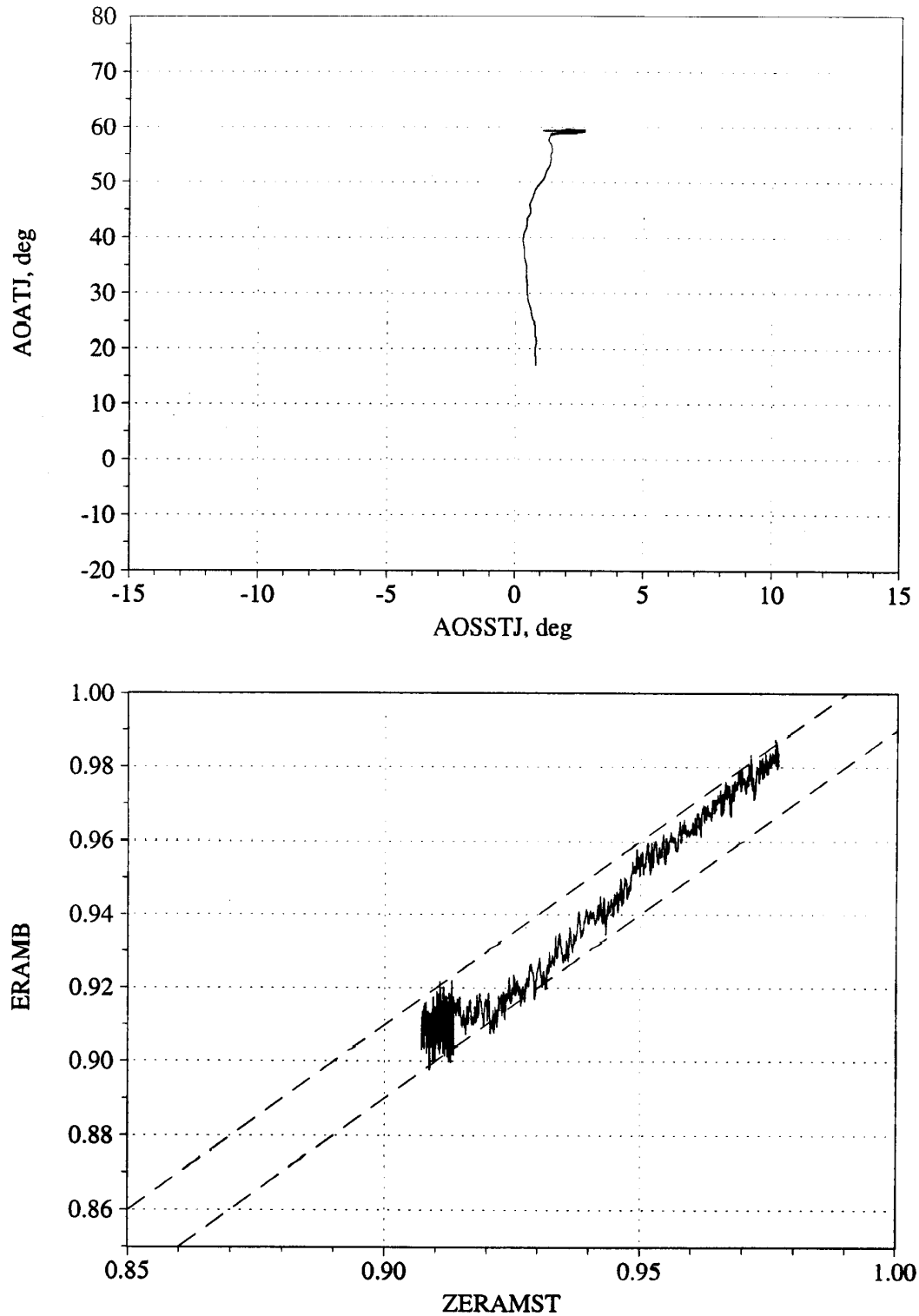

Figure B42. Angle of attack/angle of sideslip trajectory during maneuver; and measured versus estimated recovery - Flight 242, Test point 17b.

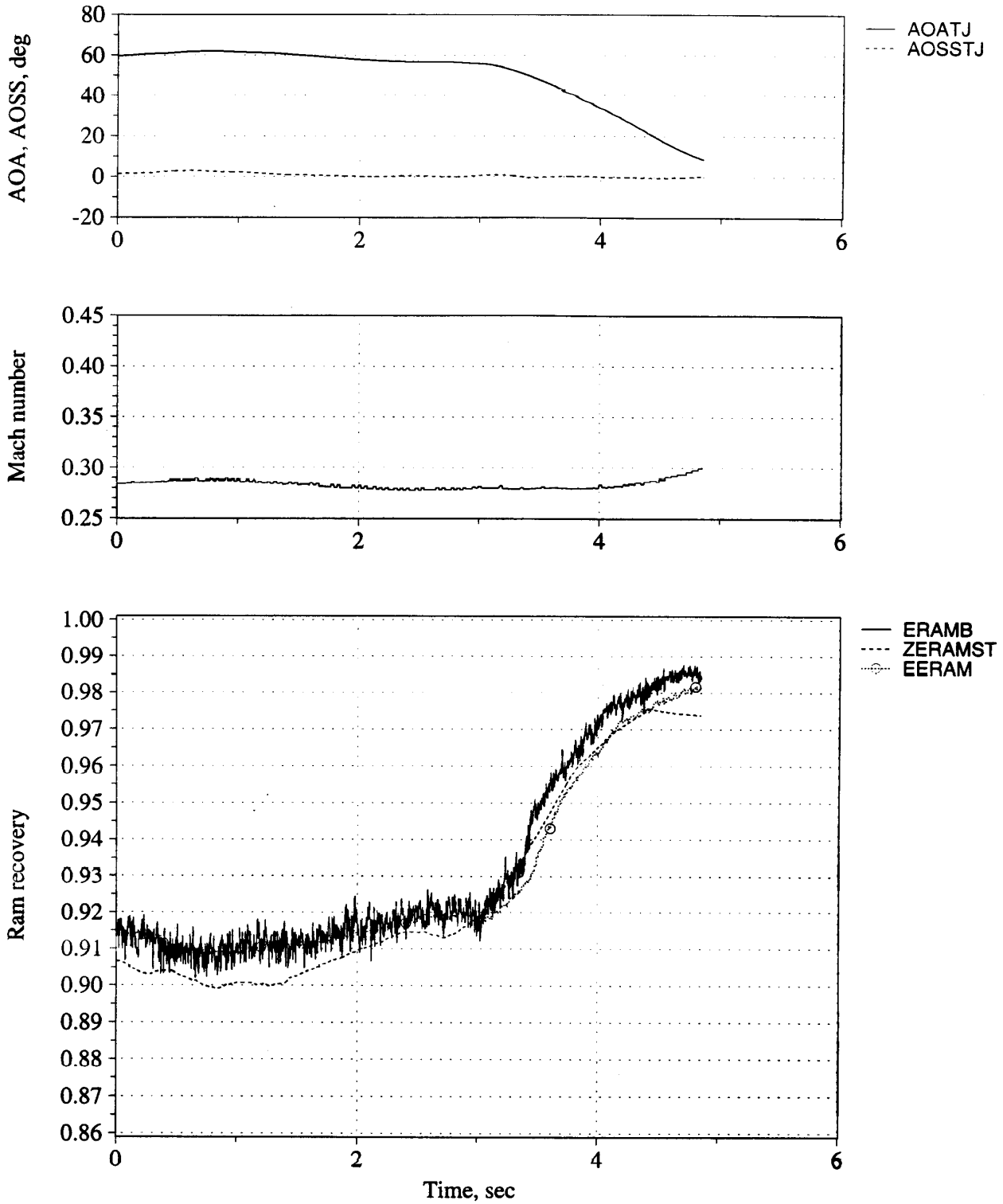

Figure B43. Time history of angle of attack, angle of sideslip, Mach number, and inlet recovery (measured and estimated) - Flight 243, Test point 16c.

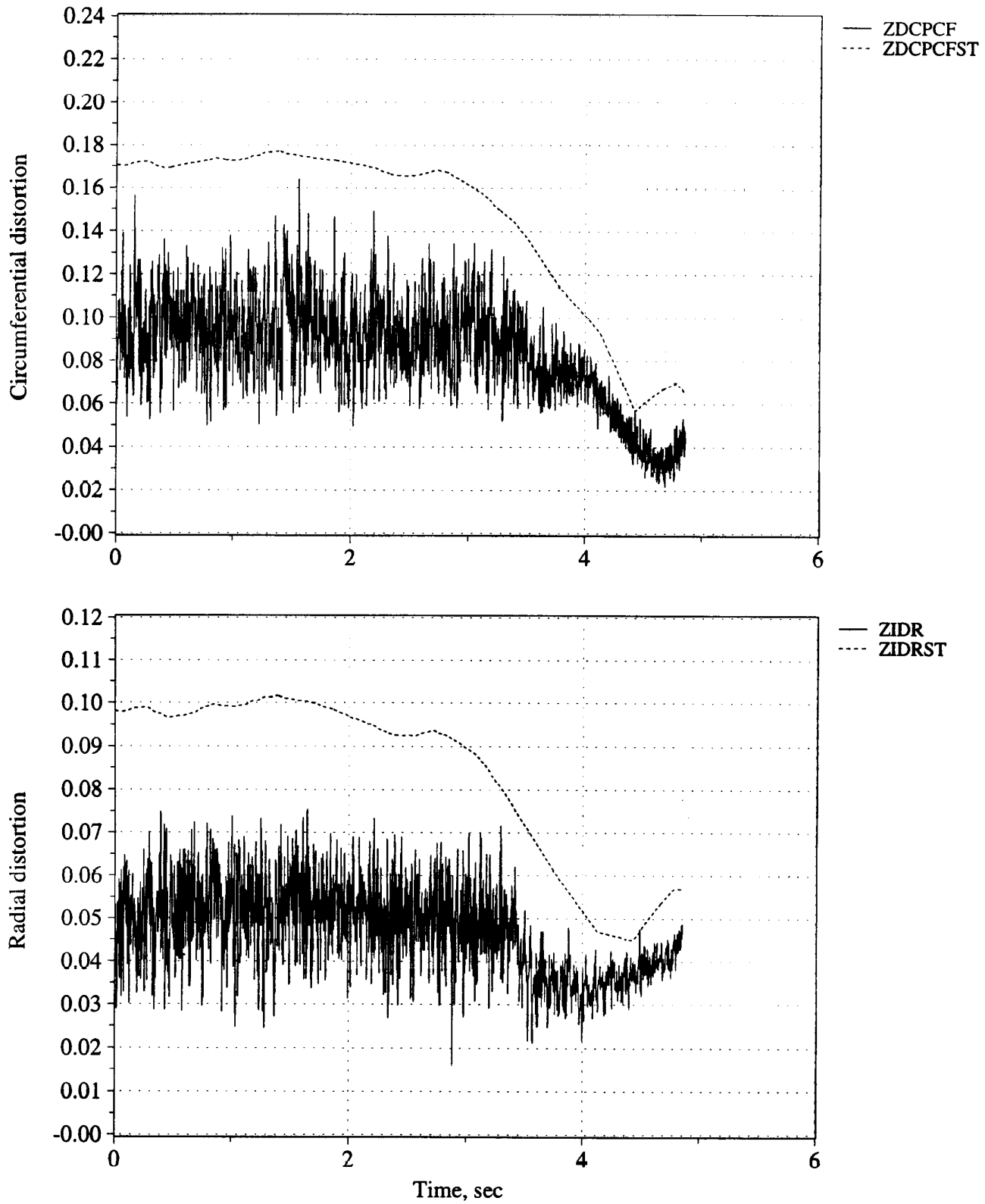

Figure B44. Time history of peak inlet dynamic circumferential and radial distortion (measured and estimated) - Flight 243, Test point 16c.

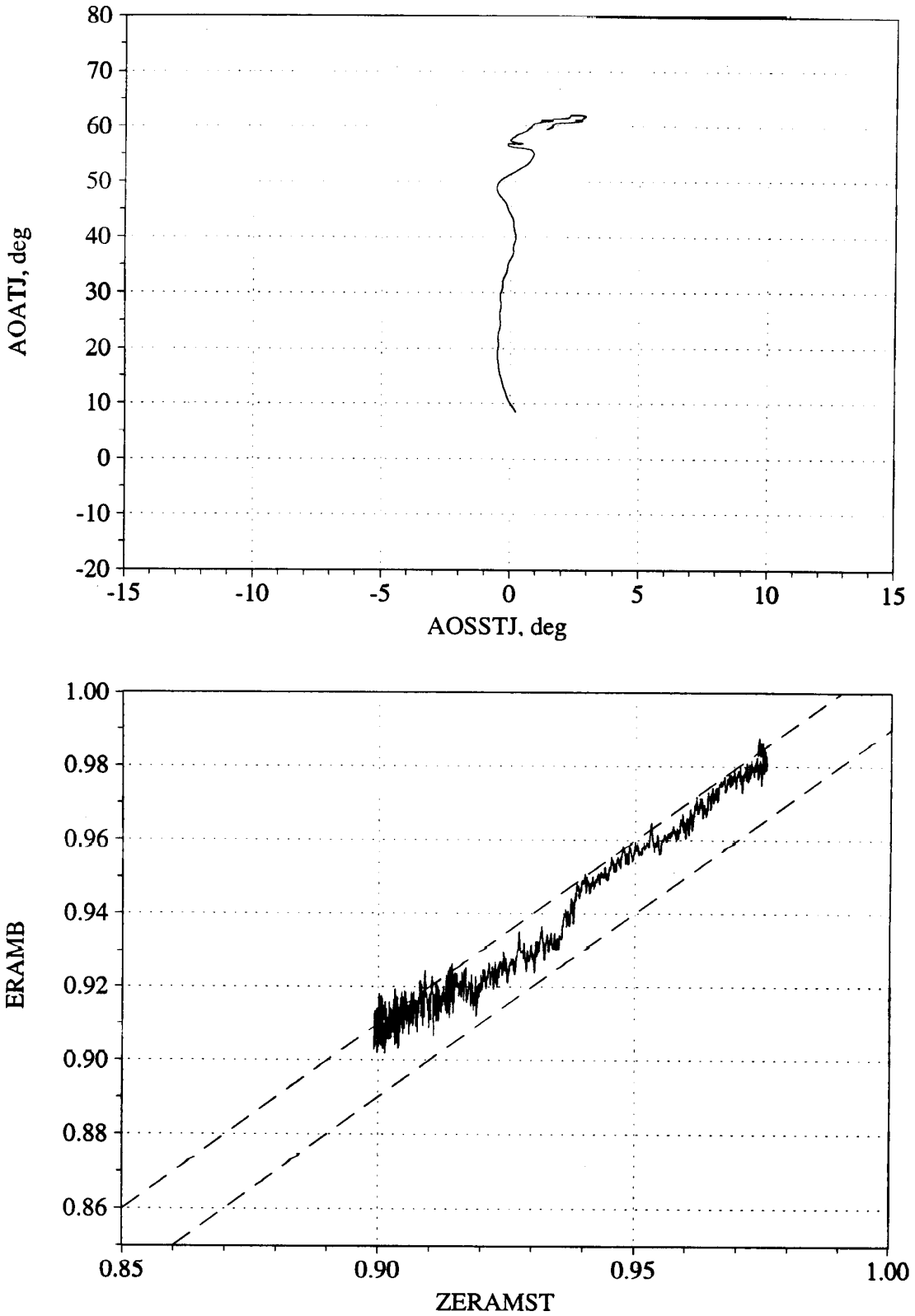

Figure B45. Angle of attack/angle of sideslip trajectory during maneuver; and measured versus estimated recovery - Flight 243, Test point 16c.

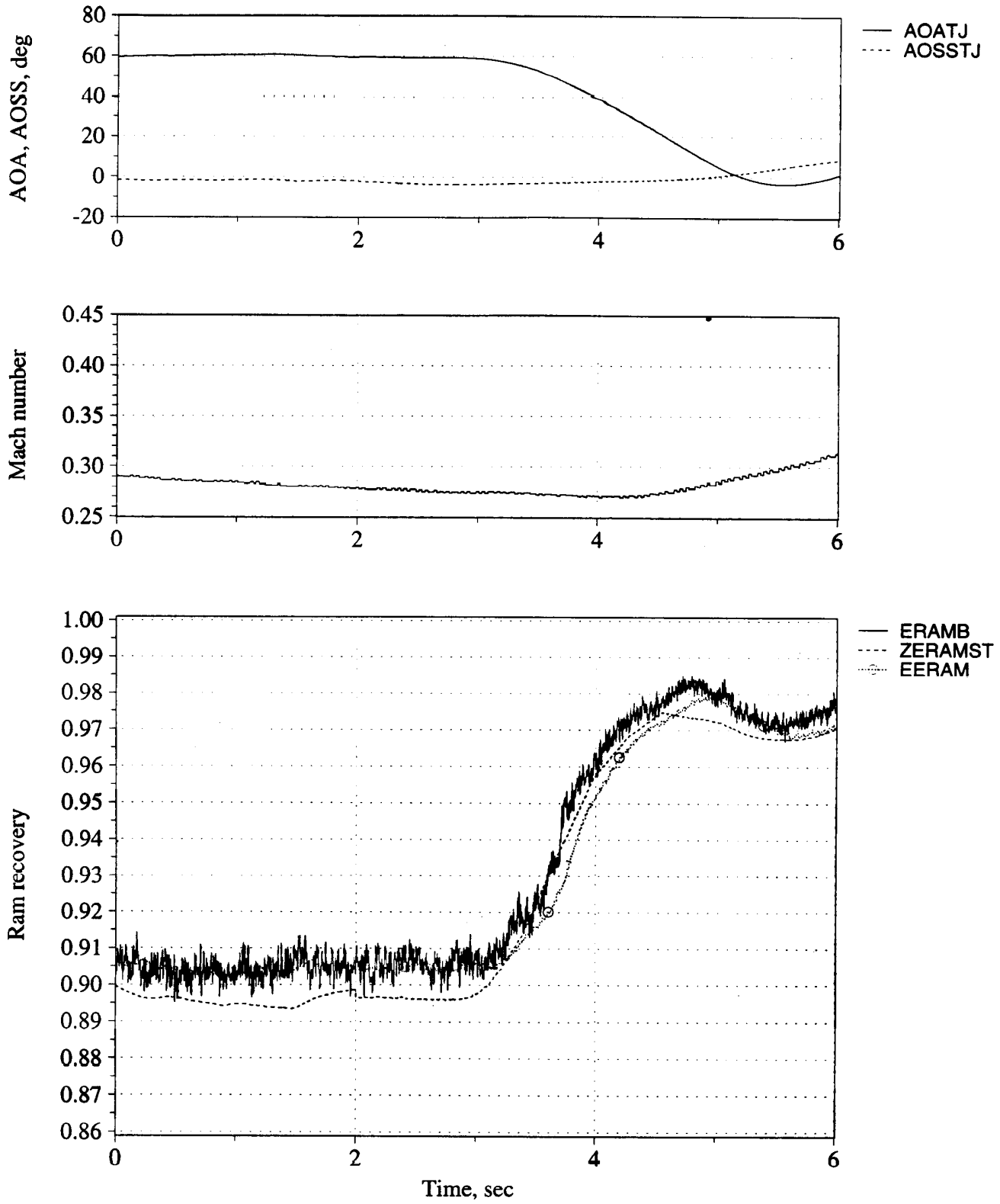

Figure B46. Time history of angle of attack, angle of sideslip, Mach number, and inlet recovery (measured and estimated) - Flight 243, Test point 29d.

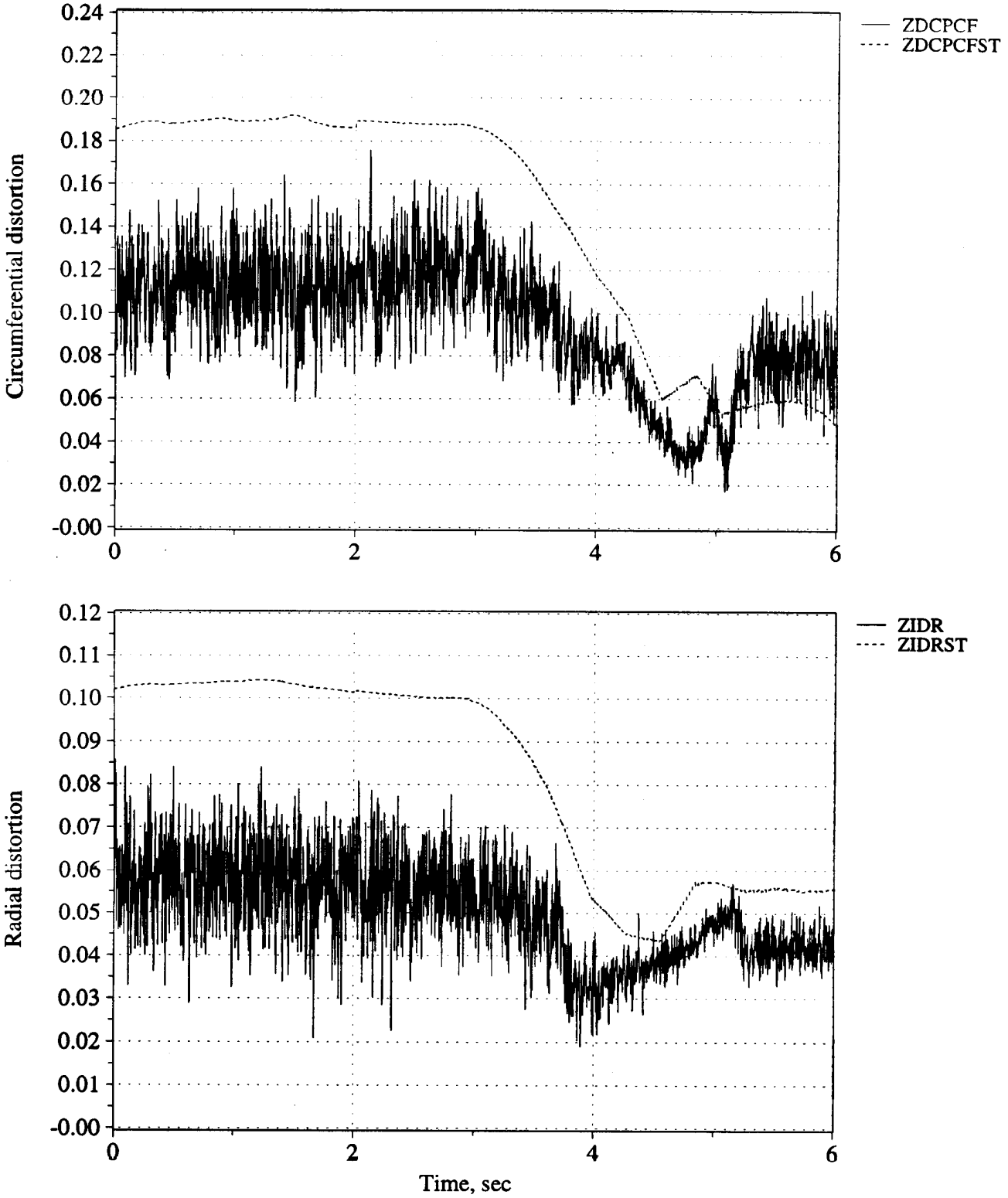

Figure B47. Time history of peak inlet dynamic circumferential and radial distortion (measured and estimated) - Flight 243, Test point 29d.

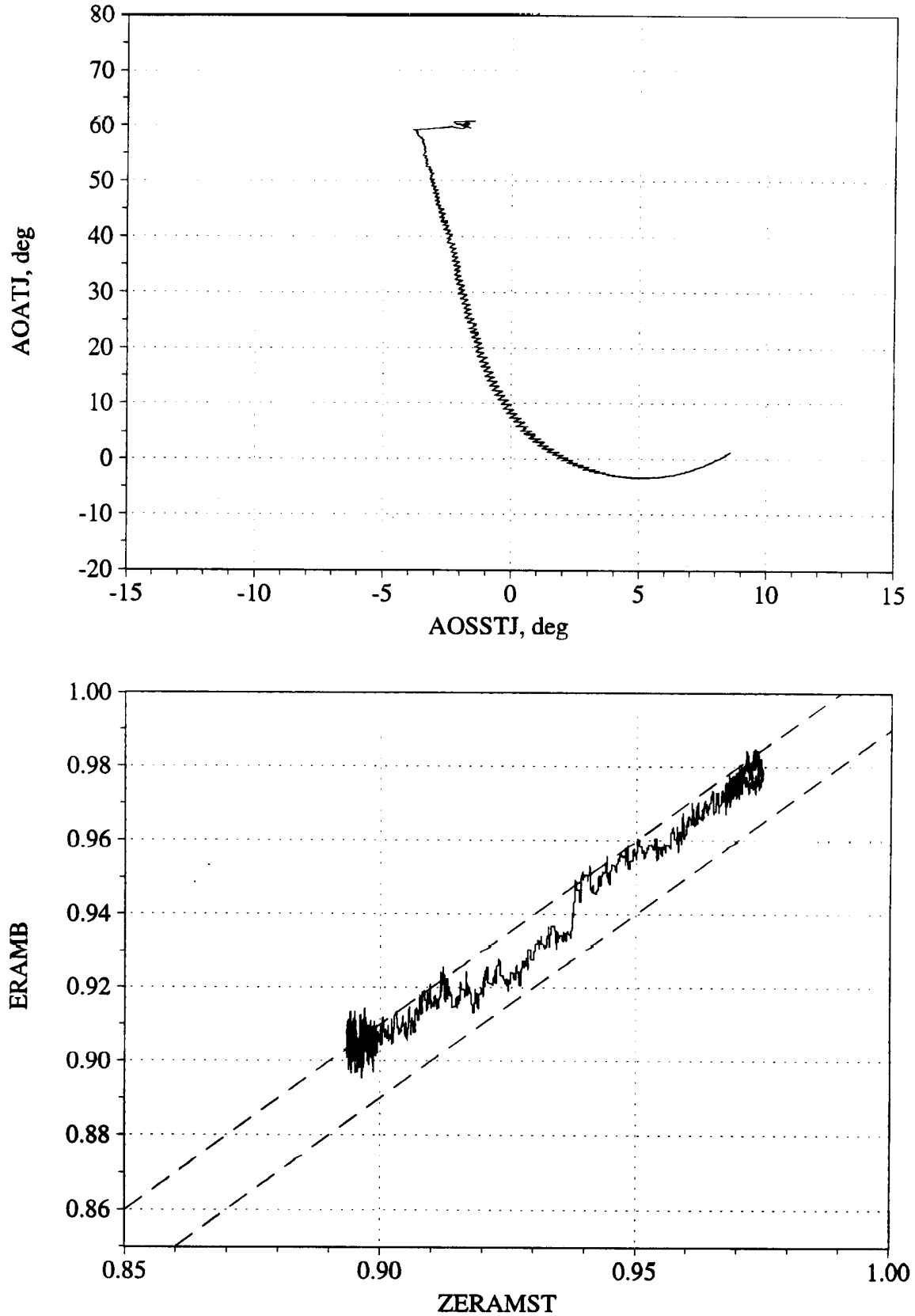

Figure B48. Angle of attack/angle of sideslip trajectory during maneuver; and measured versus estimated recovery - Flight 243, Test point 29d.

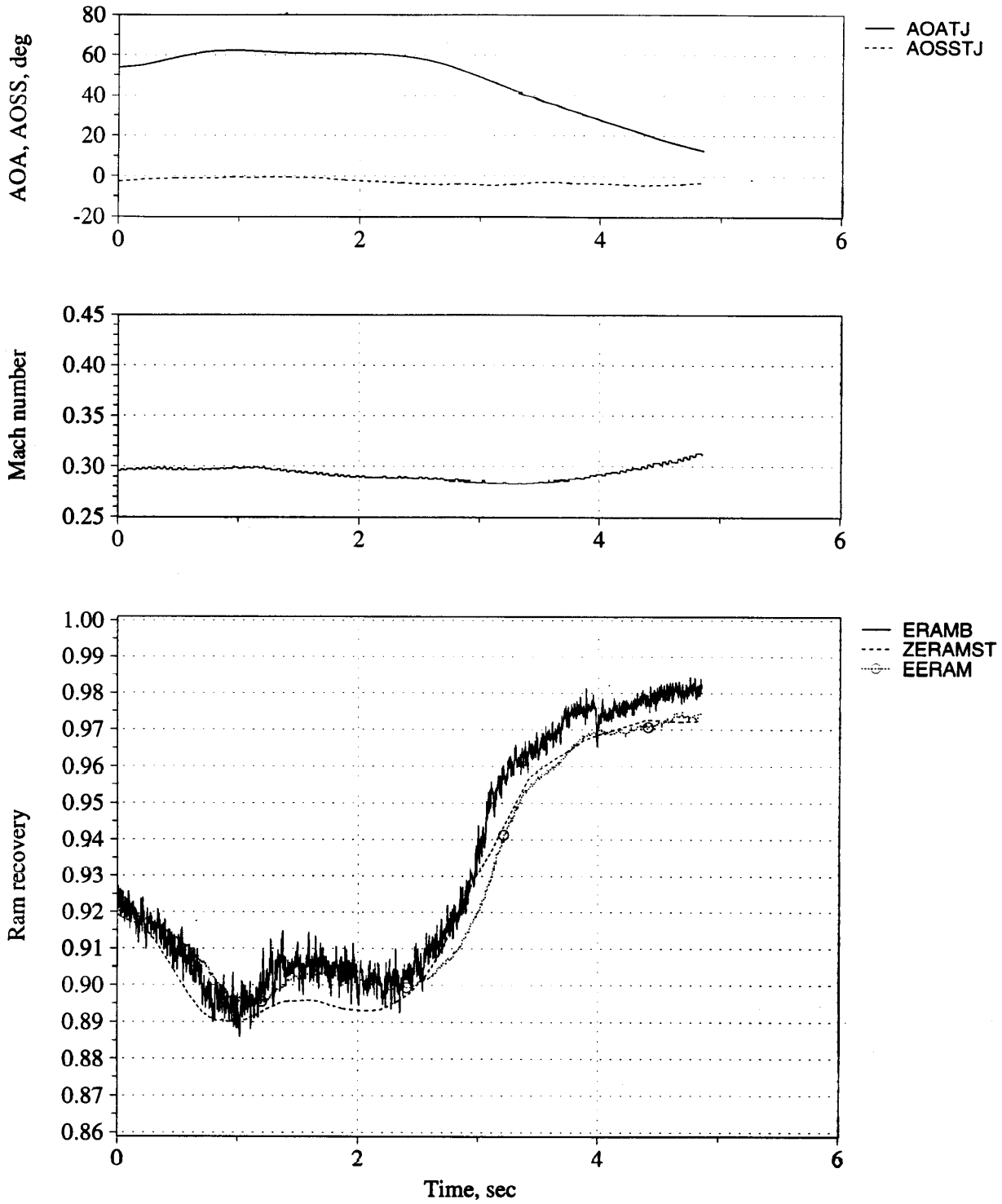

Figure B49. Time history of angle of attack, angle of sideslip, Mach number, and inlet recovery (measured and estimated) - Flight 247, Test point 6b4.

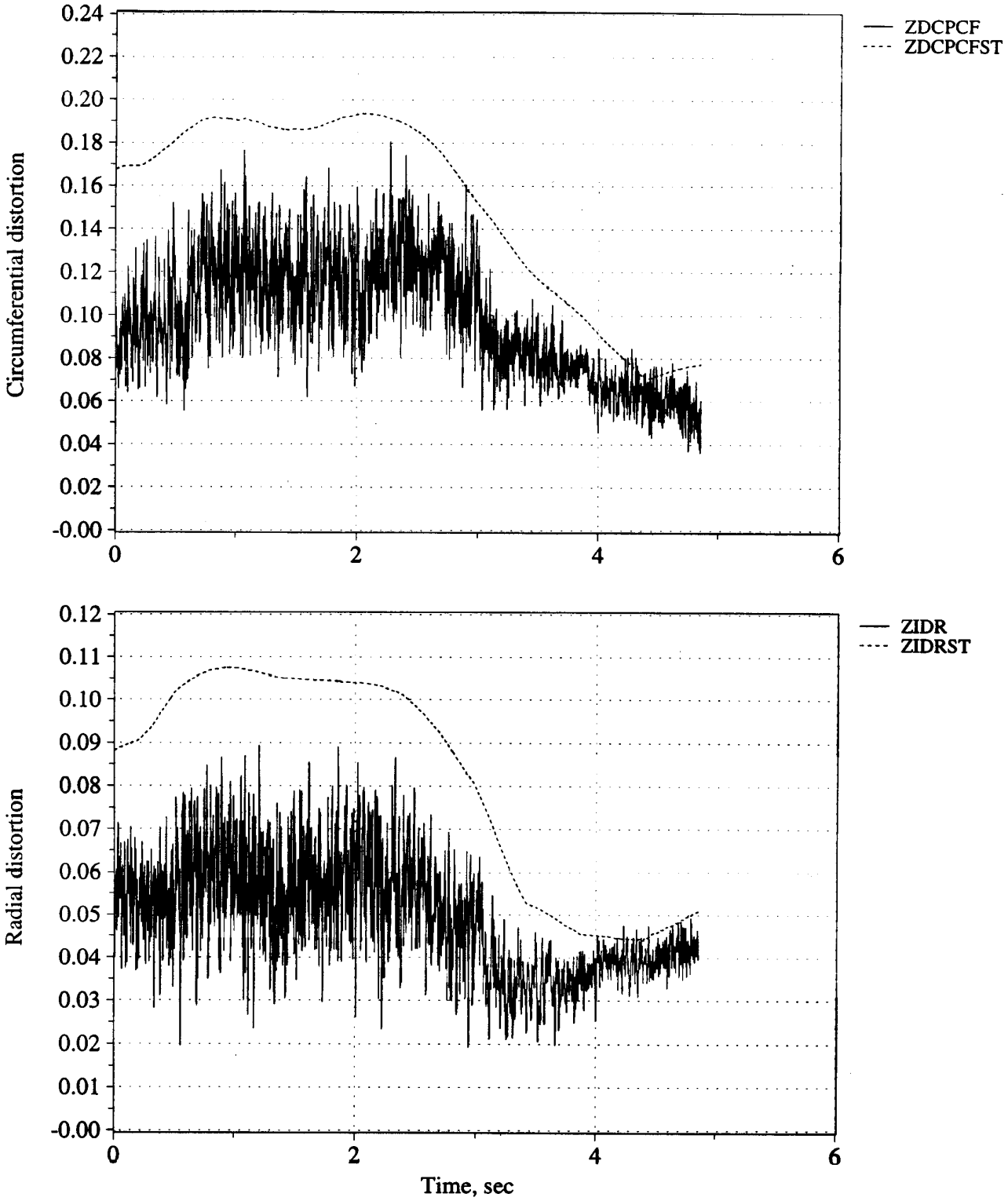

Figure B50. Time history of peak inlet dynamic circumferential and radial distortion (measured and estimated) - Flight 247, Test point 6b4.

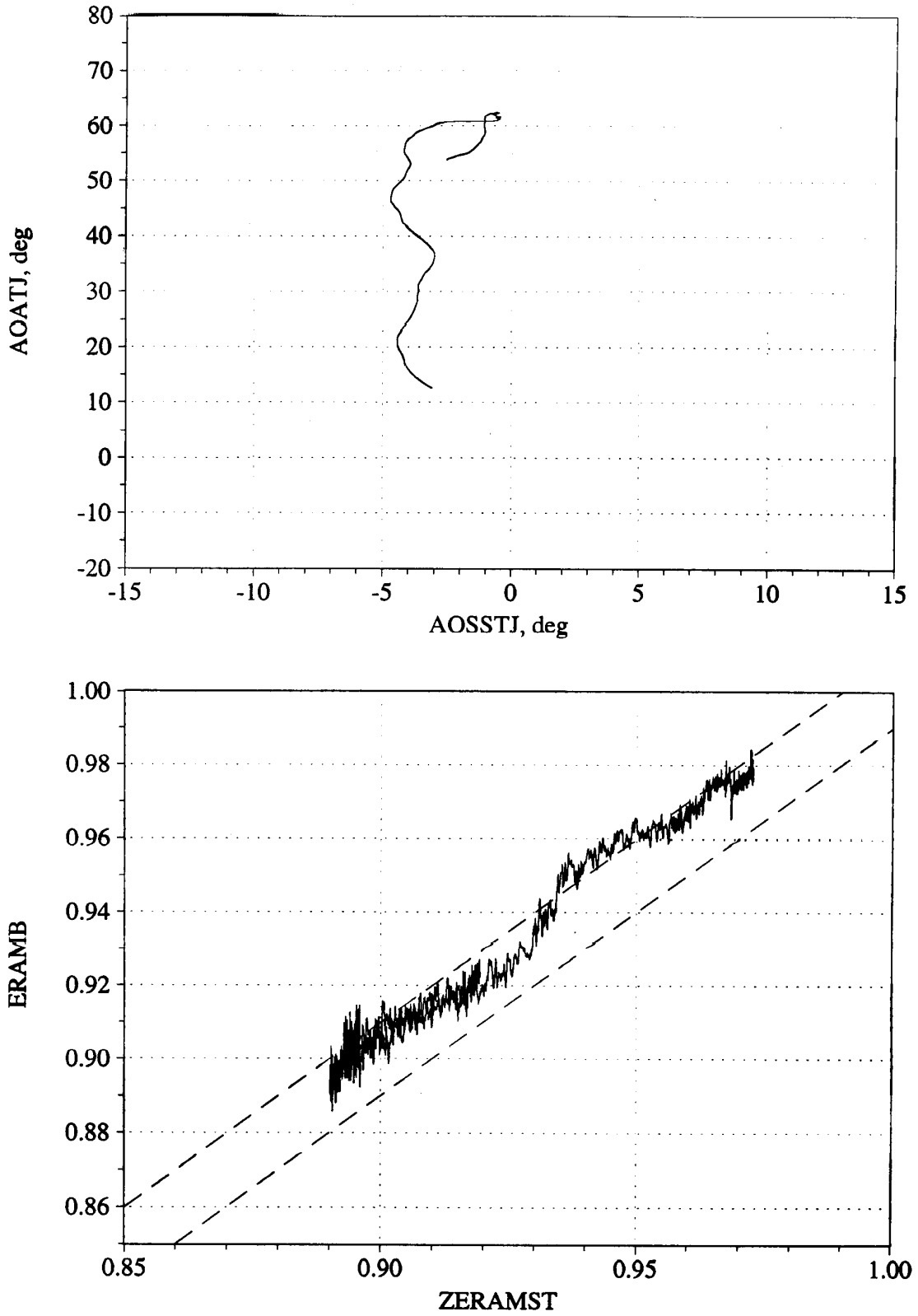

Figure B51. Angle of attack/angle of sideslip trajectory during maneuver; and measured versus estimated recovery - Flight 247, Test point 6b4.

- Mid-to-High Angle of Attack -

Figures B52 - B54, Flight 213, Test Point 12b
Figures B55 - B57, Flight 230, Test Point 15b
Figures B58 - B60, Flight 241, Test Point 19b
Figures B61 - B63, Flight 241, Test Point 19c

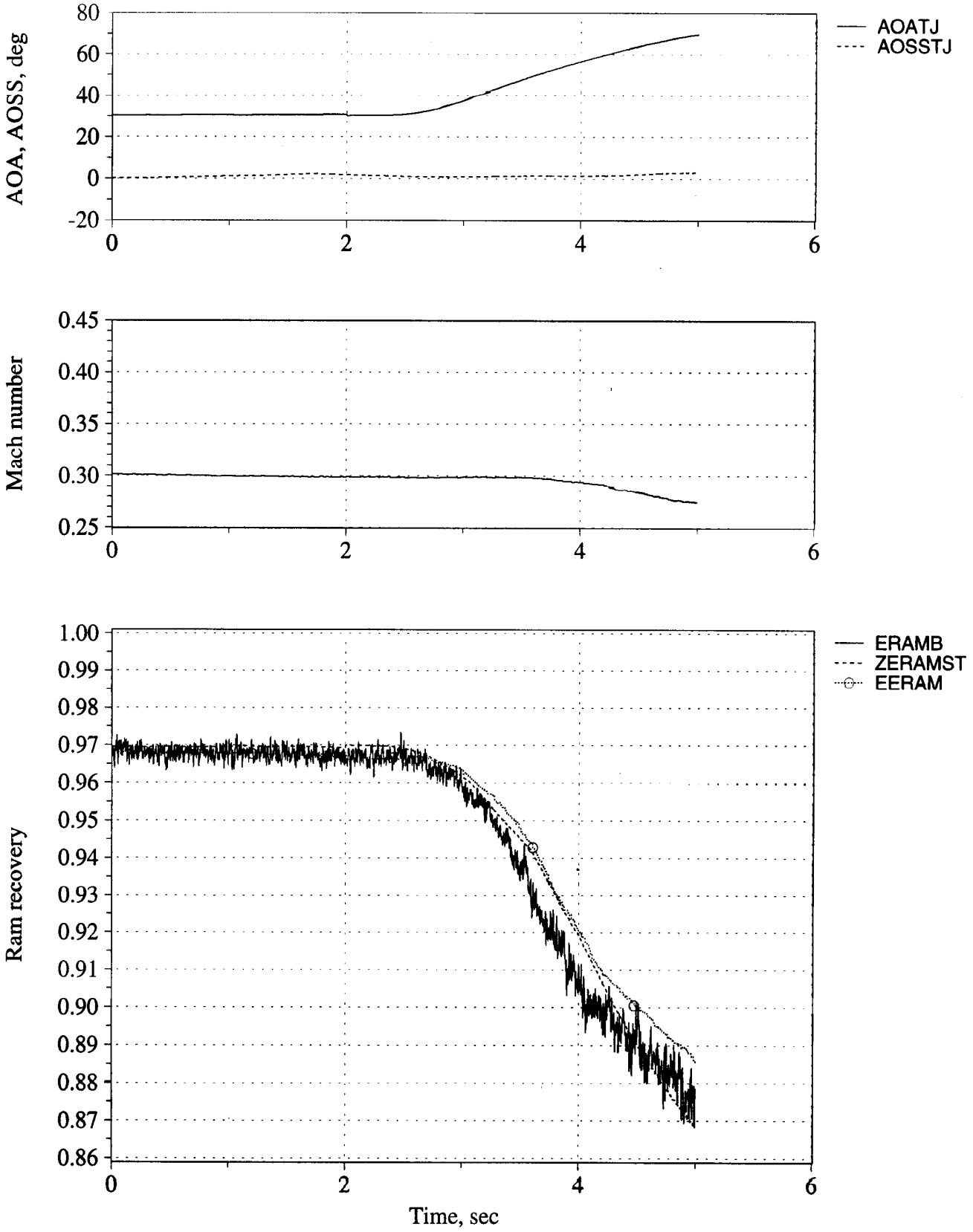

Figure B52. Time history of angle of attack, angle of sideslip, Mach number, and inlet recovery (measured and estimated) - Flight 213, Test point 12b.

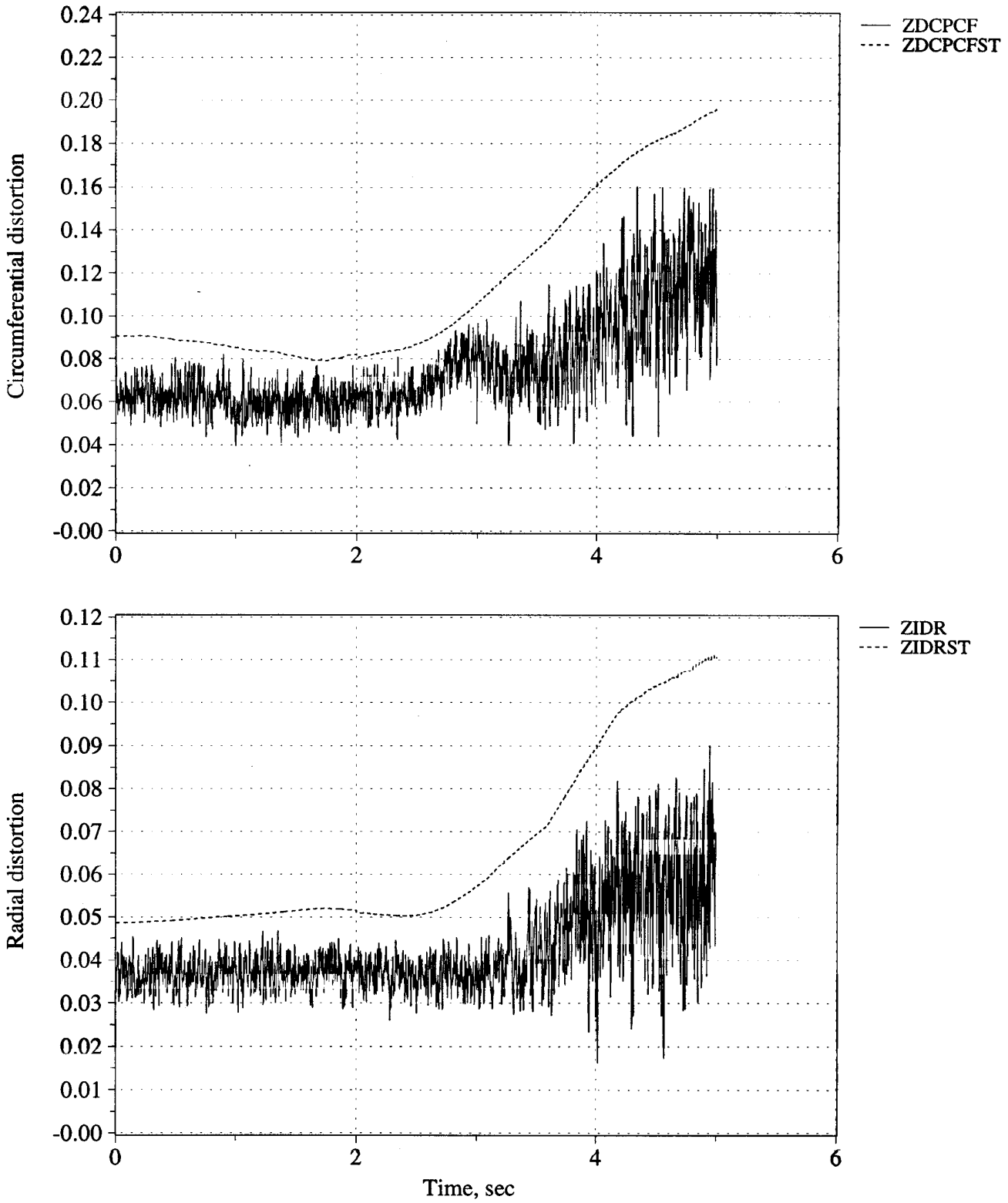

Figure B53. Time history of peak inlet dynamic circumferential and radial distortion (measured and estimated) - Flight 213, Test point 12b.

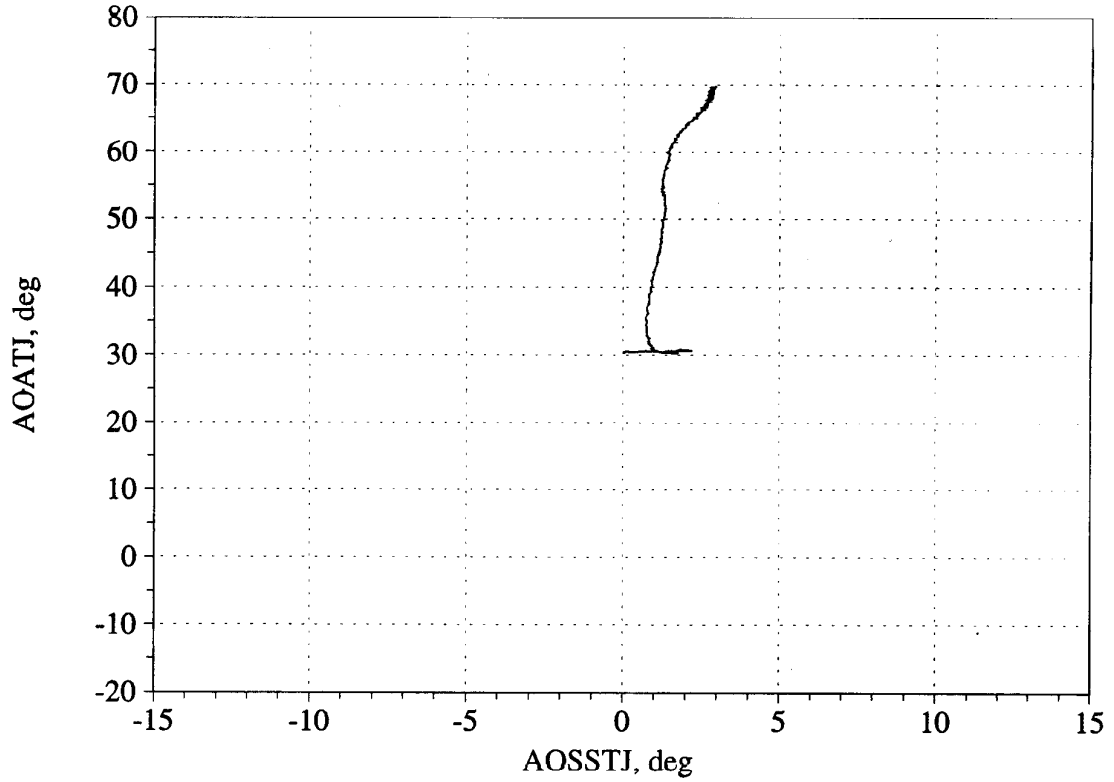

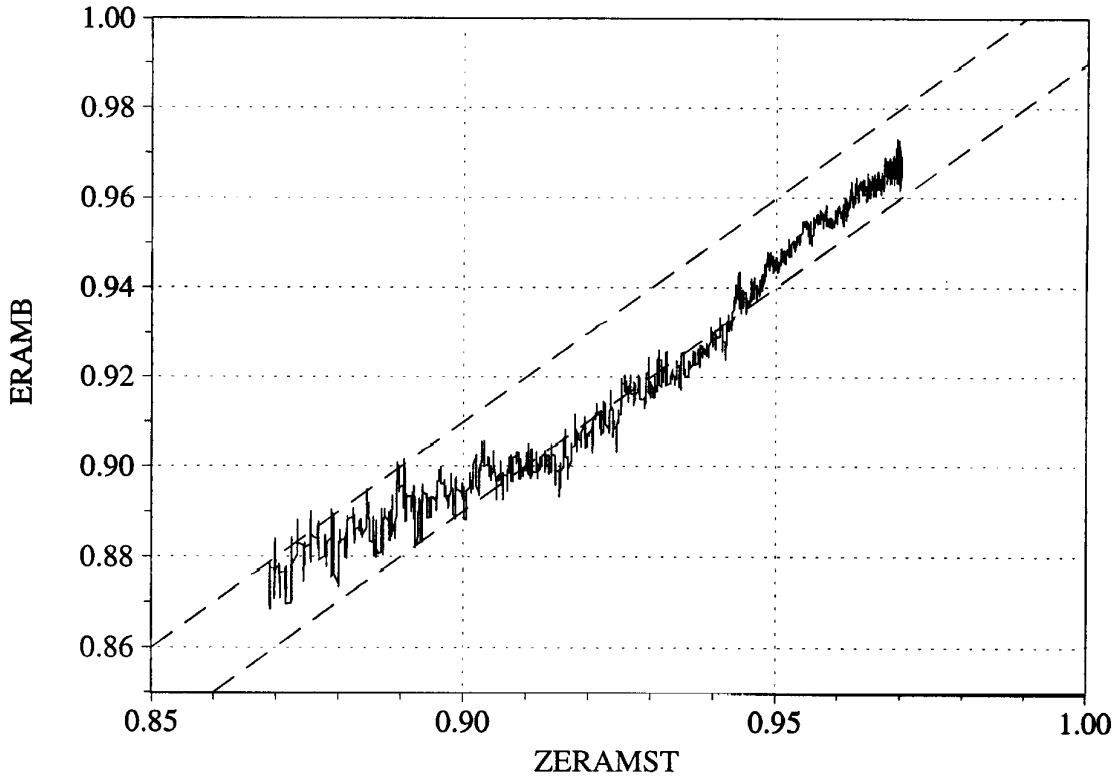

Figure B54. Angle of attack/angle of sideslip trajectory during maneuver; and measured versus estimated recovery - Flight 213, Test point 12b.

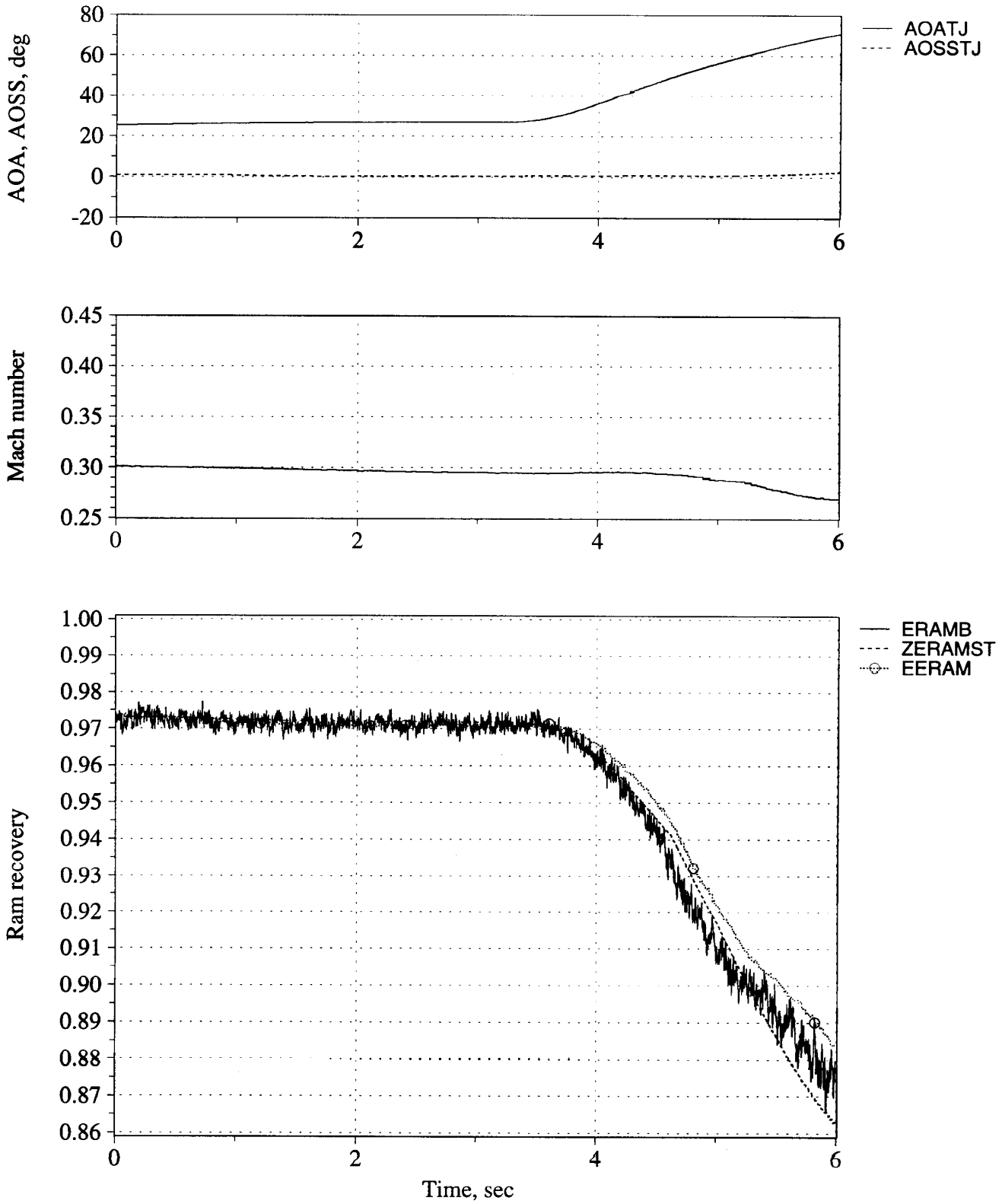

Figure B55. Time history of angle of attack, angle of sideslip, Mach number, and inlet recovery (measured and estimated) - Flight 230, Test point 15b.

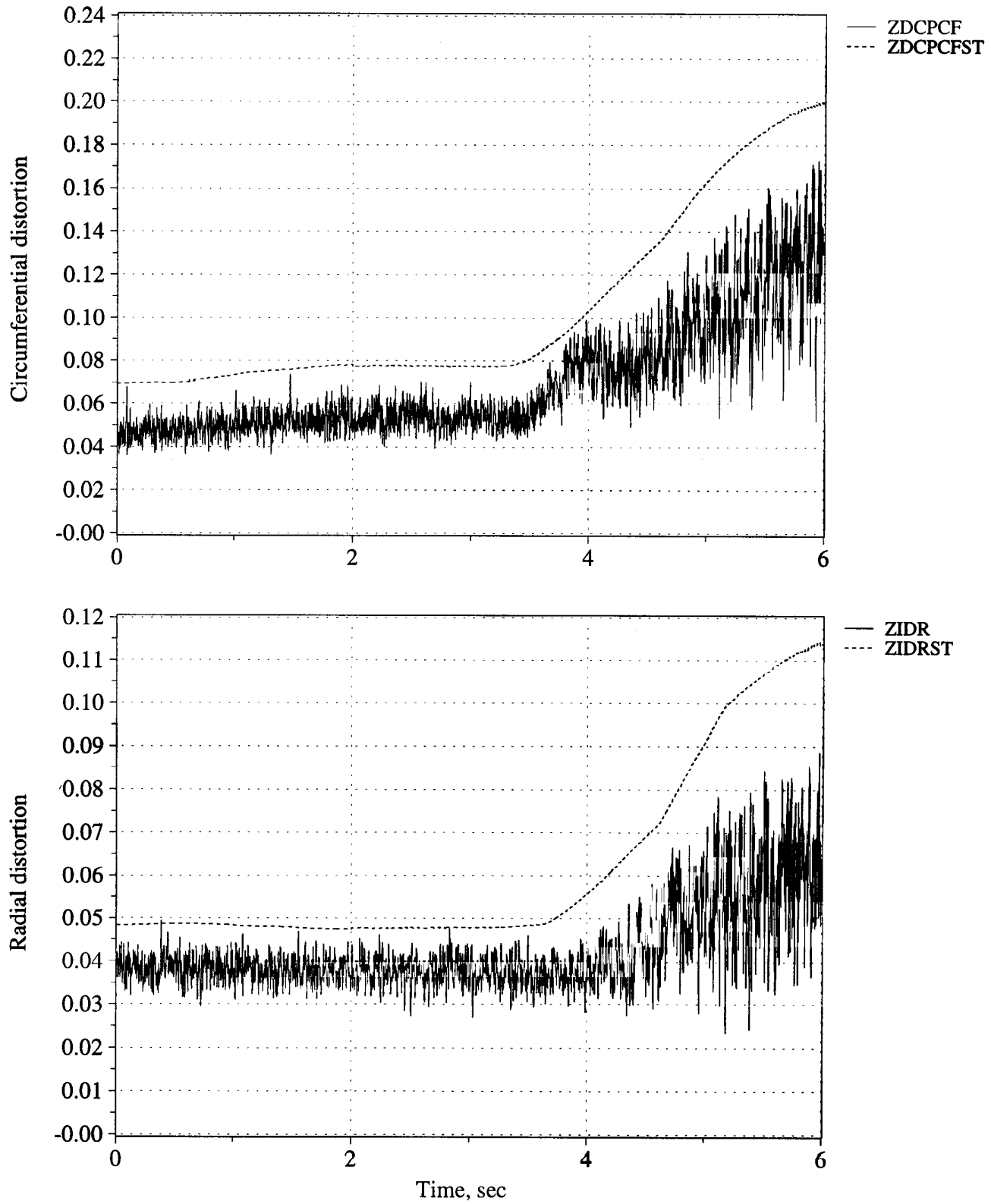

Figure B56. Time history of peak inlet dynamic circumferential and radial distortion (measured and estimated) - Flight 230, Test point 15b.

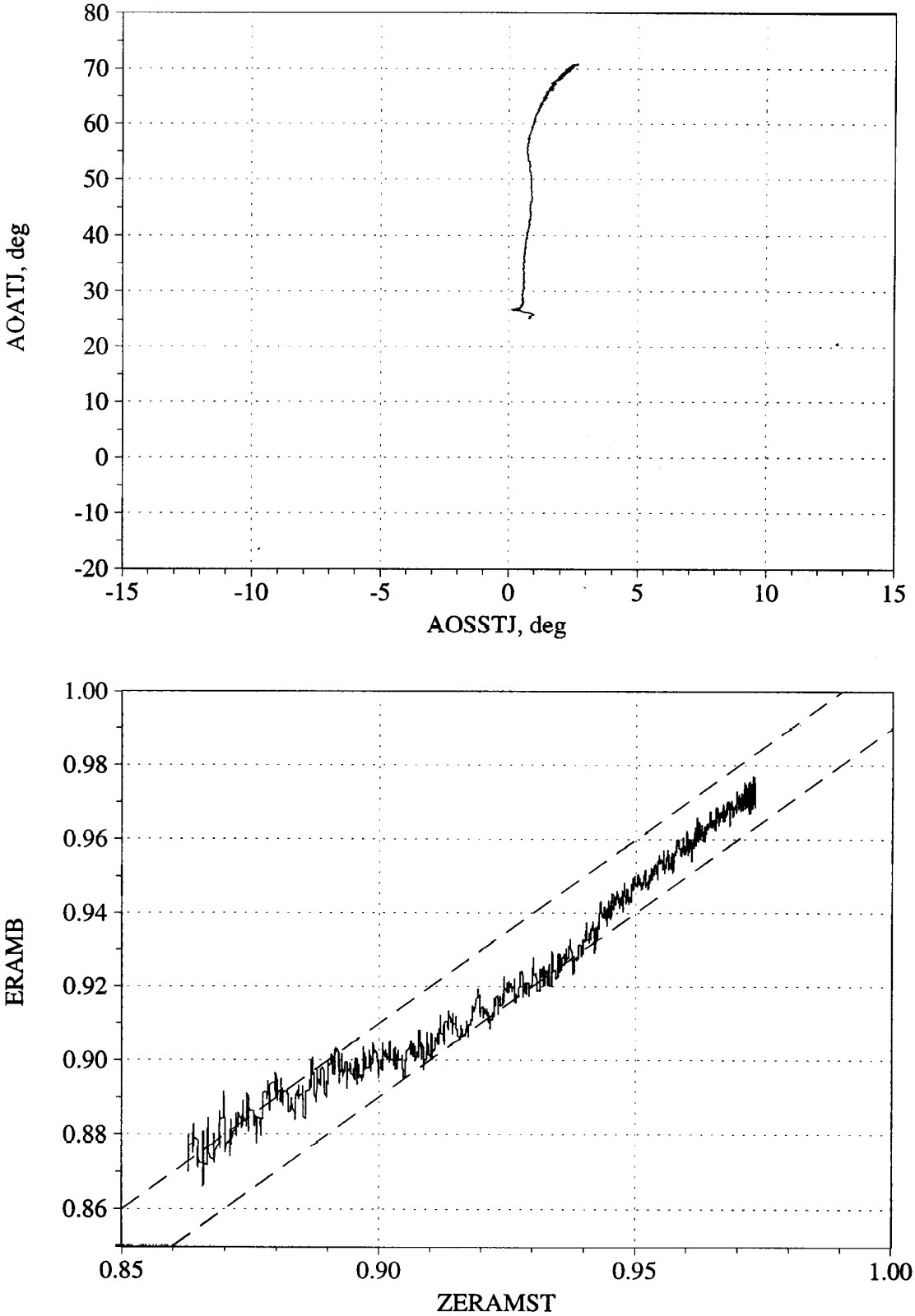

Figure B57. Angle of attack/angle of sideslip trajectory during maneuver; and measured versus estimated recovery - Flight 230, Test point 15b.

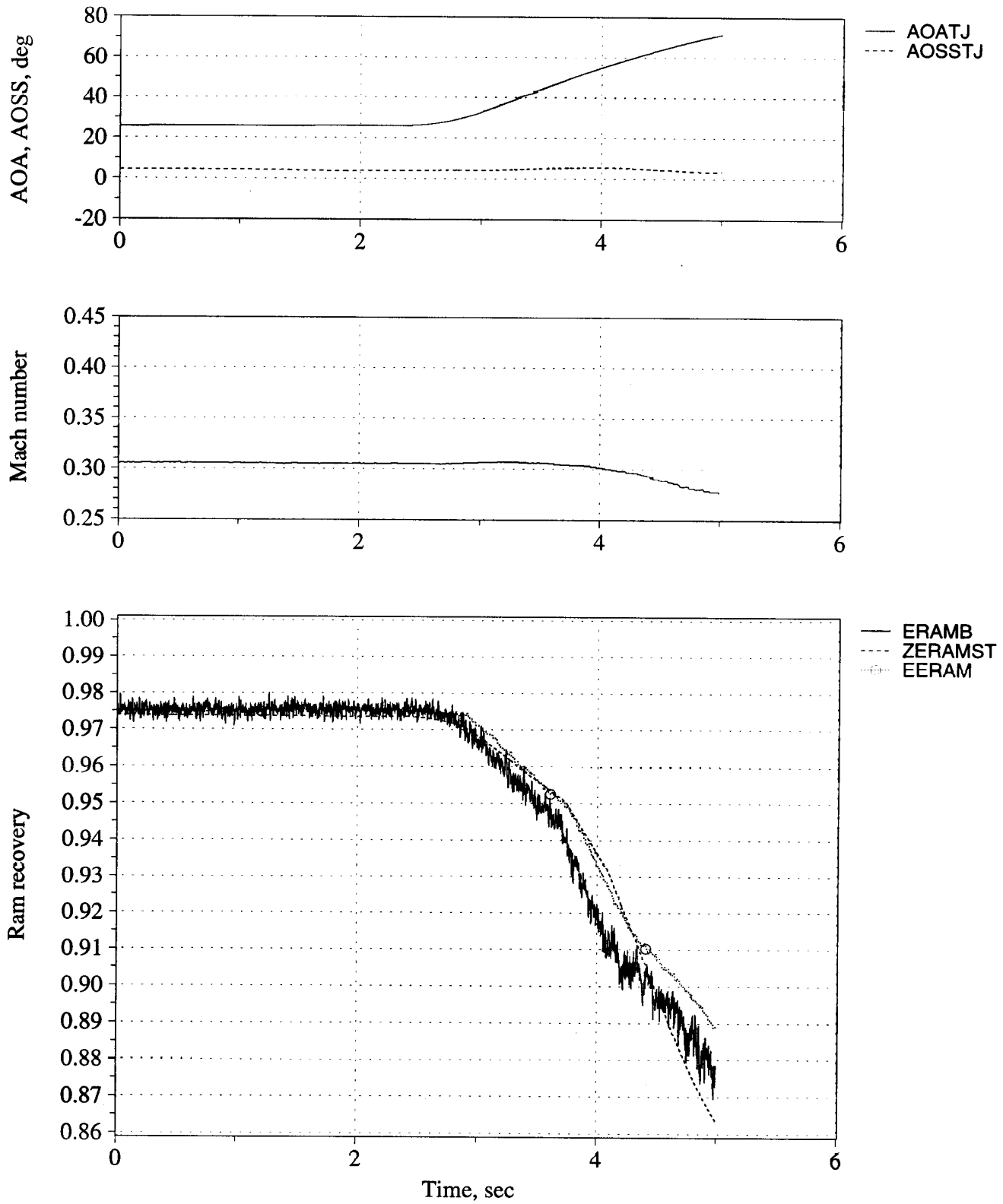

Figure B58. Time history of angle of attack, angle of sideslip, Mach number, and inlet recovery (measured and estimated) - Flight 241, Test point 19b.

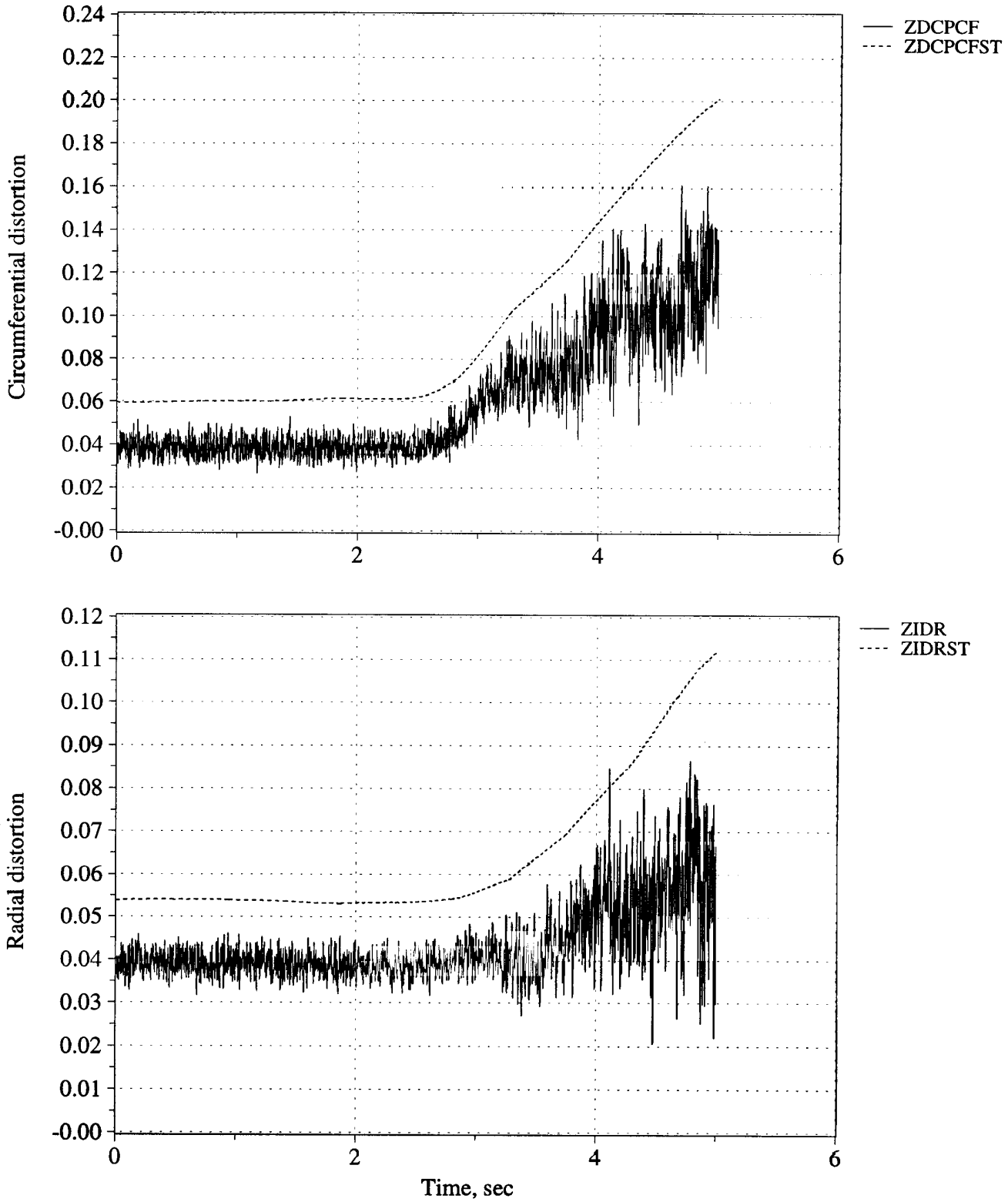

Figure B59. Time history of peak inlet dynamic circumferential and radial distortion (measured and estimated) - Flight 241, Test point 19b.

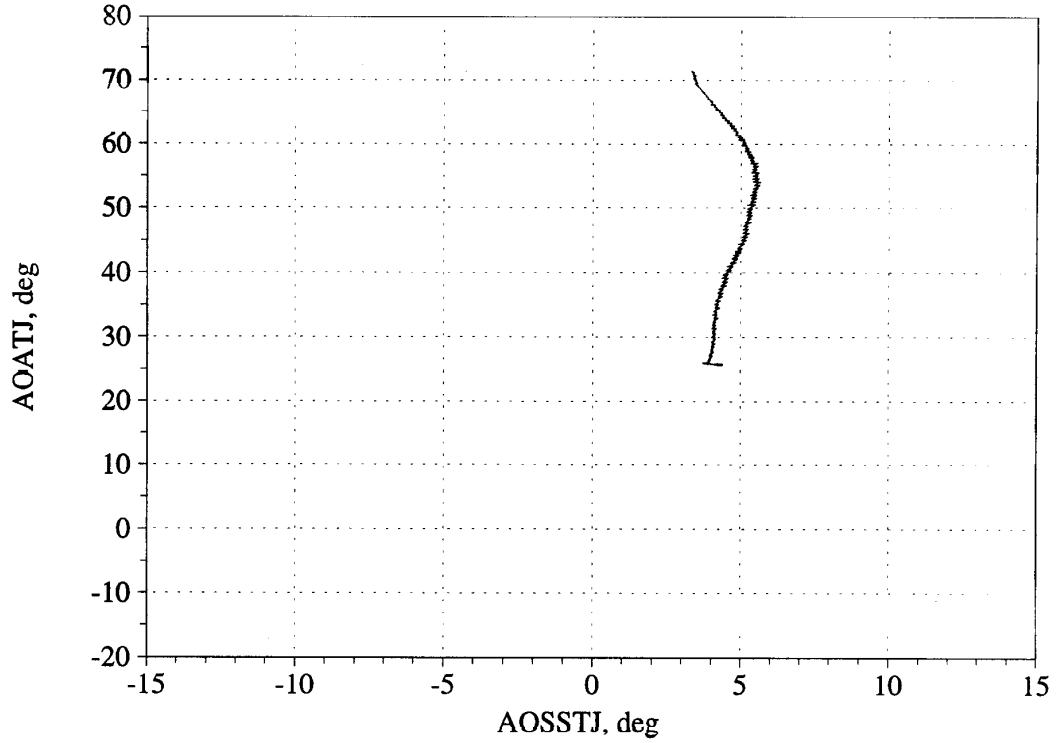

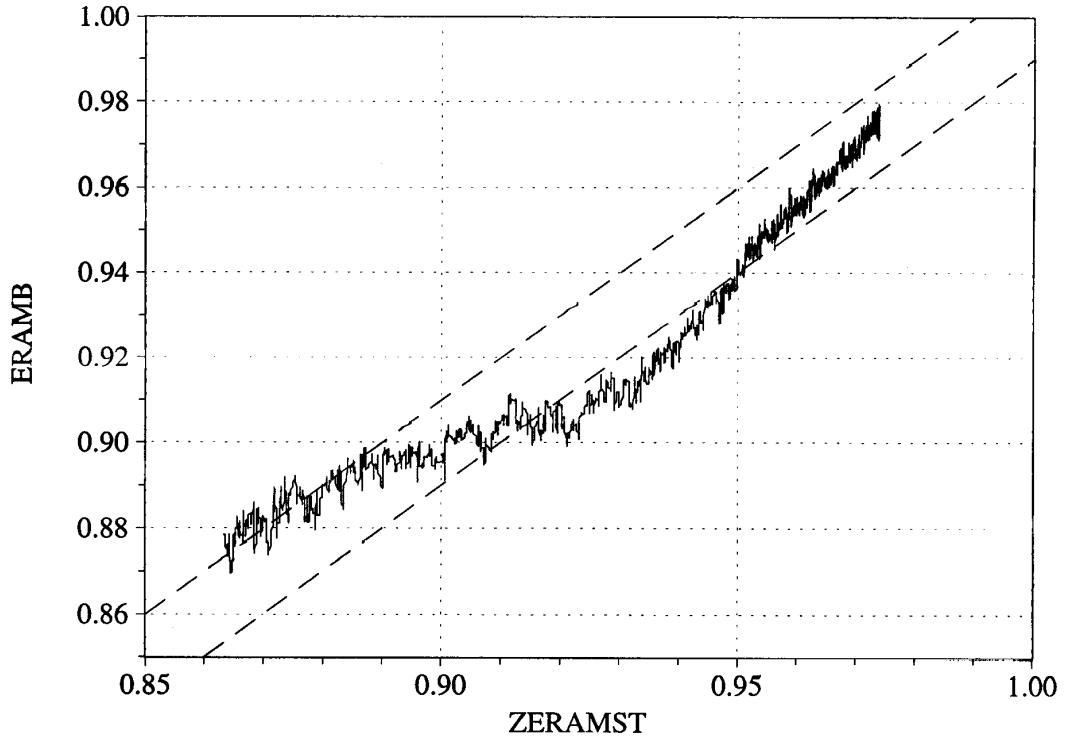

Figure B60. Angle of attack/angle of sideslip trajectory during maneuver; and measured versus estimated recovery - Flight 241, Test point 19b.

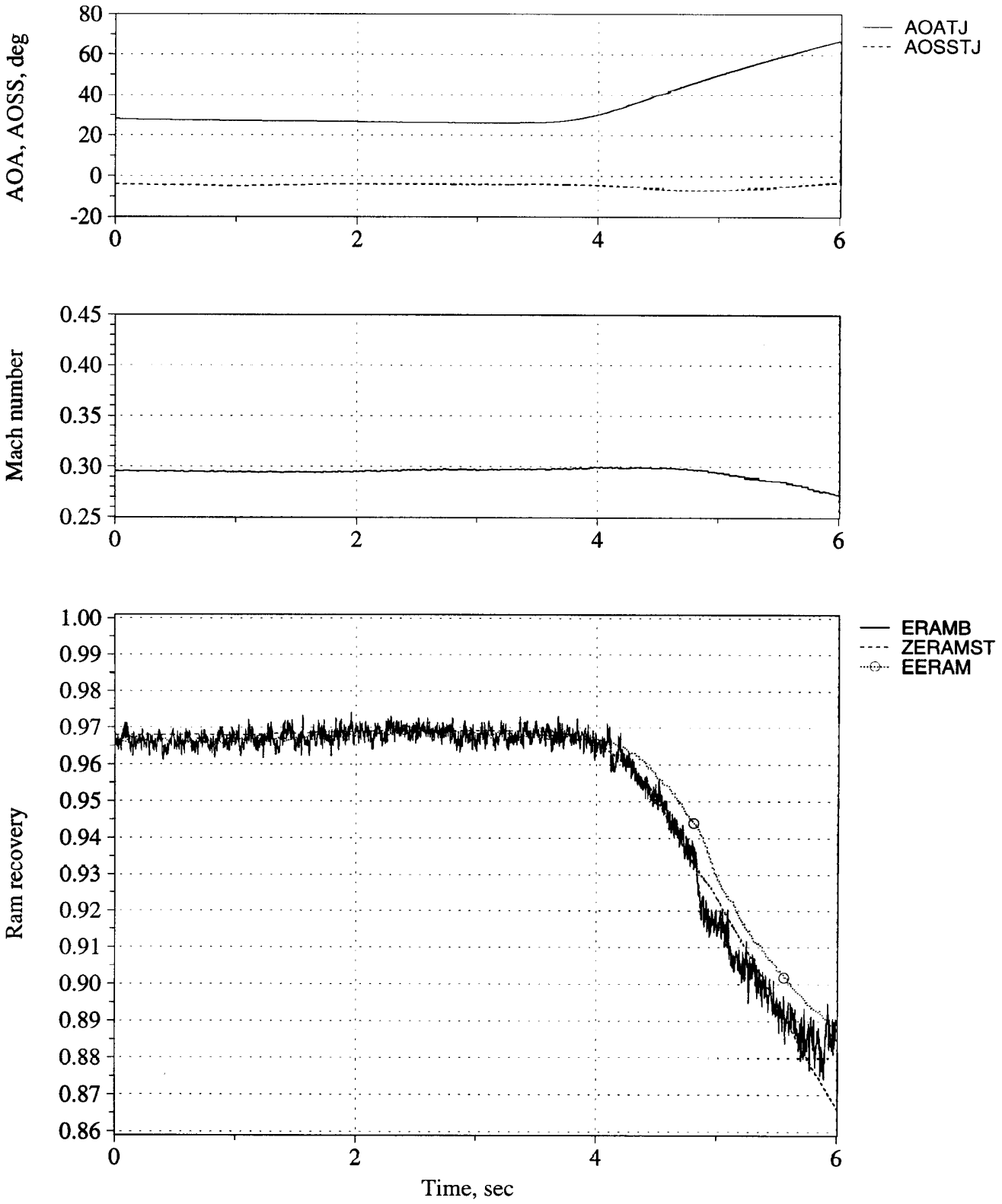

Figure B61. Time history of angle of attack, angle of sideslip, Mach number, and inlet recovery (measured and estimated) - Flight 241, Test point 19c.

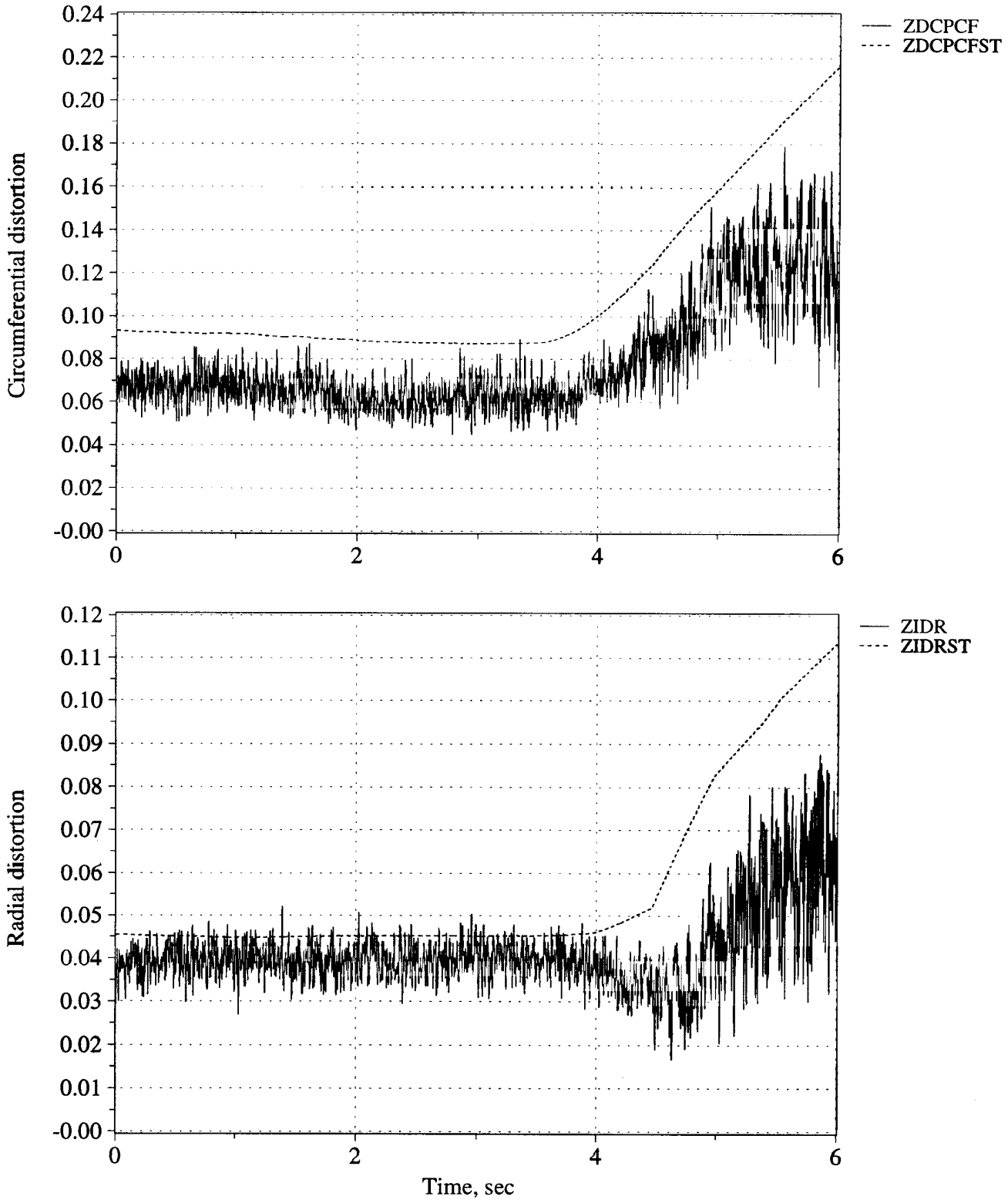

Figure B62. Time history of peak inlet dynamic circumferential and radial distortion (measured and estimated) - Flight 241, Test point 19c.

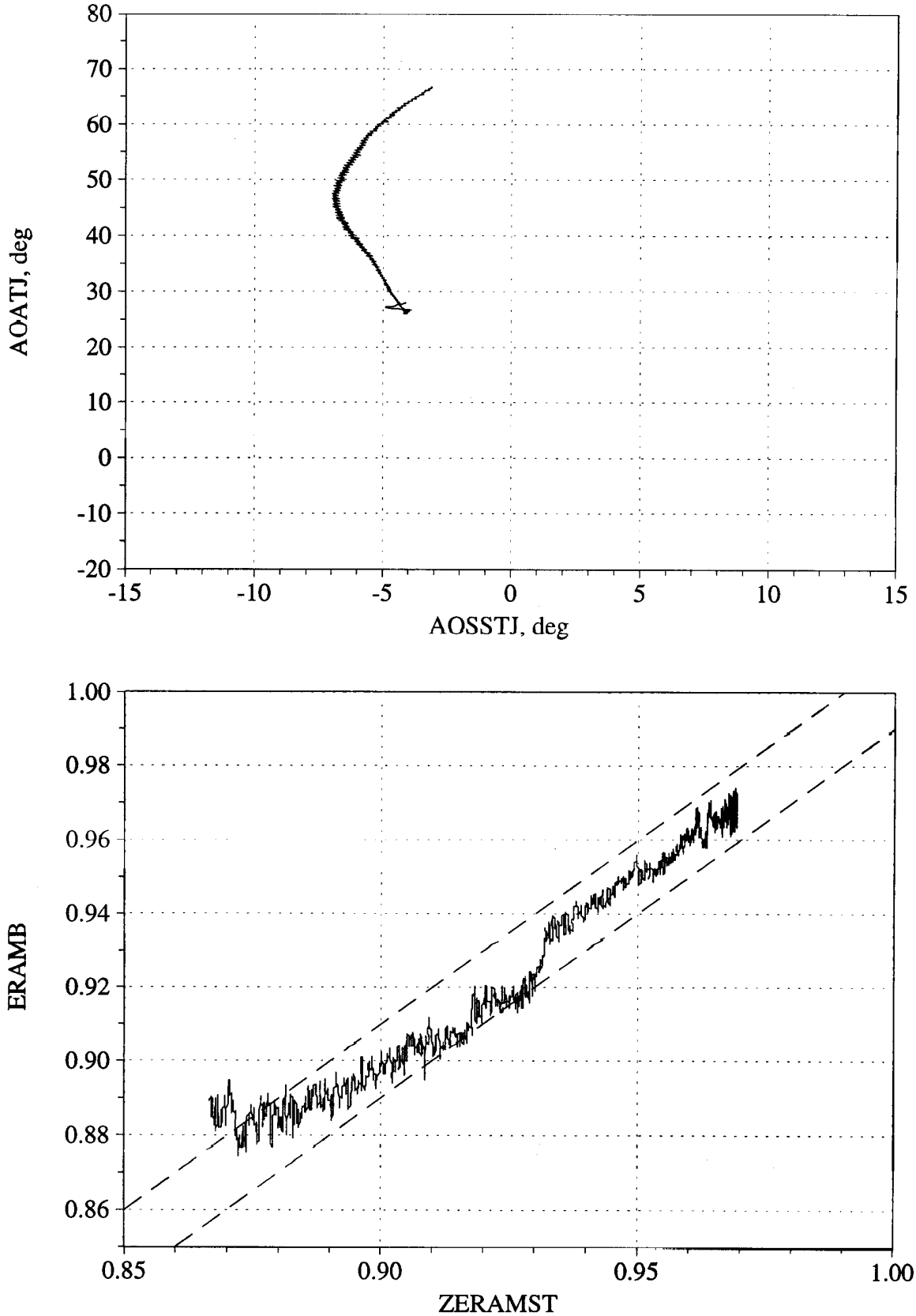

Figure B63. Angle of attack/angle of sideslip trajectory during maneuver; and measured versus estimated recovery - Flight 241, Test point 19c.

- Mid-to-Low-to-High Angle of Attack -

Figures B64 - B66, Flight 213, Test Point 11b

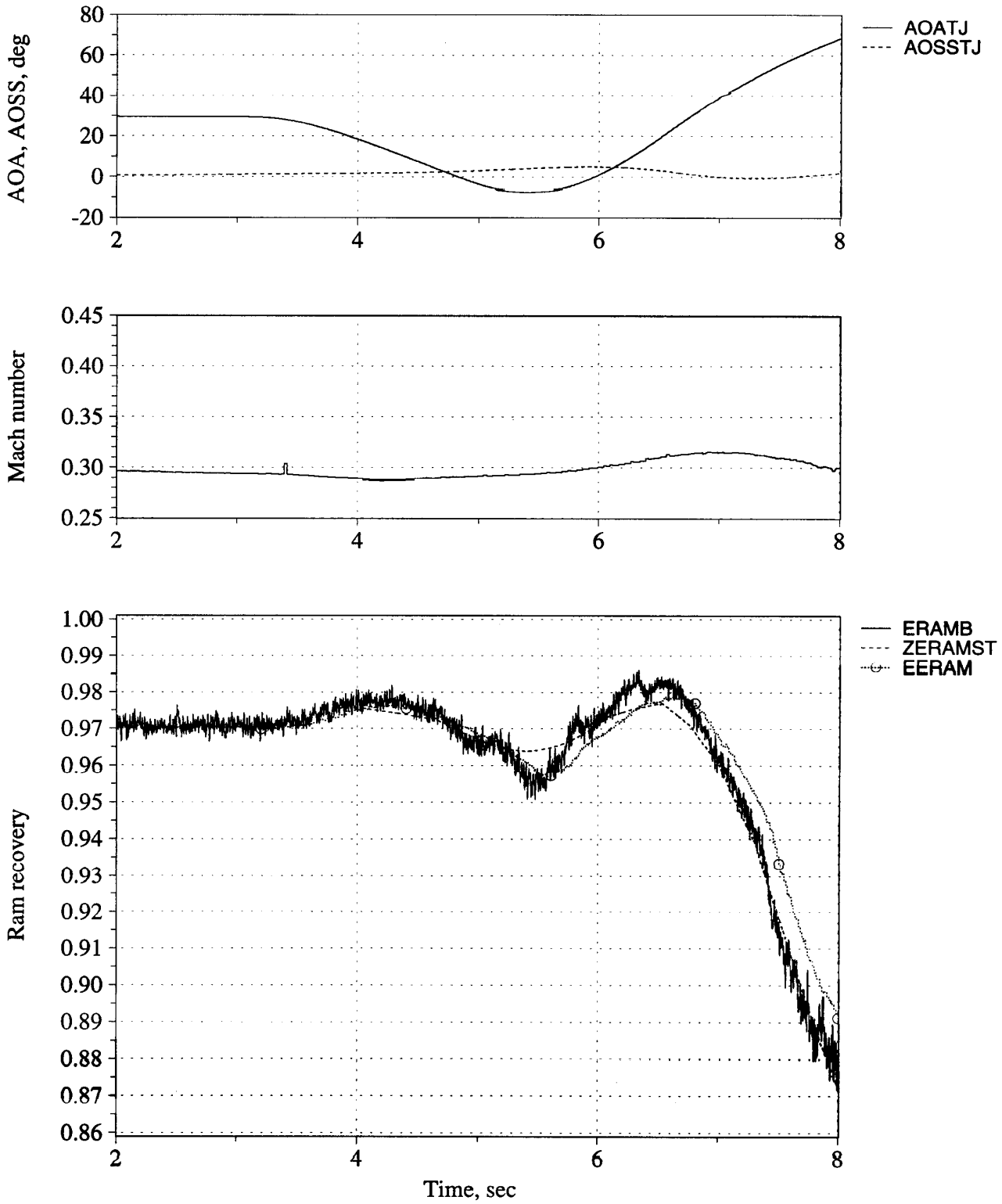

Figure B64. Time history of angle of attack, angle of sideslip, Mach number, and inlet recovery (measured and estimated) - Flight 213, Test point 11b.

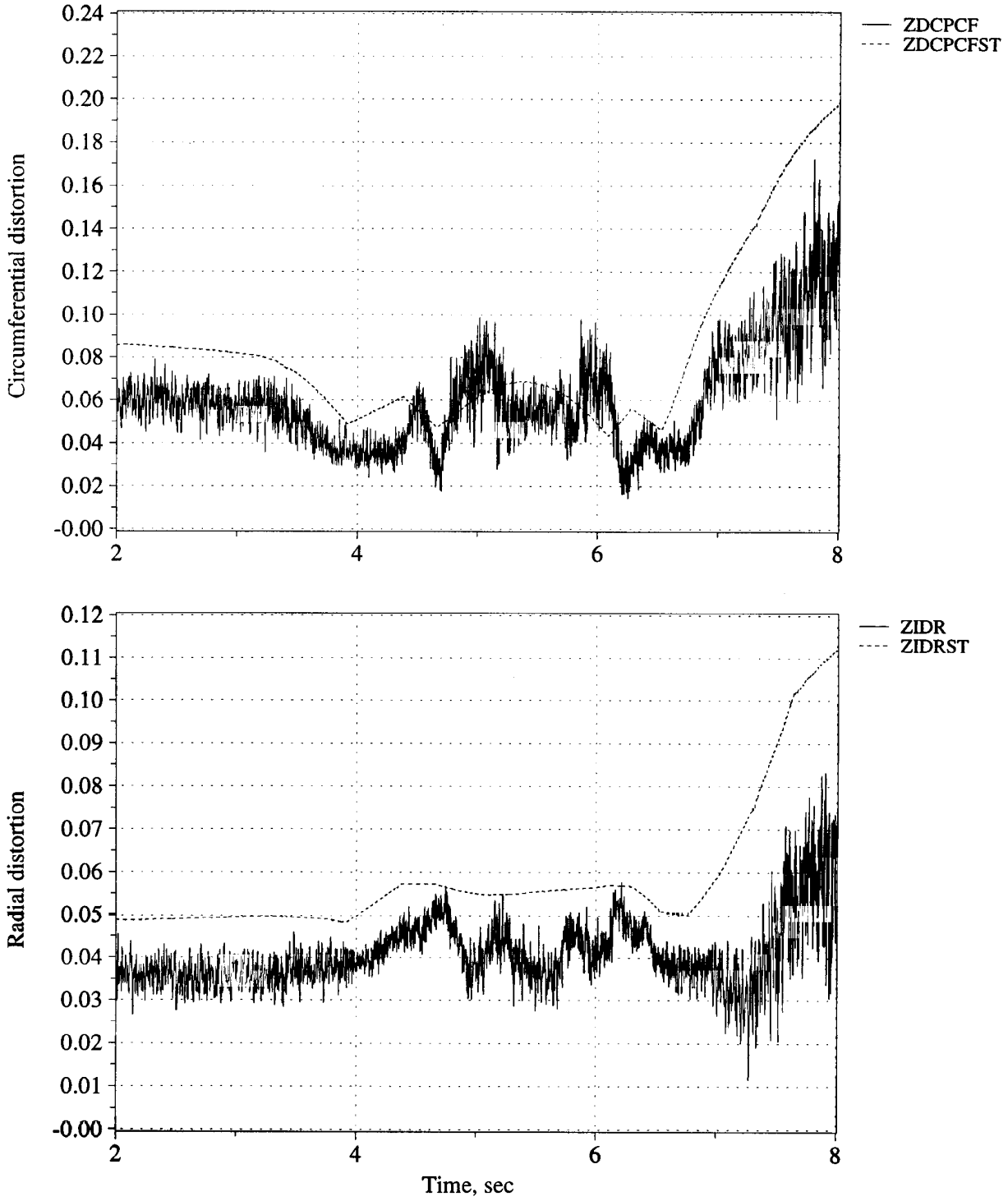

Figure B65. Time history of peak inlet dynamic circumferential and radial distortion (measured and estimated) - Flight 213, Test point 11b.

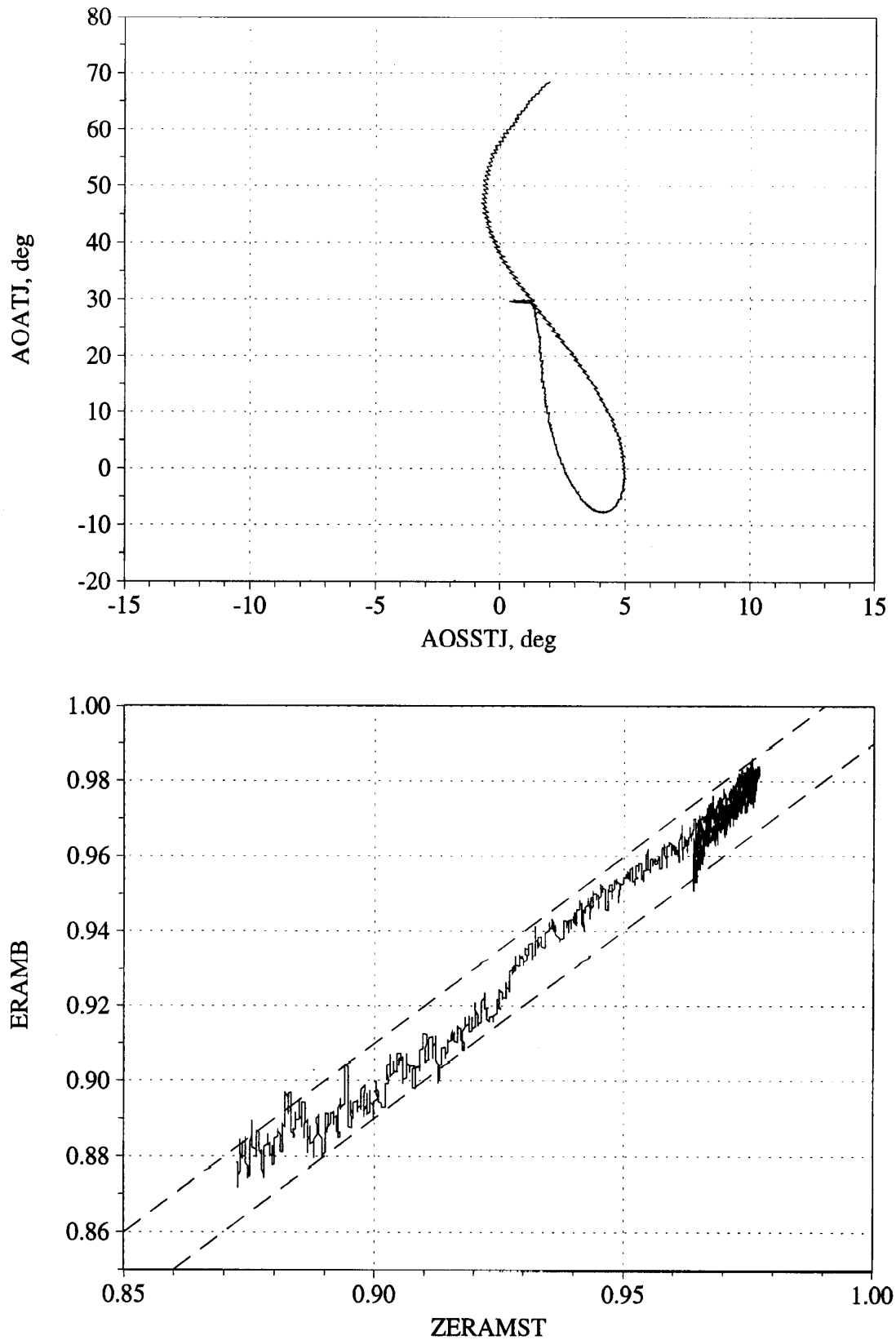

Figure B66. Angle of attack/angle of sideslip trajectory during maneuver; and measured versus estimated recovery - Flight 213, Test point 11b.

- Mid-to-Low-to-Mid Angle of Attack -

Figures B67 - B69, Flight 230, Test Point 14b
Figures B70 - B72, Flight 236, Test Point 18b
Figures B73 - B75, Flight 236, Test Point 18c

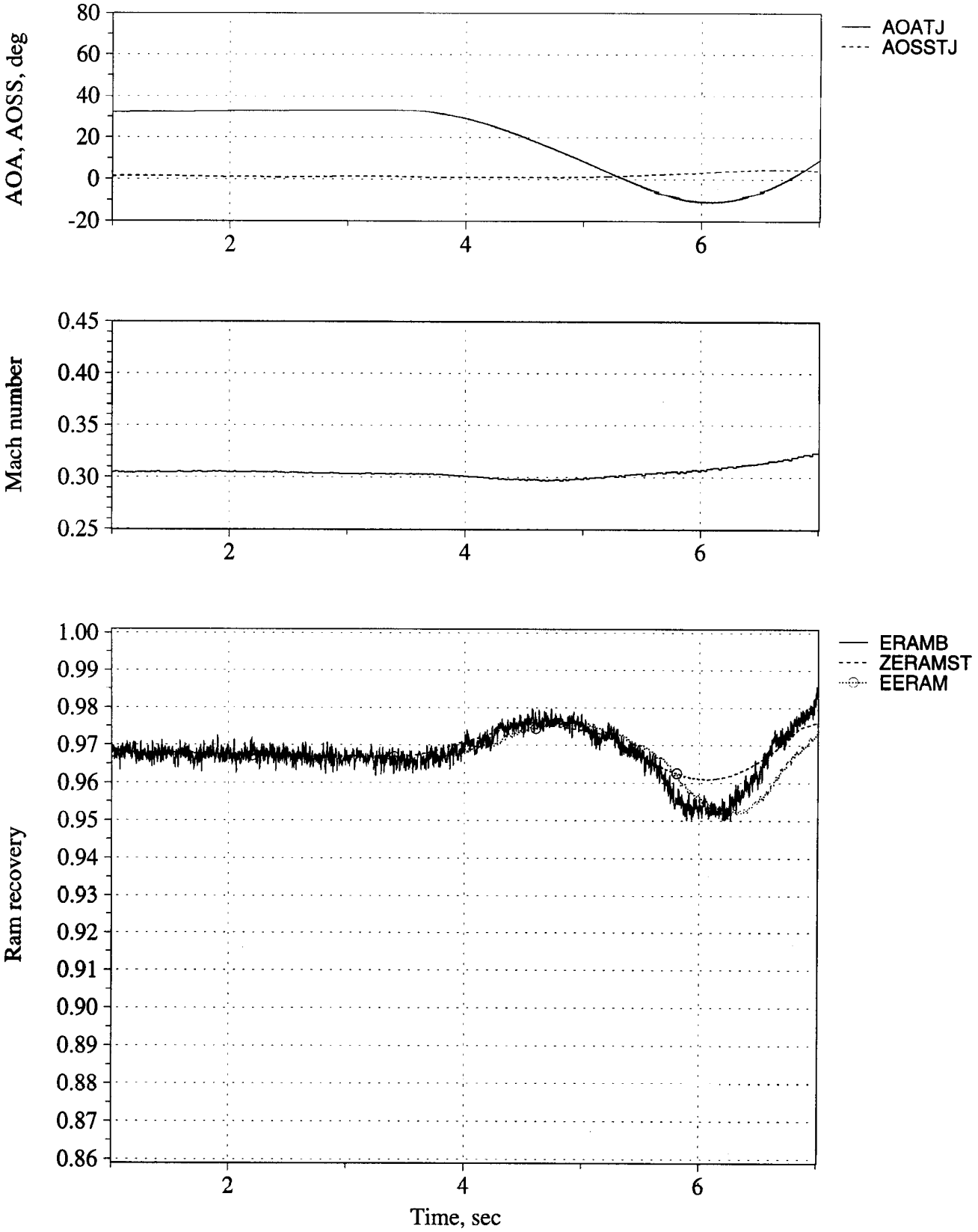

Figure B67. Time history of angle of attack, angle of sideslip, Mach number, and inlet recovery (measured and estimated) - Flight 230, Test point 14b.

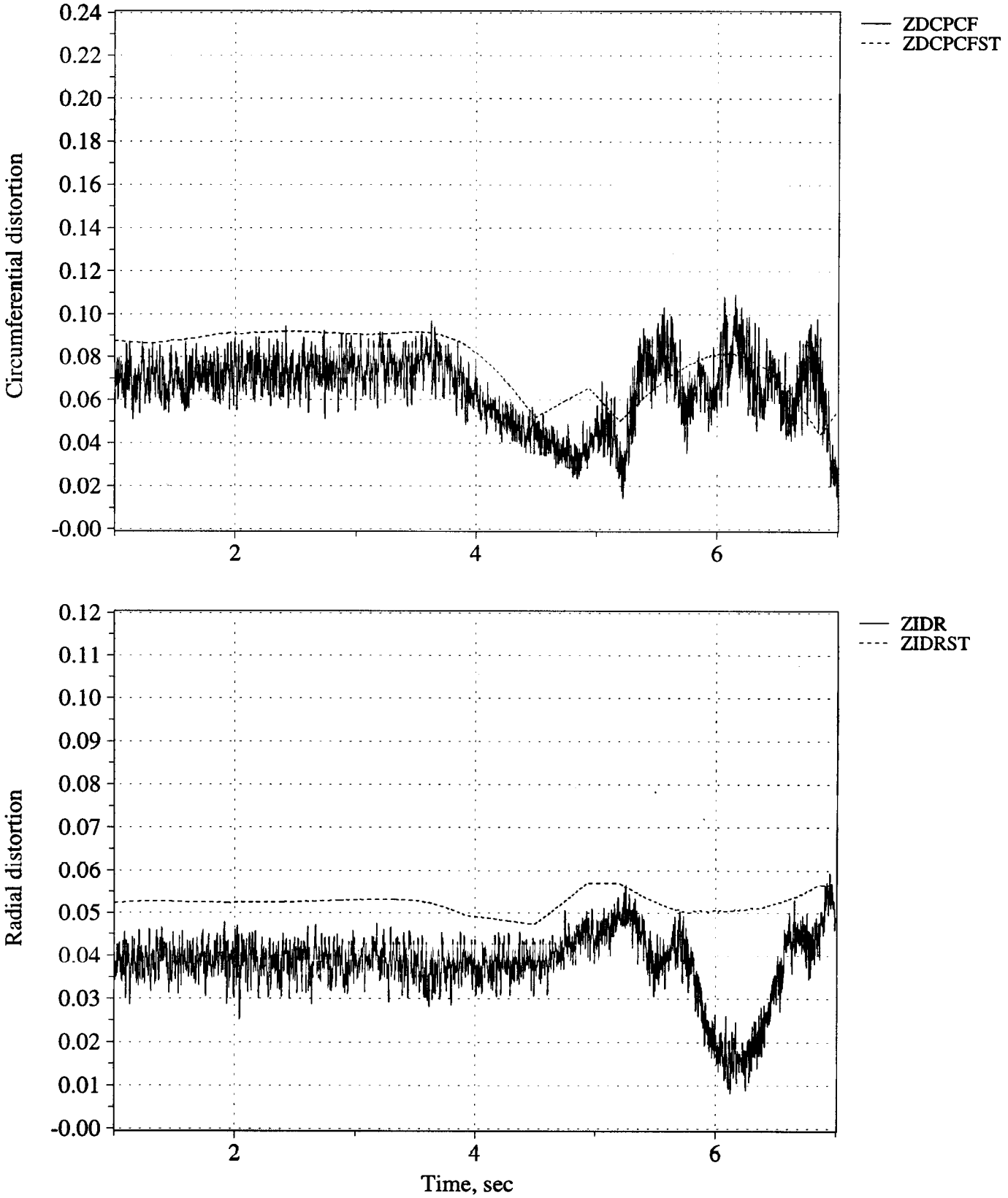

Figure B68. Time history of peak inlet dynamic circumferential and radial distortion (measured and estimated) - Flight 230, Test point 14b.

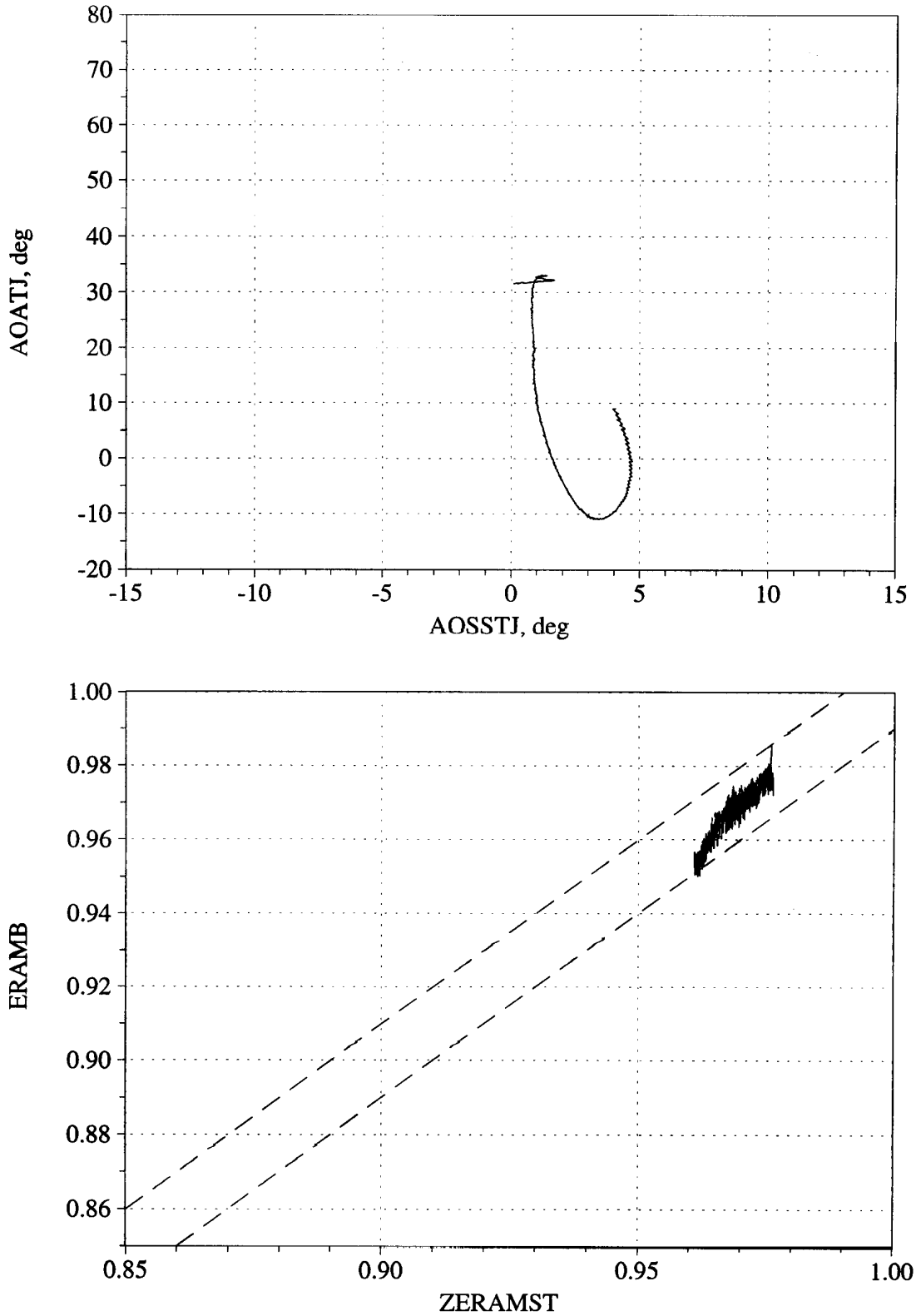

Figure B69. Angle of attack/angle of sideslip trajectory during maneuver; and measured versus estimated recovery - Flight 230, Test point 14b.

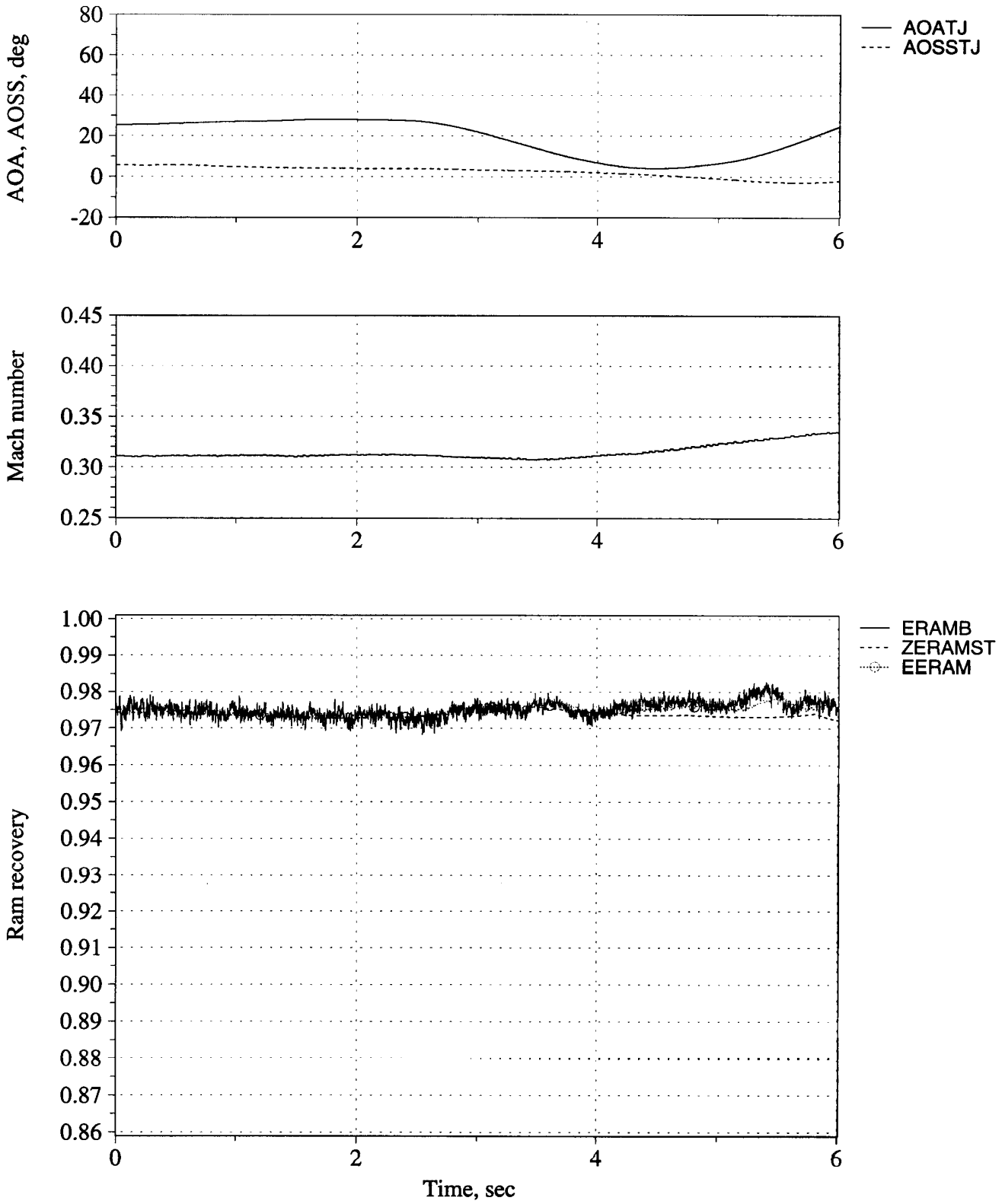

Figure B70. Time history of angle of attack, angle of sideslip, Mach number, and inlet recovery (measured and estimated) - Flight 236, Test point 18b.

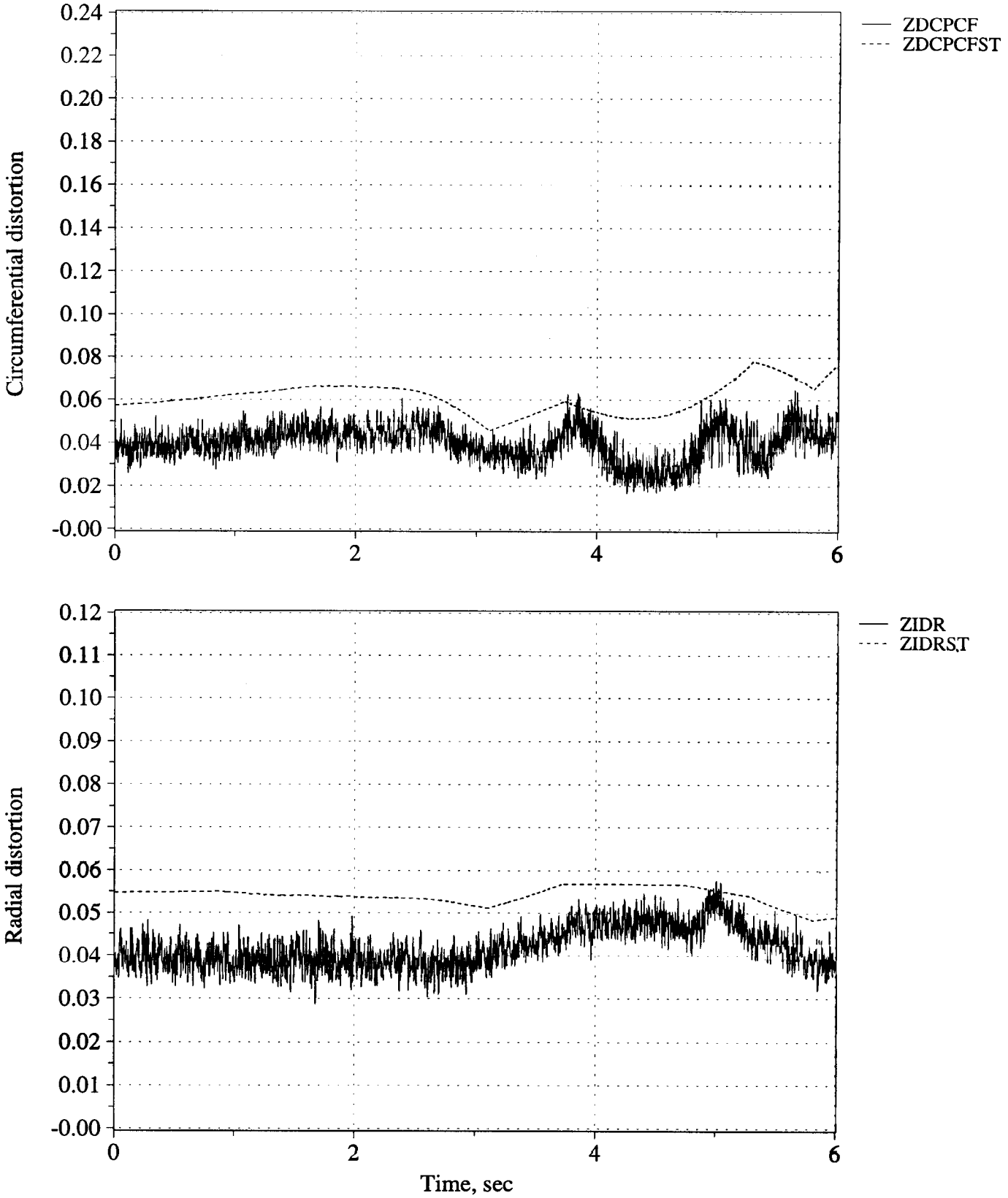

Figure B71. Time history of peak inlet dynamic circumferential and radial distortion (measured and estimated) - Flight 236, Test point 18b.

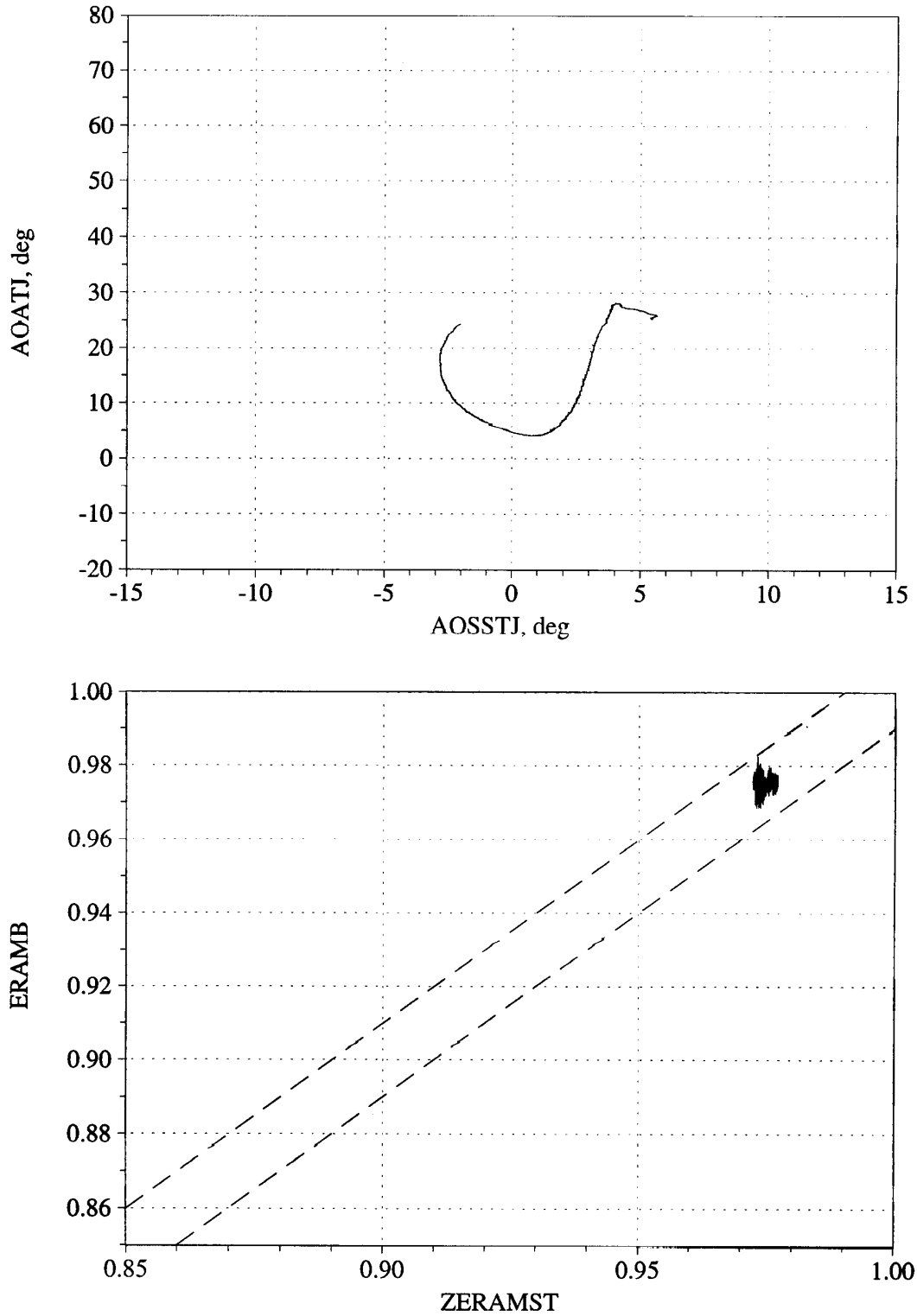

Figure B72. Angle of attack/angle of sideslip trajectory during maneuver; and measured versus estimated recovery - Flight 236, Test point 18b.

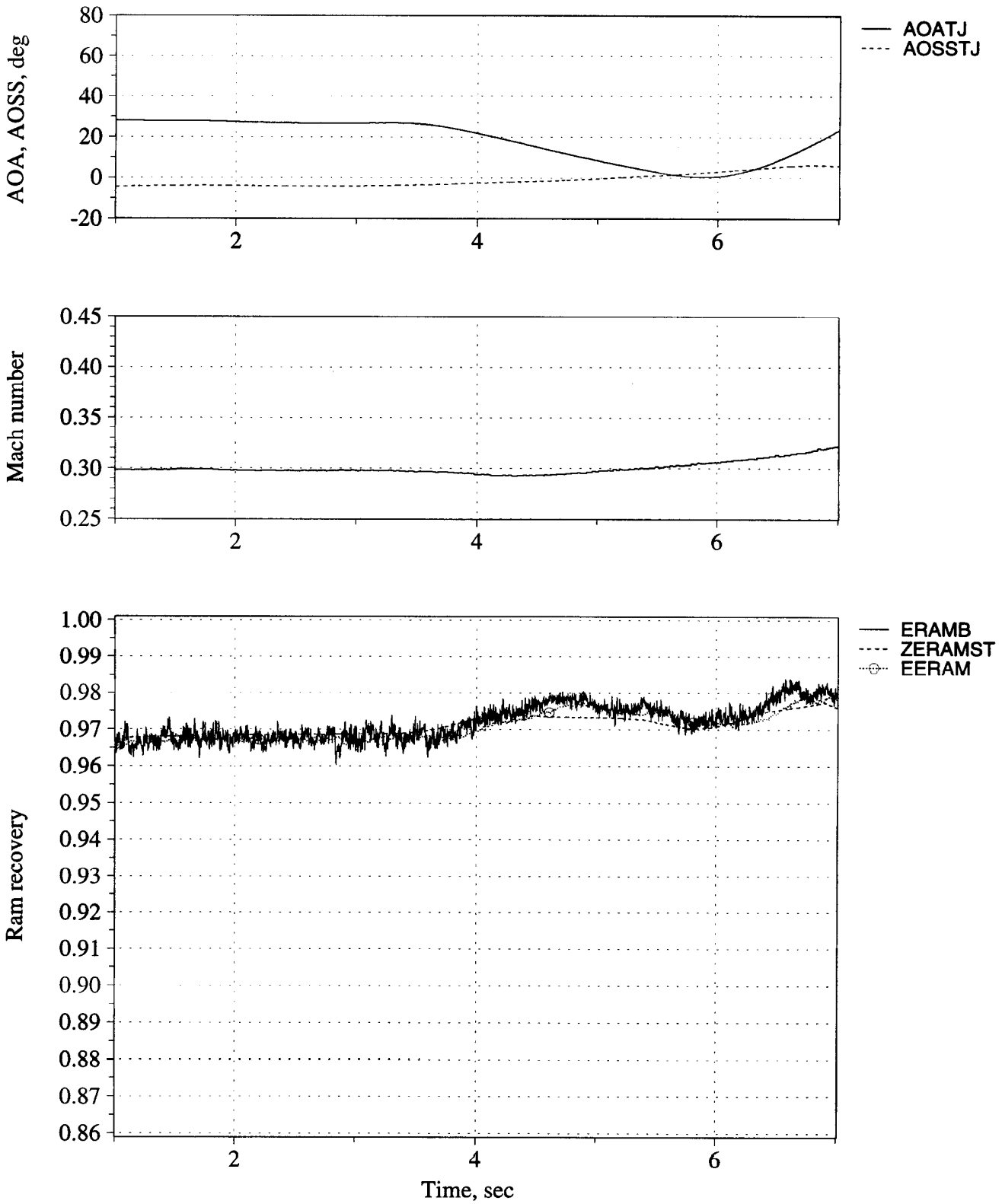

Figure B73. Time history of angle of attack, angle of sideslip, Mach number, and inlet recovery (measured and estimated) - Flight 236, Test point 18c.

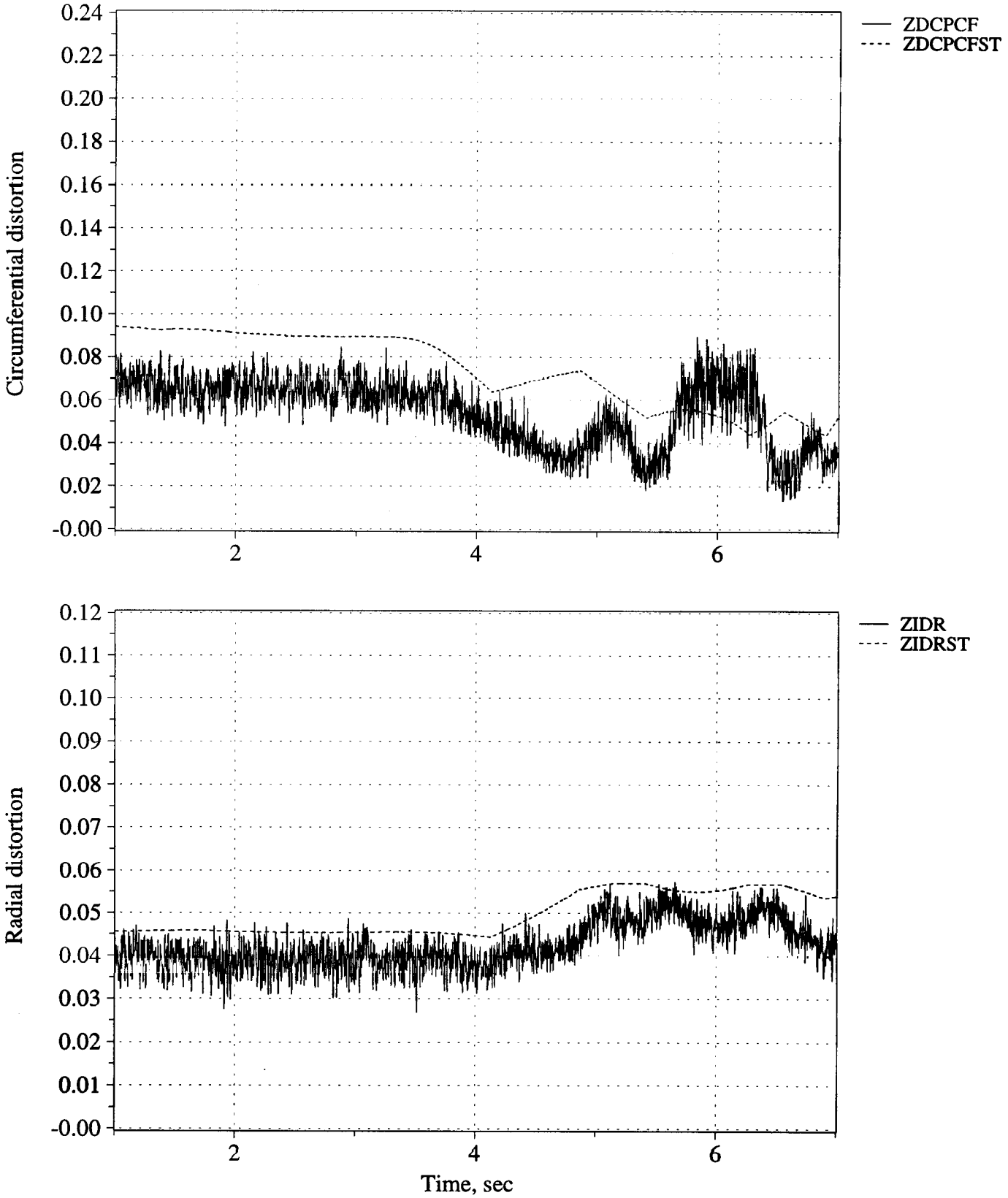

Figure B74. Time history of peak inlet dynamic circumferential and radial distortion (measured and estimated) - Flight 236, Test point 18c.

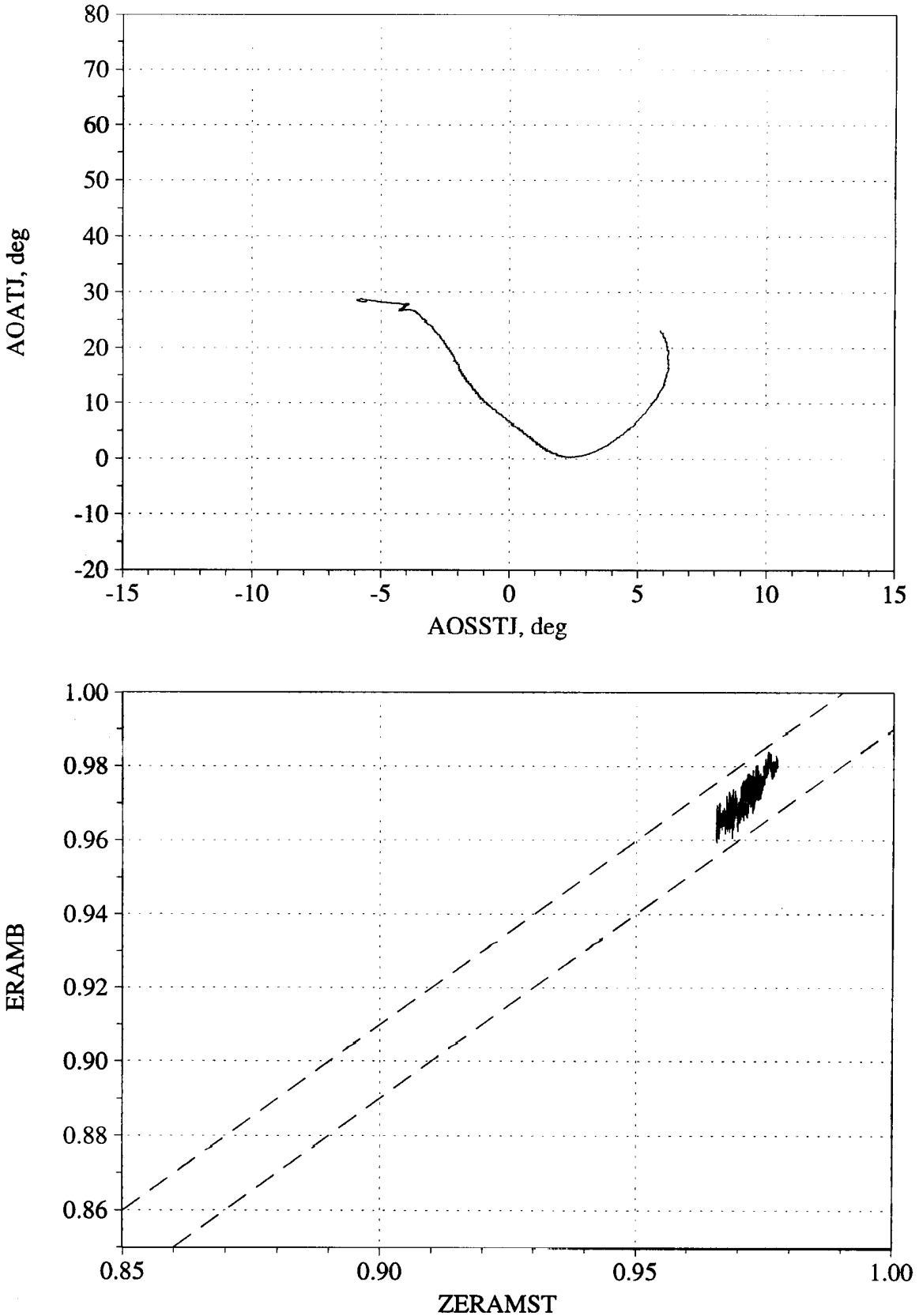

Figure B75. Angle of attack/angle of sideslip trajectory during maneuver; and measured versus estimated recovery - Flight 236, Test point 18c.

APPENDIX C: M = 0.4 RAPID MANEUVERS

- Low-to-High Angle of Attack -

Figures C1 - C3, Flight 214, Test Point 04b
Figures C4 - C6, Flight 215, Test Point 07b
Figures C7 - C9, Flight 230, Test Point 13b
Figures C10 - C12, Flight 230, Test Point 18b
Figures C13 - C15, Flight 230, Test Point 22b
Figures C16 - C18, Flight 236, Test Point 4b1
Figures C19 - C21, Flight 236, Test Point 4b2
Figures C22 - B24, Flight 236, Test Point 24c
Figures C25 - C27, Flight 242, Test Point 21b
Figures C28 - C30, Flight 242, Test Point 21c

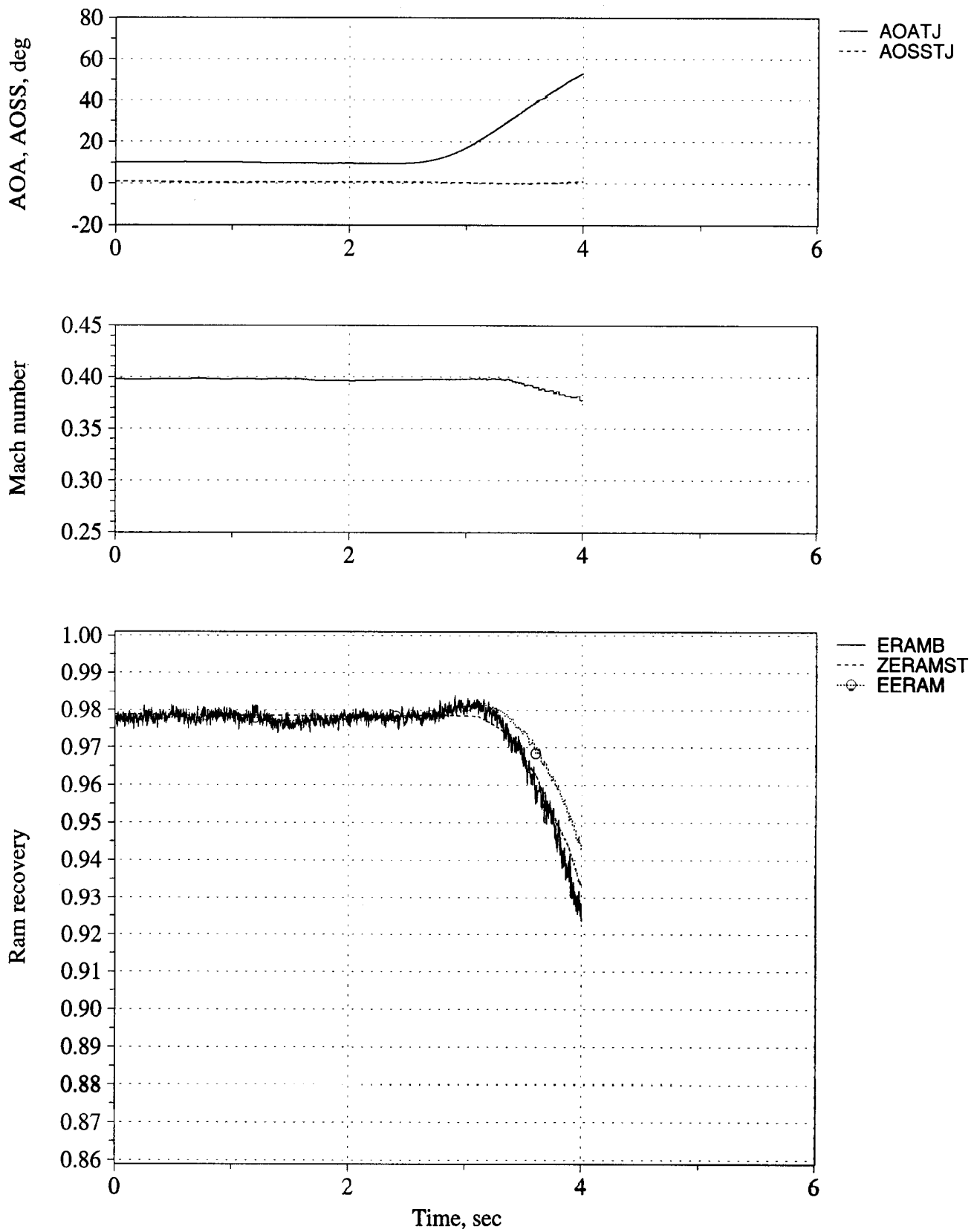

Figure C1. Time history of angle of attack, angle of sideslip, Mach number, and inlet recovery (measured and estimated) - Flight 214, Test point 04b.

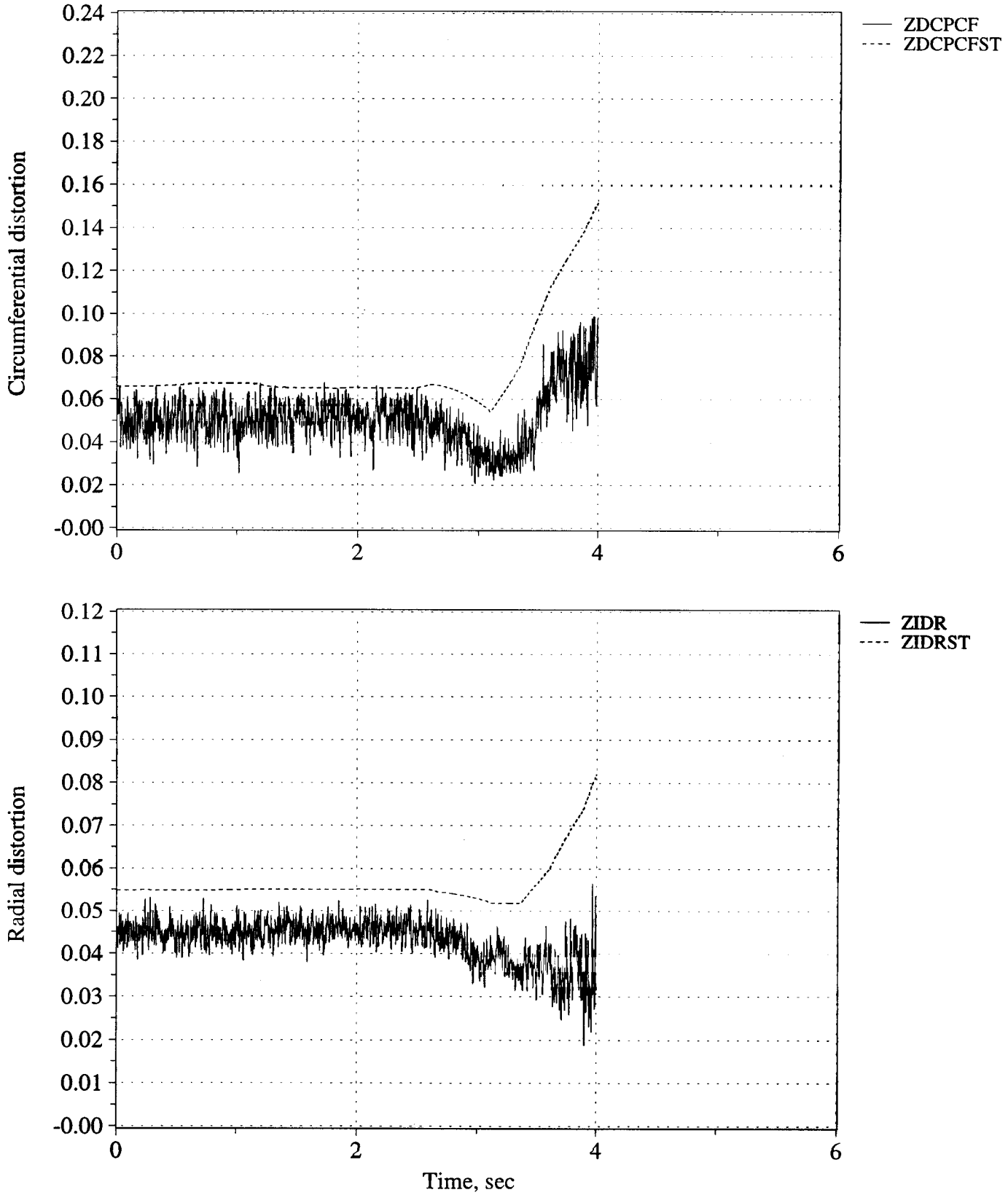

Figure C2. Time history of peak inlet dynamic circumferential and radial distortion (measured and estimated) - Flight 214, Test point 04b.

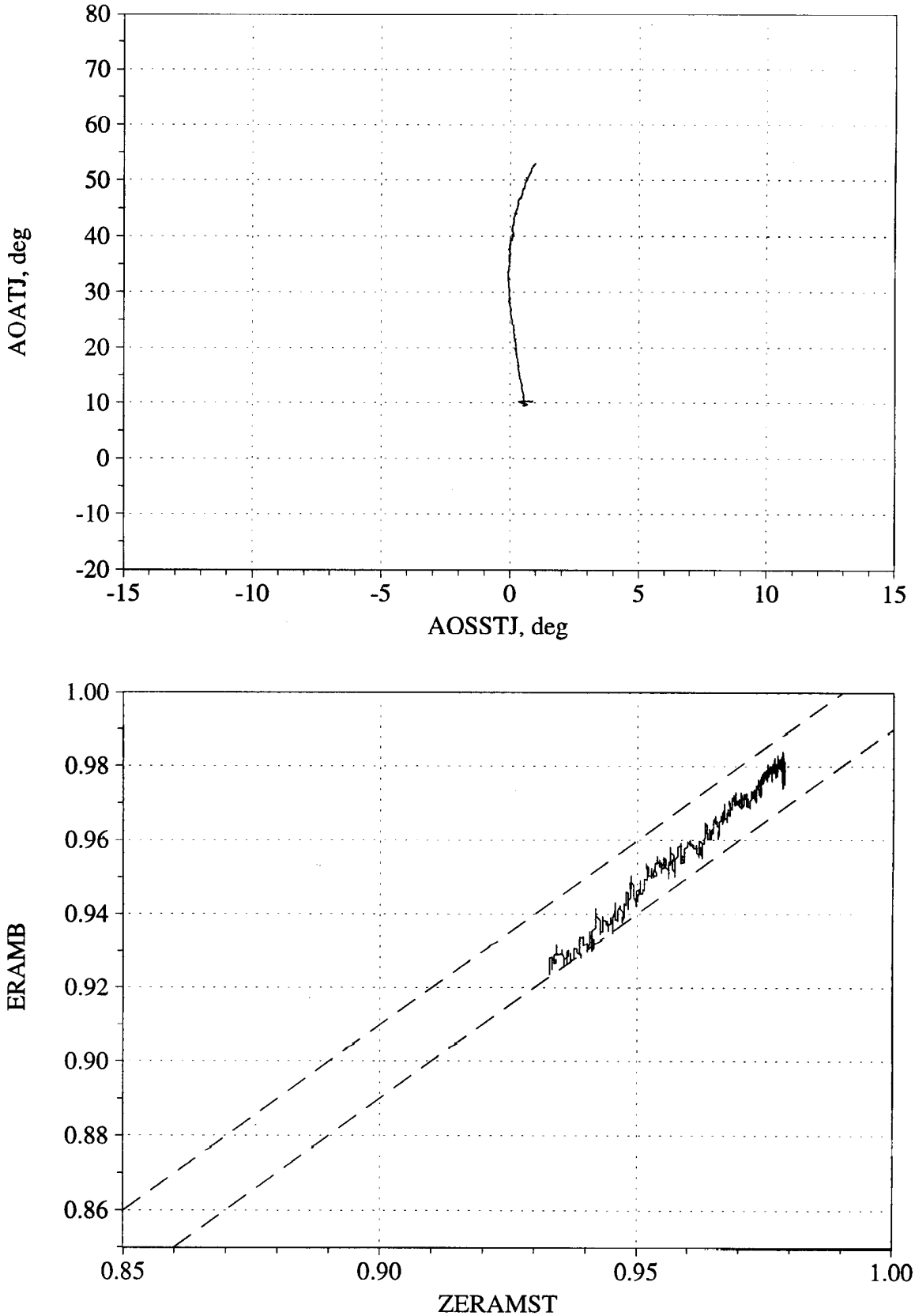

Figure C3. Angle of attack/angle of sideslip trajectory during maneuver; and measured versus estimated recovery - Flight 214, Test point 04b.

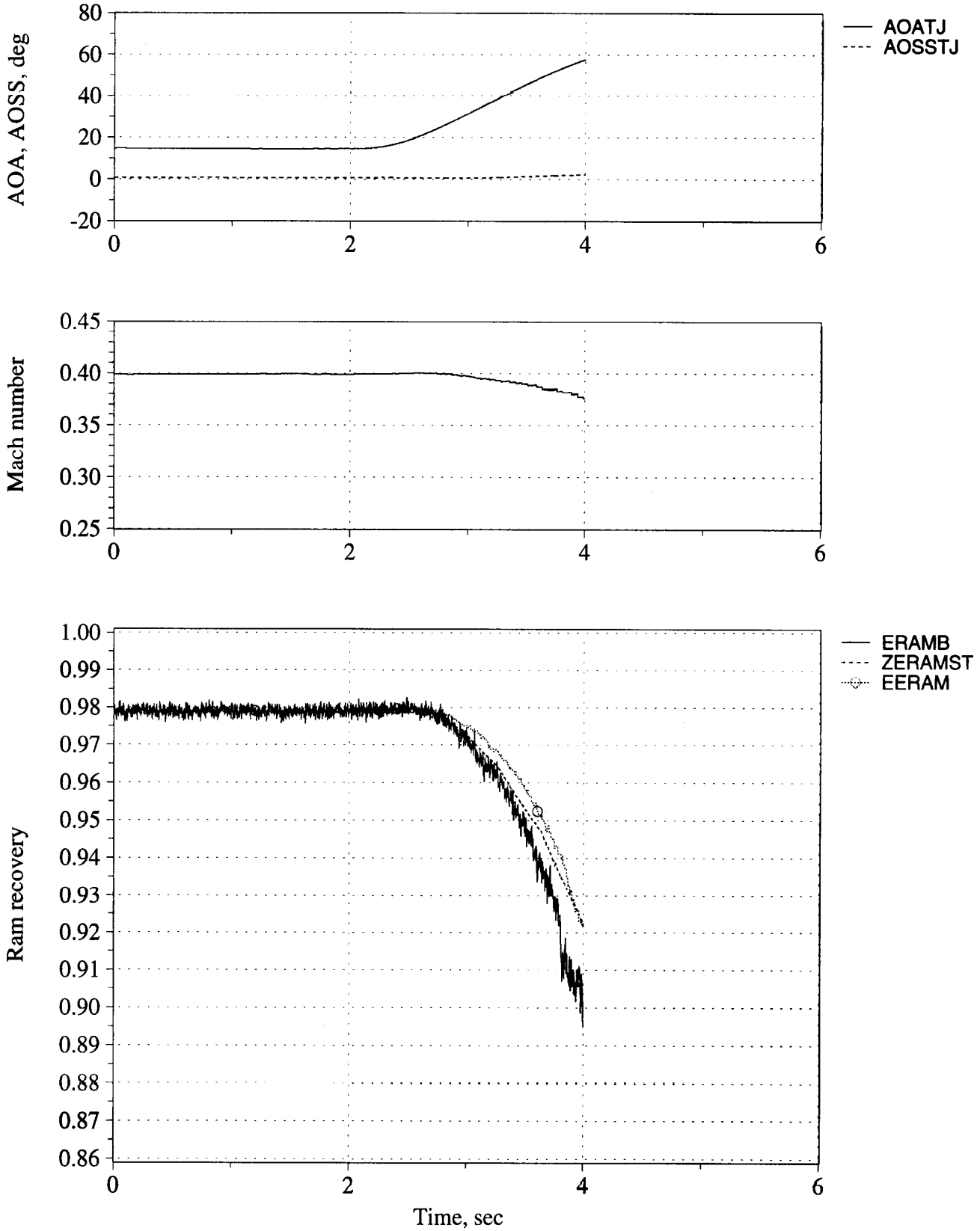

Figure C4. Time history of angle of attack, angle of sideslip, Mach number, and inlet recovery (measured and estimated) - Flight 215, Test point 07b.

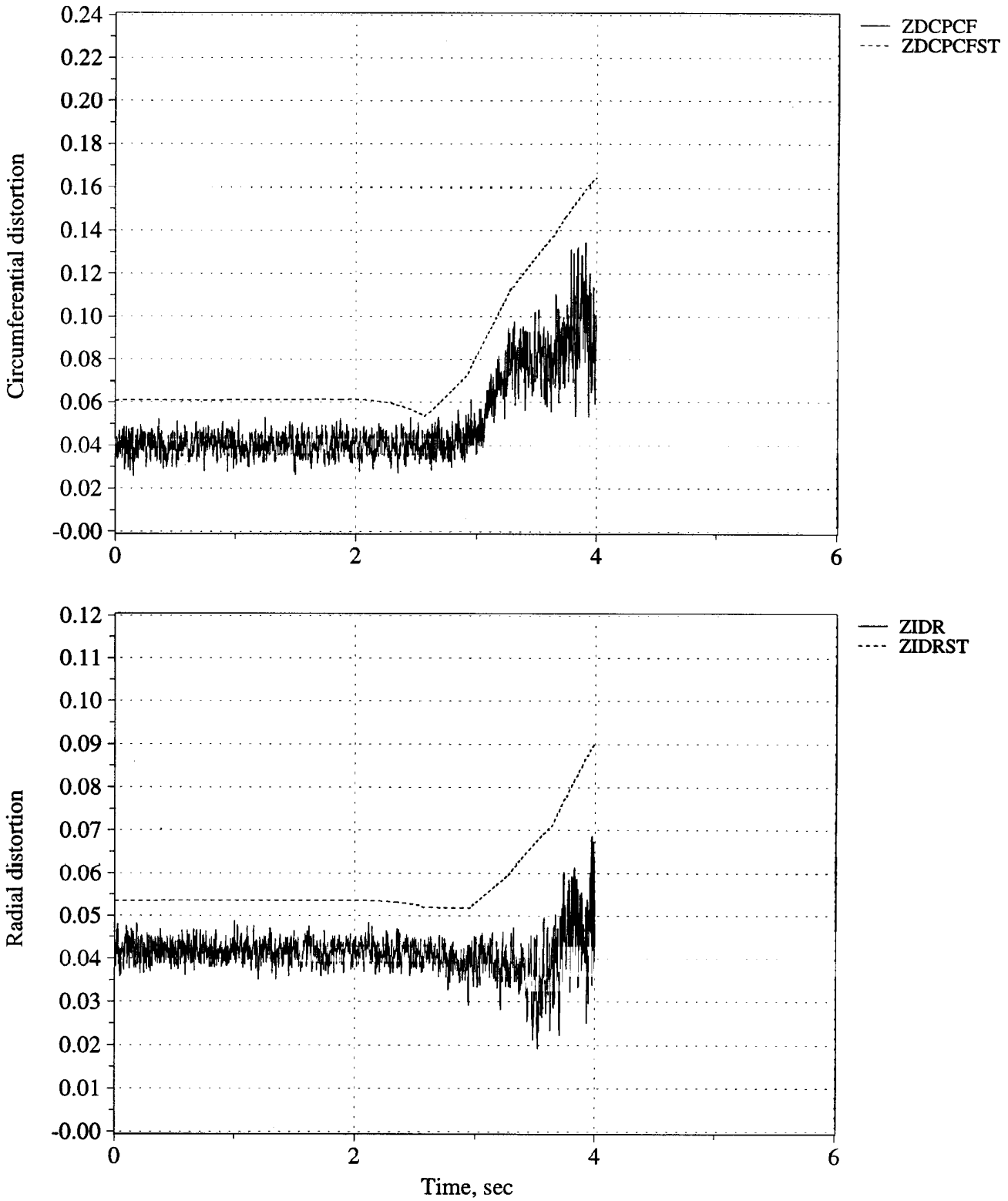

Figure C5. Time history of peak inlet dynamic circumferential and radial distortion (measured and estimated) - Flight 215, Test point 07b.

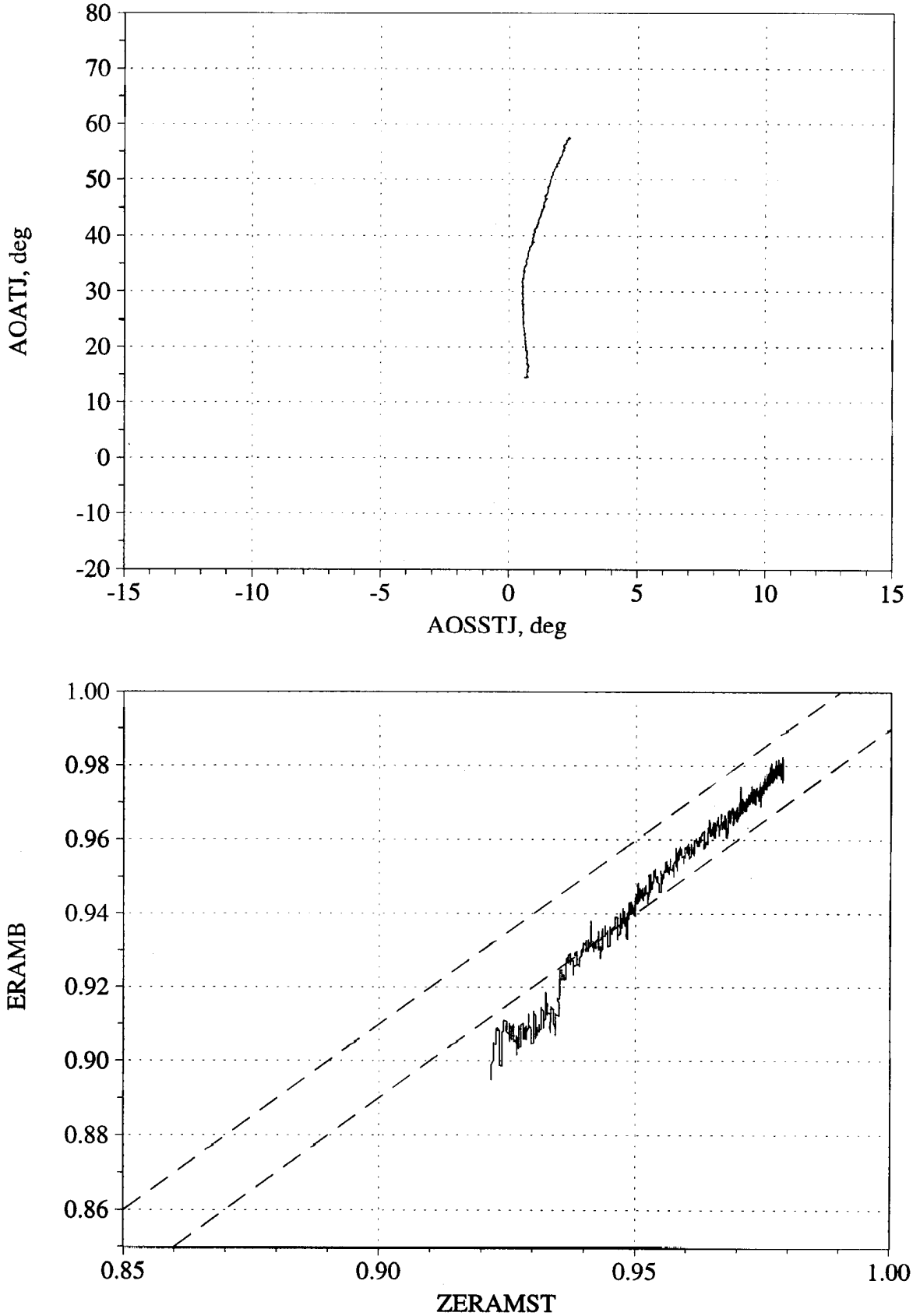

Figure C6. Angle of attack/angle of sideslip trajectory during maneuver; and measured versus estimated recovery - Flight 215, Test point 07b.

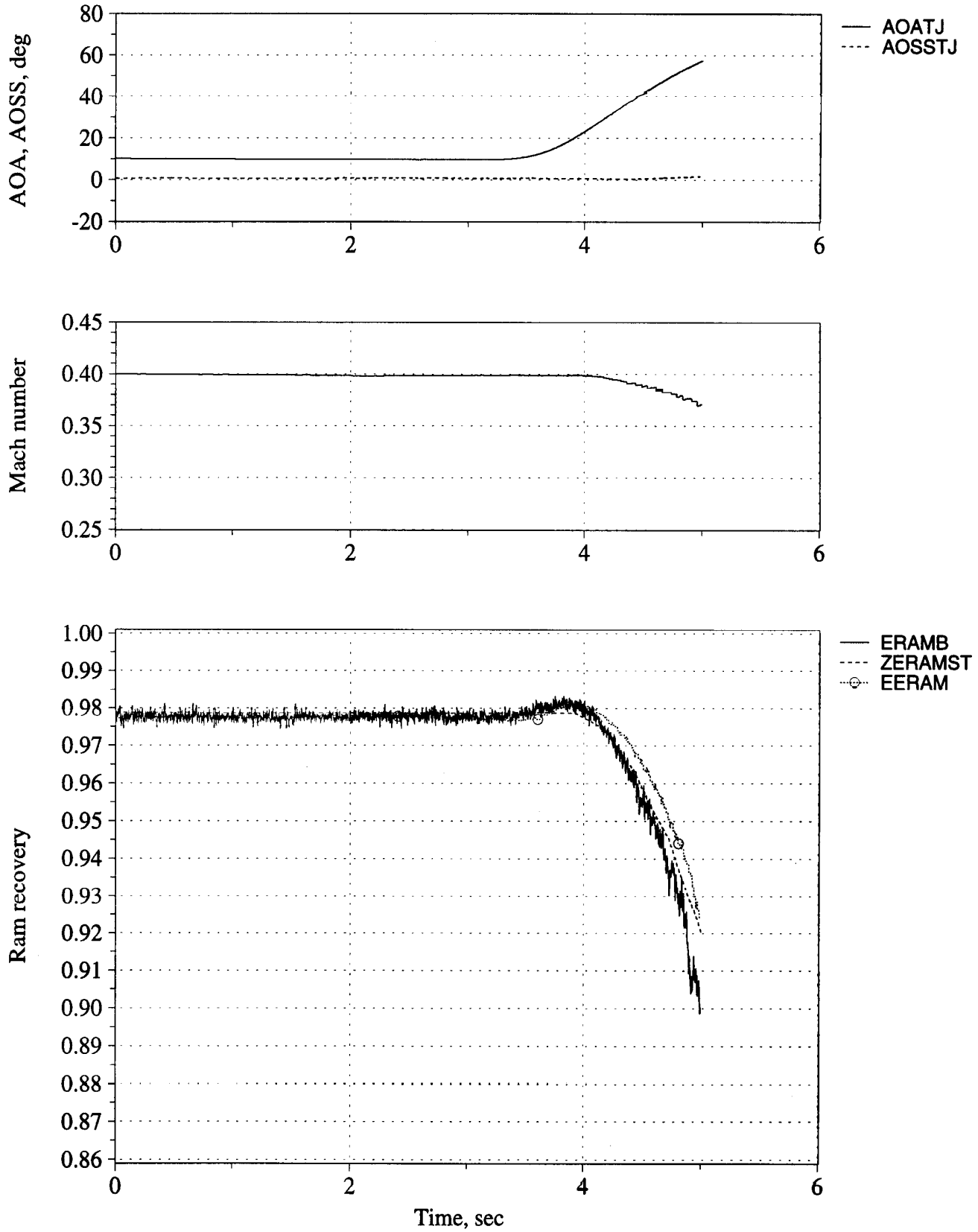

Figure C7. Time history of angle of attack, angle of sideslip, Mach number, and inlet recovery (measured and estimated) - Flight 230, Test point 13b.

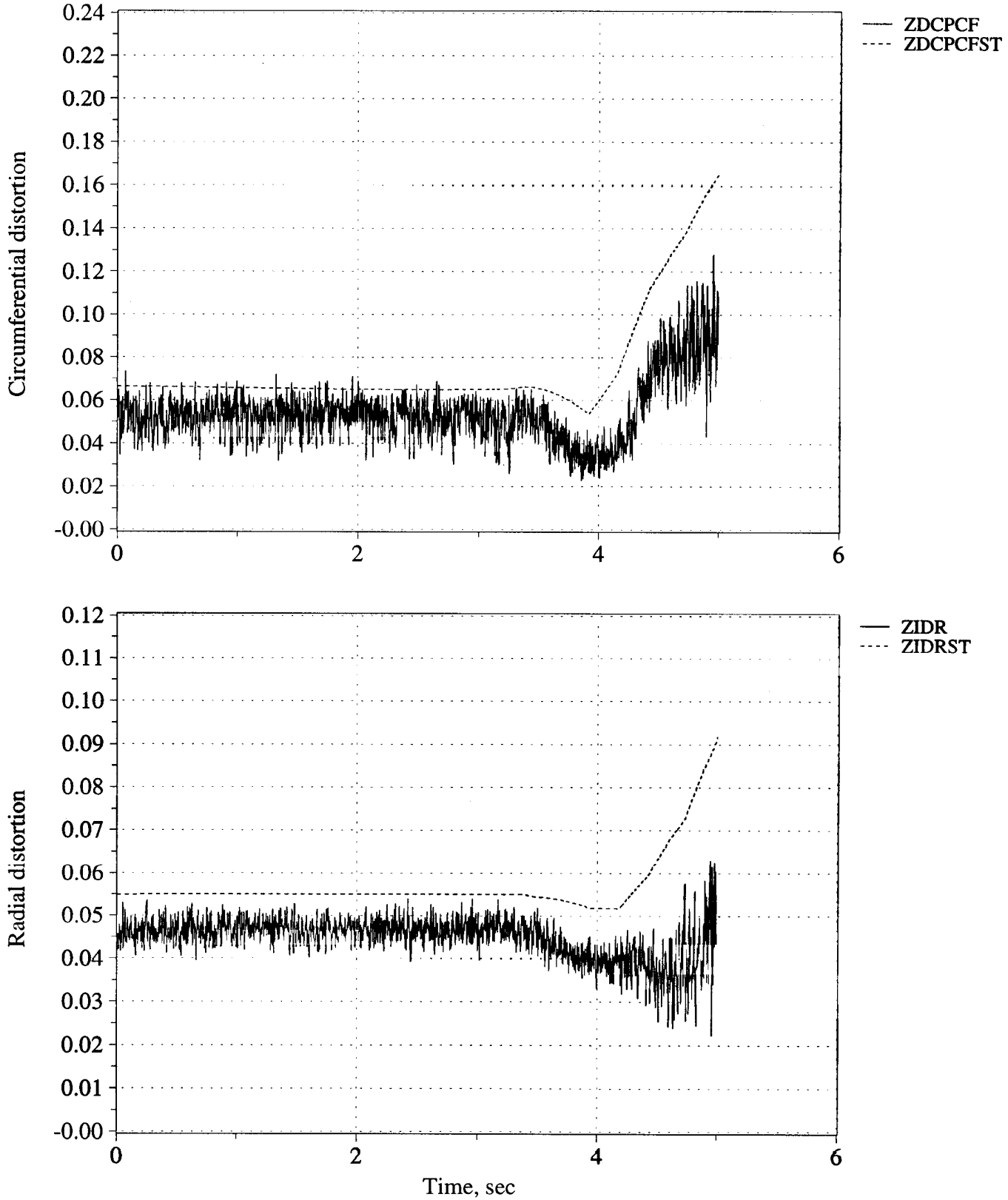

Figure C8. Time history of peak inlet dynamic circumferential and radial distortion (measured and estimated) - Flight 230, Test point 13b.

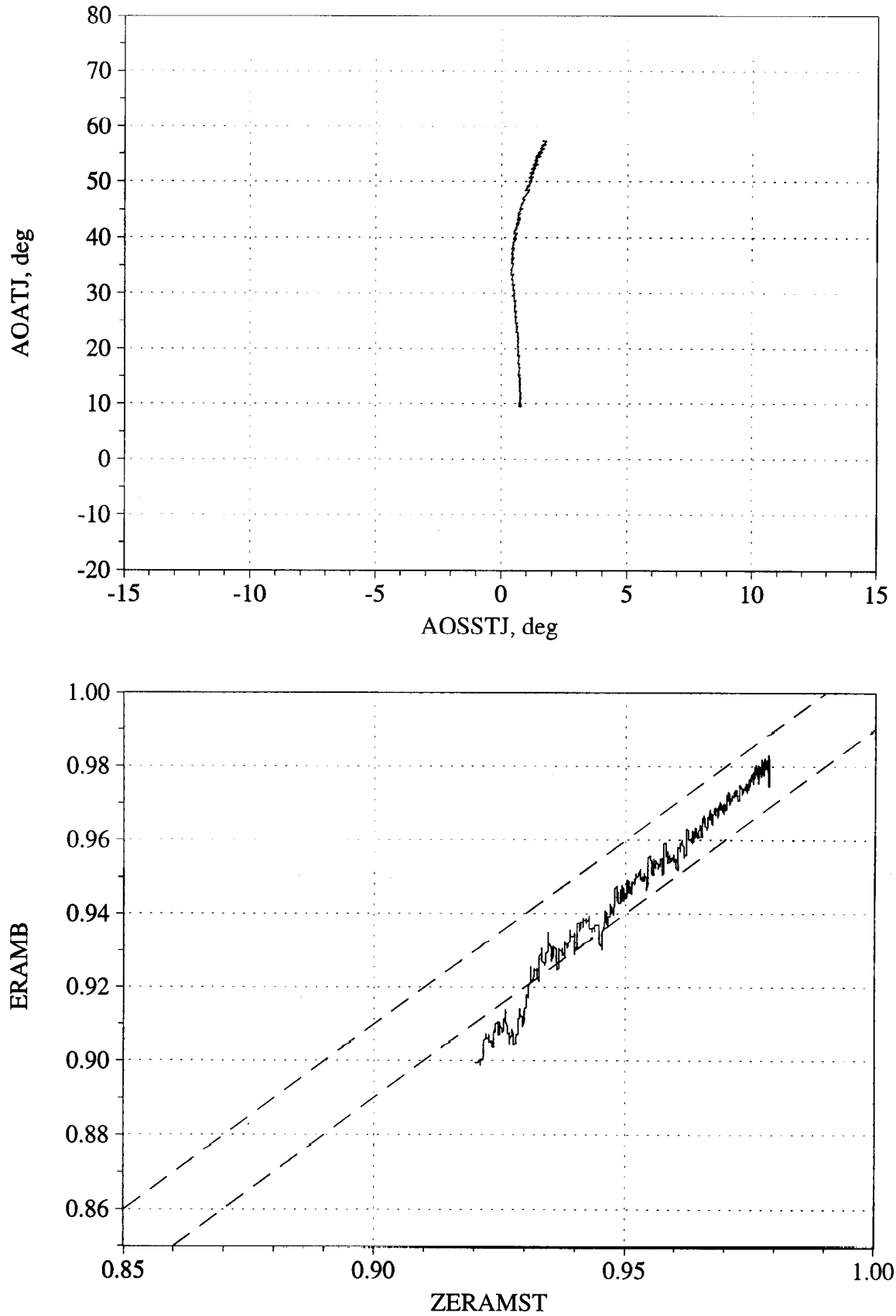

Figure C9. Angle of attack/angle of sideslip trajectory during maneuver; and measured versus estimated recovery - Flight 230, Test point 13b.

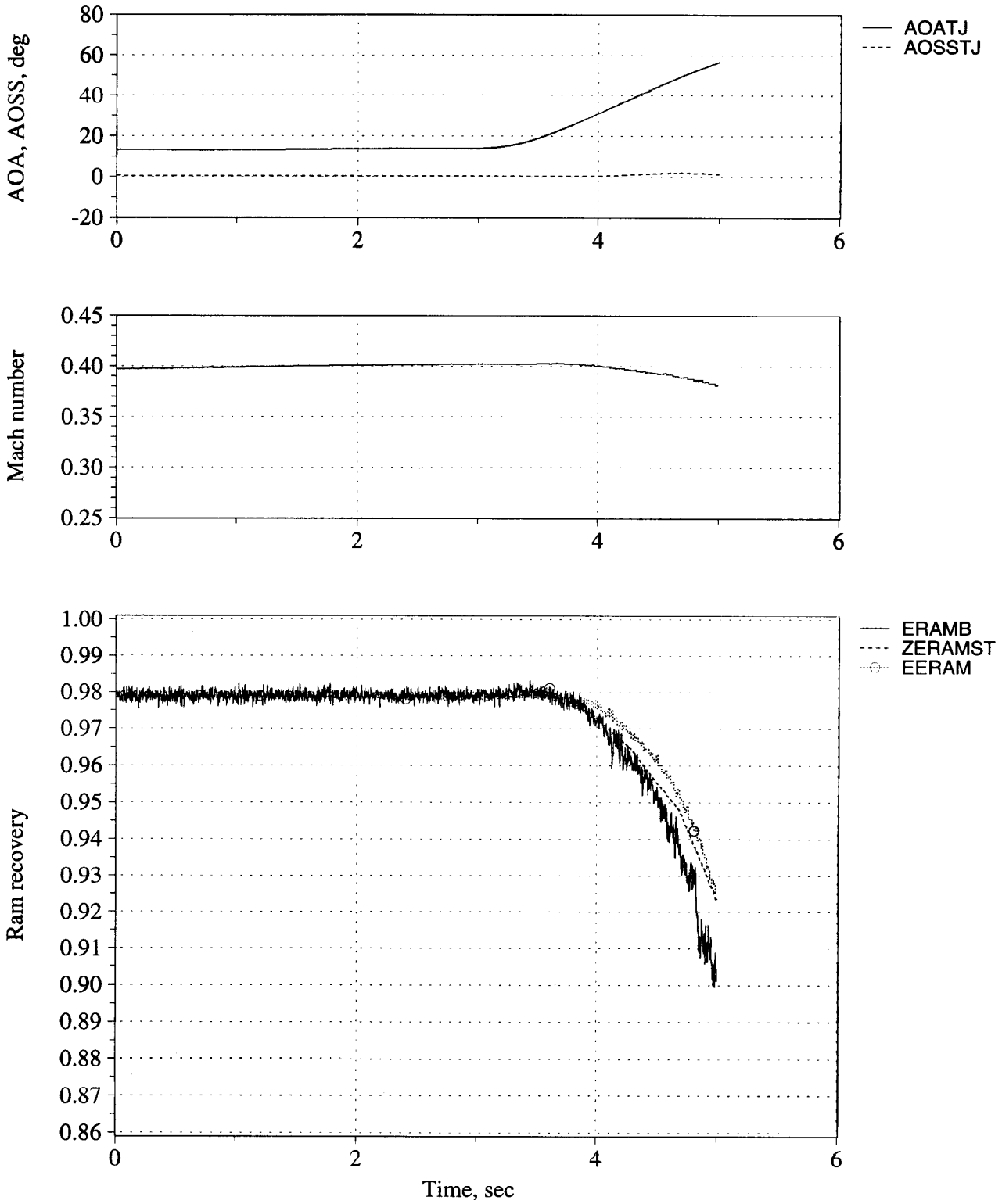

Figure C10. Time history of angle of attack, angle of sideslip, Mach number, and inlet recovery (measured and estimated) - Flight 230, Test point 18b.

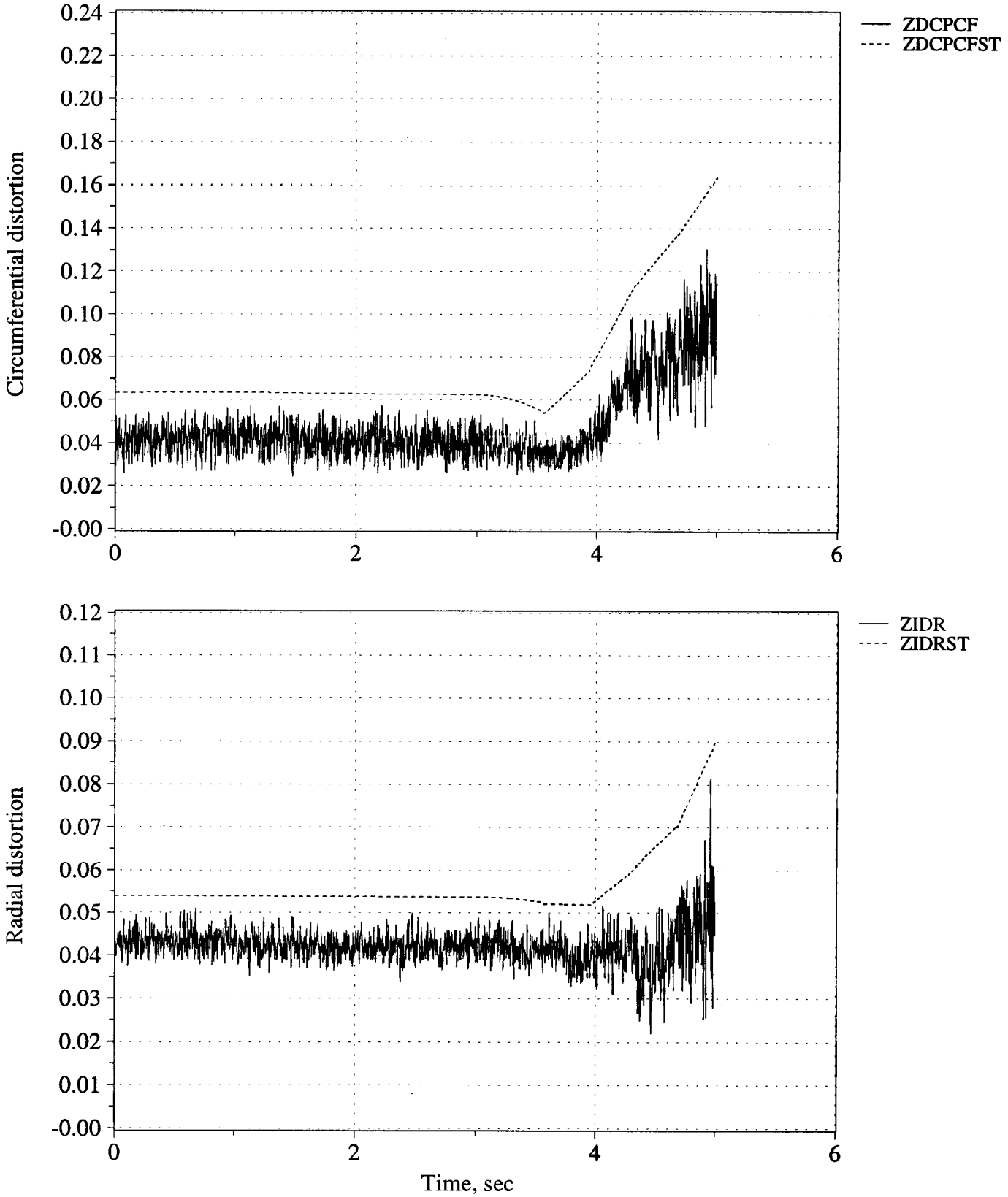

Figure C11. Time history of peak inlet dynamic circumferential and radial distortion (measured and estimated) - Flight 230, Test point 18b.

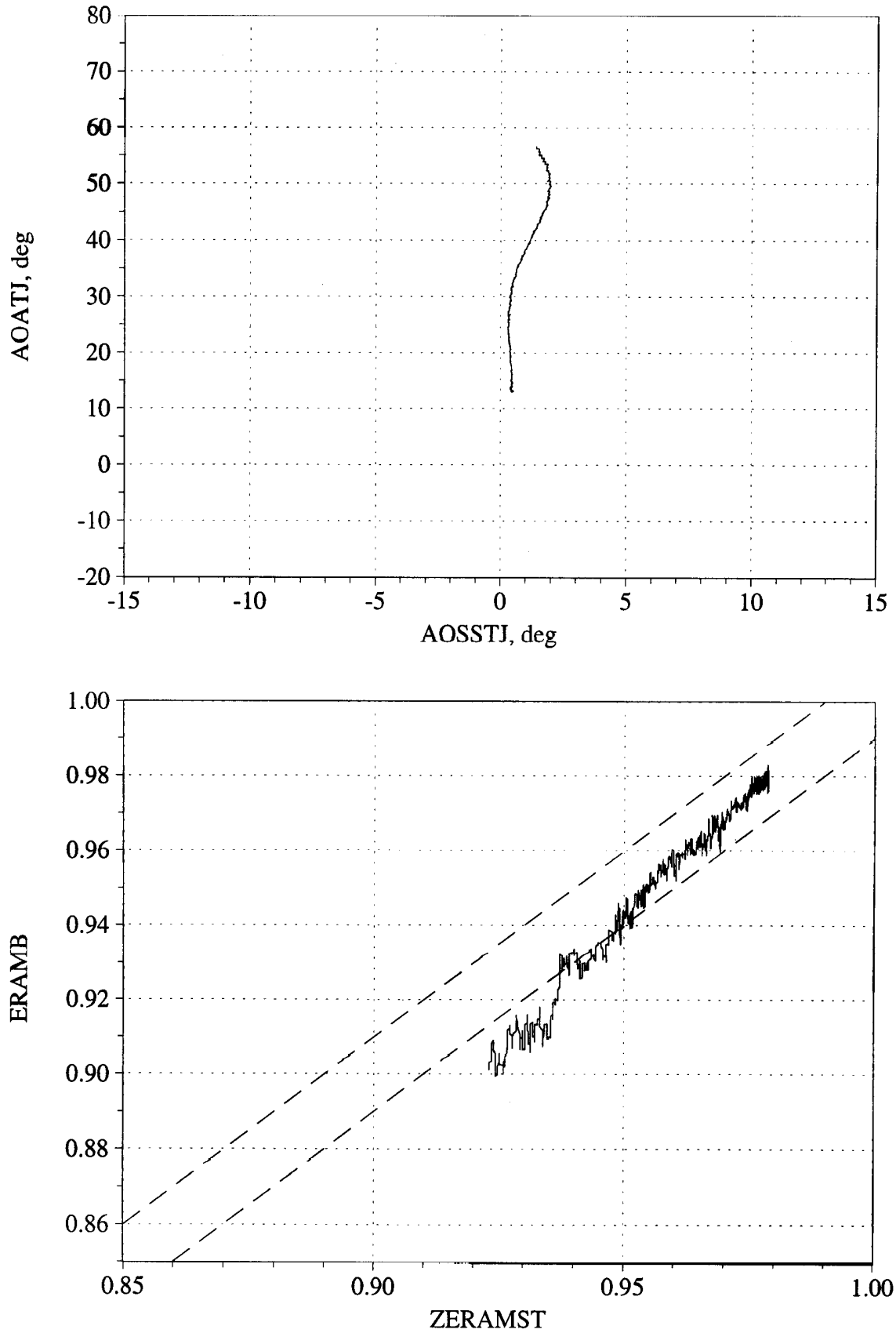

Figure C12. Angle of attack/angle of sideslip trajectory during maneuver; and measured versus estimated recovery - Flight 230, Test point 18b.

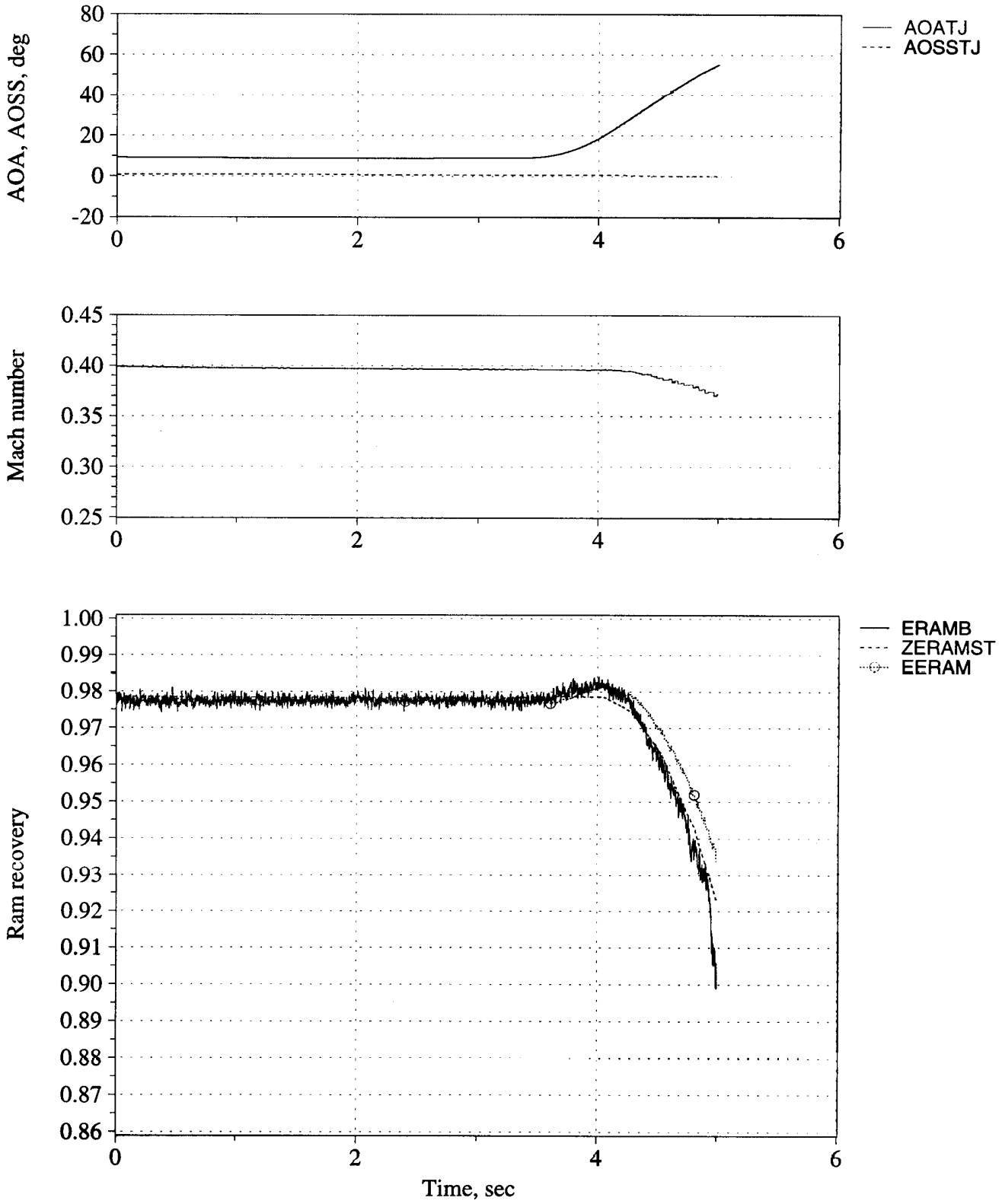

Figure C13. Time history of angle of attack, angle of sideslip, Mach number, and inlet recovery (measured and estimated) - Flight 230, Test point 22b.

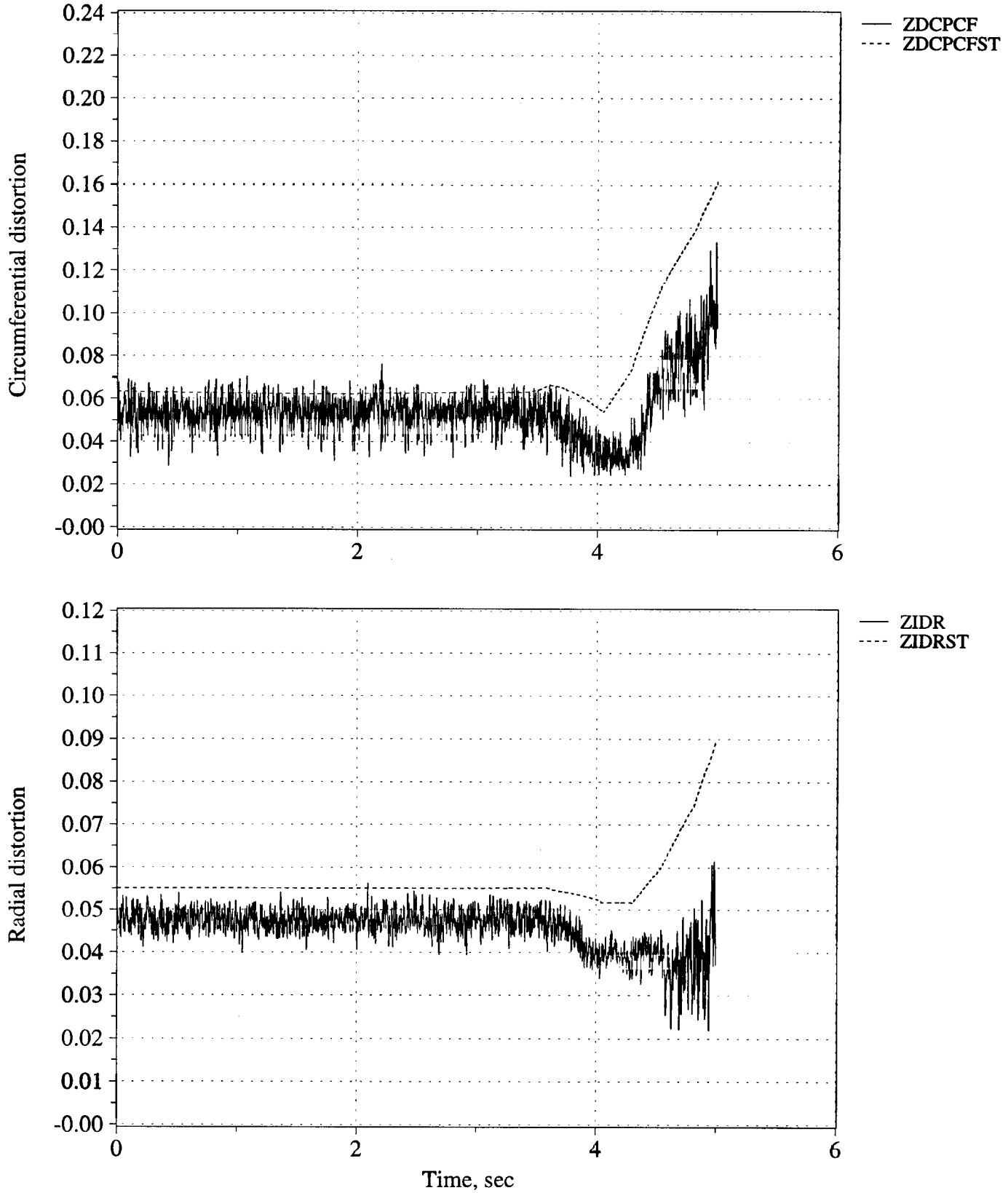

Figure C14. Time history of peak inlet dynamic circumferential and radial distortion (measured and estimated) - Flight 230, Test point 22b.

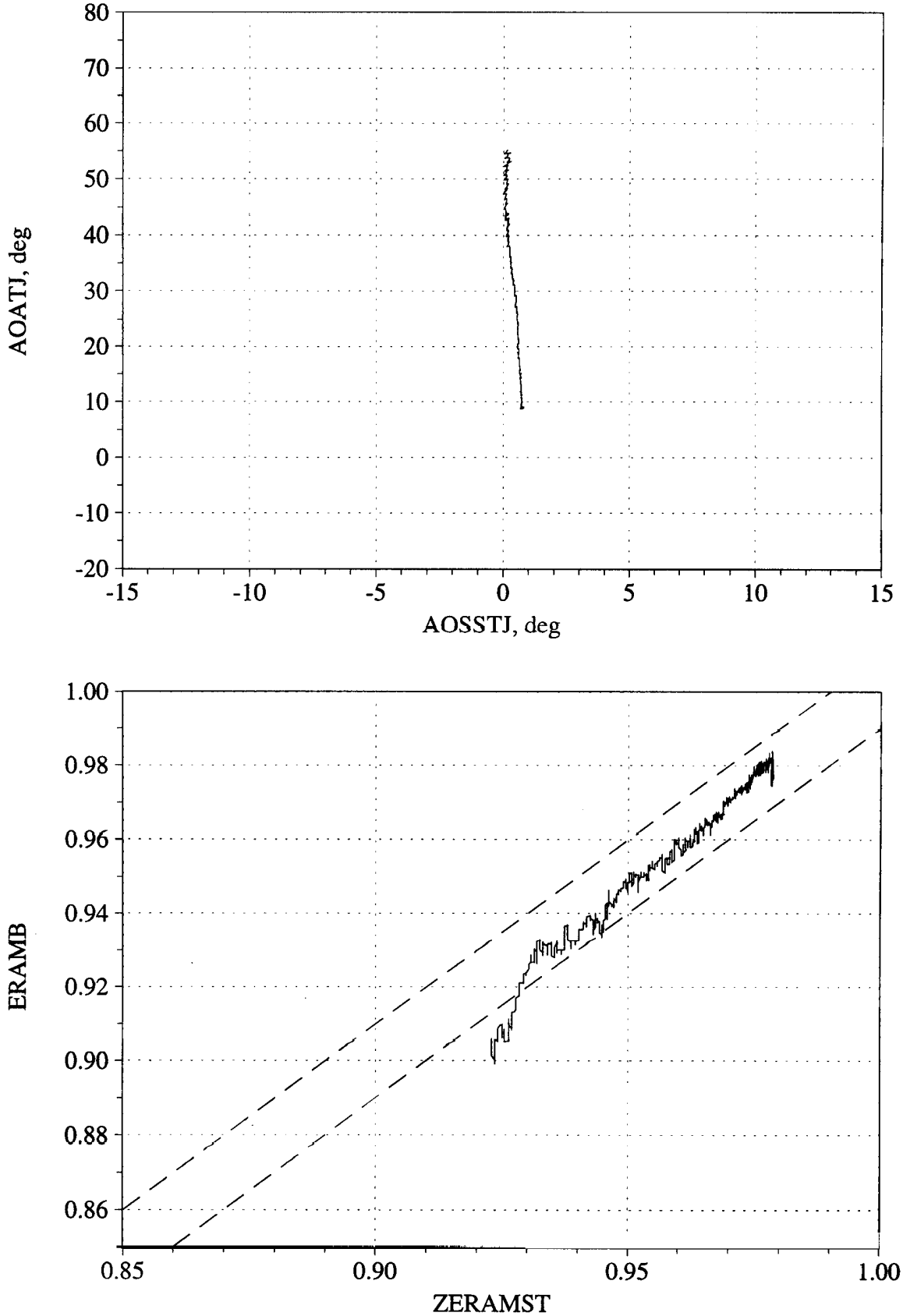

Figure C15. Angle of attack/angle of sideslip trajectory during maneuver; and measured versus estimated recovery - Flight 230, Test point 22b.

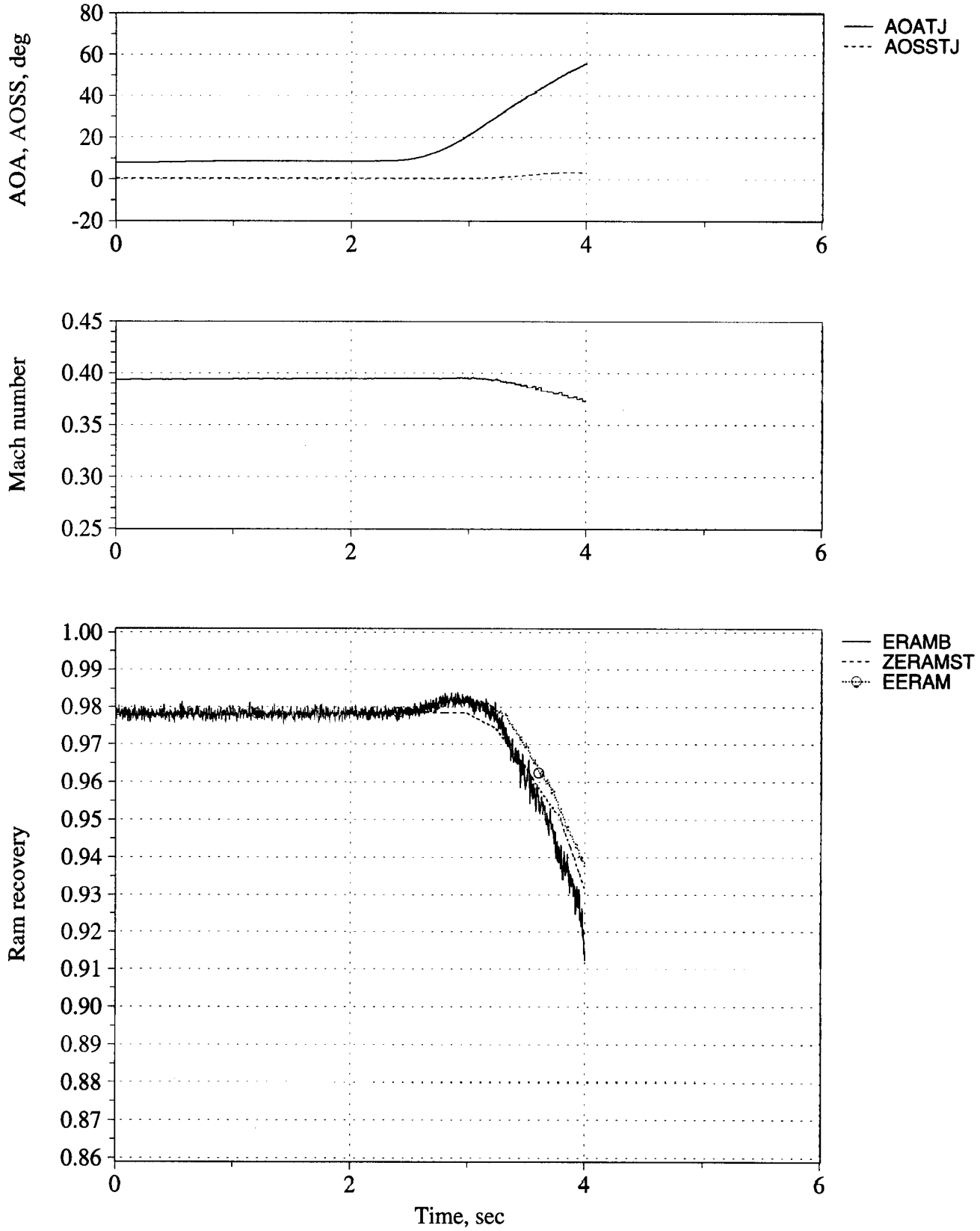

Figure C16. Time history of angle of attack, angle of sideslip, Mach number, and inlet recovery (measured and estimated) - Flight 236, Test point 4b1.

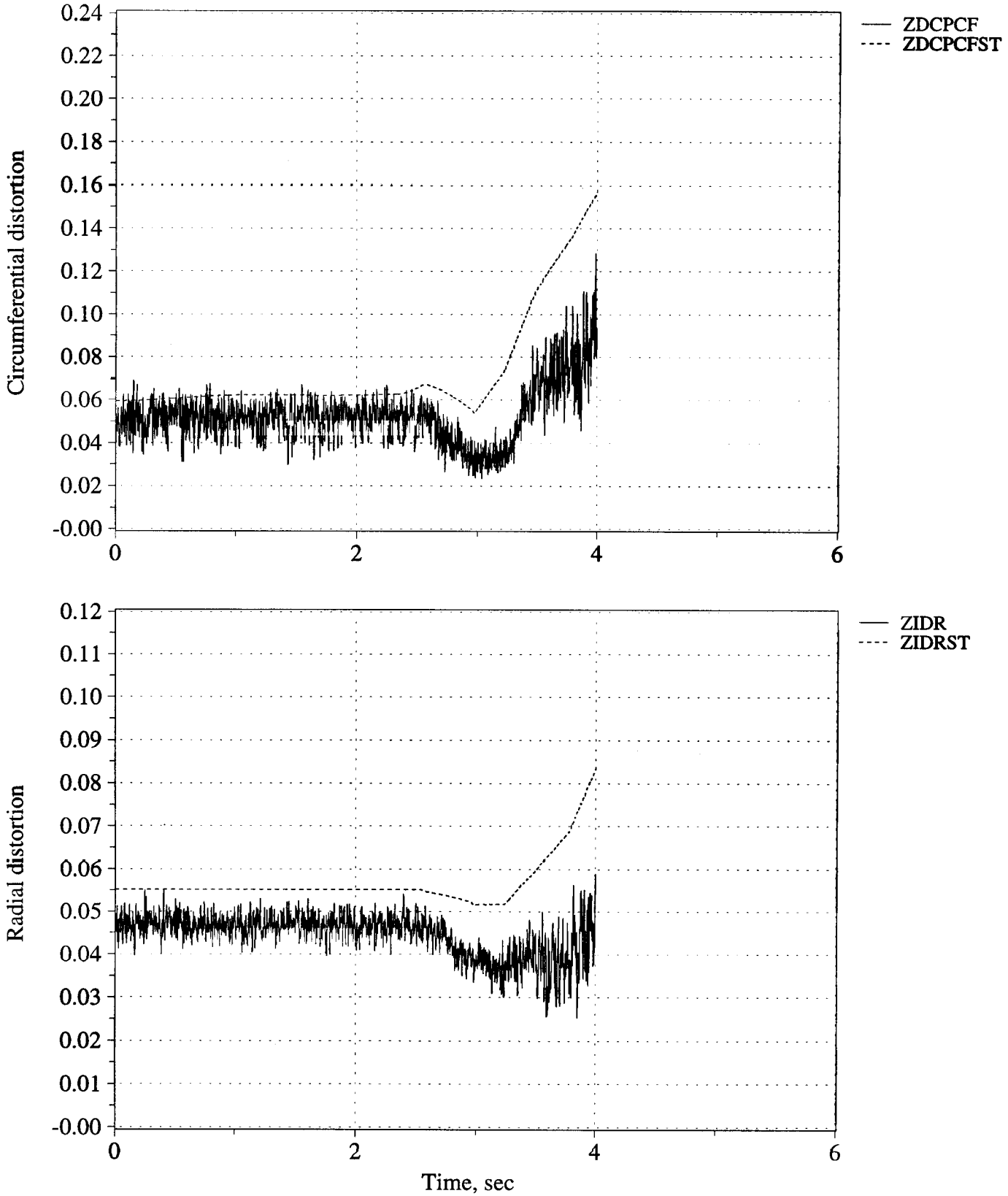

Figure C17. Time history of peak inlet dynamic circumferential and radial distortion (measured and estimated) - Flight 236, Test point 4b1.

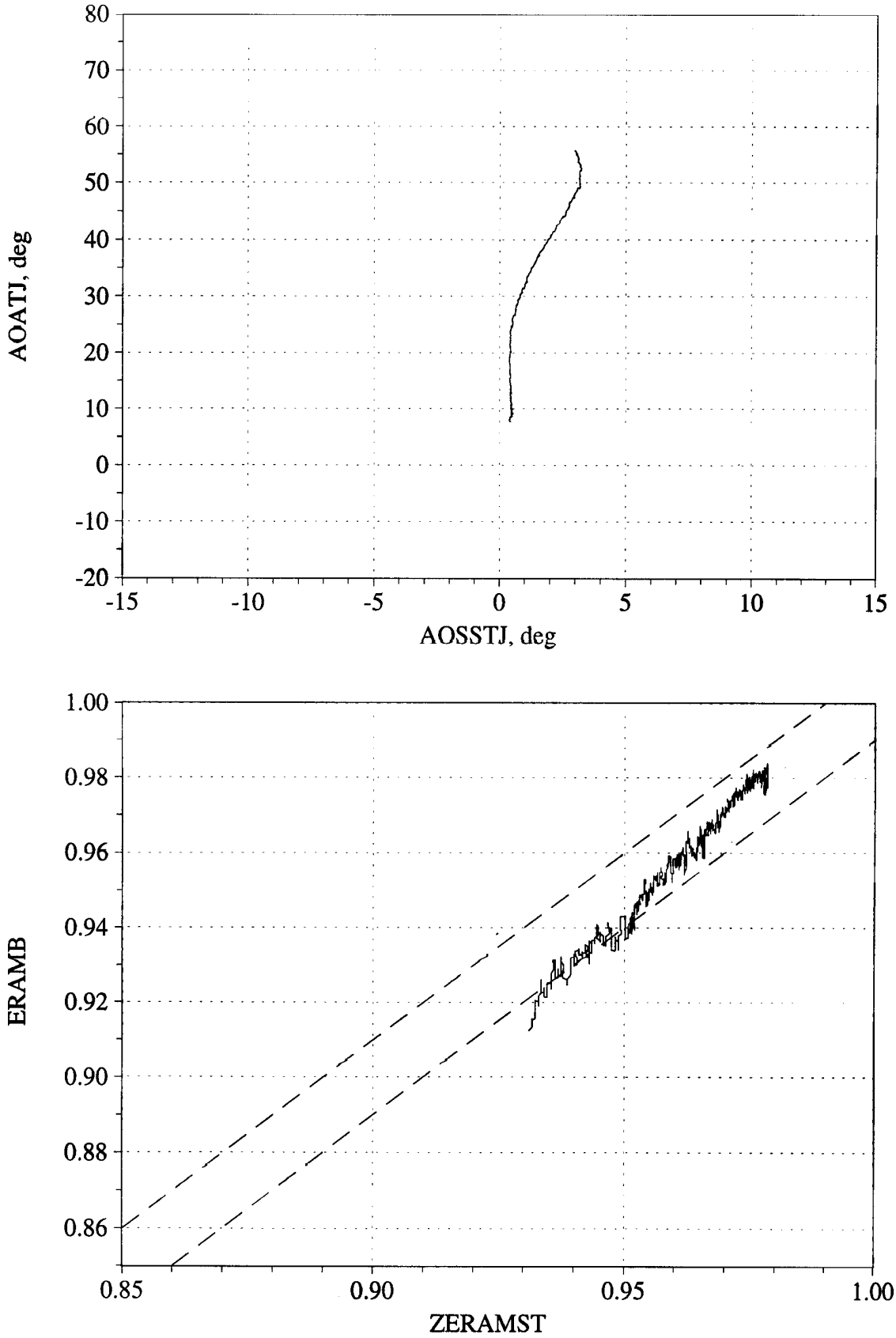

Figure C18. Angle of attack/angle of sideslip trajectory during maneuver; and measured versus estimated recovery - Flight 236, Test point 4b1.

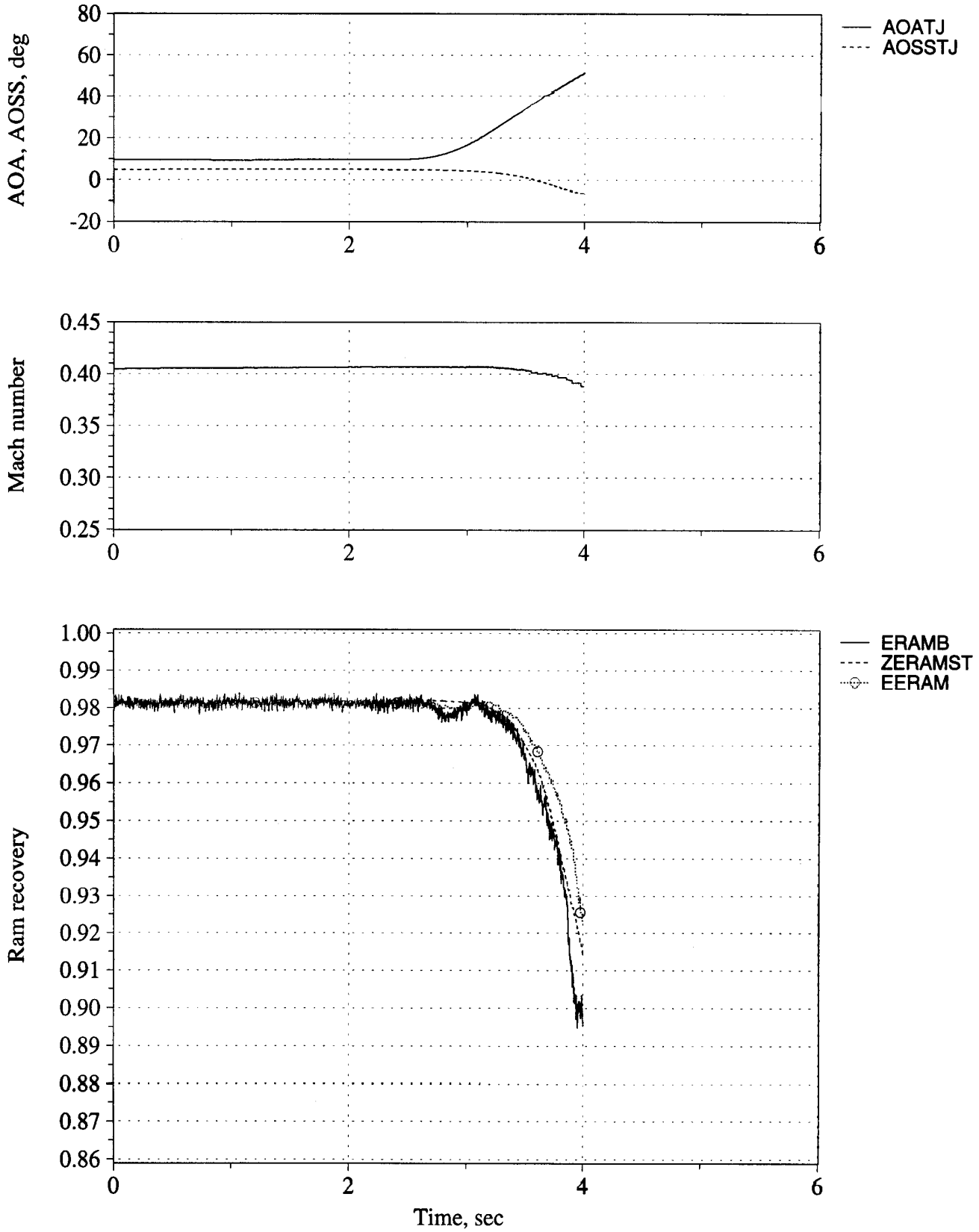

Figure C19. Time history of angle of attack, angle of sideslip, Mach number, and inlet recovery (measured and estimated) - Flight 236, Test point 4b2.

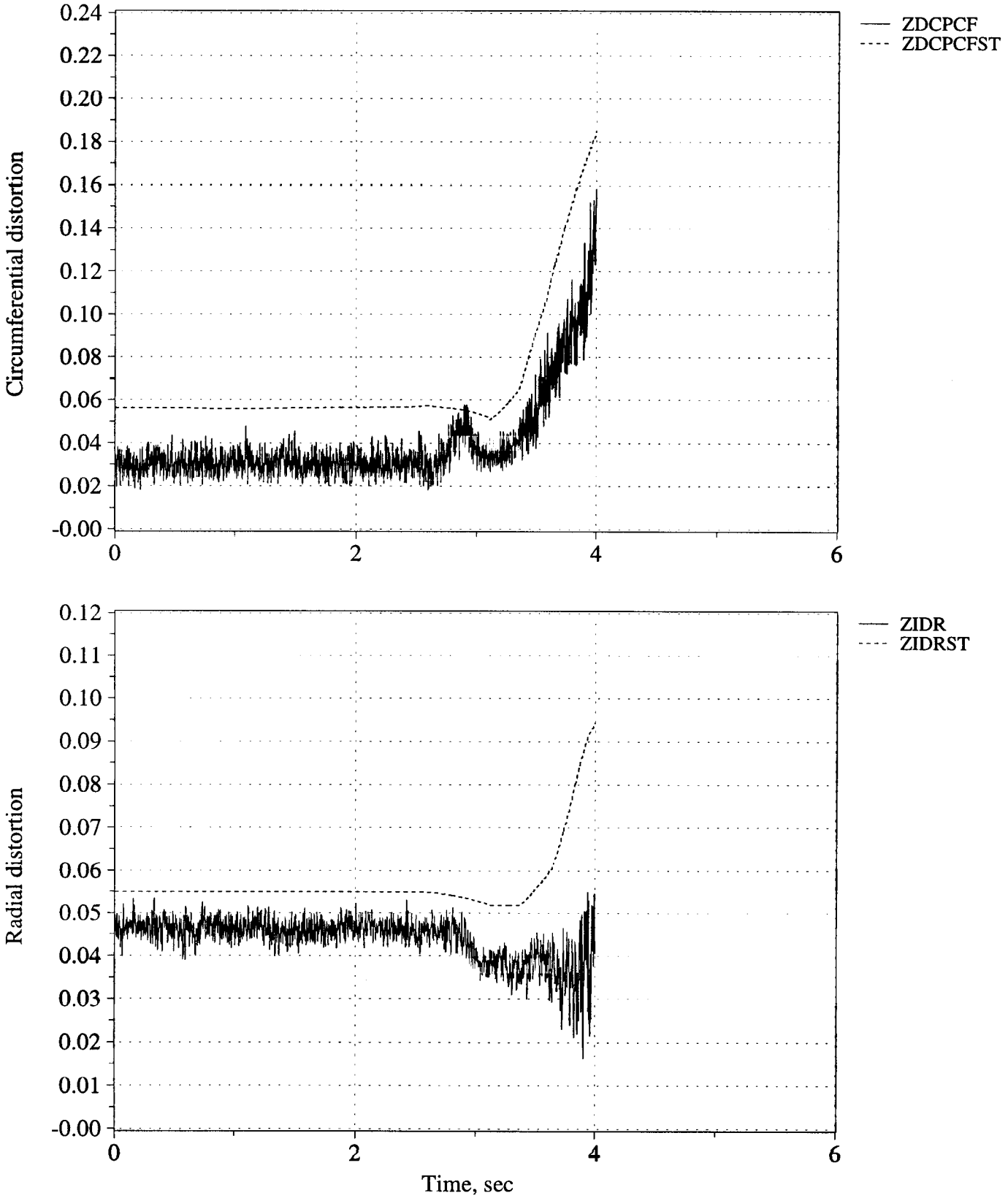

Figure C20. Time history of peak inlet dynamic circumferential and radial distortion (measured and estimated) - Flight 236, Test point 4b2.

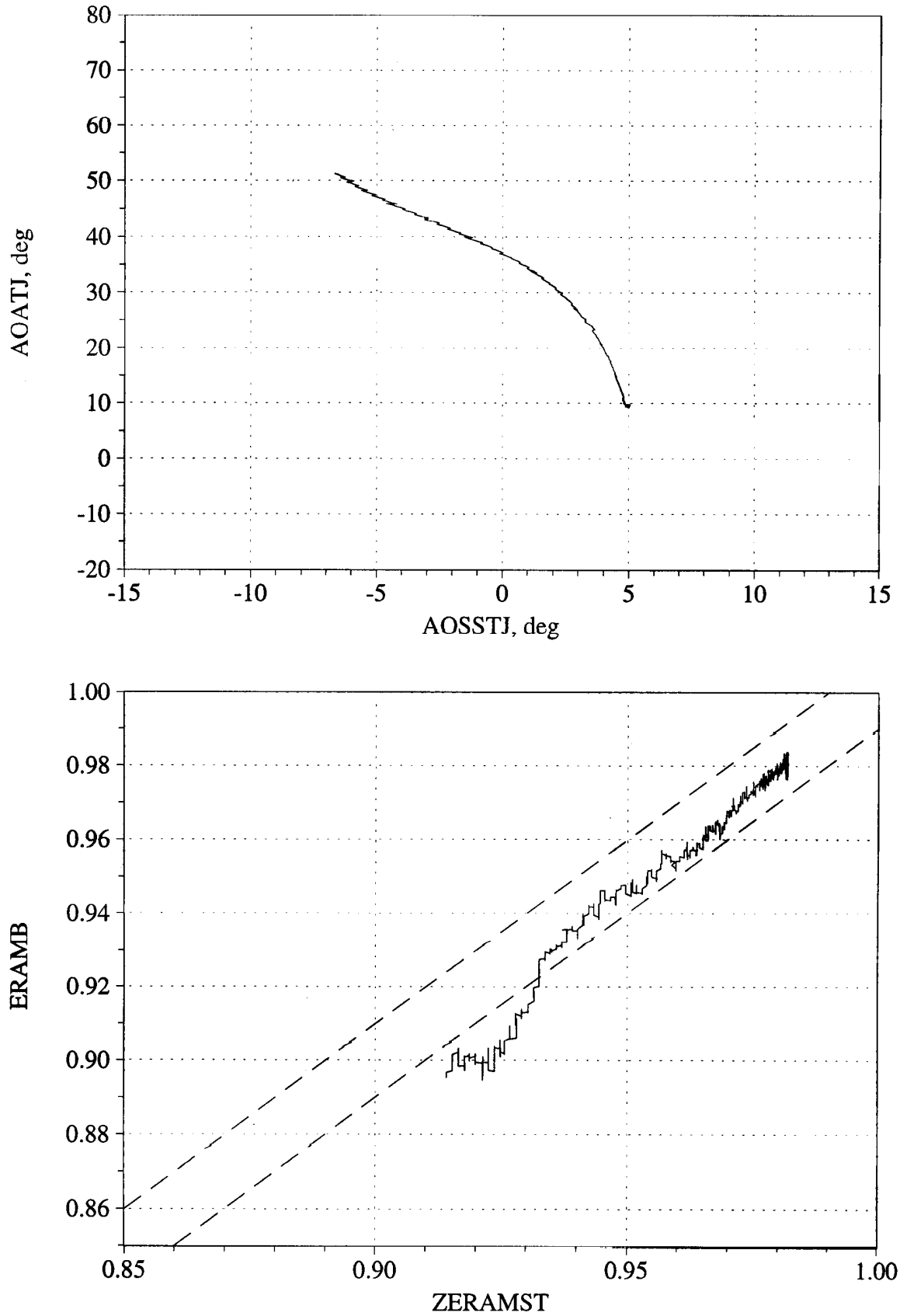

Figure C21. Angle of attack/angle of sideslip trajectory during maneuver; and measured versus estimated recovery - Flight 236, Test point 4b2.

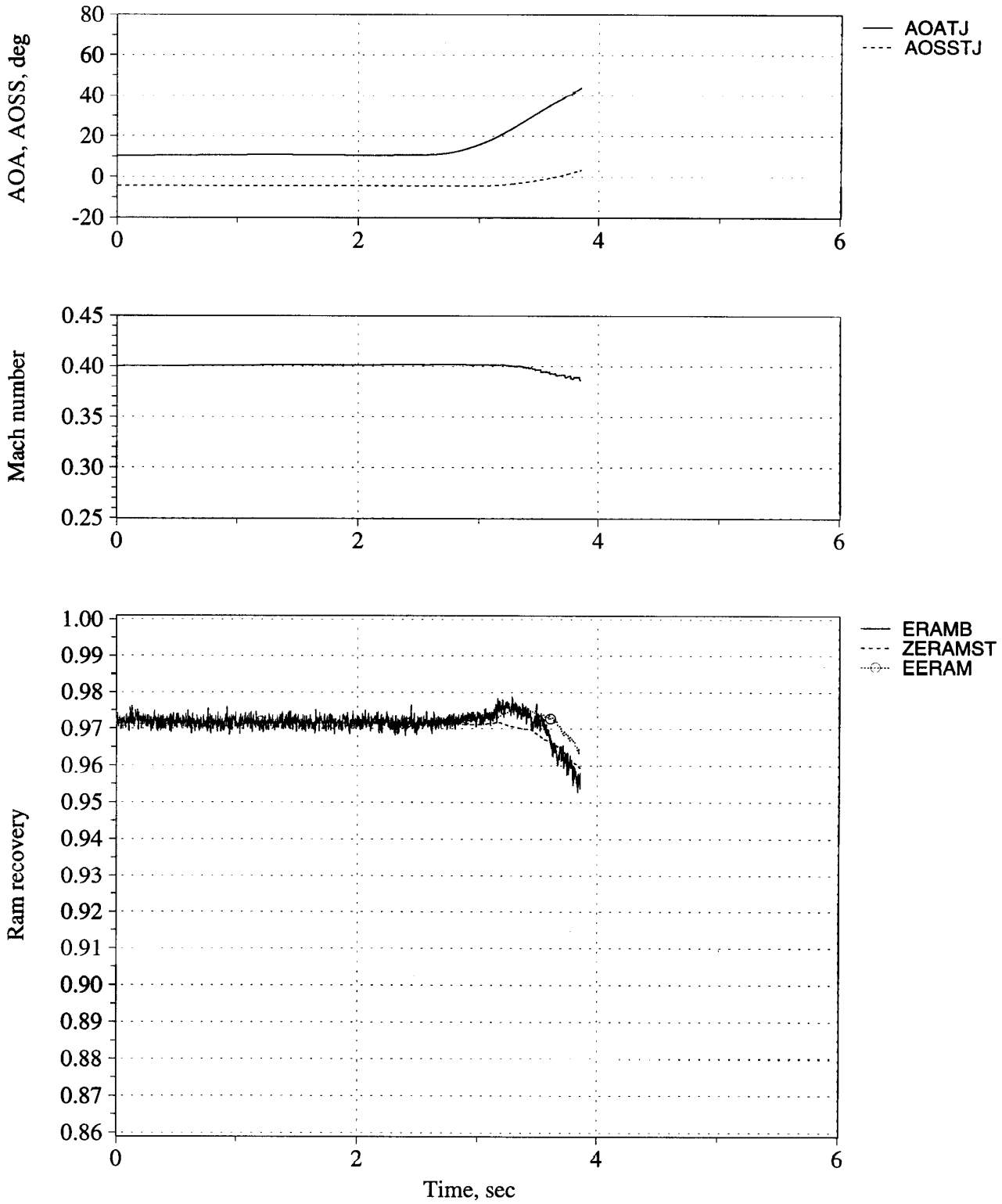

Figure C22. Time history of angle of attack, angle of sideslip, Mach number, and inlet recovery (measured and estimated) - Flight 236, Test point 24c.

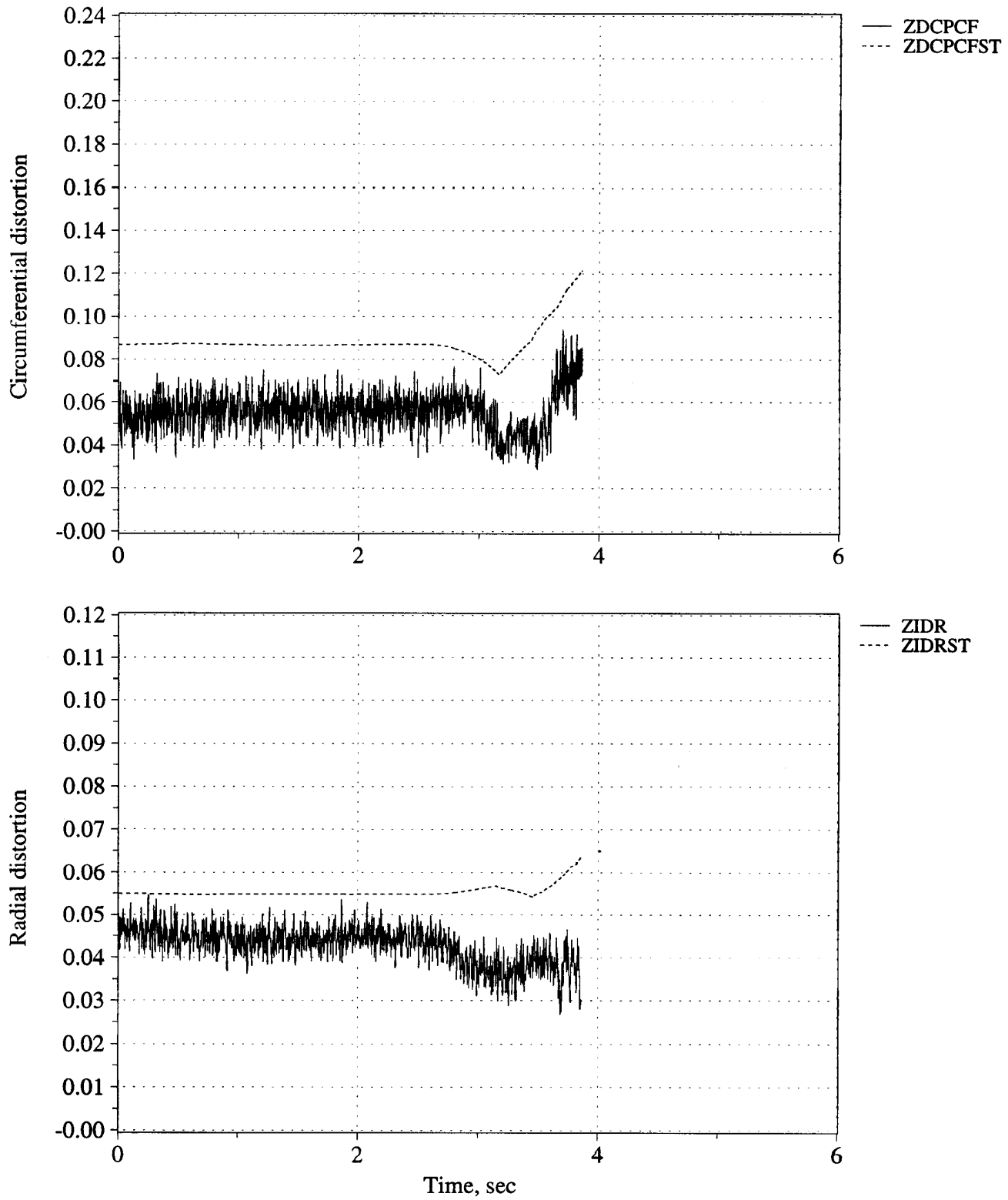

Figure C23. Time history of peak inlet dynamic circumferential and radial distortion (measured and estimated) - Flight 236, Test point 24c.

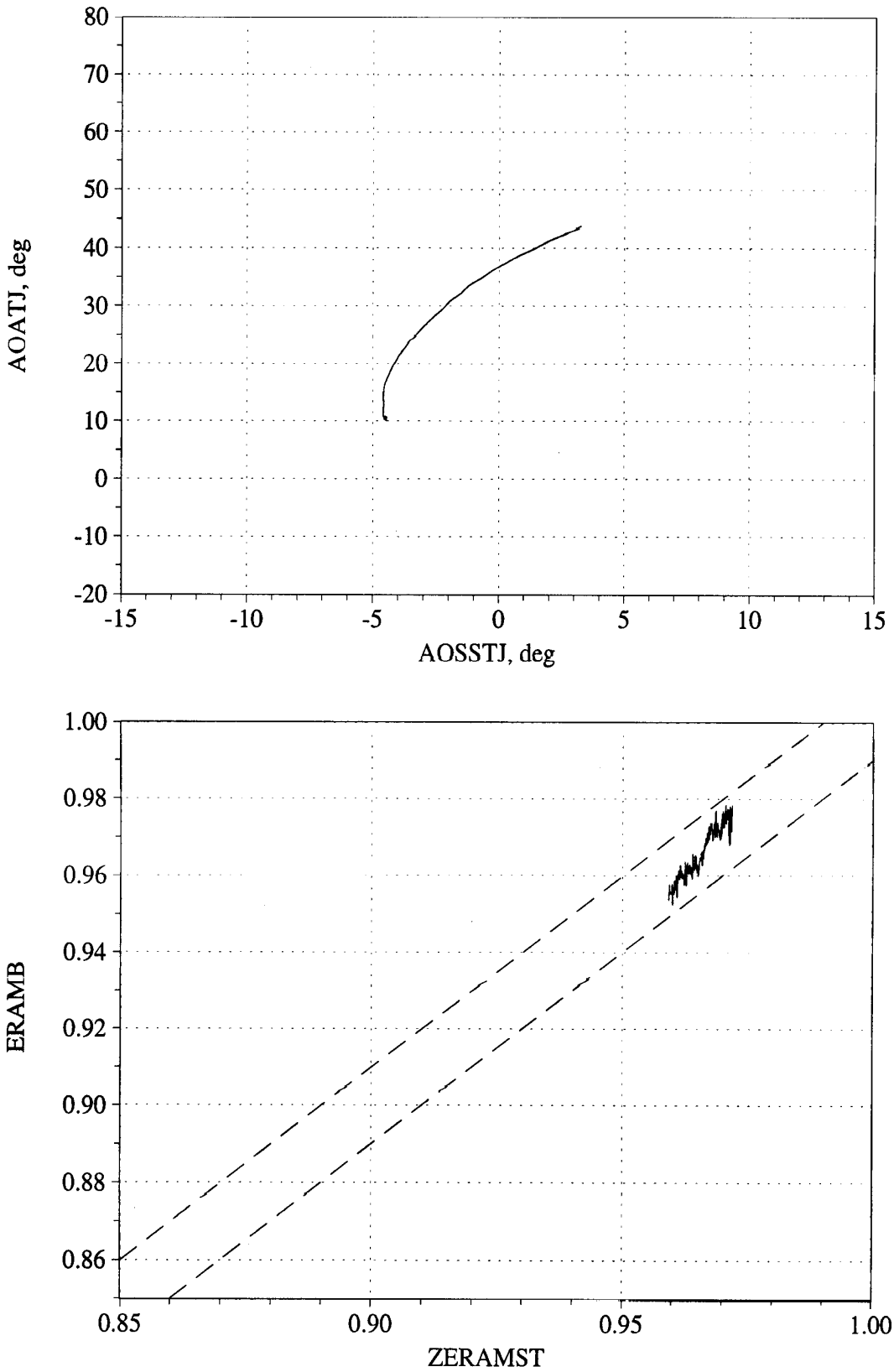

Figure C24. Angle of attack/angle of sideslip trajectory during maneuver; and measured versus estimated recovery - Flight 236, Test point 24c.

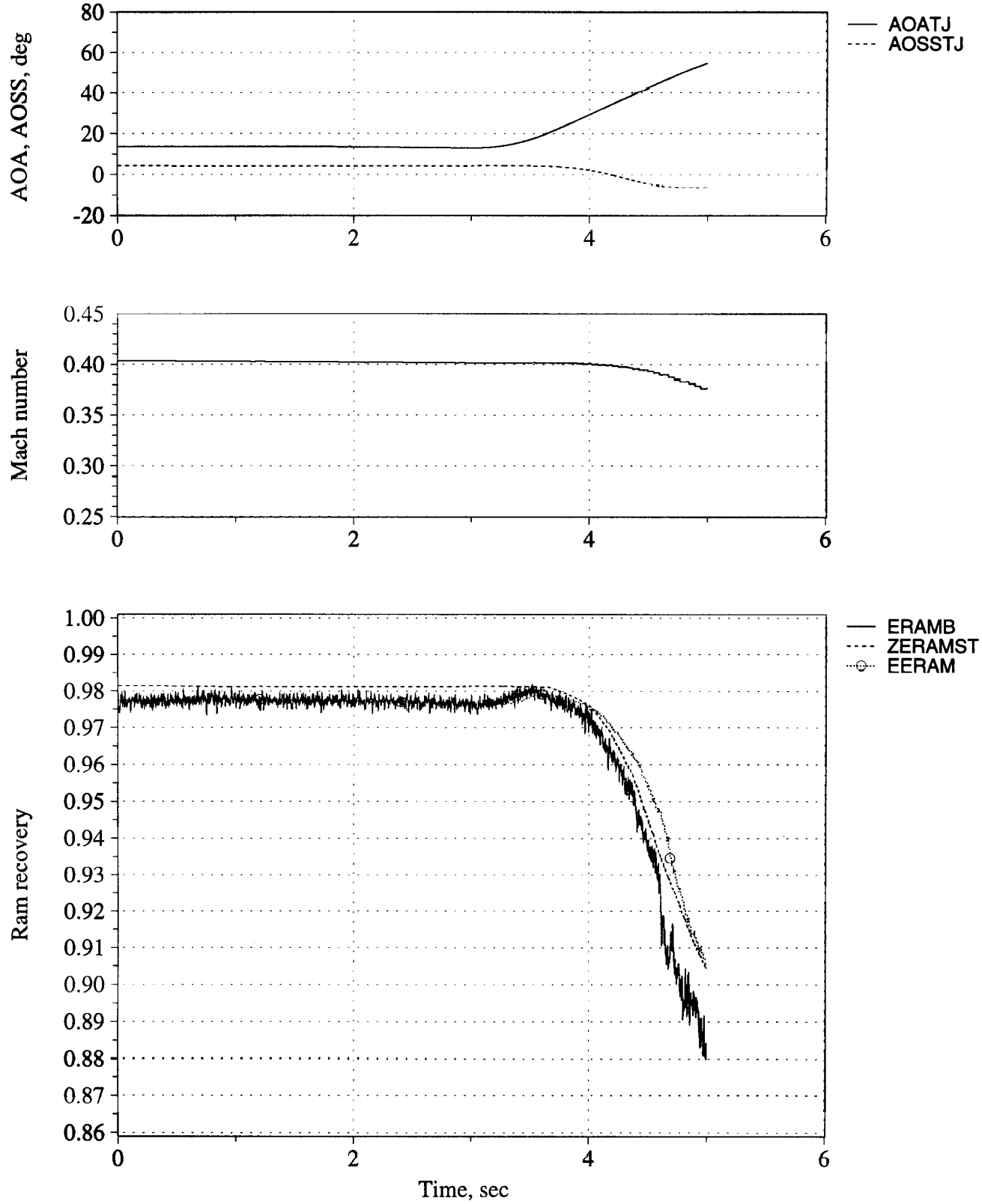

Figure C25. Time history of angle of attack, angle of sideslip, Mach number, and inlet recovery (measured and estimated) - Flight 242, Test point 21b.

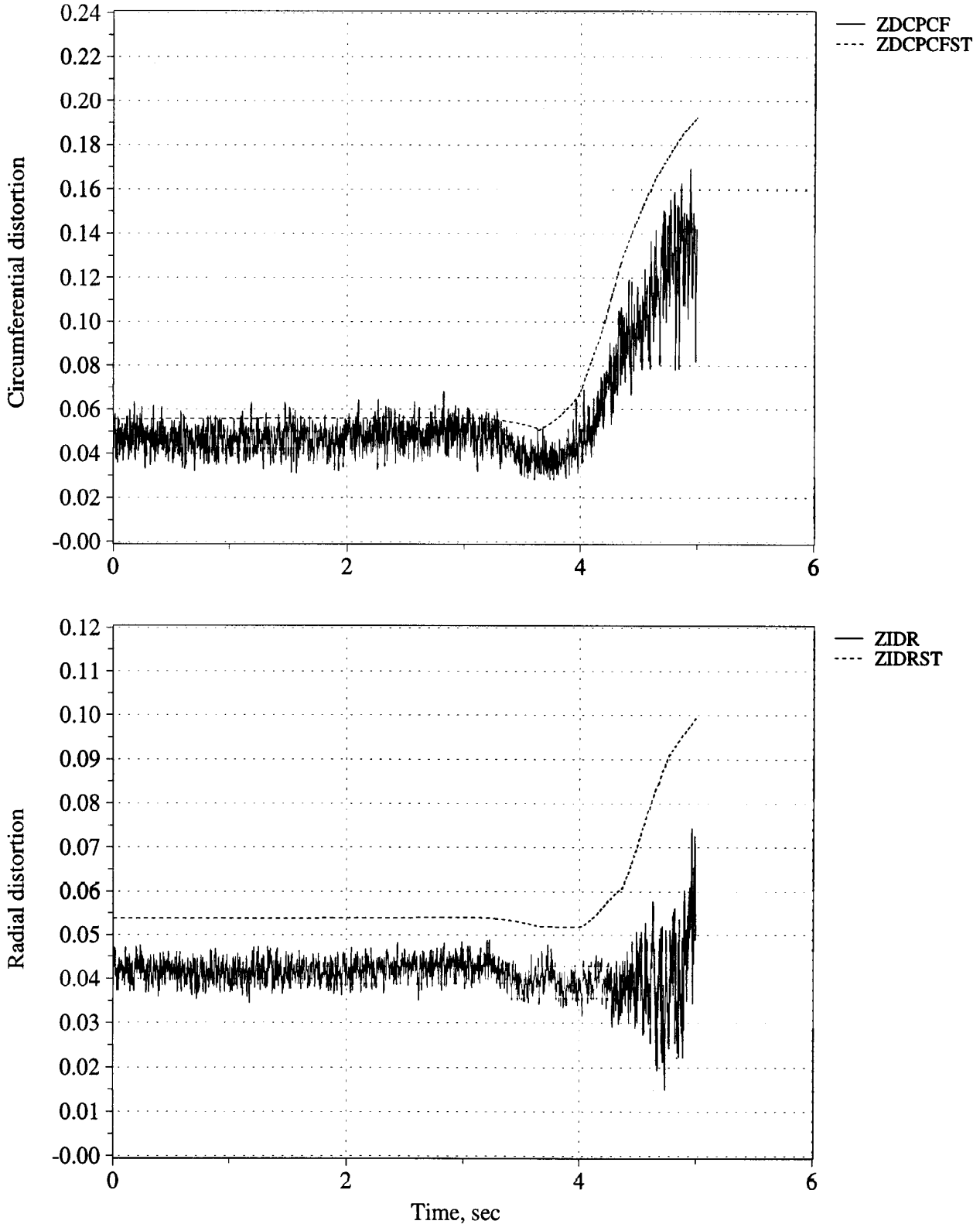

Figure C26. Time history of peak inlet dynamic circumferential and radial distortion (measured and estimated) - Flight 242, Test point 21b.

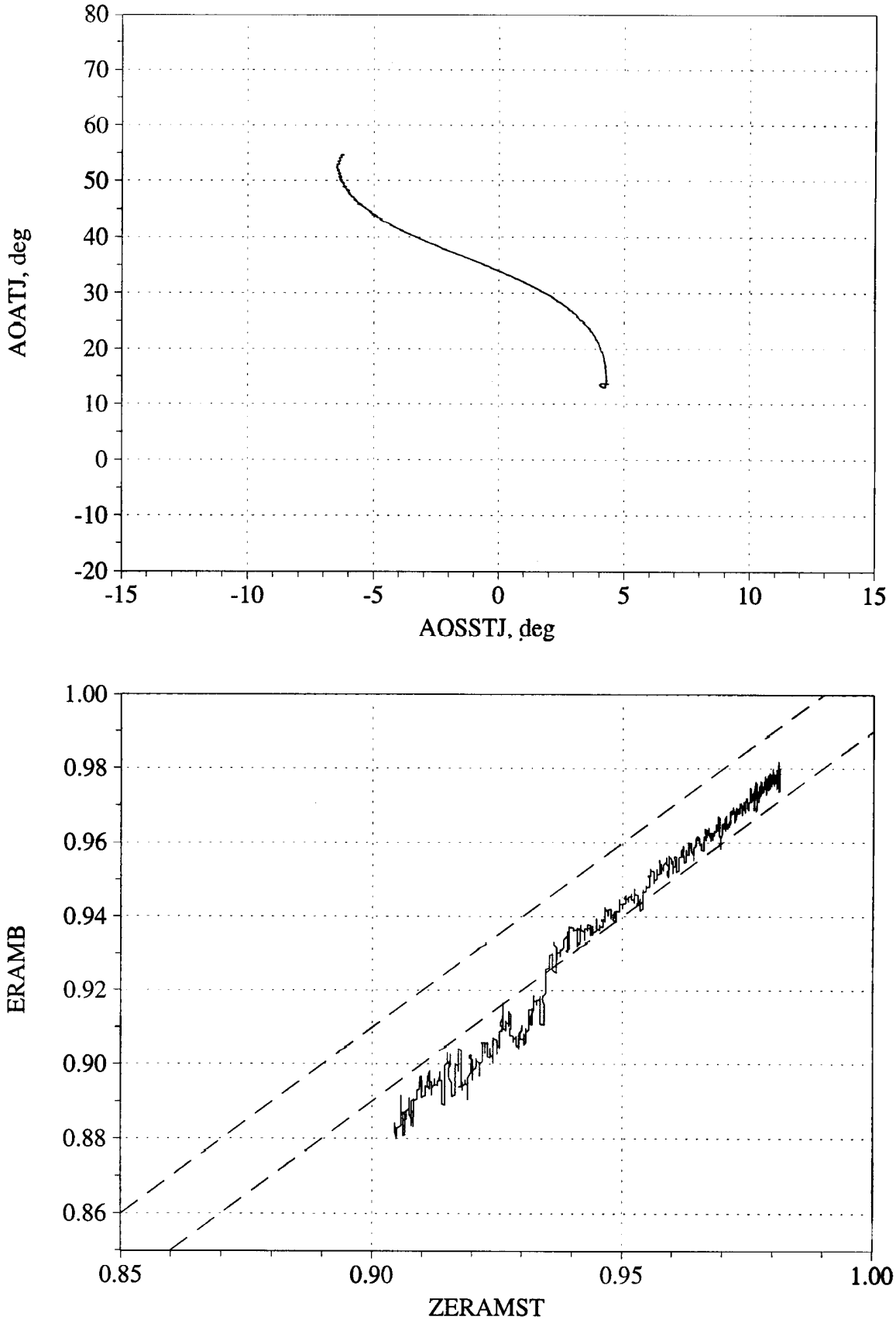

Figure C27. Angle of attack/angle of sideslip trajectory during maneuver; and measured versus estimated recovery - Flight 242, Test point 21b.

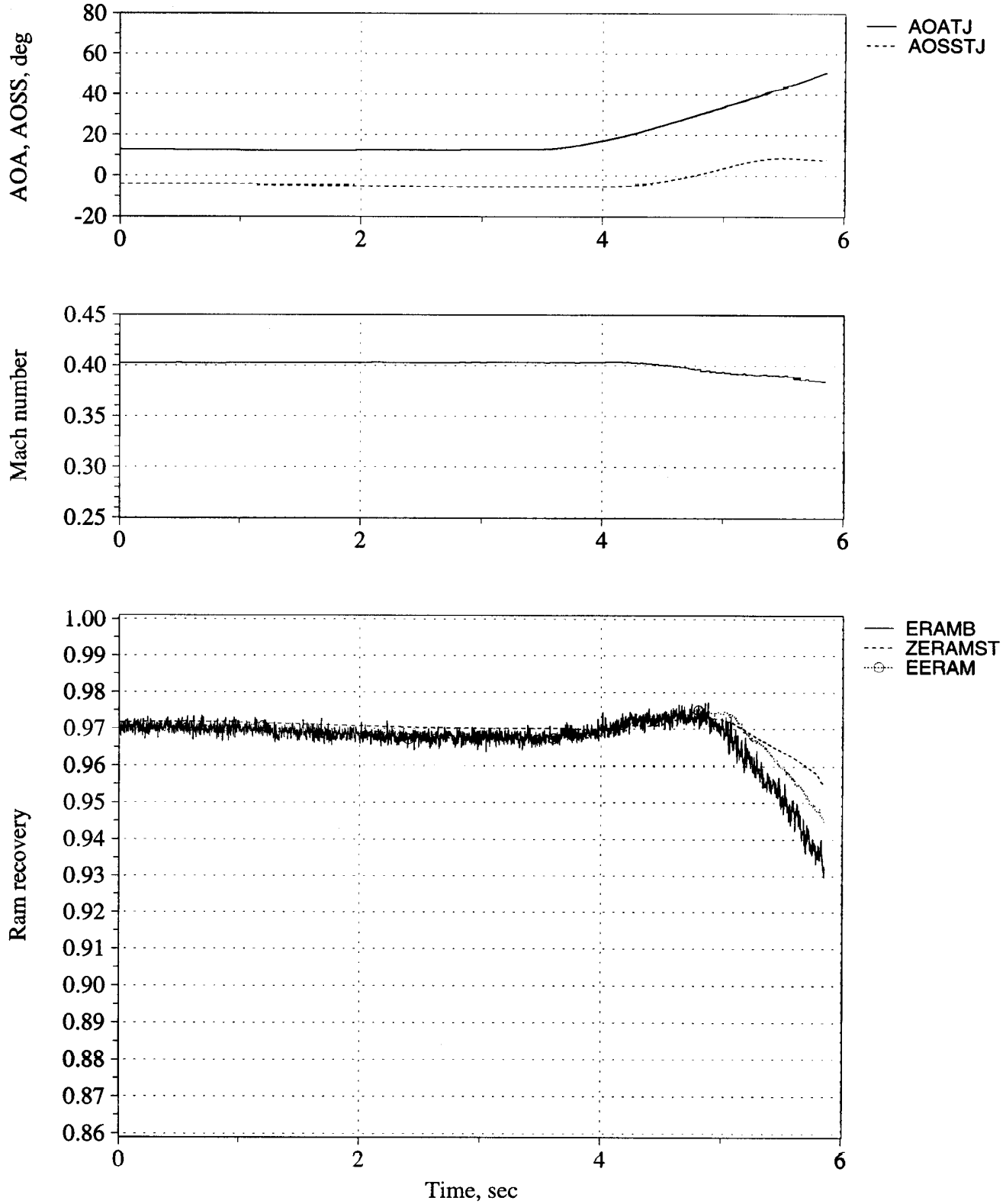

Figure C28. Time history of angle of attack, angle of sideslip, Mach number, and inlet recovery (measured and estimated) - Flight 242, Test point 21c.

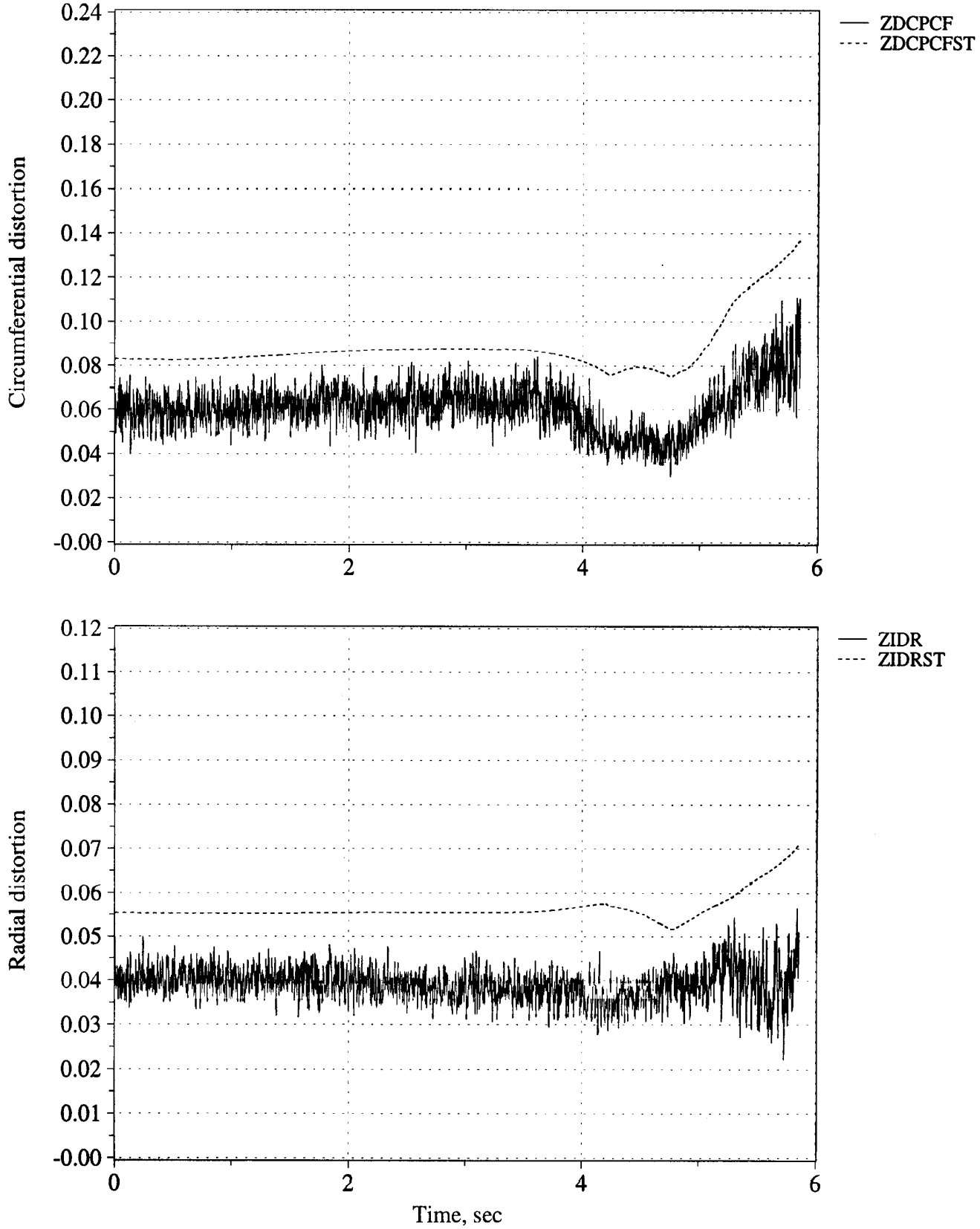

Figure C29. Time history of peak inlet dynamic circumferential and radial distortion (measured and estimated) - Flight 242, Test point 21c.

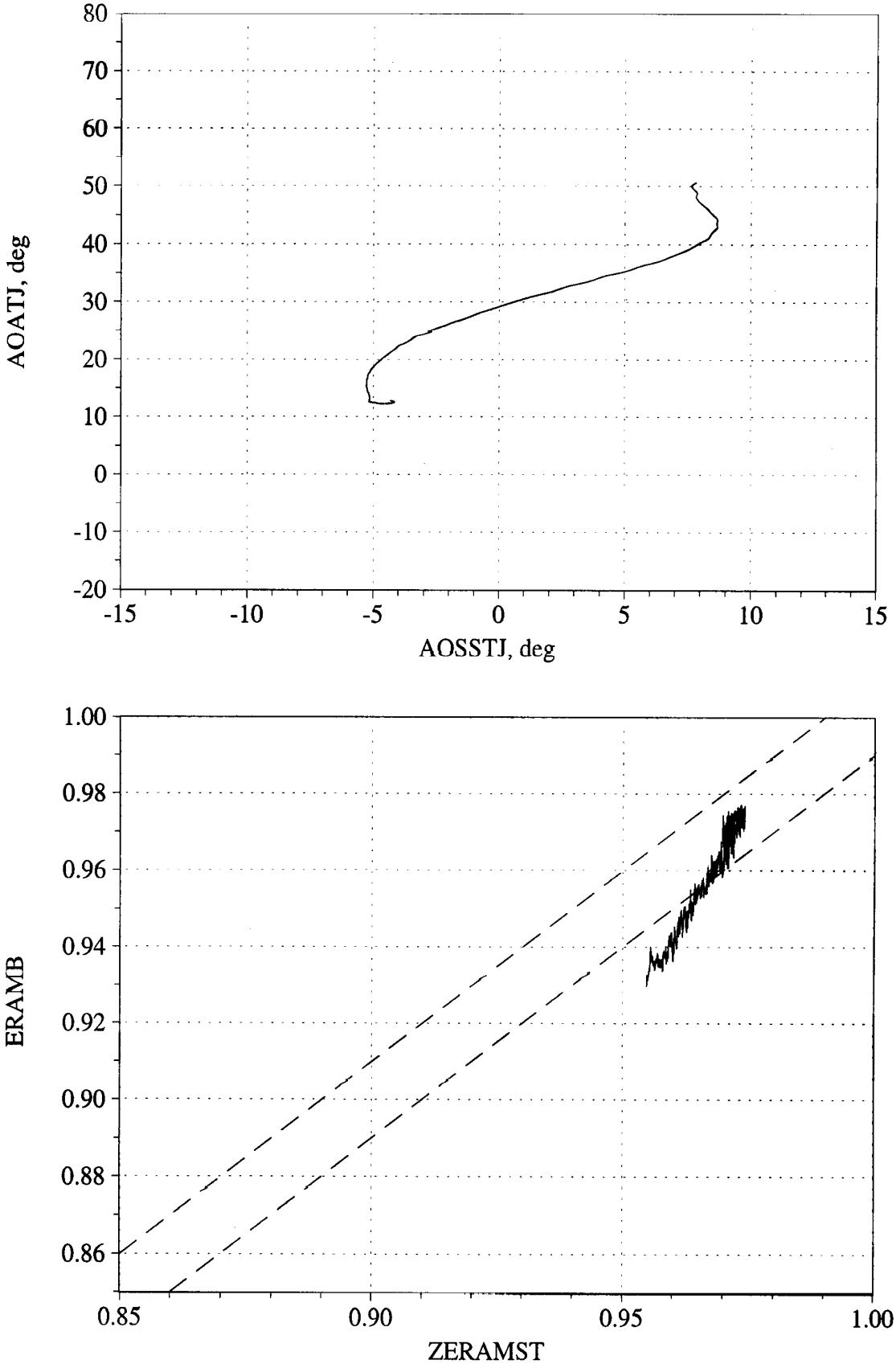

Figure C30. Angle of attack/angle of sideslip trajectory during maneuver; and measured versus estimated recovery - Flight 242, Test point 21c.

- High-to-Low Angle of Attack -

Figures C31 - C33, Flight 233, Test Point 4c1
Figures C34 - C36, Flight 235, Test Point 09b
Figures C37 - C39, Flight 235, Test Point 9b1
Figures C40 - C41, Flight 245, Test Point 03b
Figures C43 - C45, Flight 245, Test Point 03c
Figures C46 - C48, Flight 245, Test Point 04b
Figures C49 - C51, Flight 245, Test Point 04c

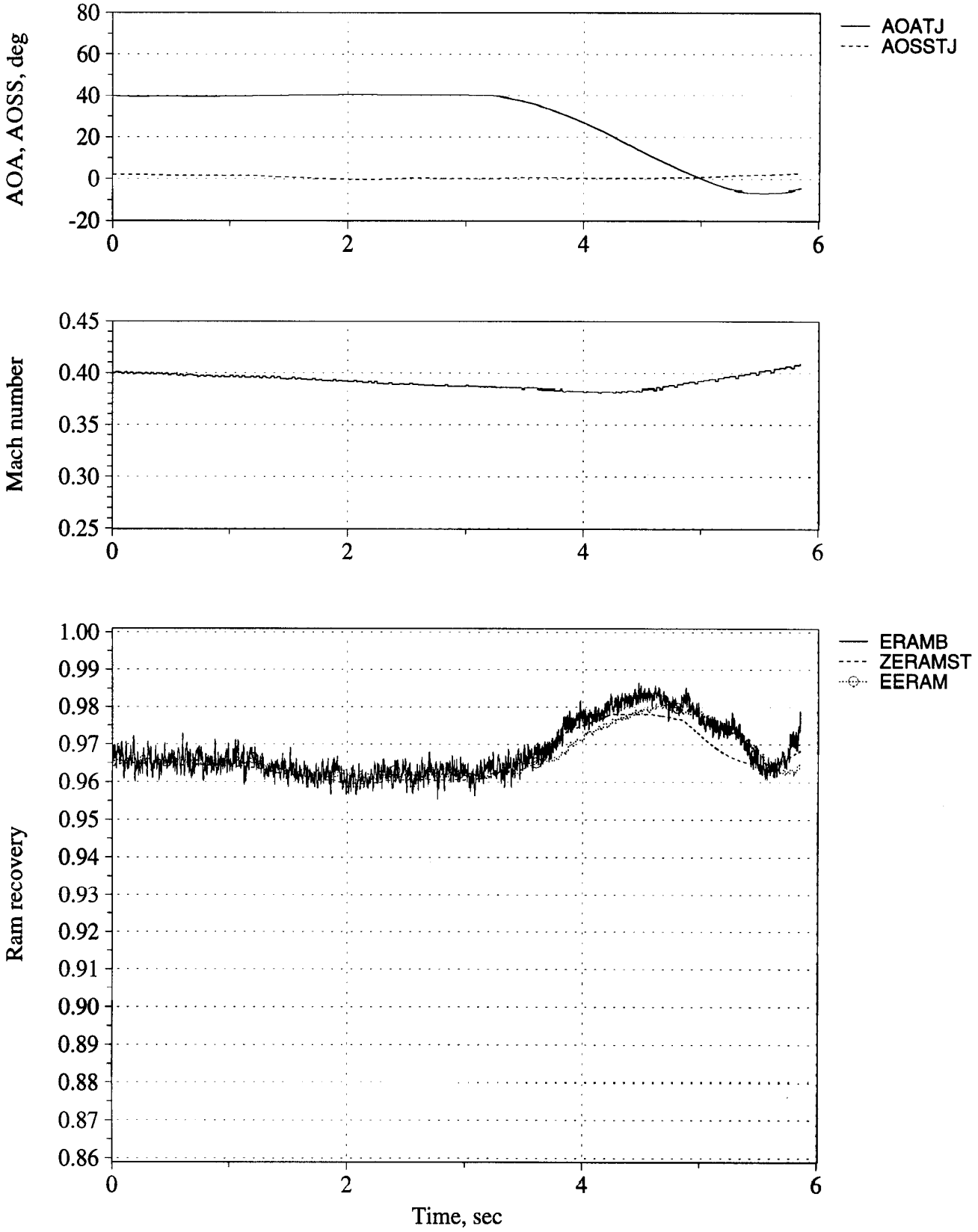

Figure C31. Time history of angle of attack, angle of sideslip, Mach number, and inlet recovery (measured and estimated) - Flight 233, Test point 4c1.

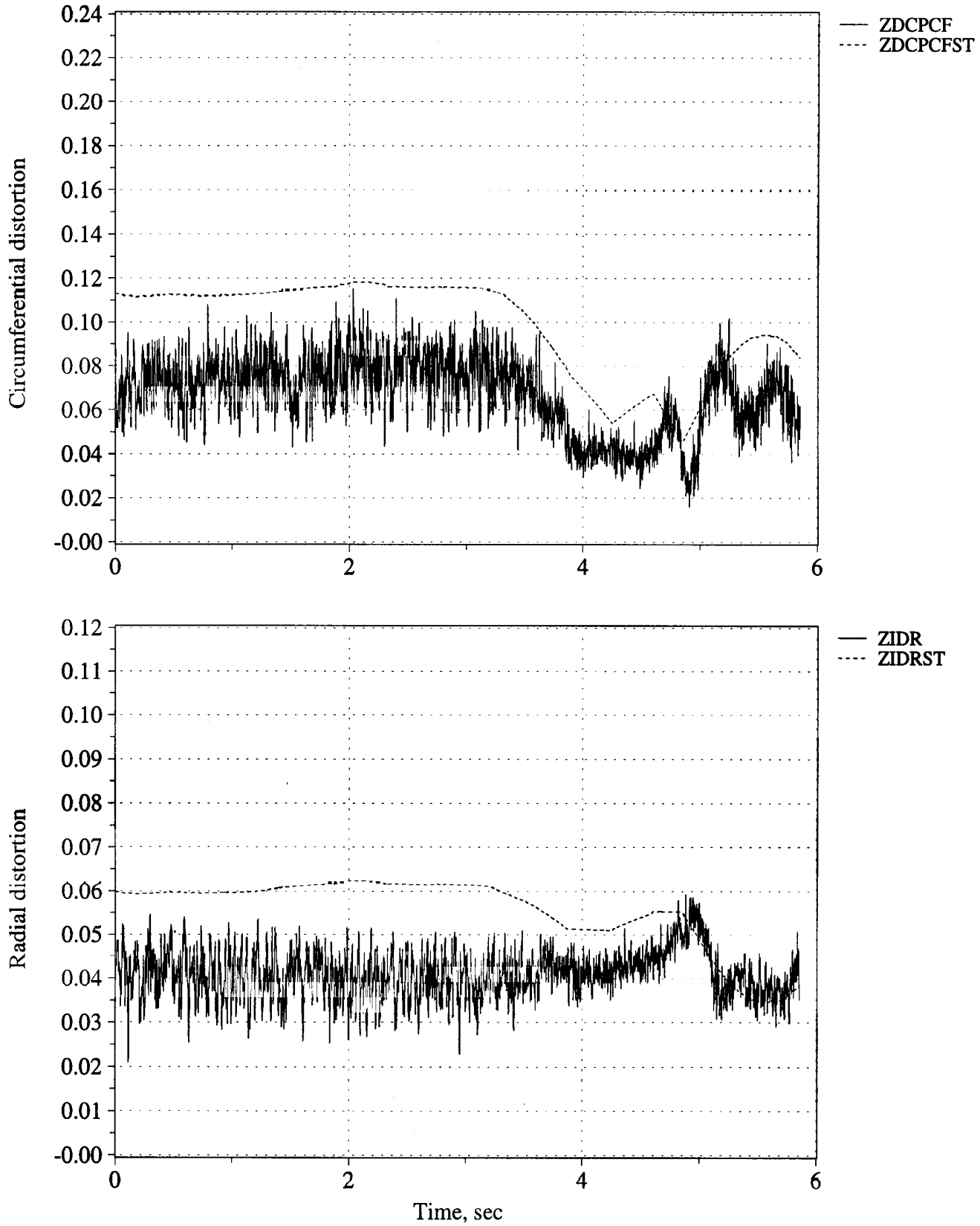

Figure C32. Time history of peak inlet dynamic circumferential and radial distortion (measured and estimated) - Flight 233, Test point 4c1.

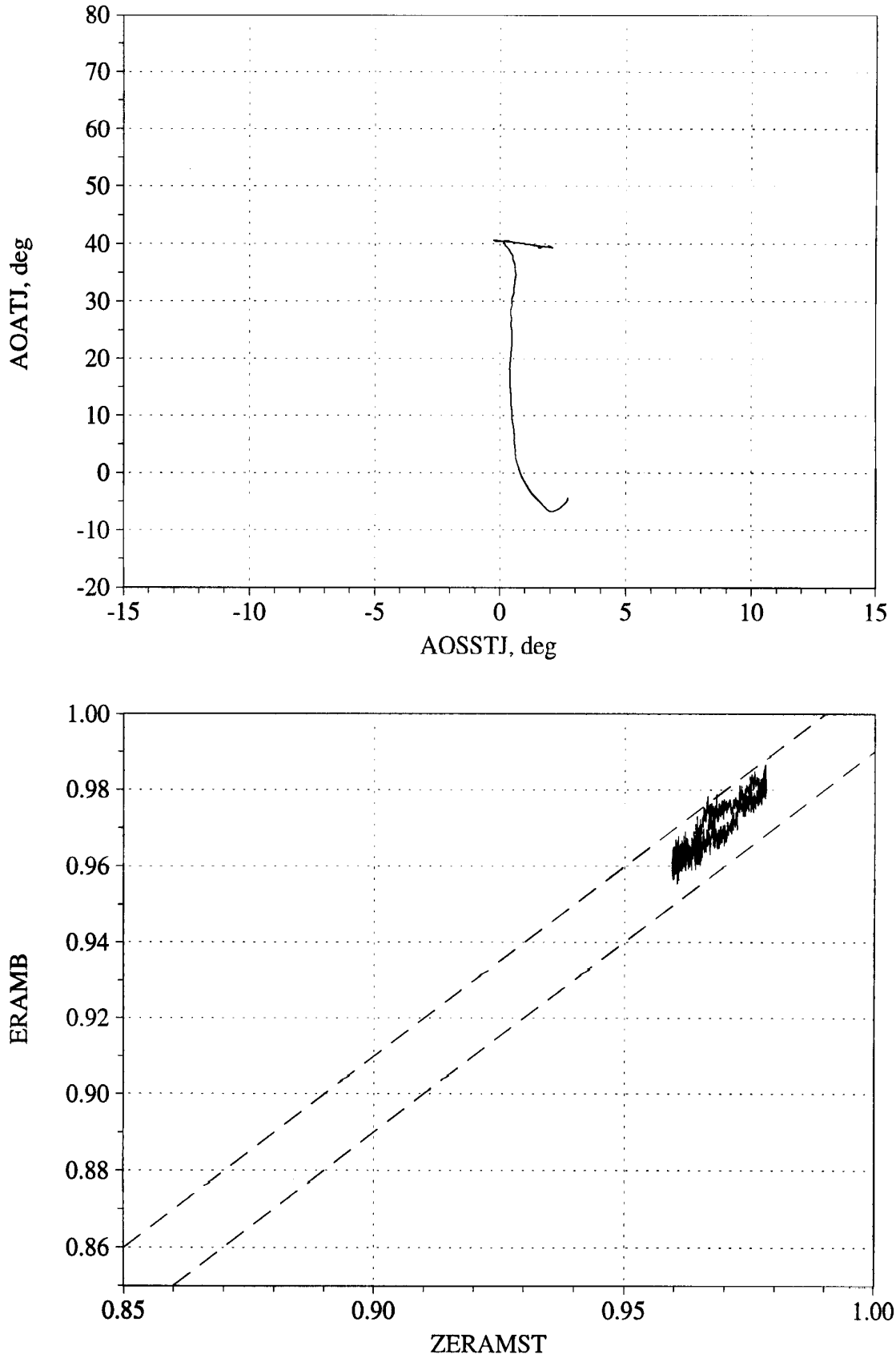

Figure C33. Angle of attack/angle of sideslip trajectory during maneuver; and measured versus estimated recovery - Flight 233, Test point 4c1.

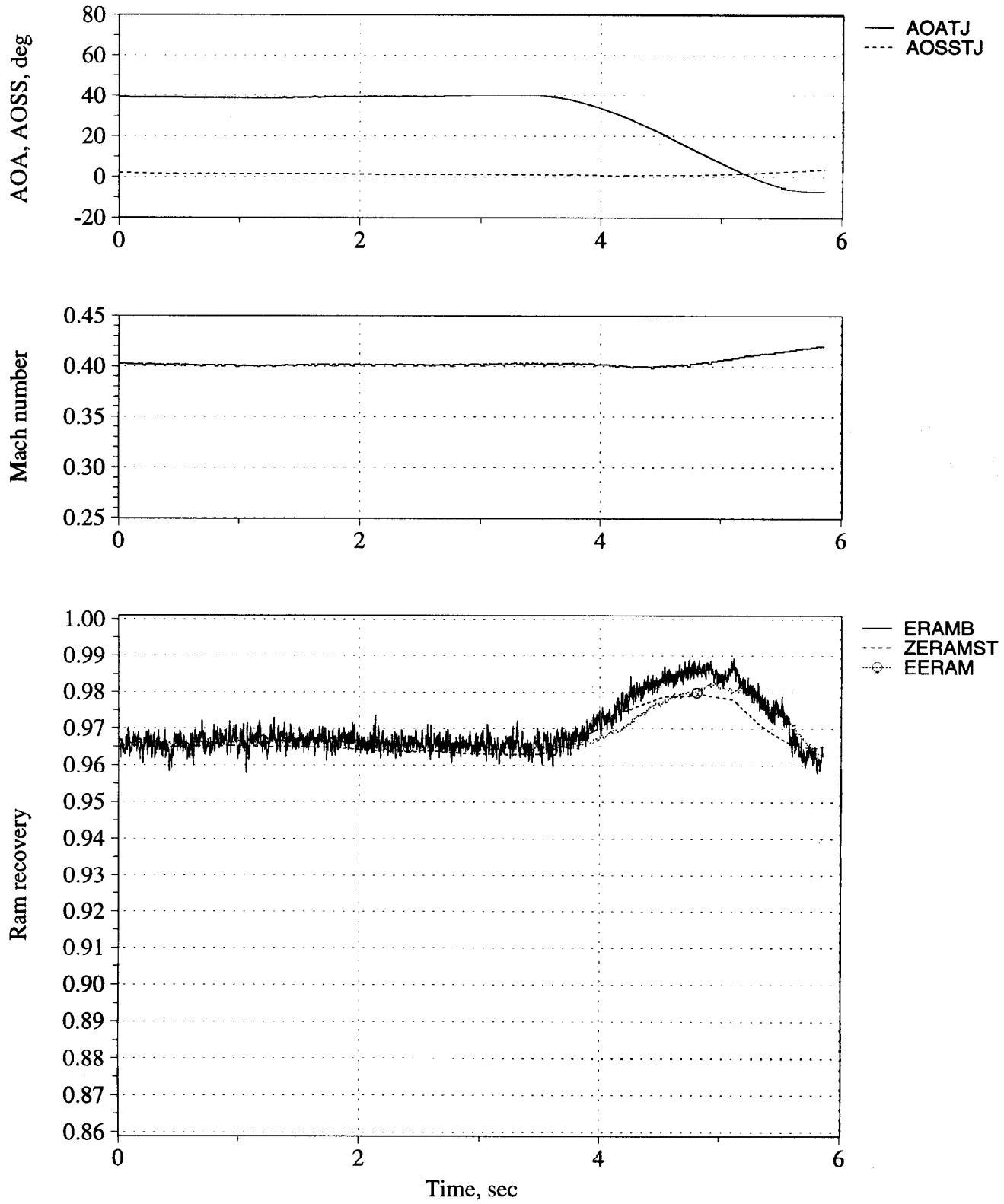

Figure C34. Time history of angle of attack, angle of sideslip, Mach number, and inlet recovery (measured and estimated) - Flight 235, Test point 09b.

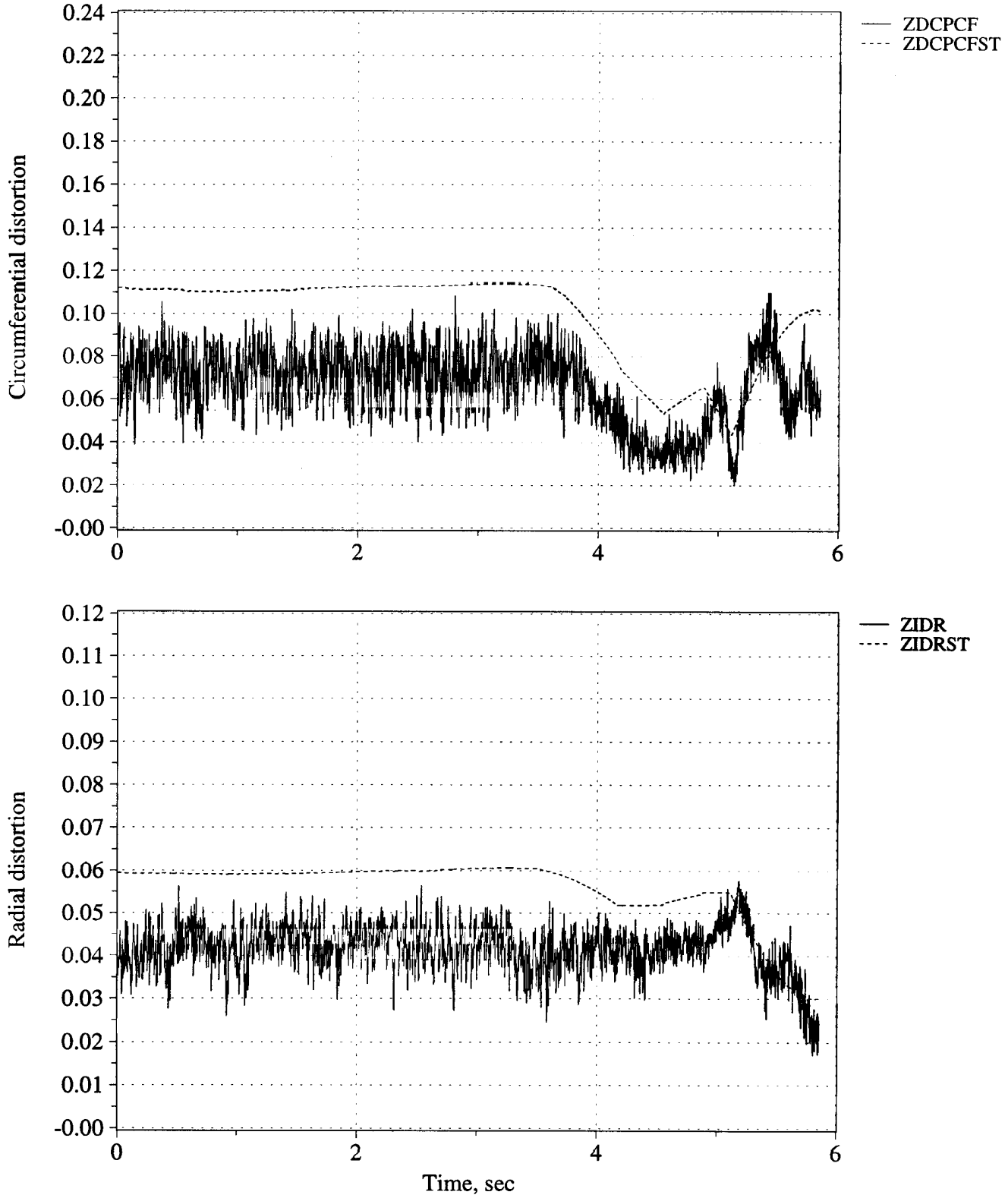

Figure C35. Time history of peak inlet dynamic circumferential and radial distortion (measured and estimated) - Flight 235, Test point 09b.

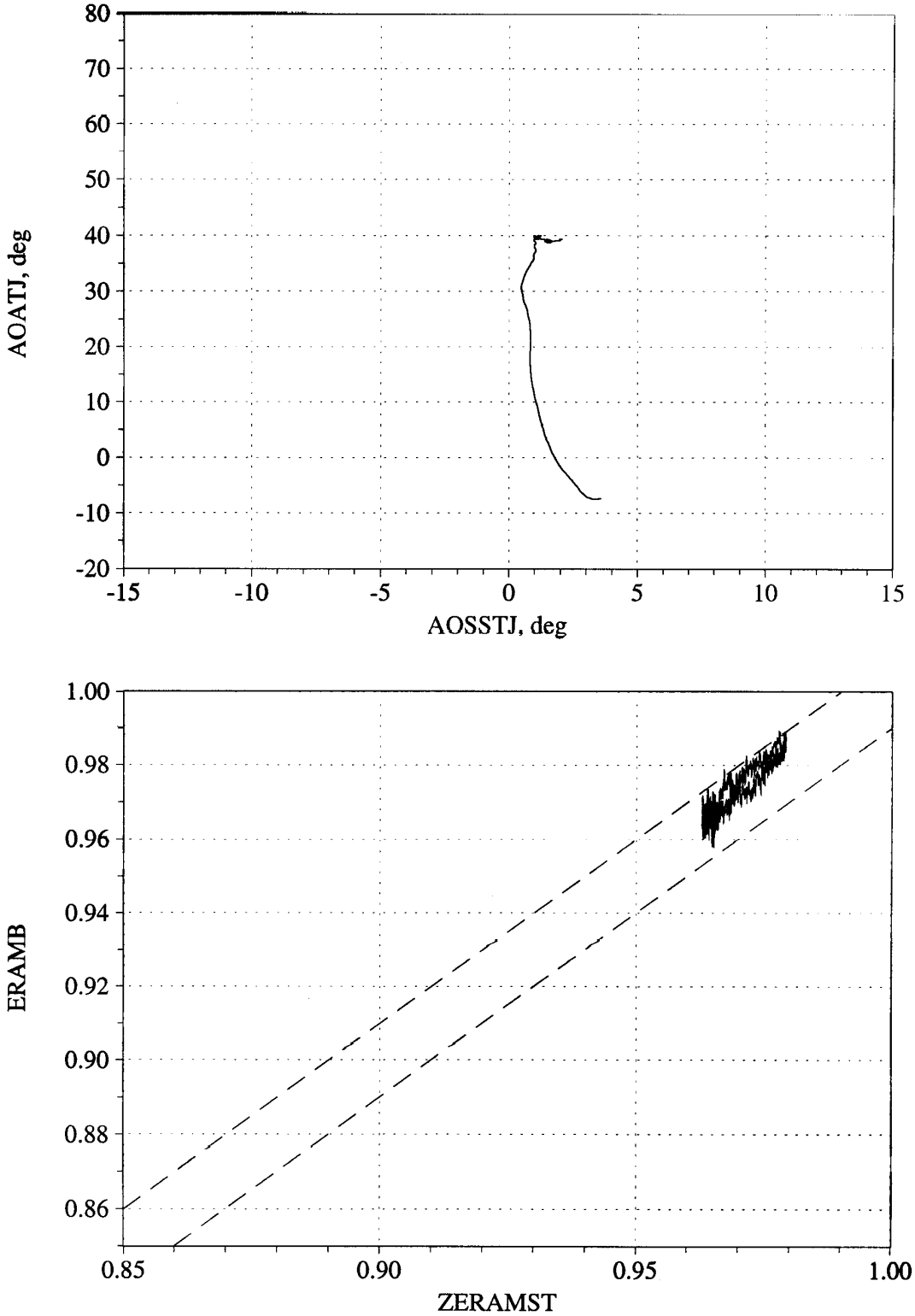

Figure C36. Angle of attack/angle of sideslip trajectory during maneuver; and measured versus estimated recovery - Flight 235, Test point 09b.

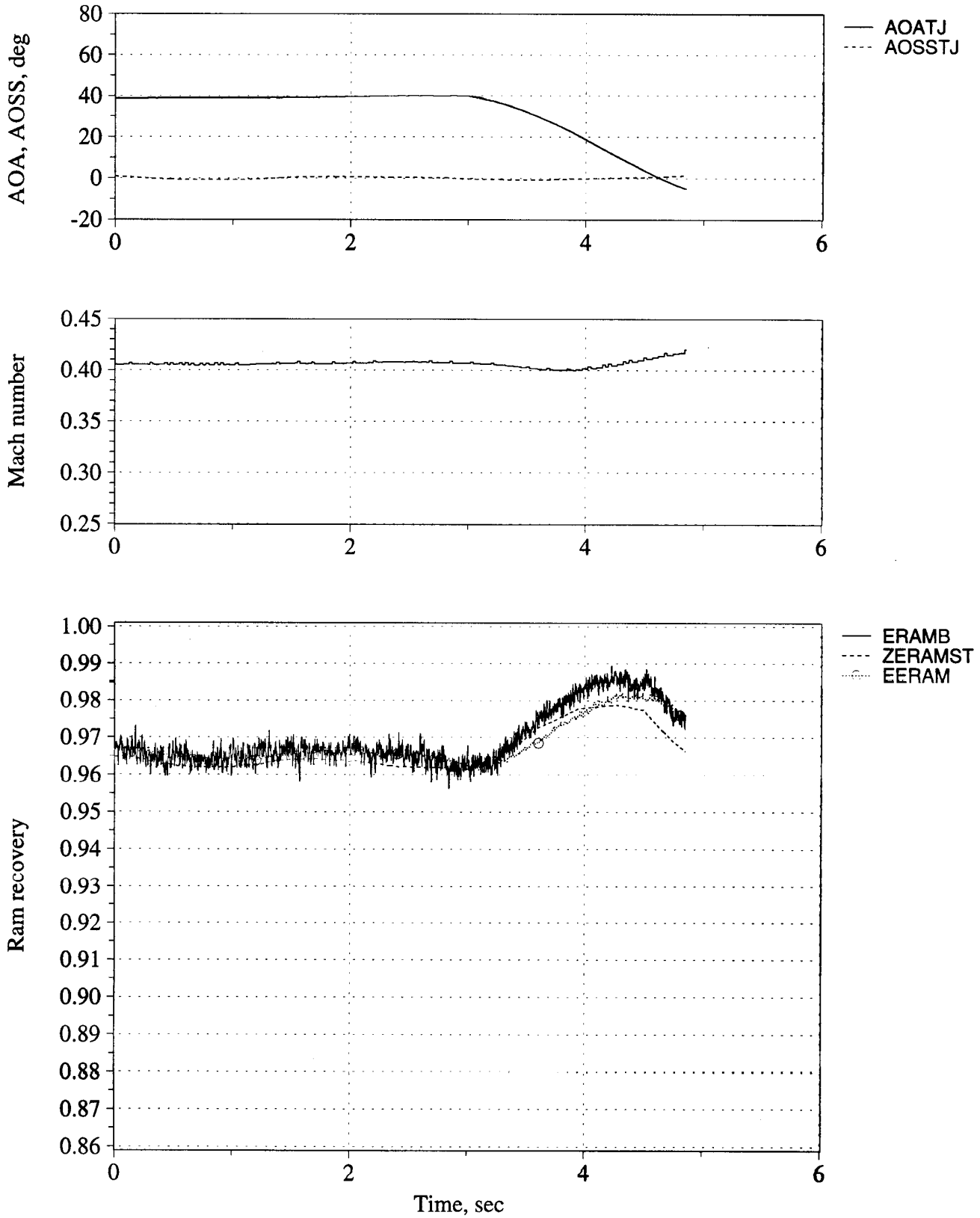

Figure C37. Time history of angle of attack, angle of sideslip, Mach number, and inlet recovery (measured and estimated) - Flight 235, Test point 9b1.

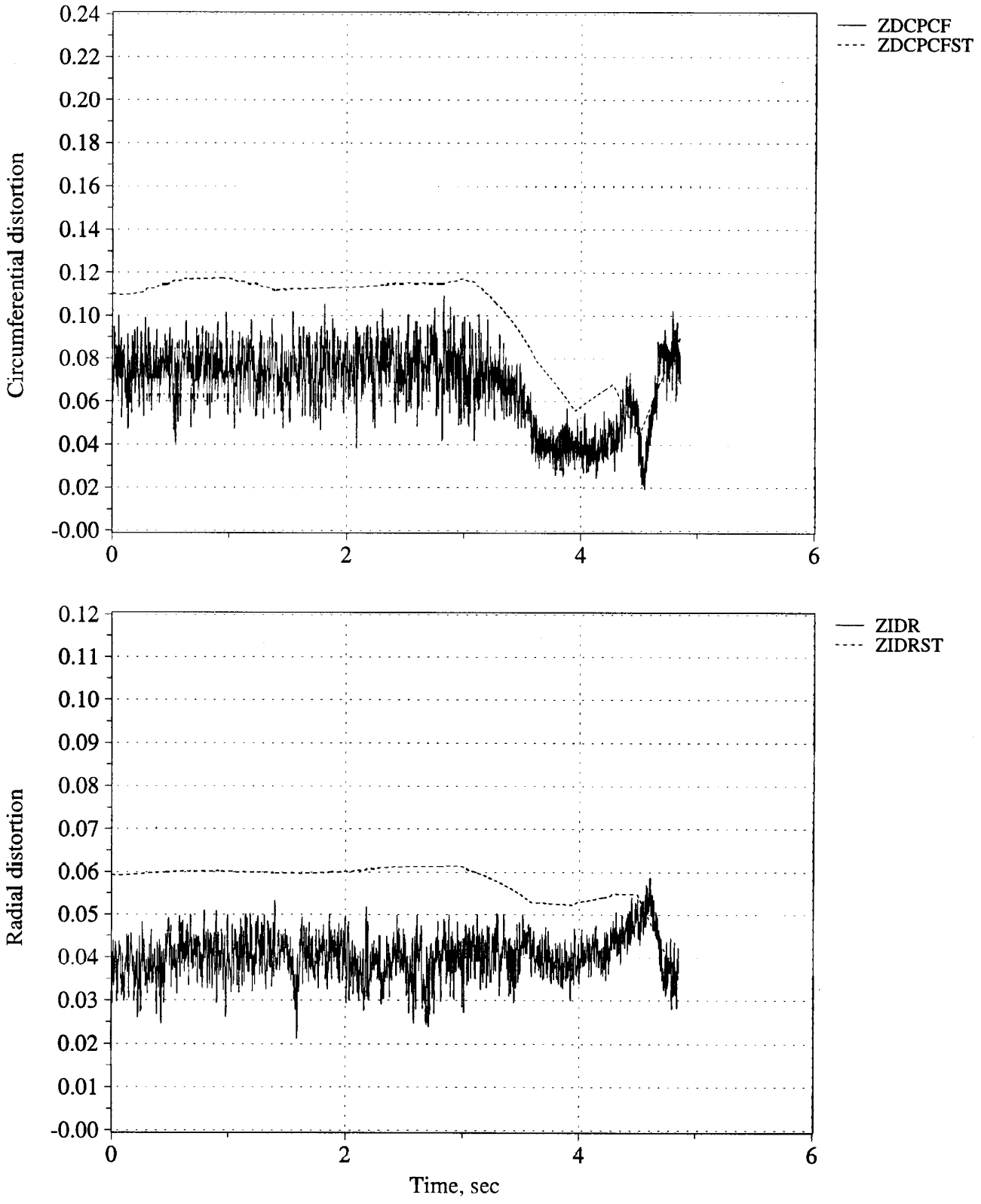

Figure C38. Time history of peak inlet dynamic circumferential and radial distortion (measured and estimated) - Flight 235, Test point 9b1.

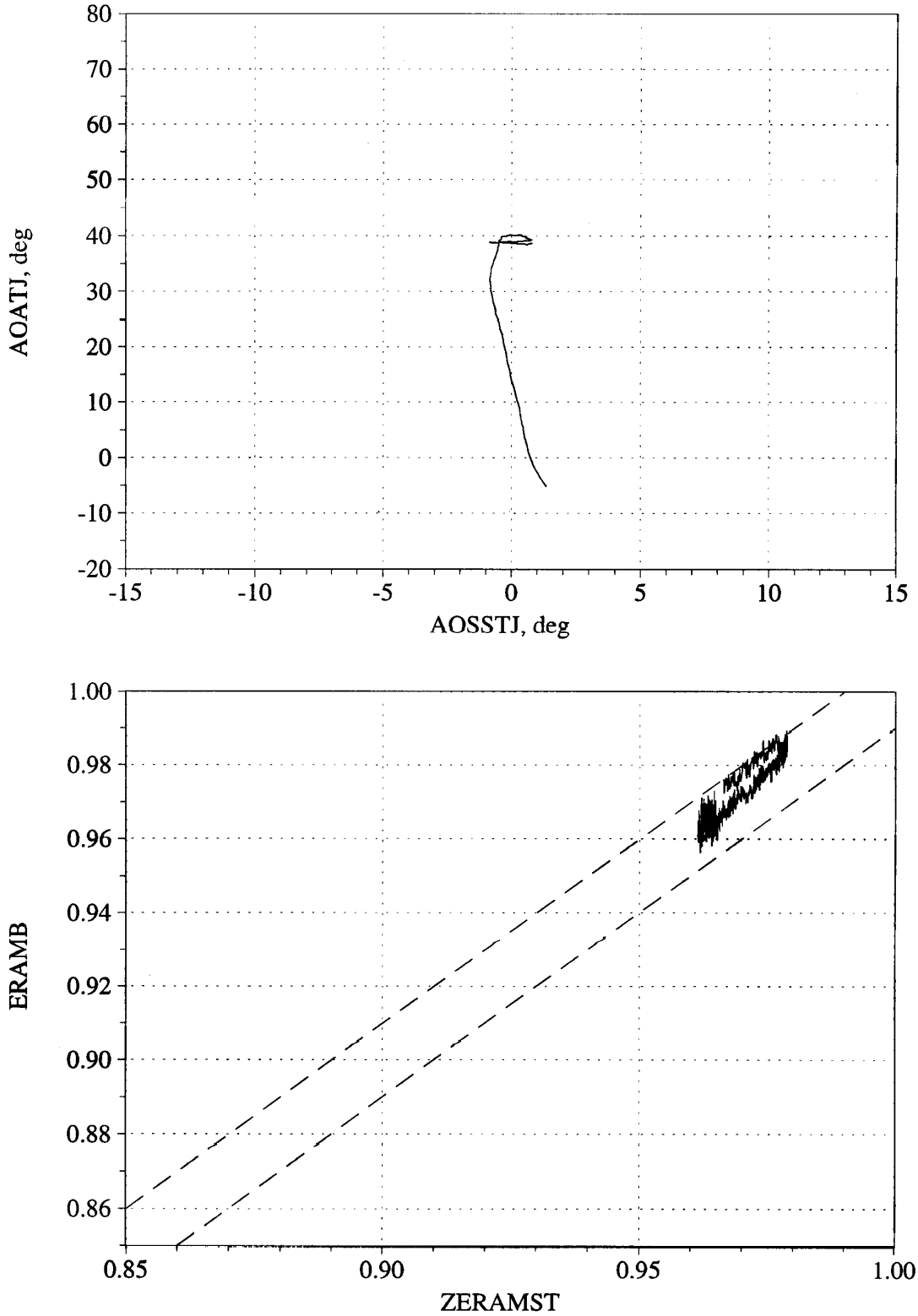

Figure C39. Angle of attack/angle of sideslip trajectory during maneuver; and measured versus estimated recovery - Flight 235, Test point 9b1.

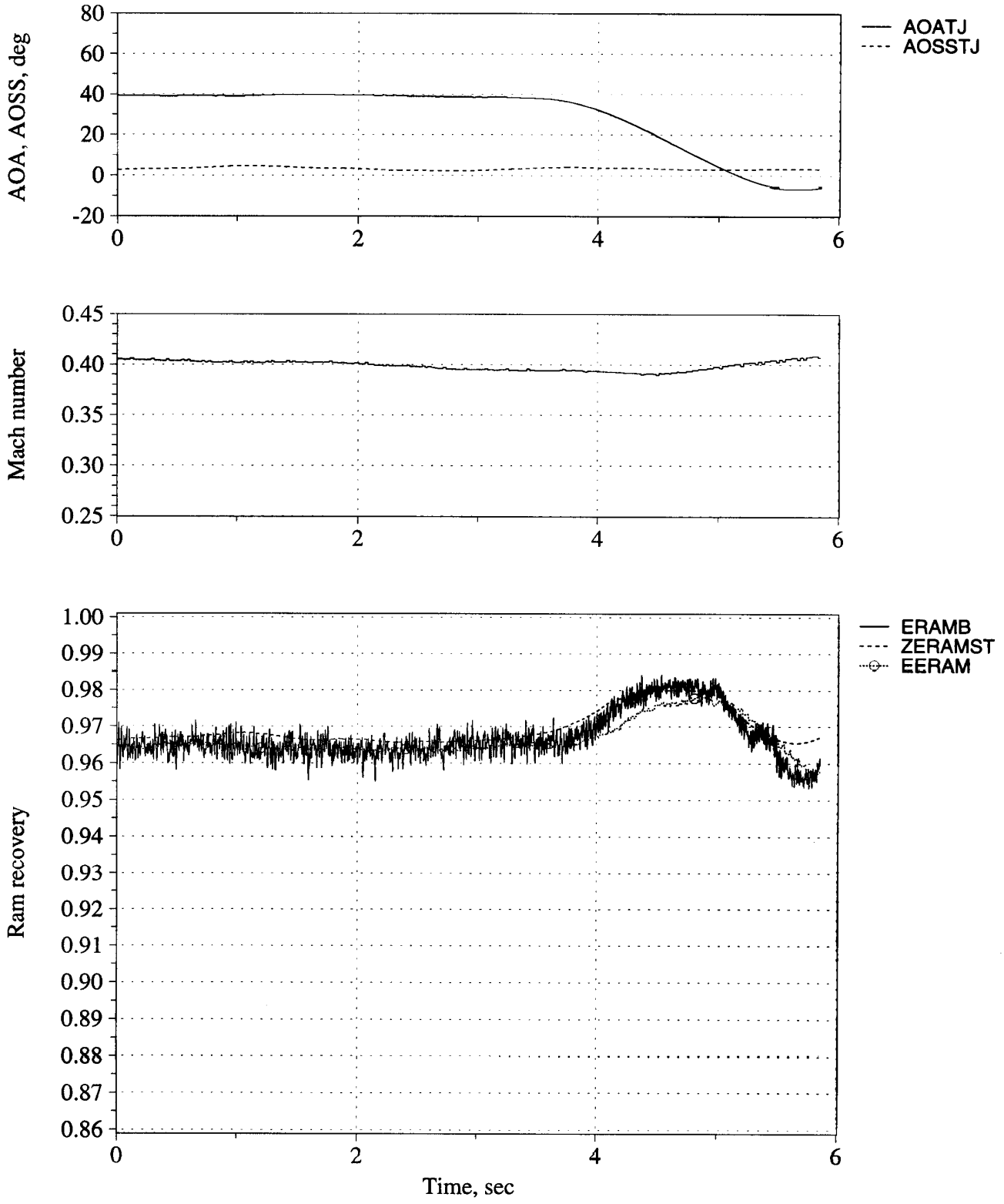

Figure C40. Time history of angle of attack, angle of sideslip, Mach number, and inlet recovery (measured and estimated) - Flight 245, Test point 03b.

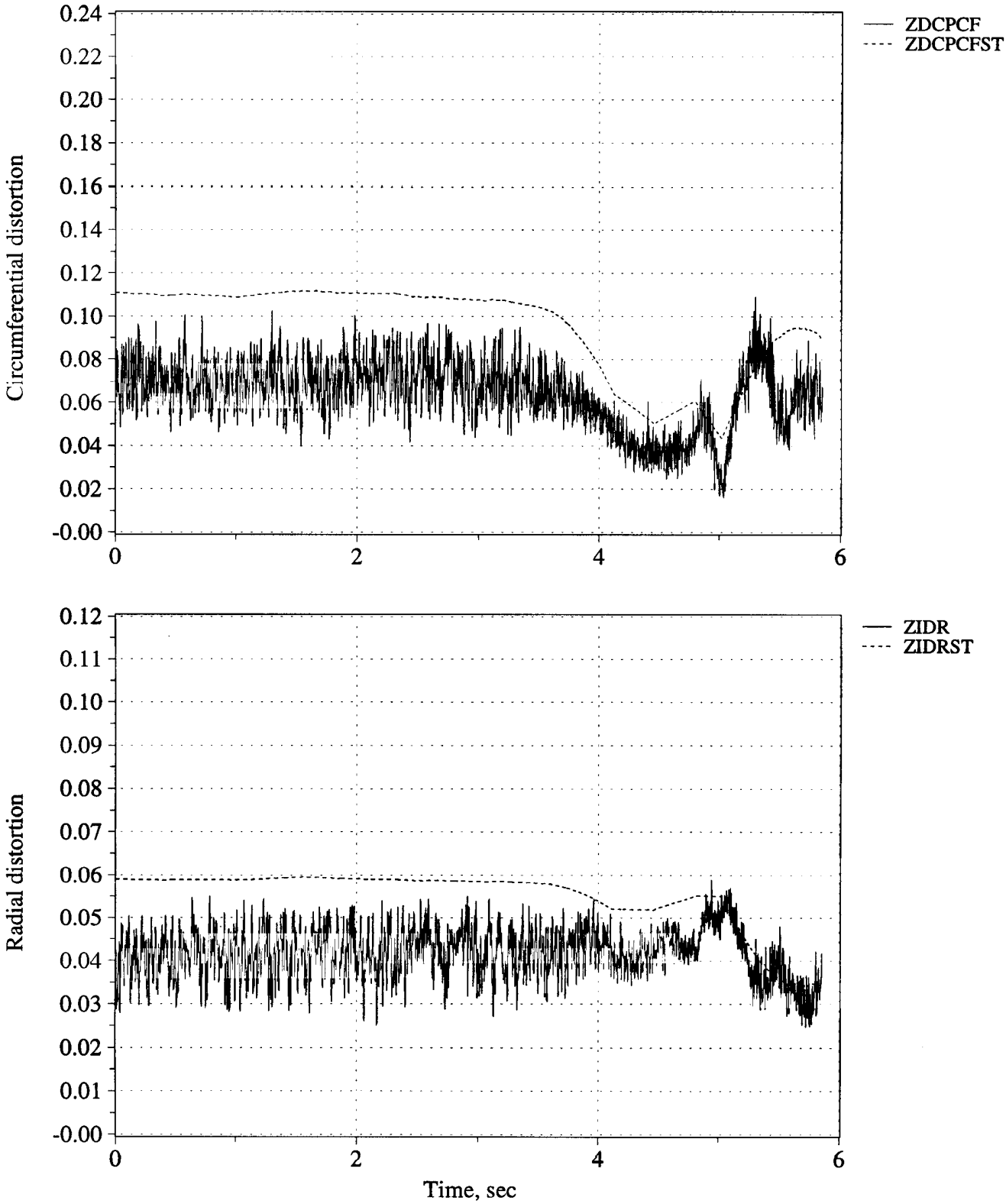

Figure C41. Time history of peak inlet dynamic circumferential and radial distortion (measured and estimated) - Flight 245, Test point 03b.

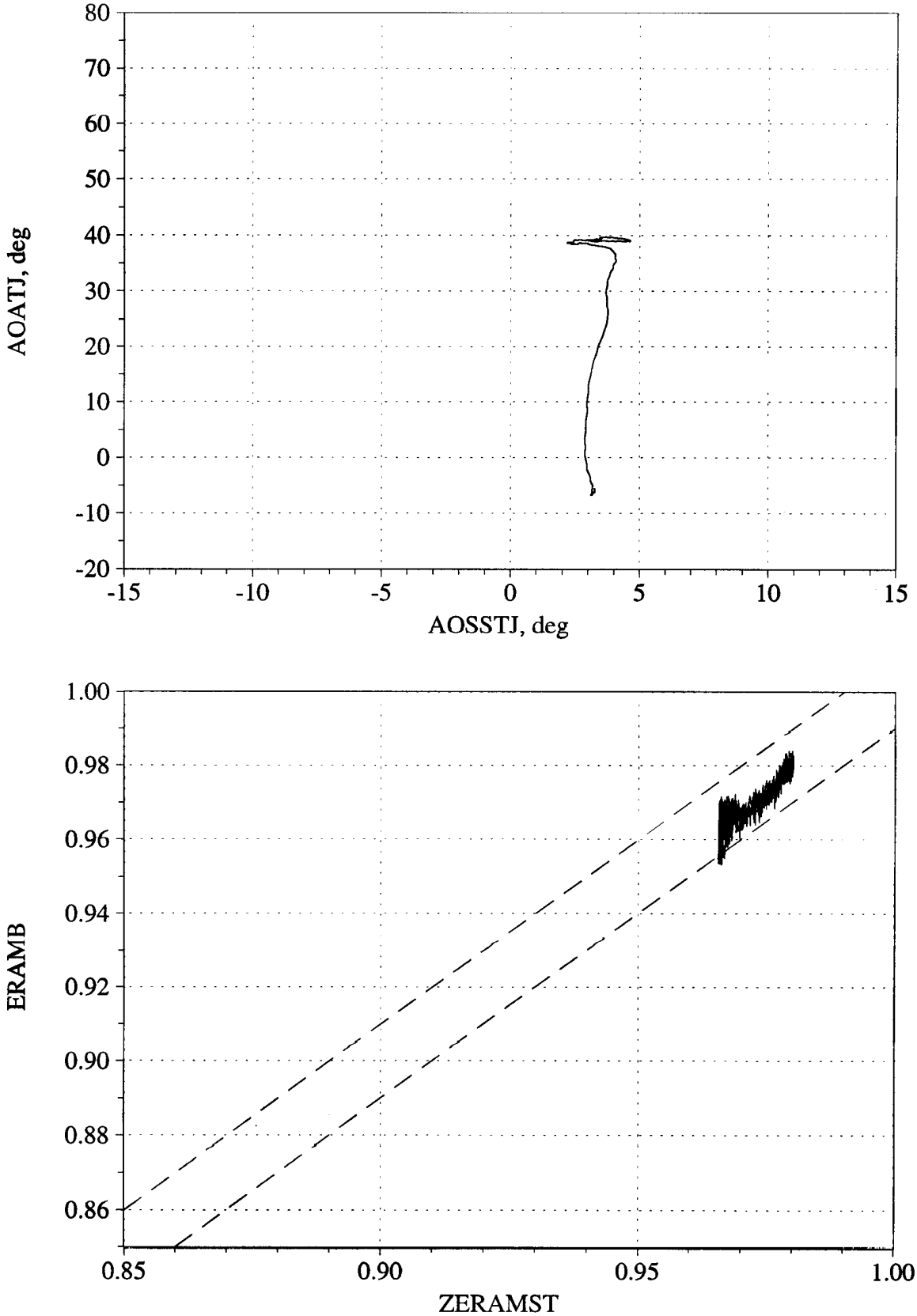

Figure C42. Angle of attack/angle of sideslip trajectory during maneuver; and measured versus estimated recovery - Flight 245, Test point 03b.

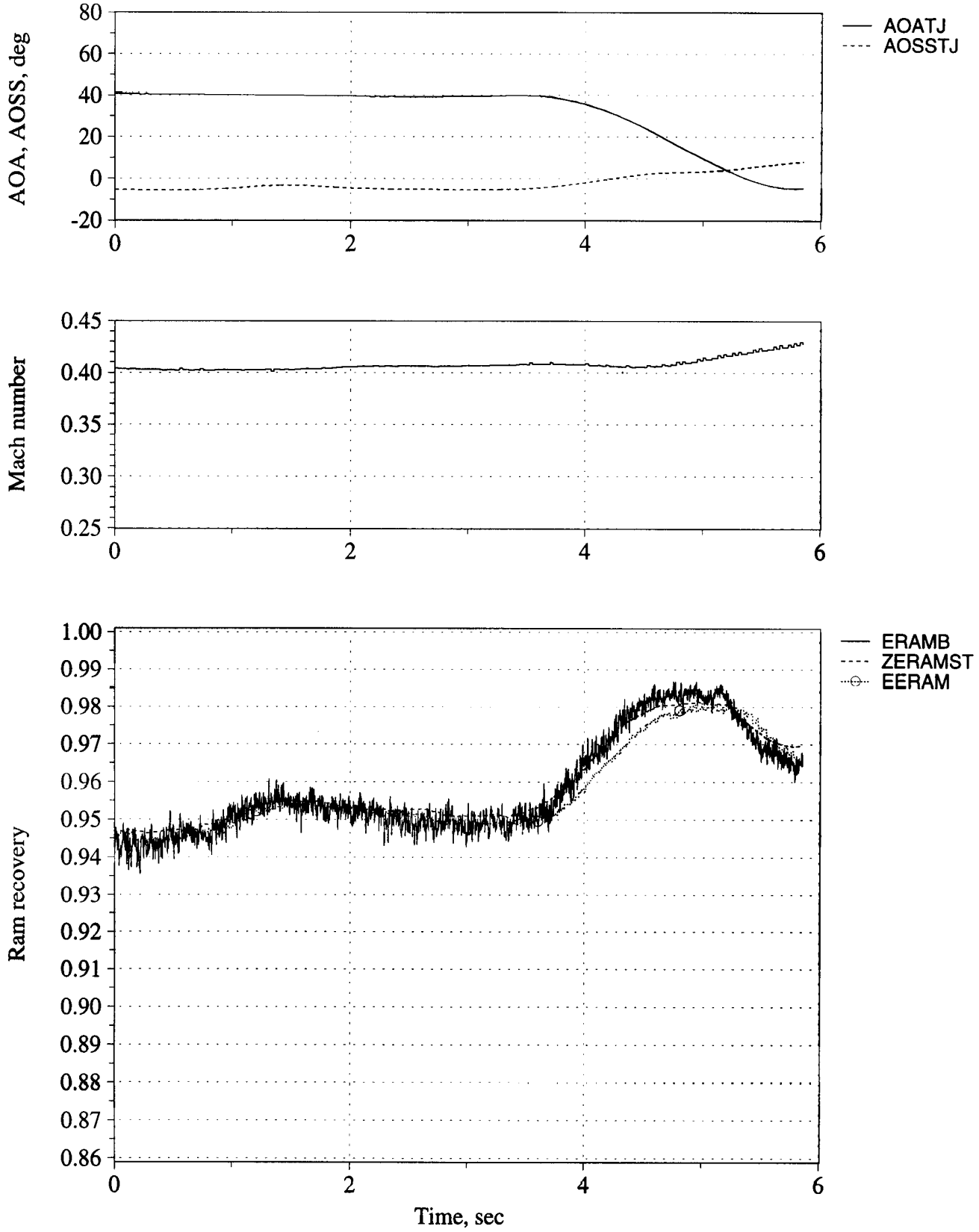

Figure C43. Time history of angle of attack, angle of sideslip, Mach number, and inlet recovery (measured and estimated) - Flight 245, Test point 03c.

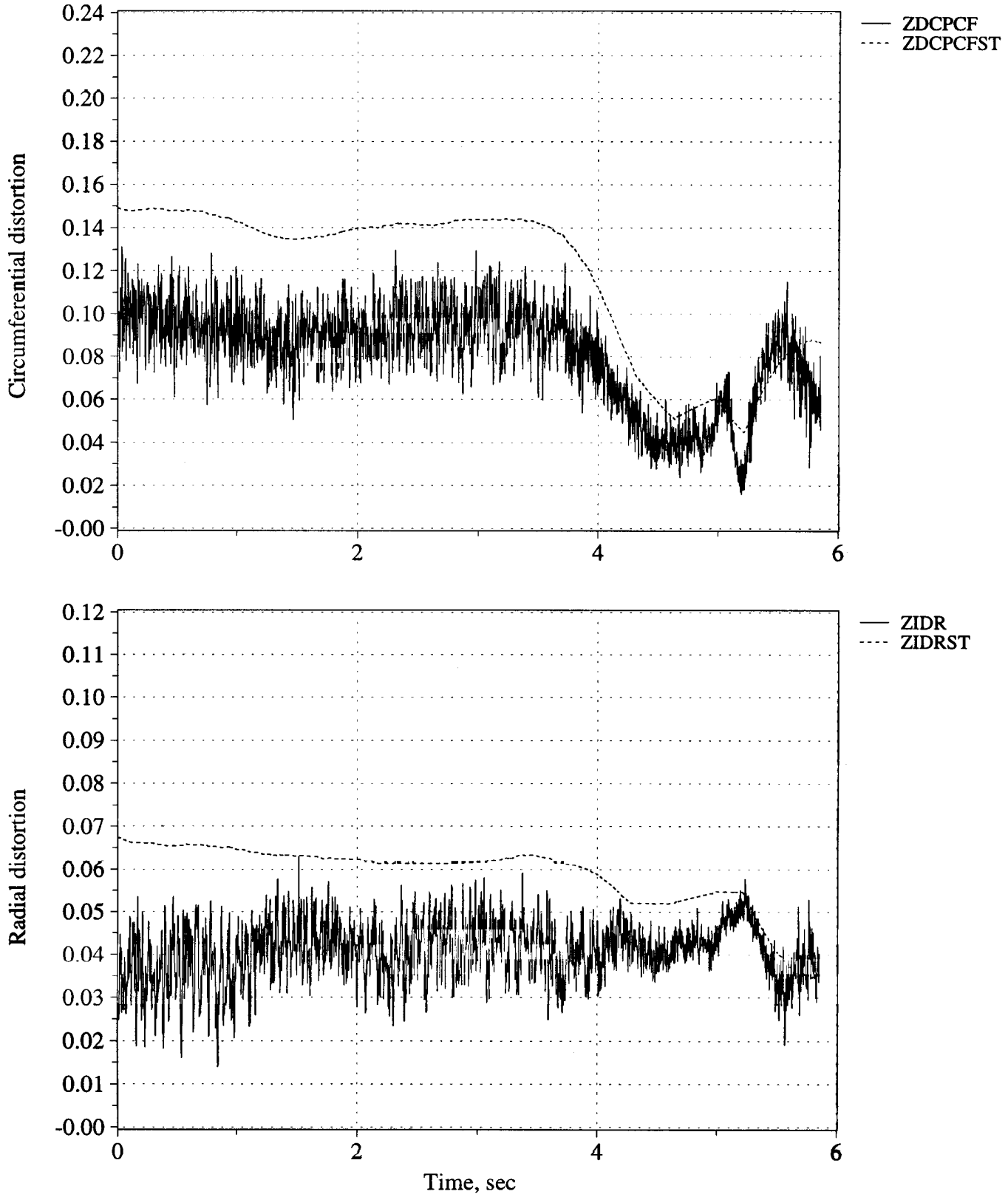

Figure C44. Time history of peak inlet dynamic circumferential and radial distortion (measured and estimated) - Flight 245, Test point 03c.

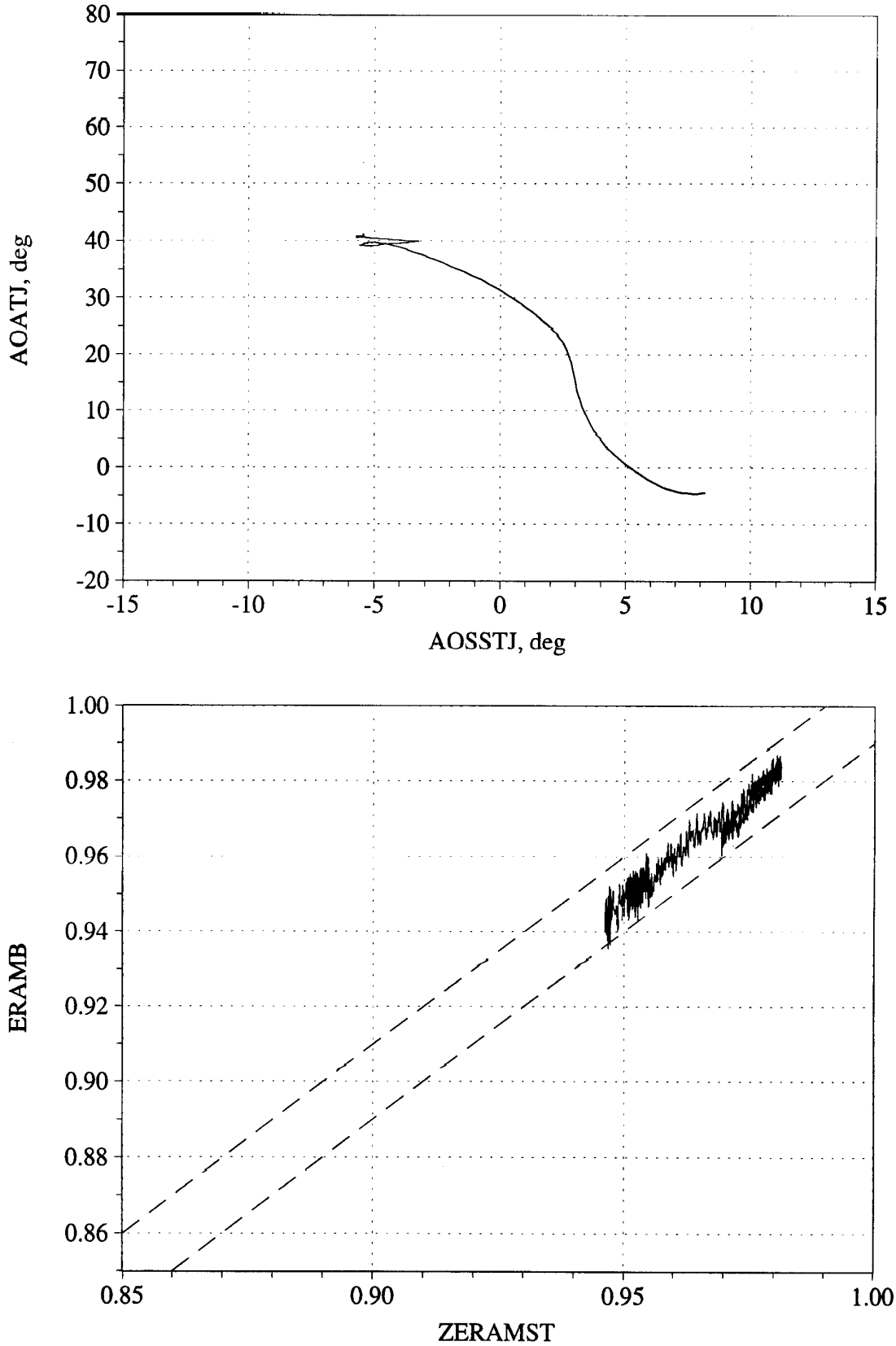

Figure C45. Angle of attack/angle of sideslip trajectory during maneuver; and measured versus estimated recovery - Flight 245, Test point 03c.

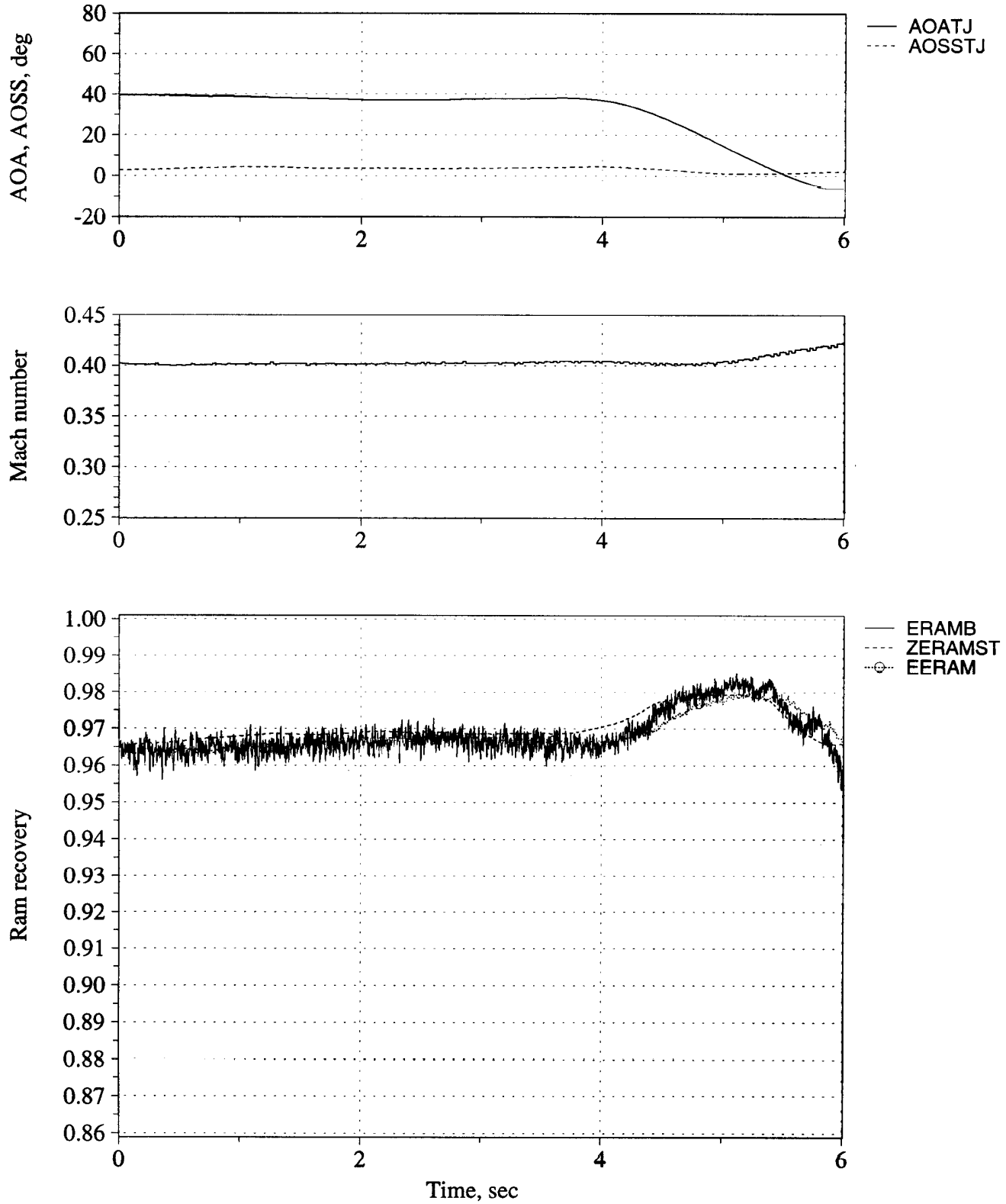

Figure C46. Time history of angle of attack, angle of sideslip, Mach number, and inlet recovery (measured and estimated) - Flight 245, Test point 04b.

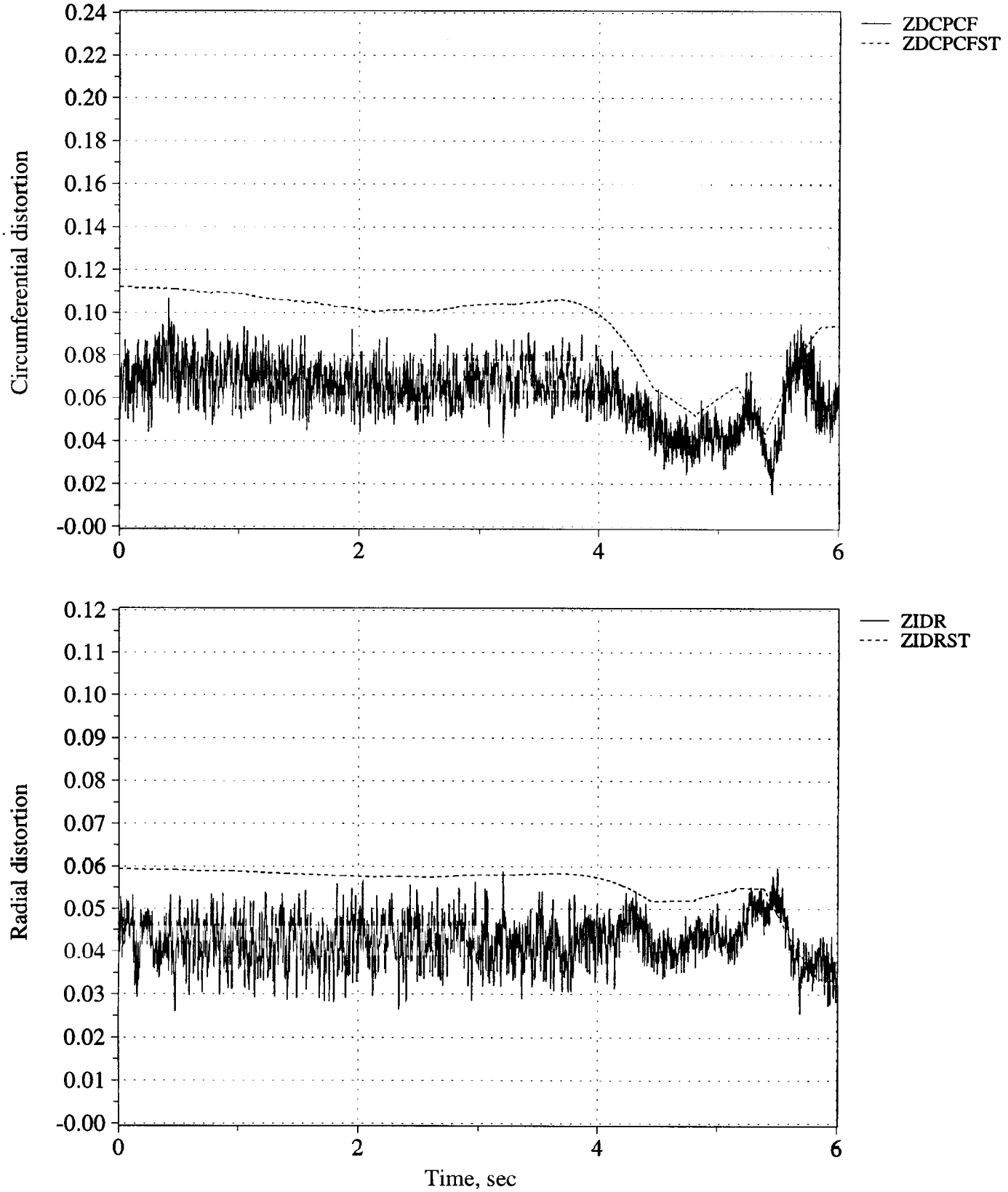

Figure C47. Time history of peak inlet dynamic circumferential and radial distortion (measured and estimated) - Flight 245, Test point 04b.

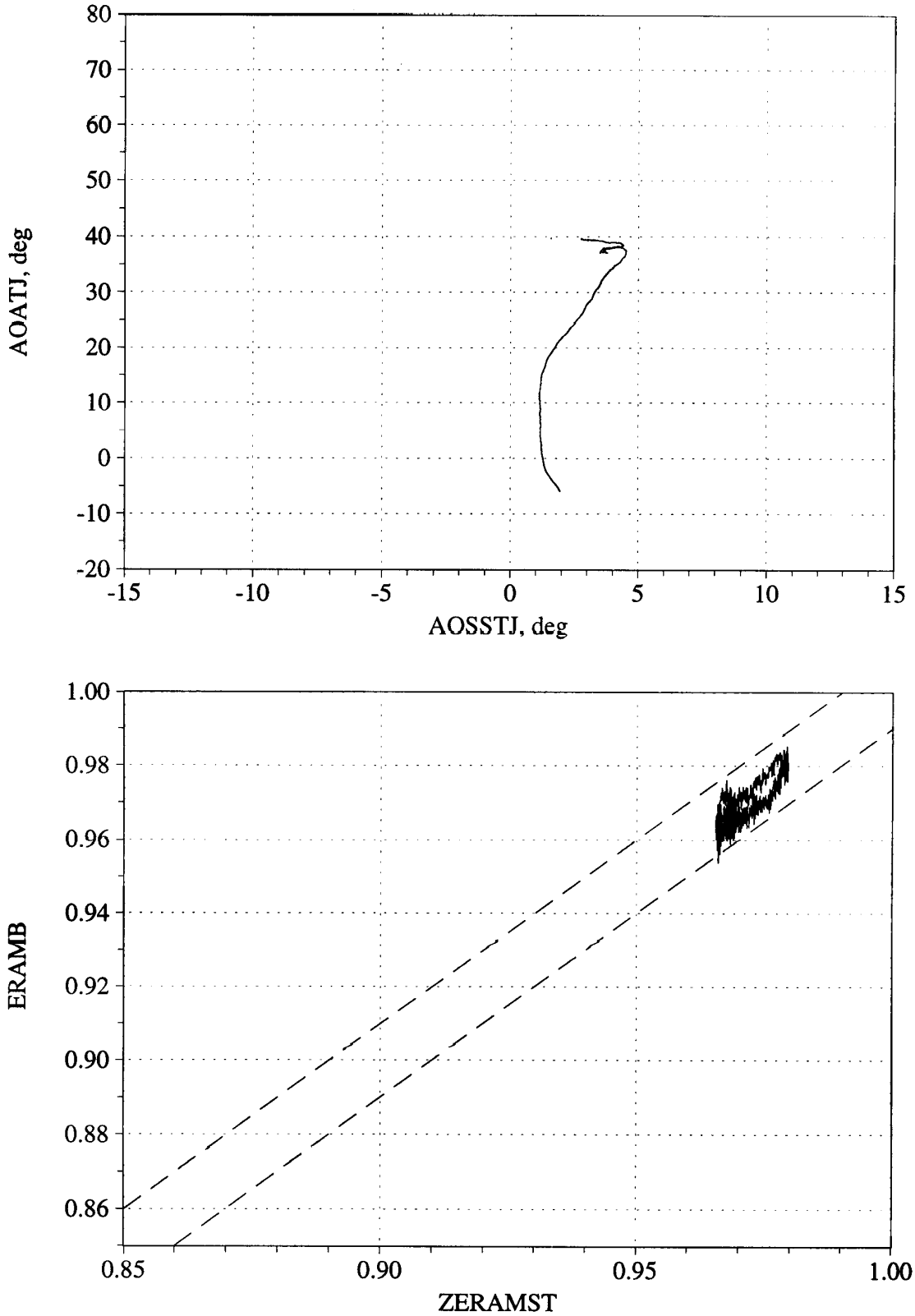

Figure C48. Angle of attack/angle of sideslip trajectory during maneuver; and measured versus estimated recovery - Flight 245, Test point 04b.

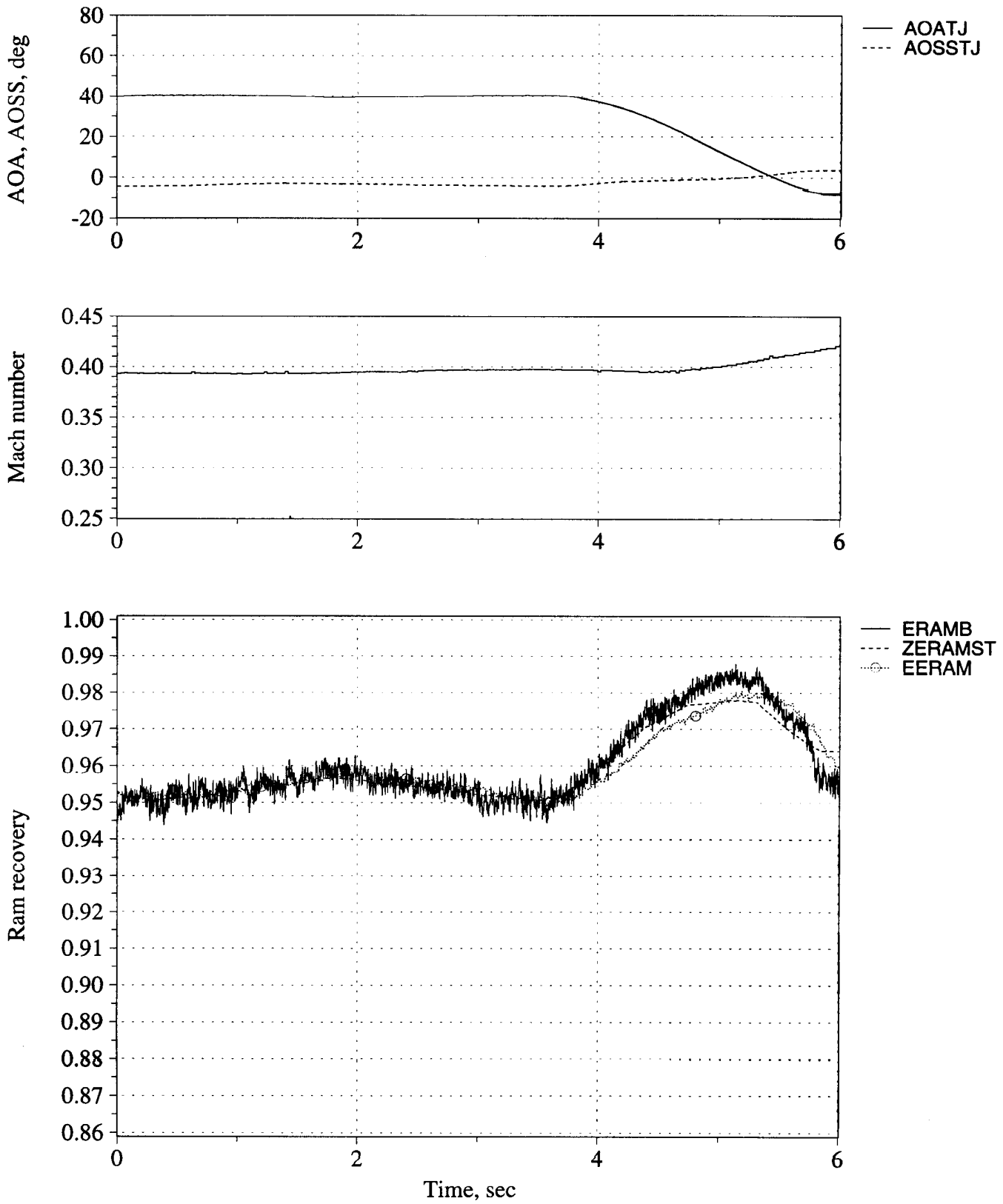

Figure C49. Time history of angle of attack, angle of sideslip, Mach number, and inlet recovery (measured and estimated) - Flight 245, Test point 04c.

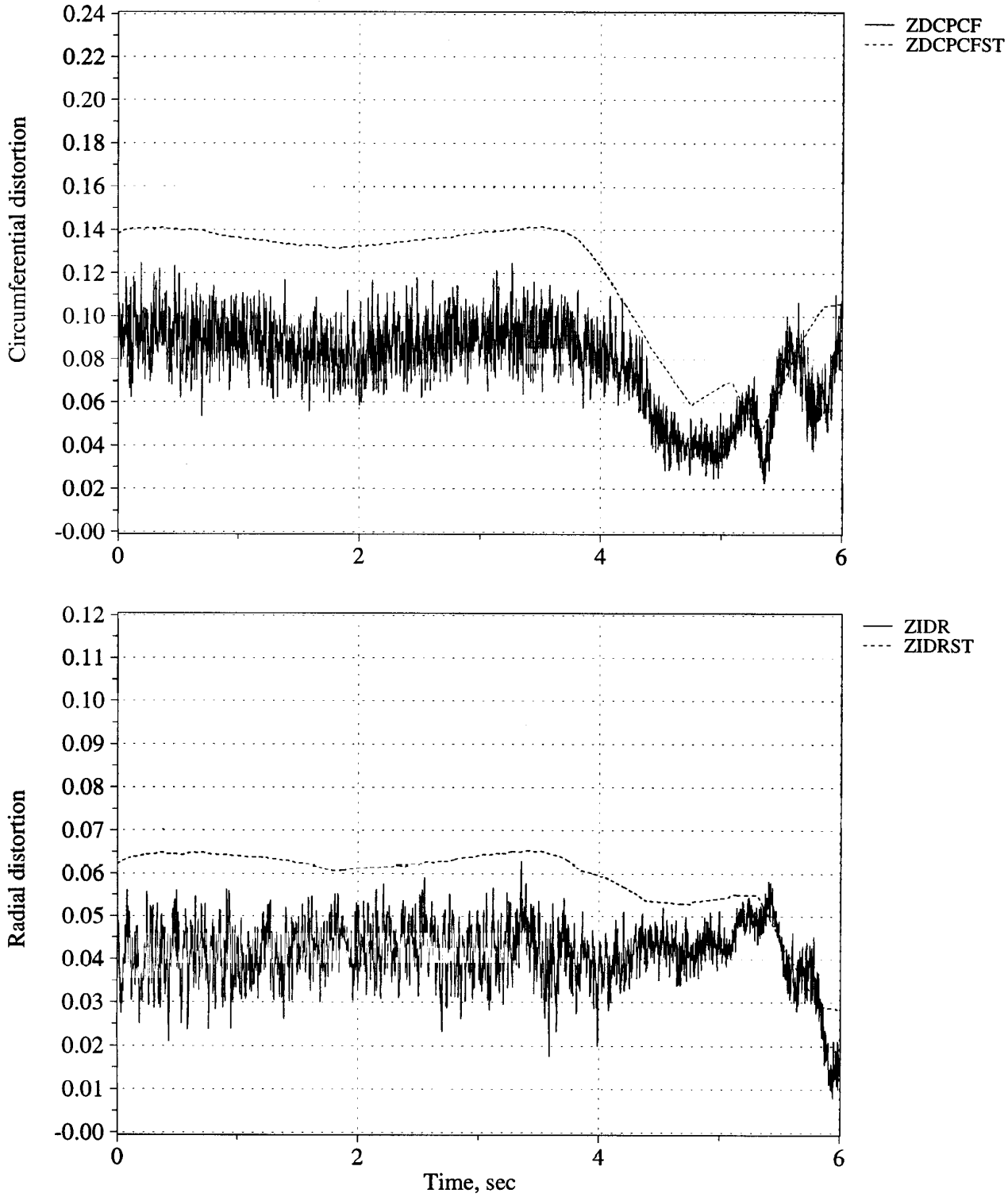

Figure C50. Time history of peak inlet dynamic circumferential and radial distortion (measured and estimated) - Flight 245, Test point 04c.

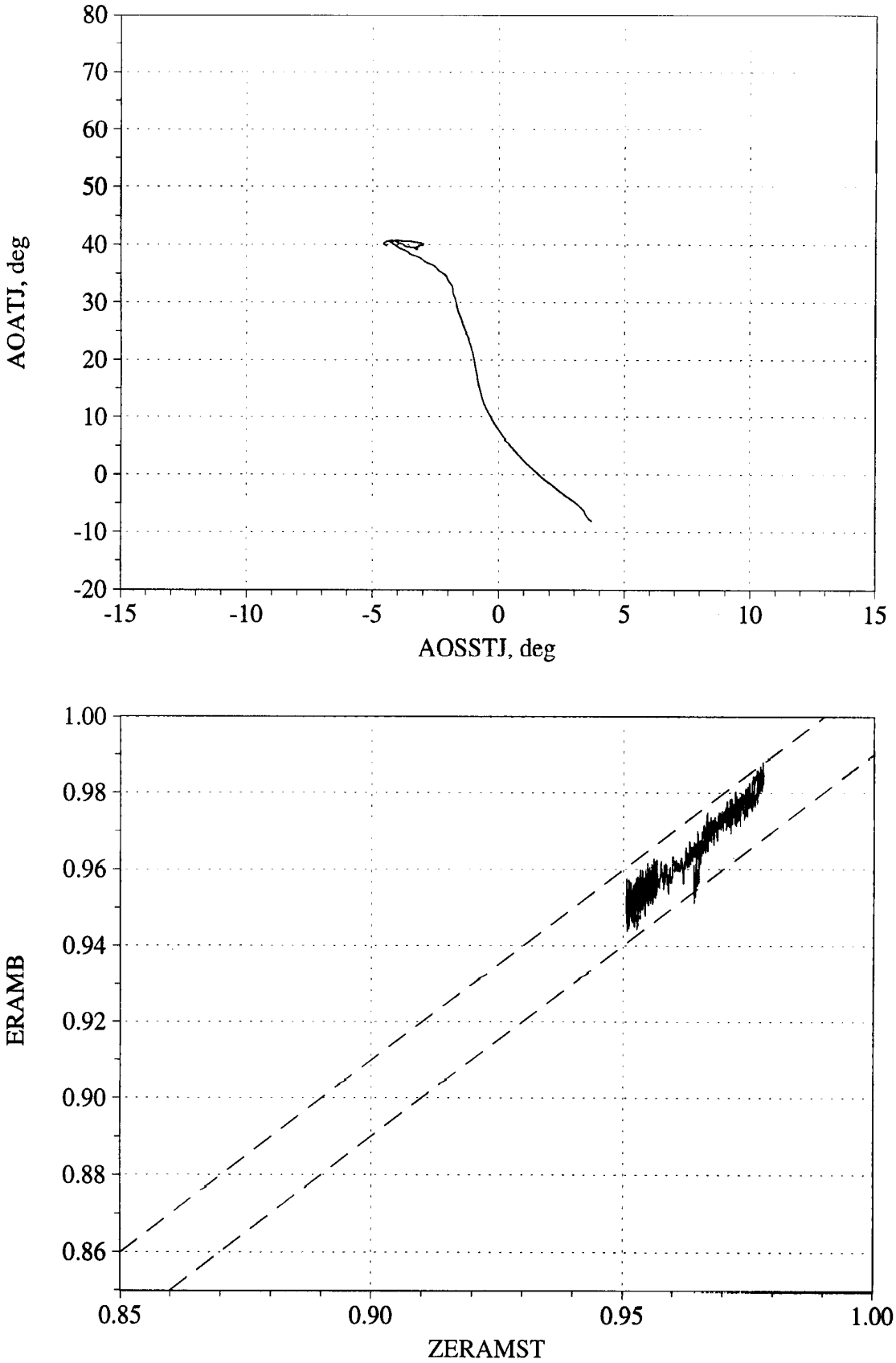

Figure C51. Angle of attack/angle of sideslip trajectory during maneuver; and measured versus estimated recovery - Flight 245, Test point 04c.

- Mid-to-High Angle of Attack -

Figures C52 - C54, Flight 241, Test Point 0d1
Figures C55 - C57, Flight 241, Test Point 0d2
Figures C58 - C60, Flight 243, Test Point 25b
Figures C61 - C63, Flight 243, Test Point 25c

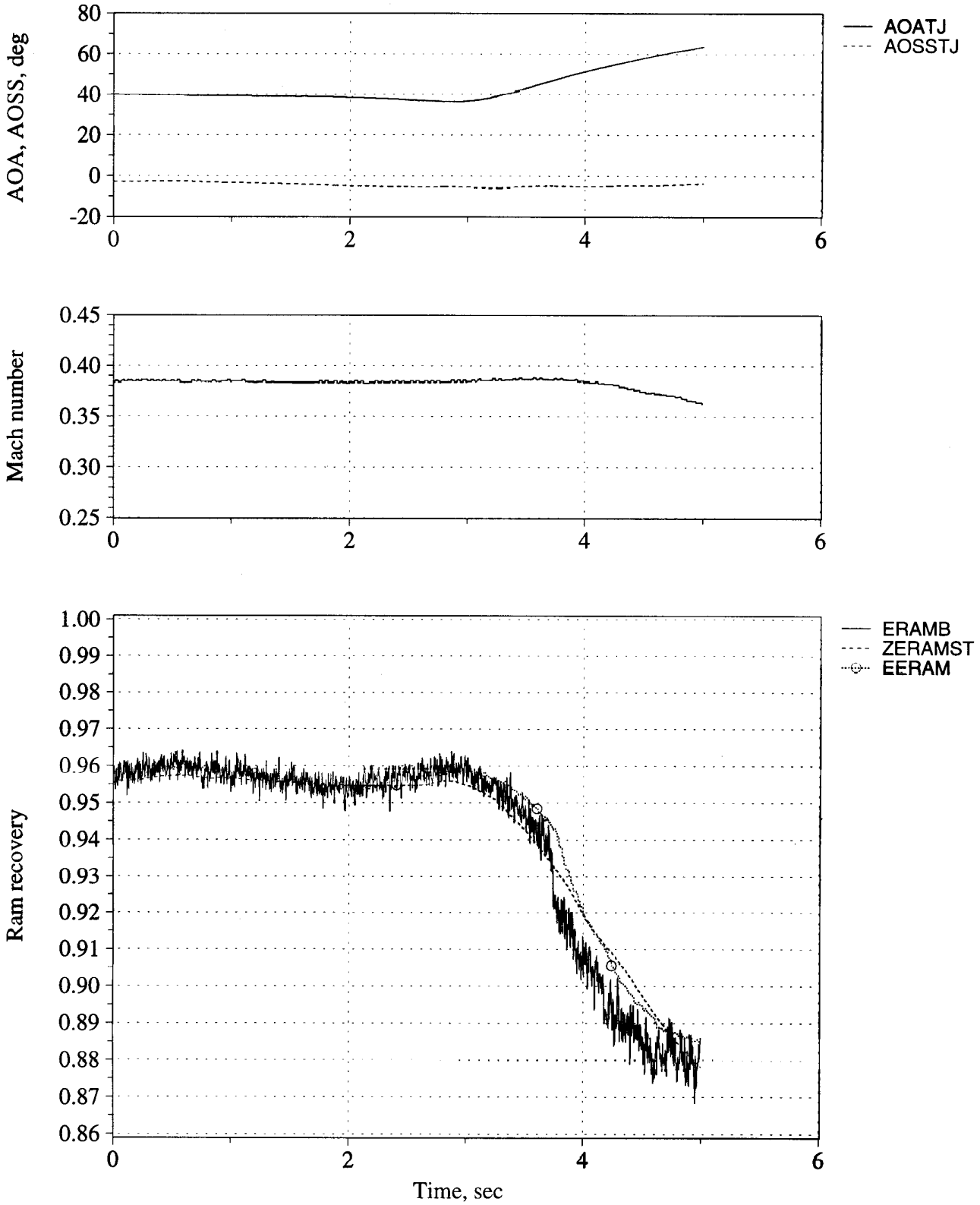

Figure C52. Time history of angle of attack, angle of sideslip, Mach number, and inlet recovery (measured and estimated) - Flight 241, Test point 0d1.

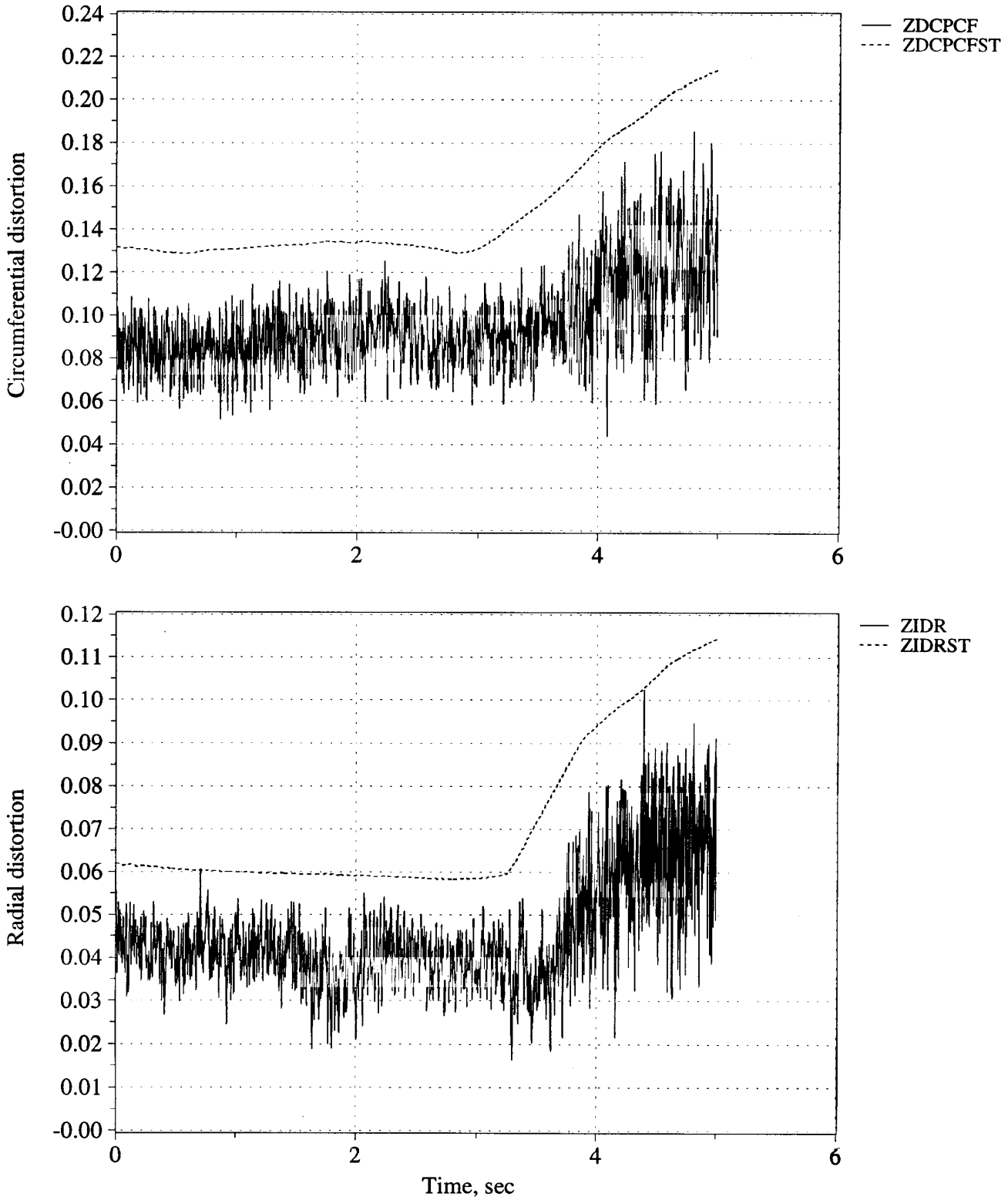

Figure C53. Time history of peak inlet dynamic circumferential and radial distortion (measured and estimated) - Flight 241, Test point 0d1.

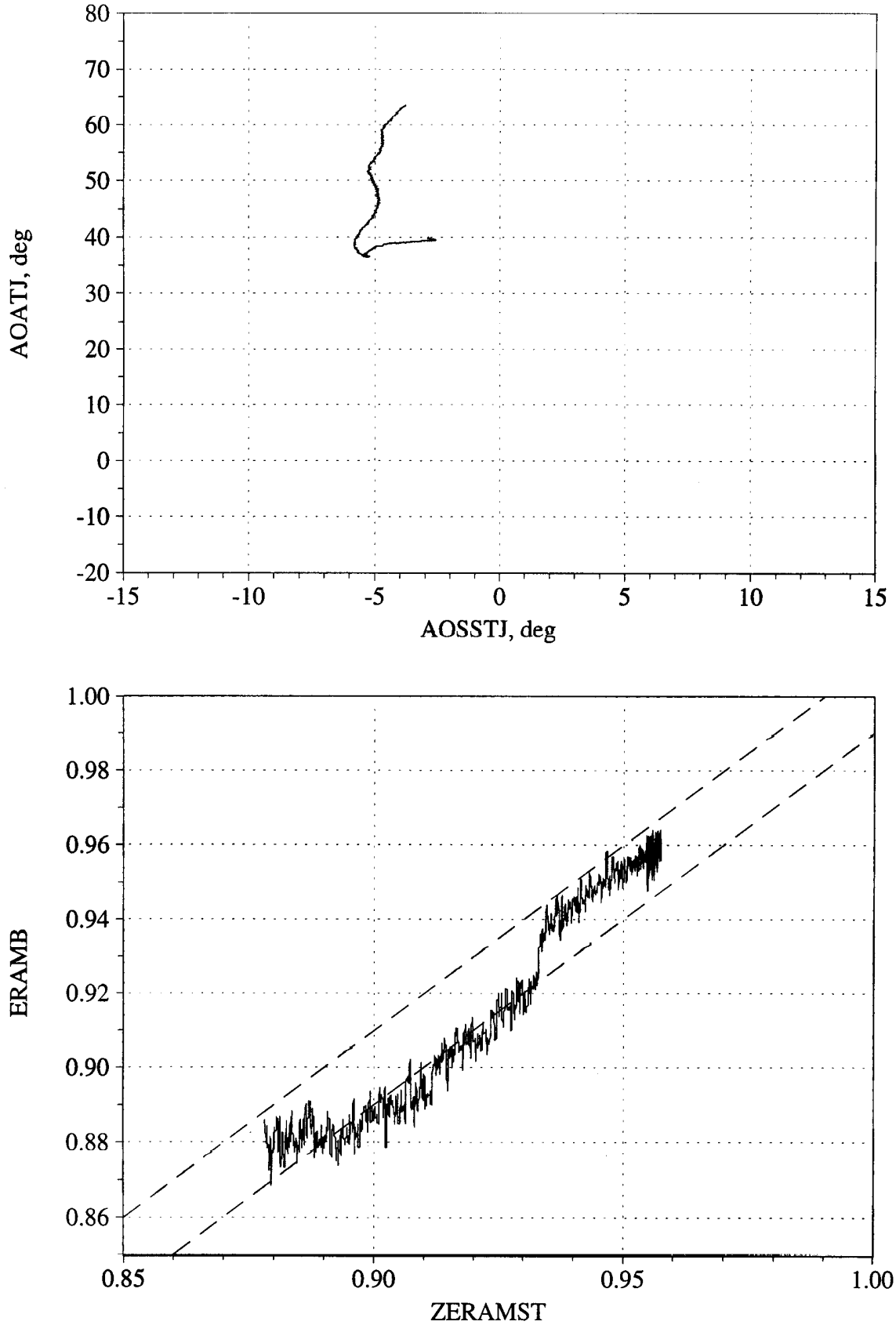

Figure C54. Angle of attack/angle of sideslip trajectory during maneuver; and measured versus estimated recovery - Flight 241, Test point 0d1.

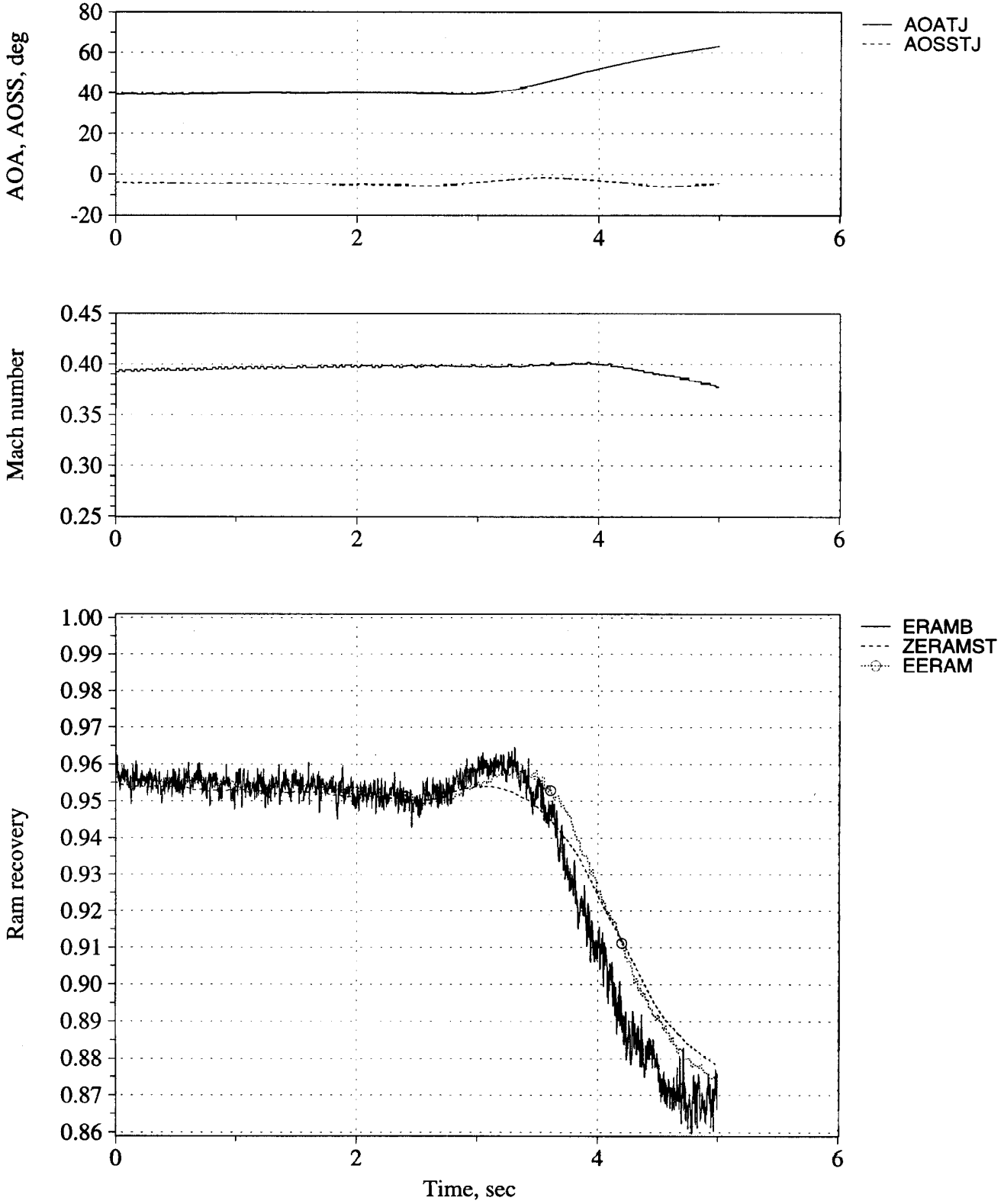

Figure C55. Time history of angle of attack, angle of sideslip, Mach number, and inlet recovery (measured and estimated) - Flight 241, Test point 0d2.

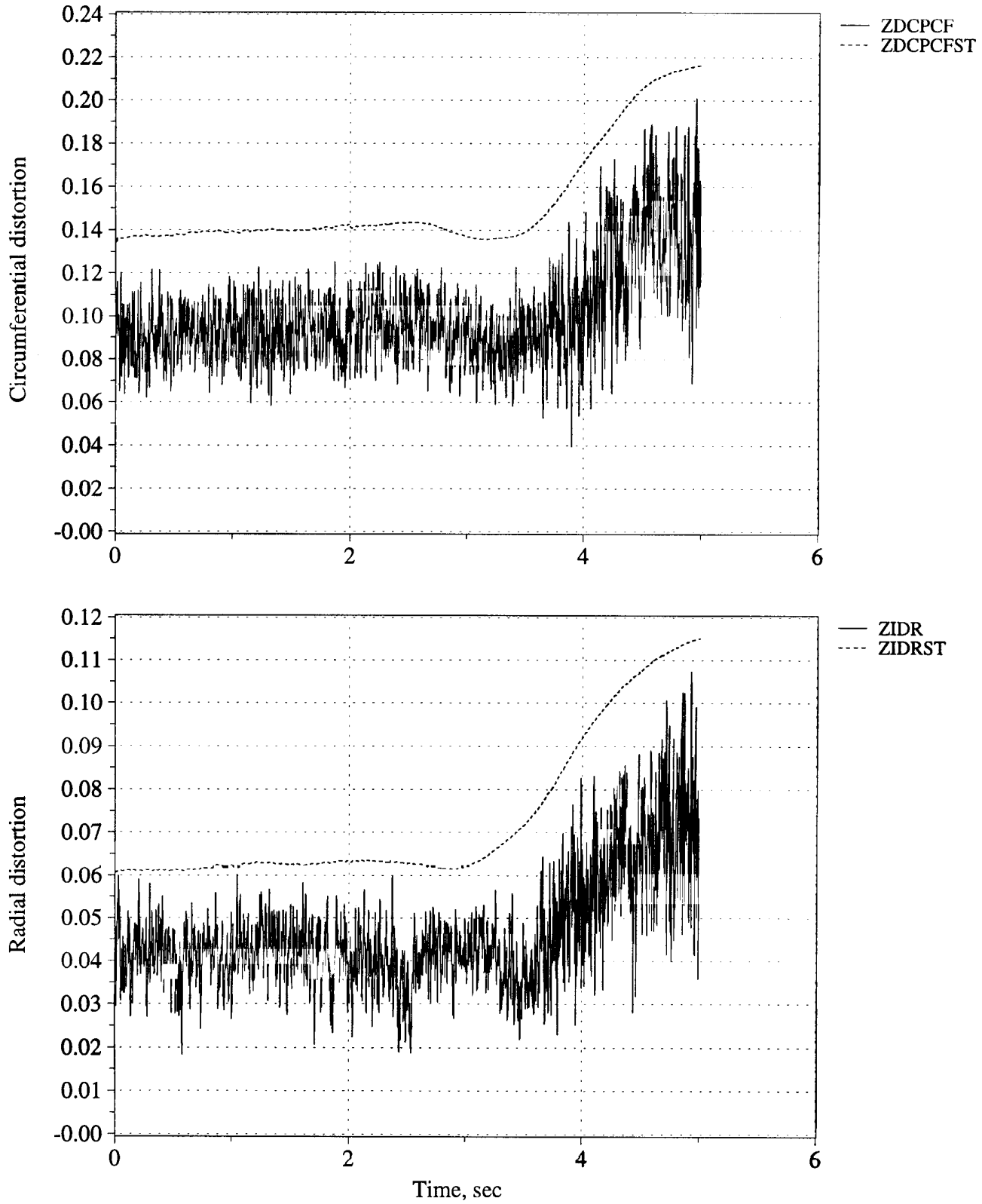

Figure C56. Time history of peak inlet dynamic circumferential and radial distortion (measured and estimated) - Flight 241, Test point 0d2.

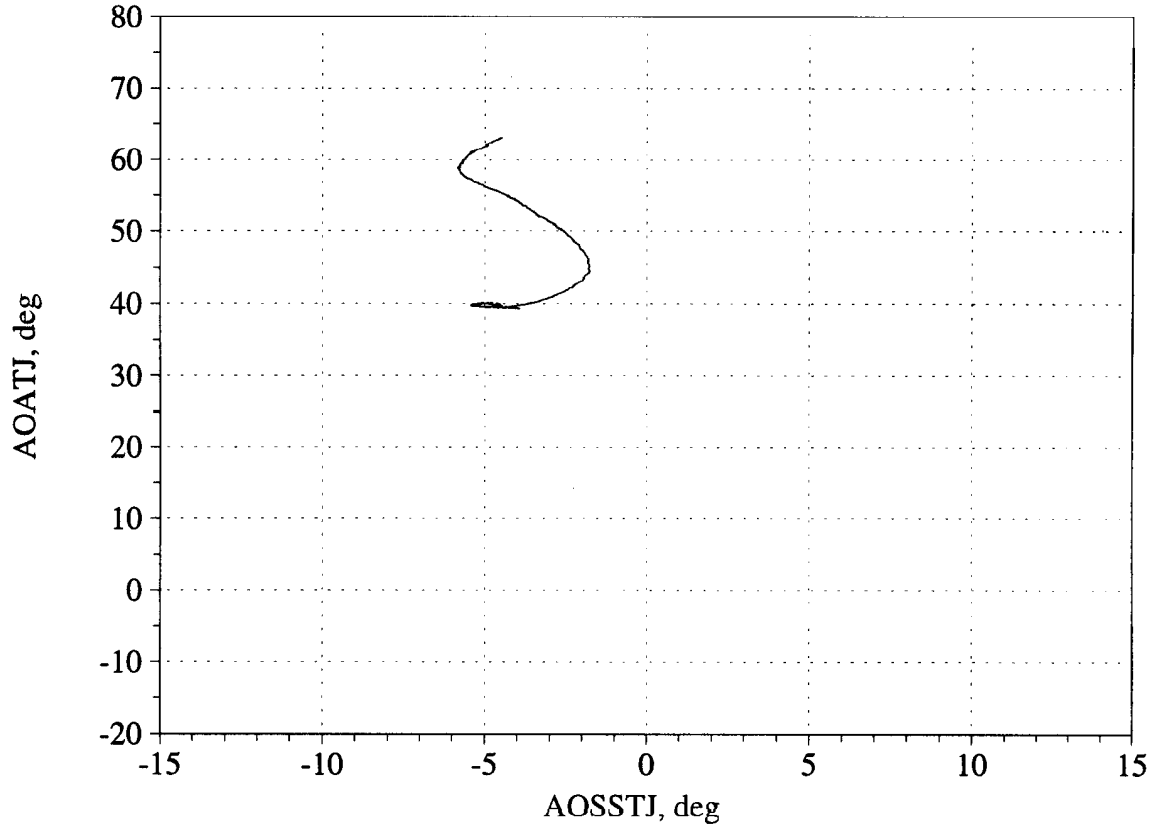

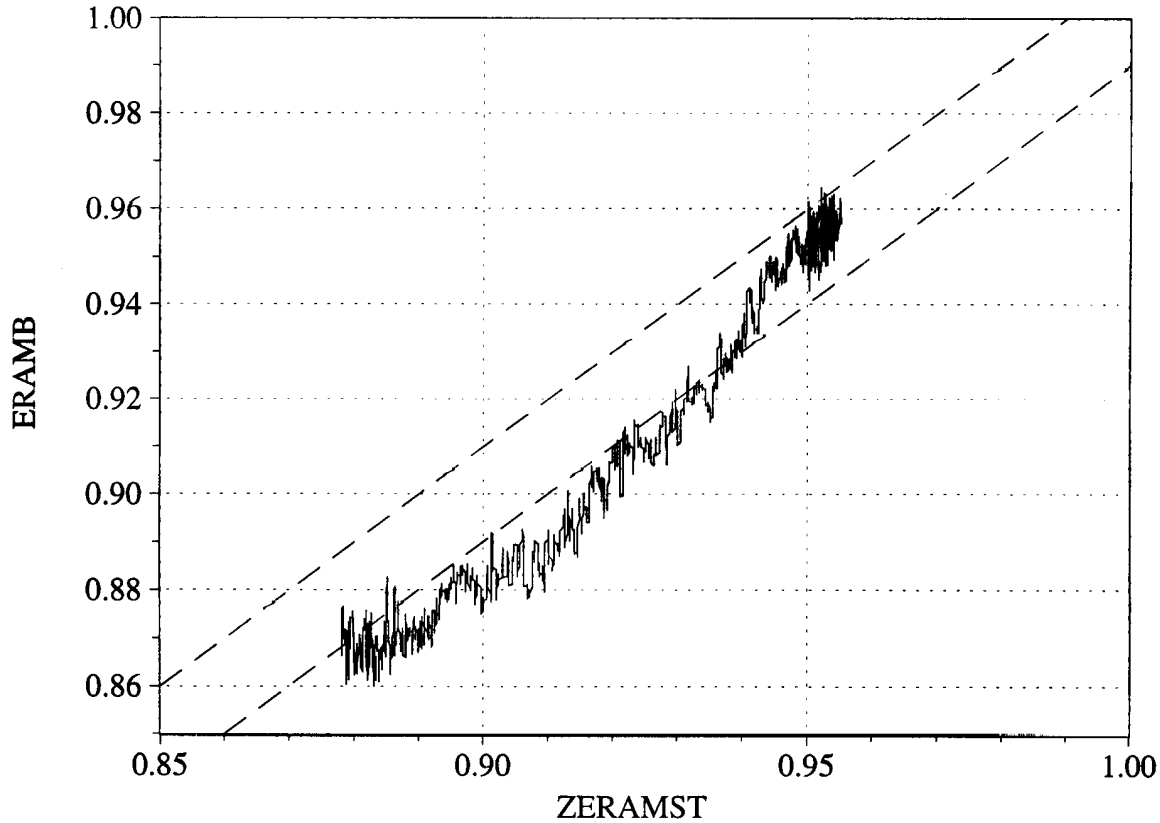

Figure C57. Angle of attack/angle of sideslip trajectory during maneuver; and measured versus estimated recovery - Flight 241, Test point 0d2.

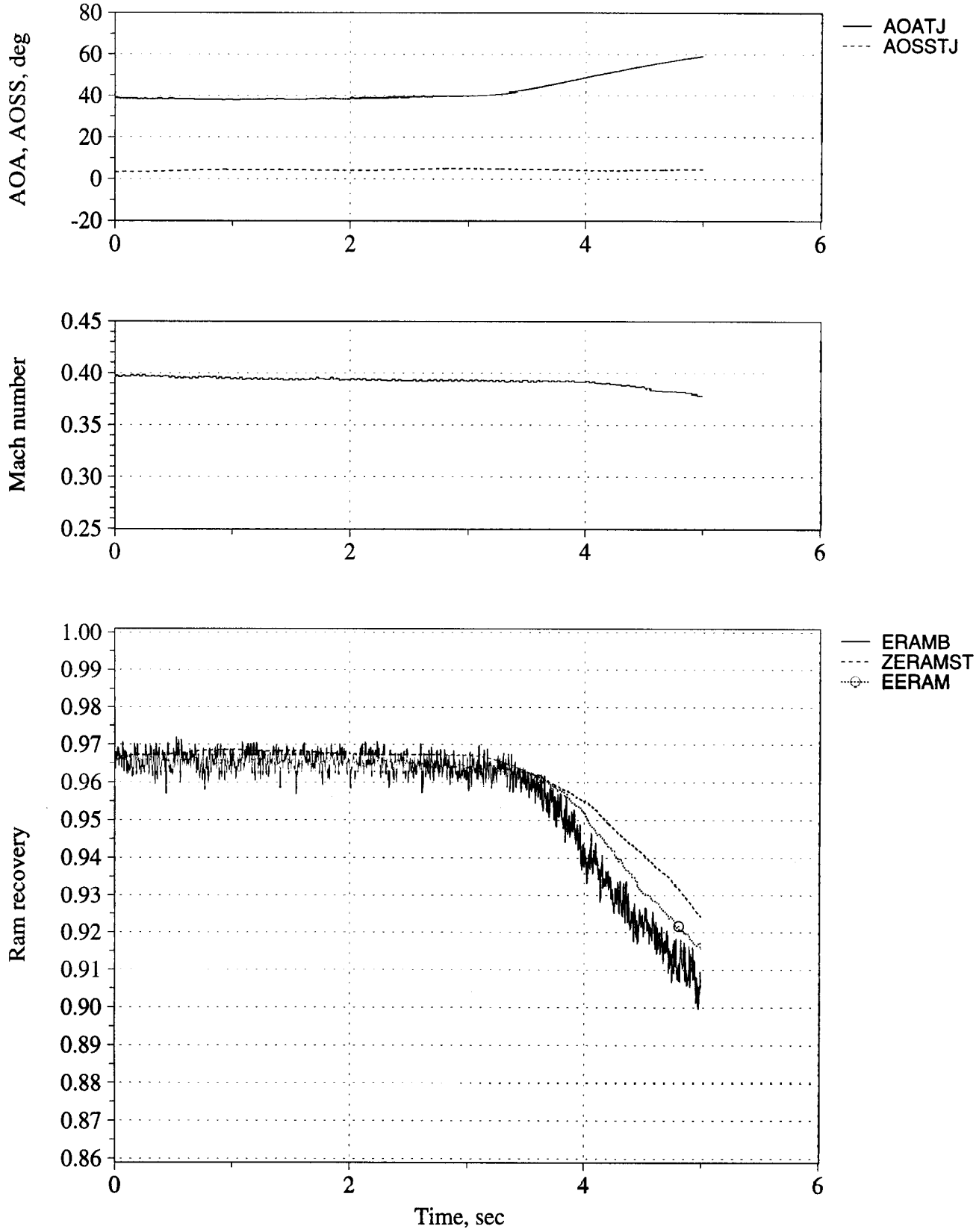

Figure C58. Time history of angle of attack, angle of sideslip, Mach number, and inlet recovery (measured and estimated) - Flight 243, Test point 25b.

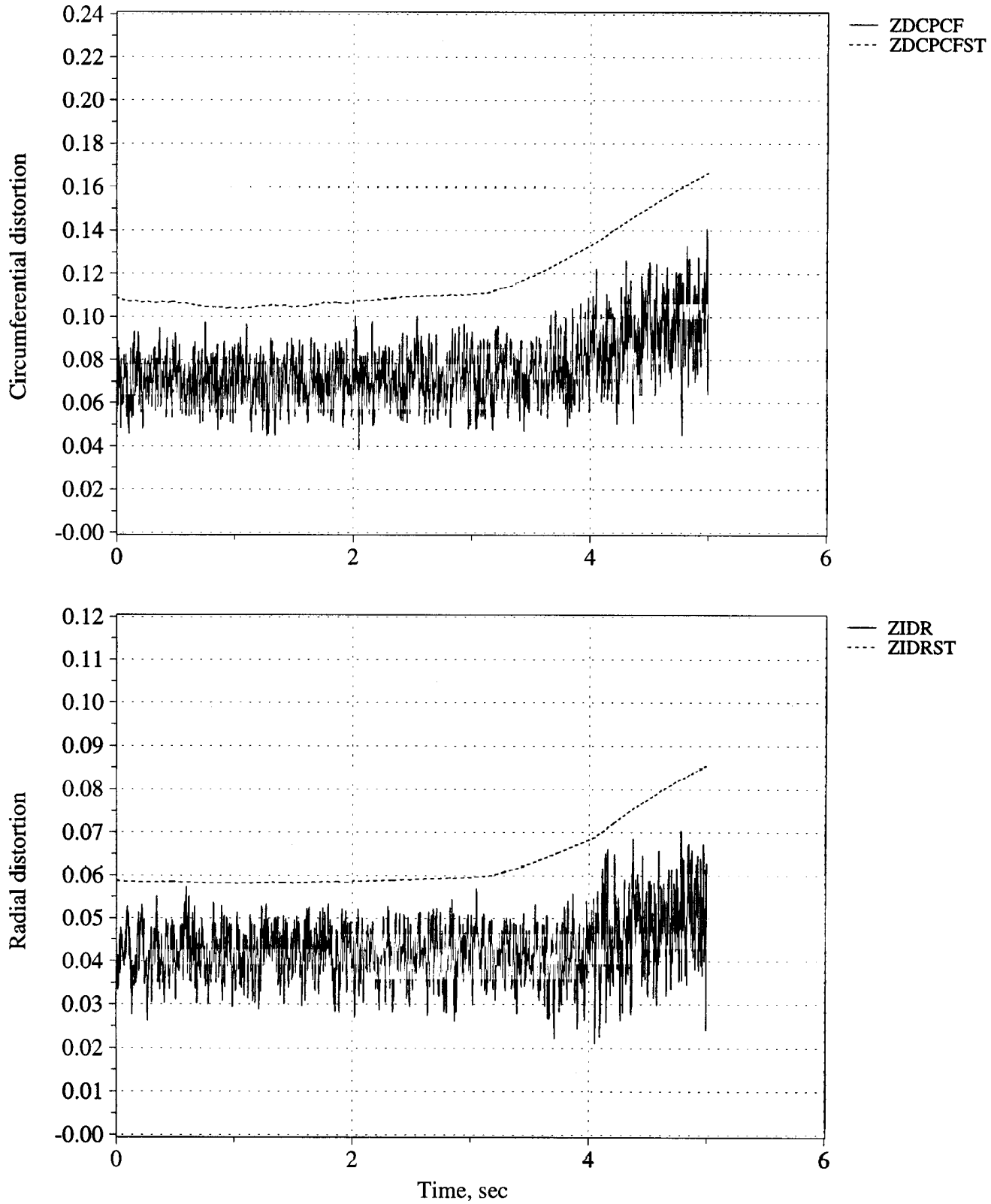

Figure C59. Time history of peak inlet dynamic circumferential and radial distortion (measured and estimated) - Flight 243, Test point 25b.

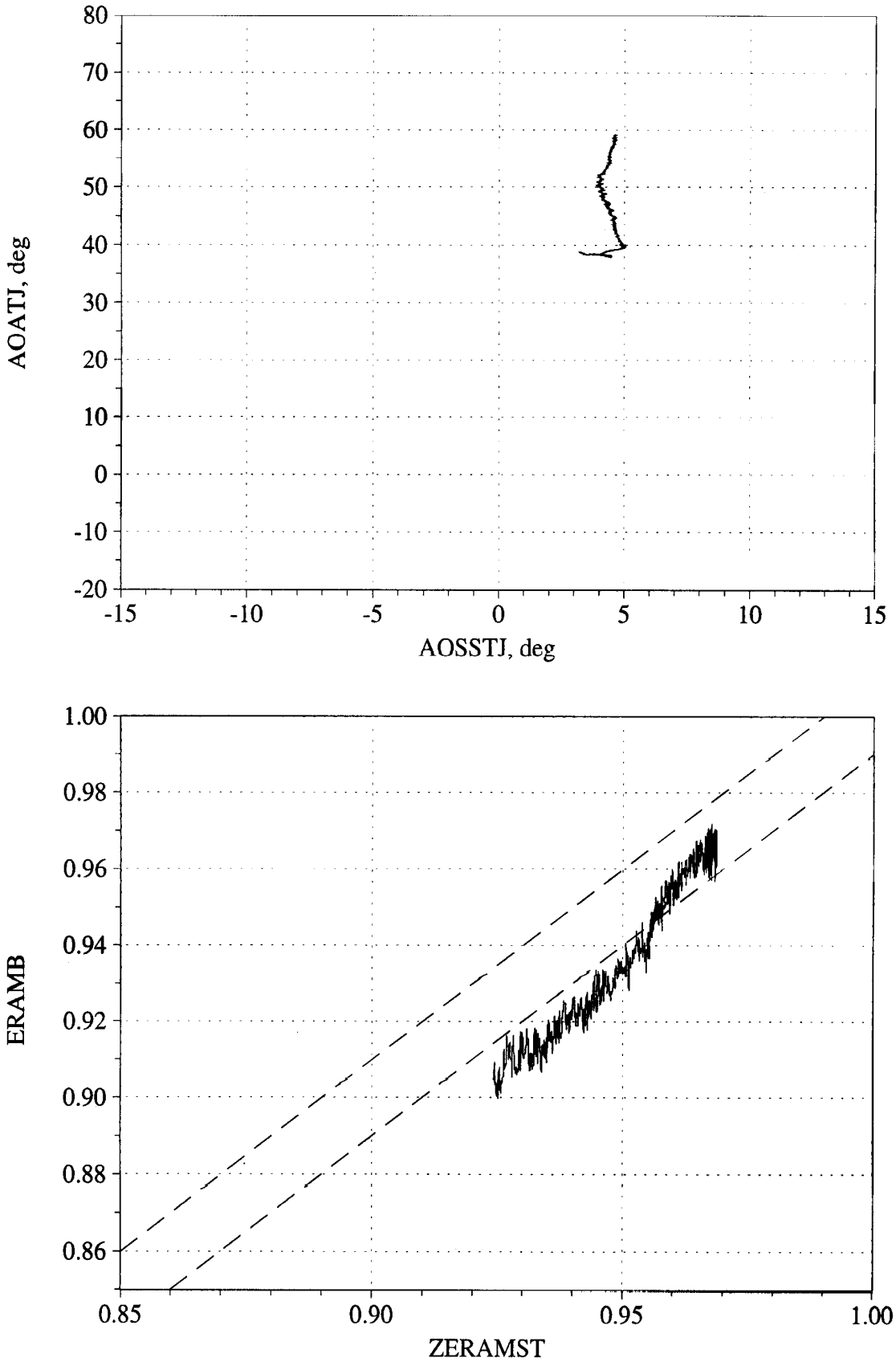

Figure C60. Angle of attack/angle of sideslip trajectory during maneuver; and measured versus estimated recovery - Flight 243, Test point 25b.

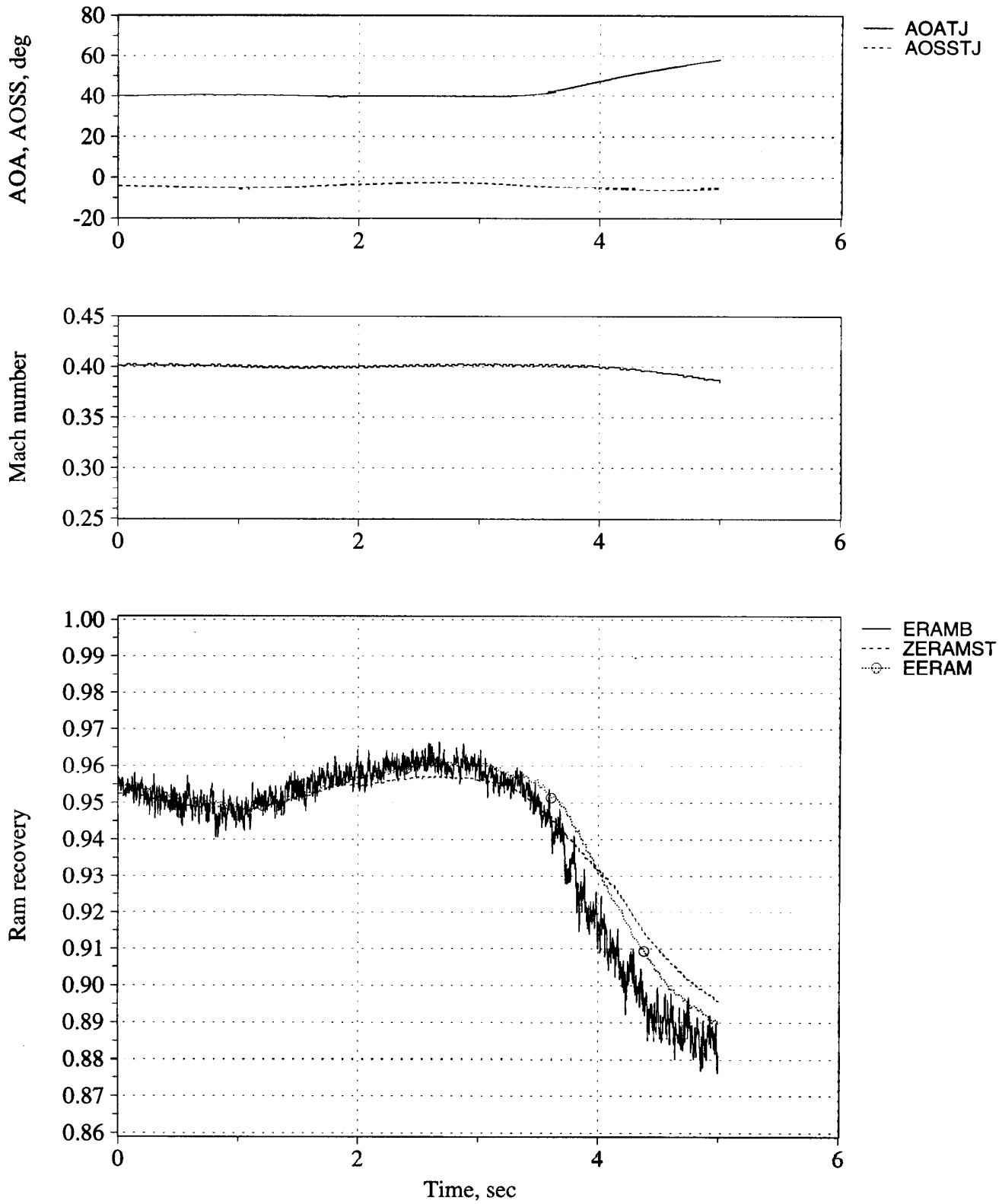

Figure C61. Time history of angle of attack, angle of sideslip, Mach number, and inlet recovery (measured and estimated) - Flight 243, Test point 25c.

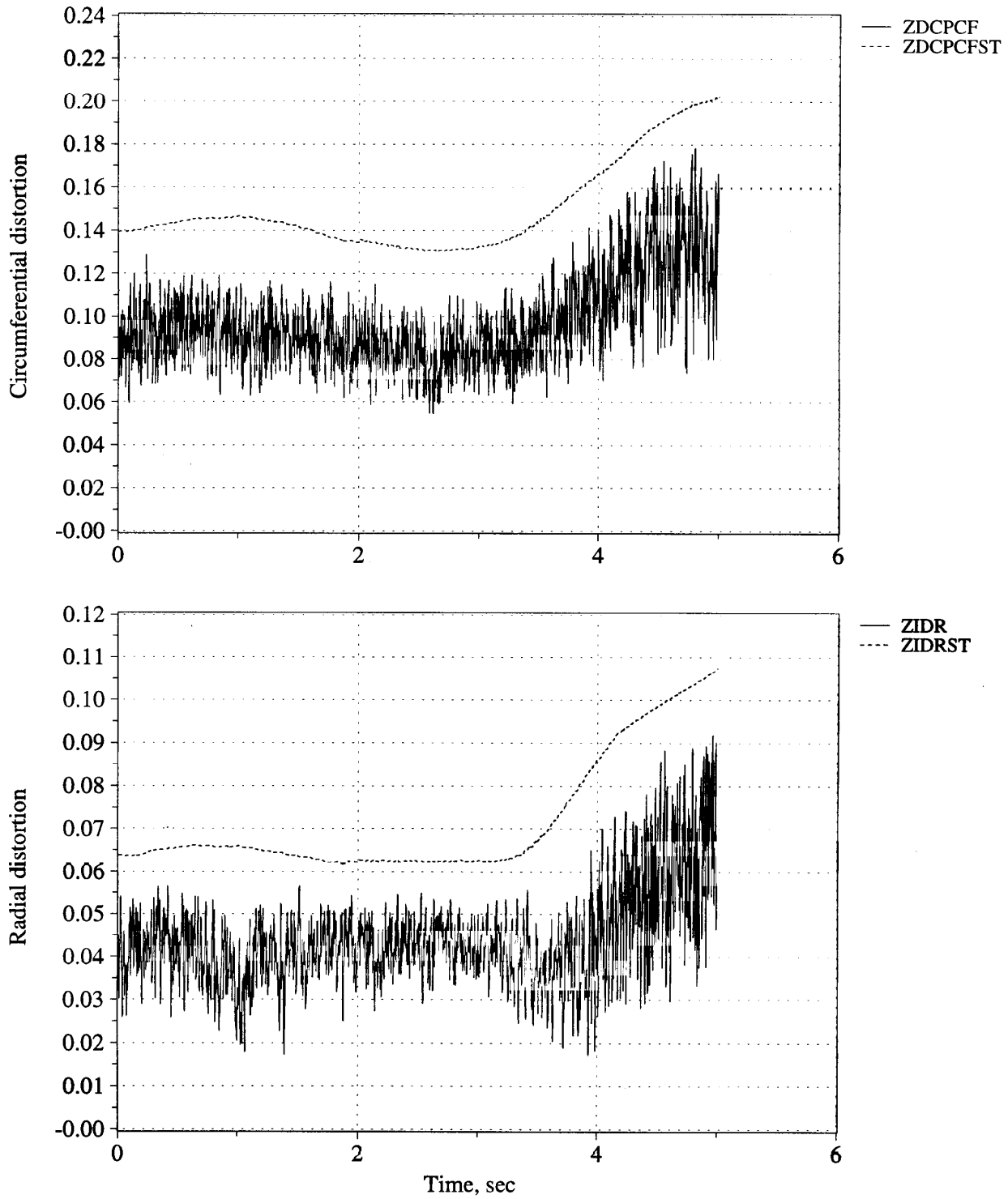

Figure C62. Time history of peak inlet dynamic circumferential and radial distortion (measured and estimated) - Flight 243, Test point 25c.

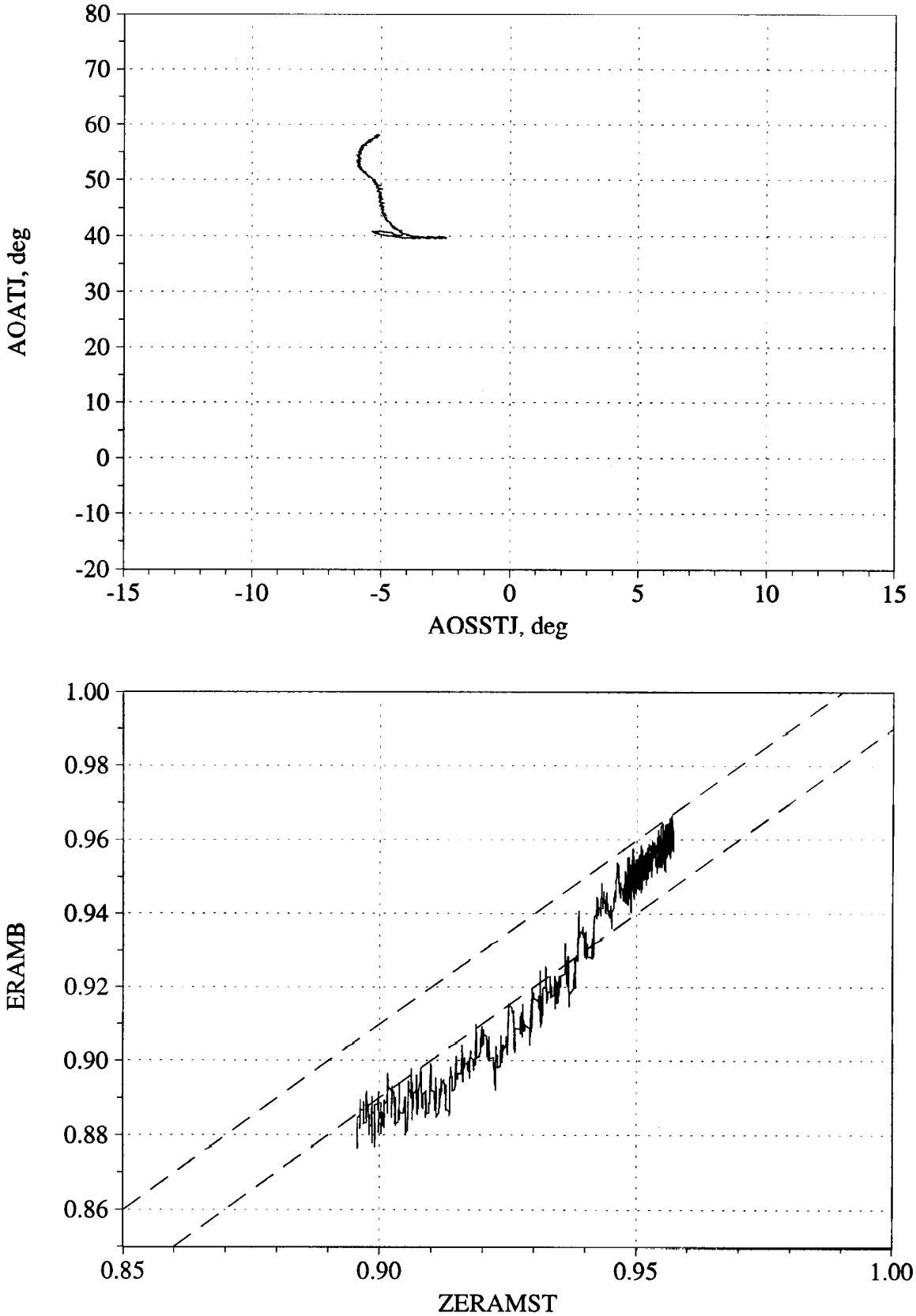

Figure C63. Angle of attack/angle of sideslip trajectory during maneuver; and measured versus estimated recovery - Flight 243, Test point 25c.

- Mid-to-Low-to-High Angle of Attack -

Figures C64 - C66, Flight 215, Test Point 06b
Figures C67 - C69, Flight 230, Test Point 17b
Figures C70 - C72, Flight 242, Test Point 20b
Figures C73 - C75, Flight 242, Test Point 20c

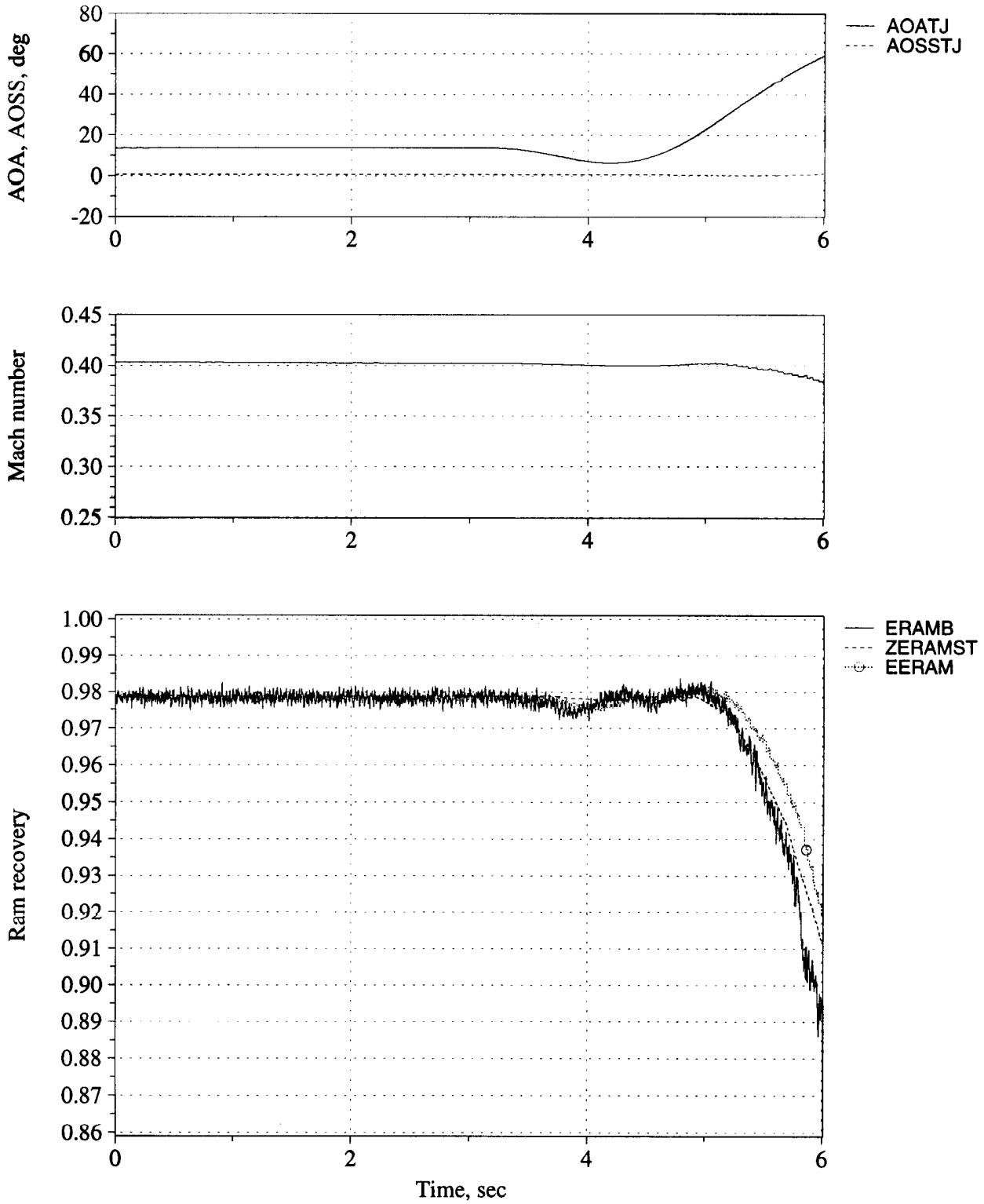

Figure C64. Time history of angle of attack, angle of sideslip, Mach number, and inlet recovery (measured and estimated) - Flight 215, Test point 06b.

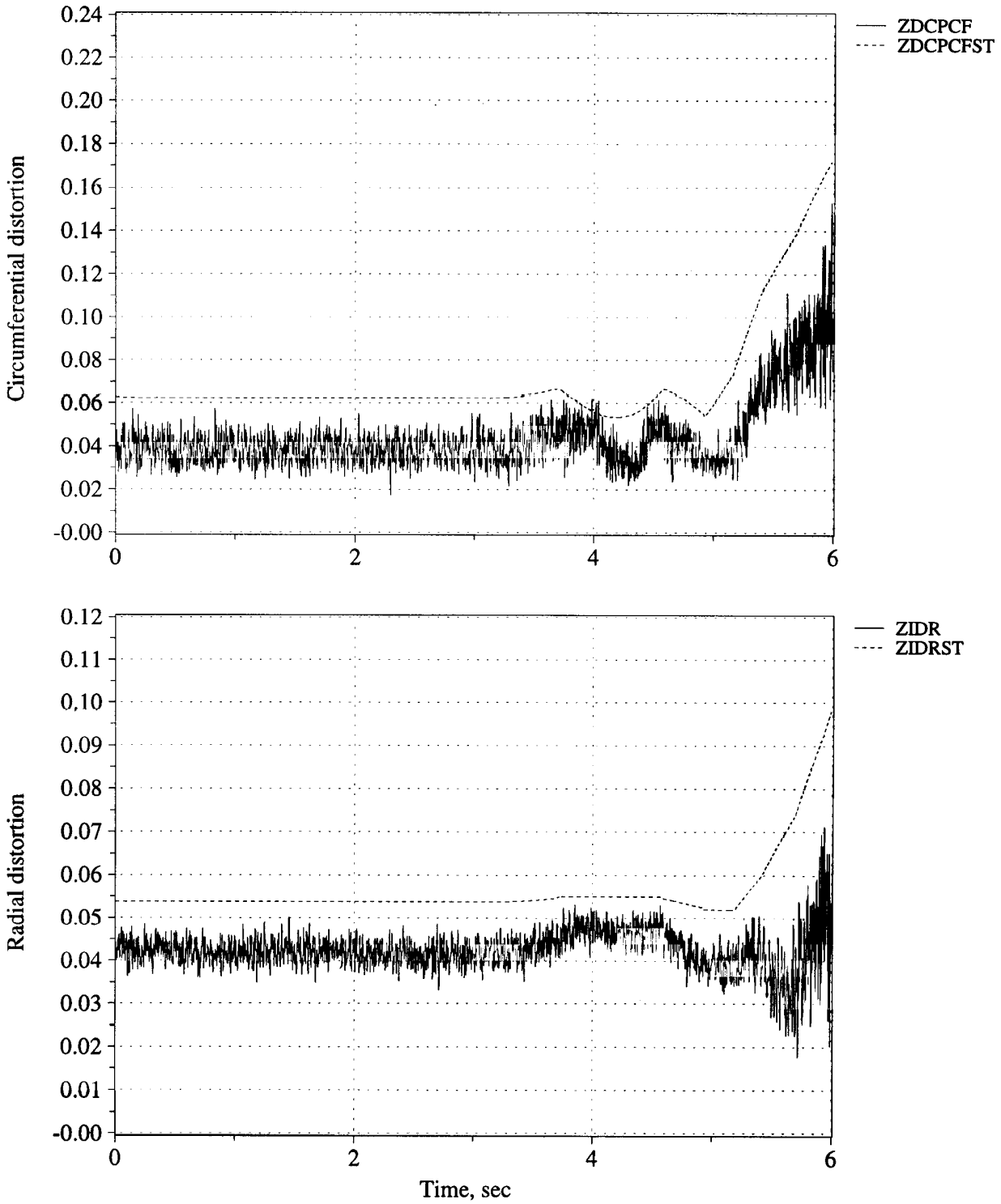

Figure C65. Time history of peak inlet dynamic circumferential and radial distortion (measured and estimated) - Flight 215, Test point 06b.

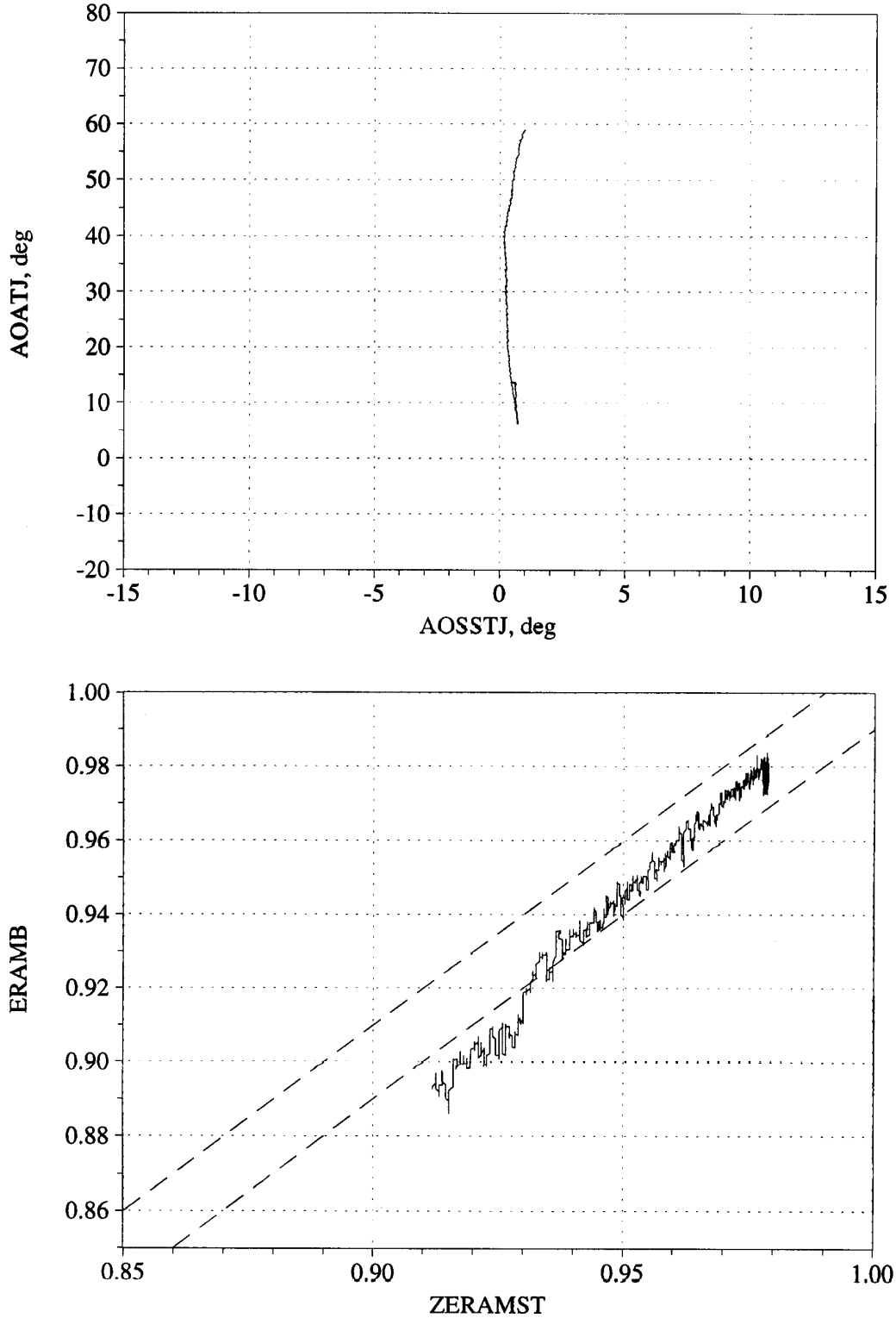

Figure C66. Angle of attack/angle of sideslip trajectory during maneuver; and measured versus estimated recovery - Flight 215, Test point 06b.

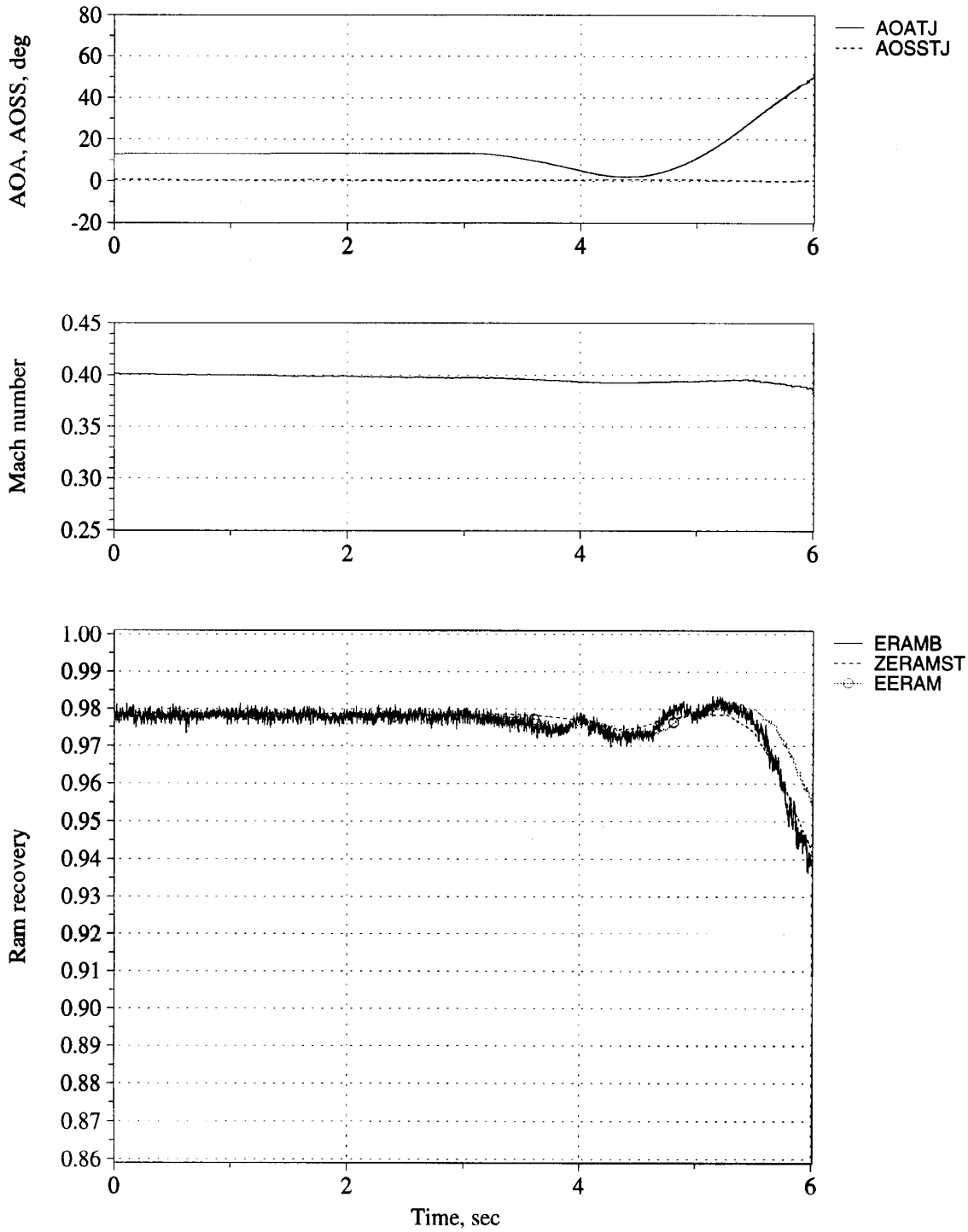

Figure C67. Time history of angle of attack, angle of sideslip, Mach number, and inlet recovery (measured and estimated) - Flight 230, Test point 17b.

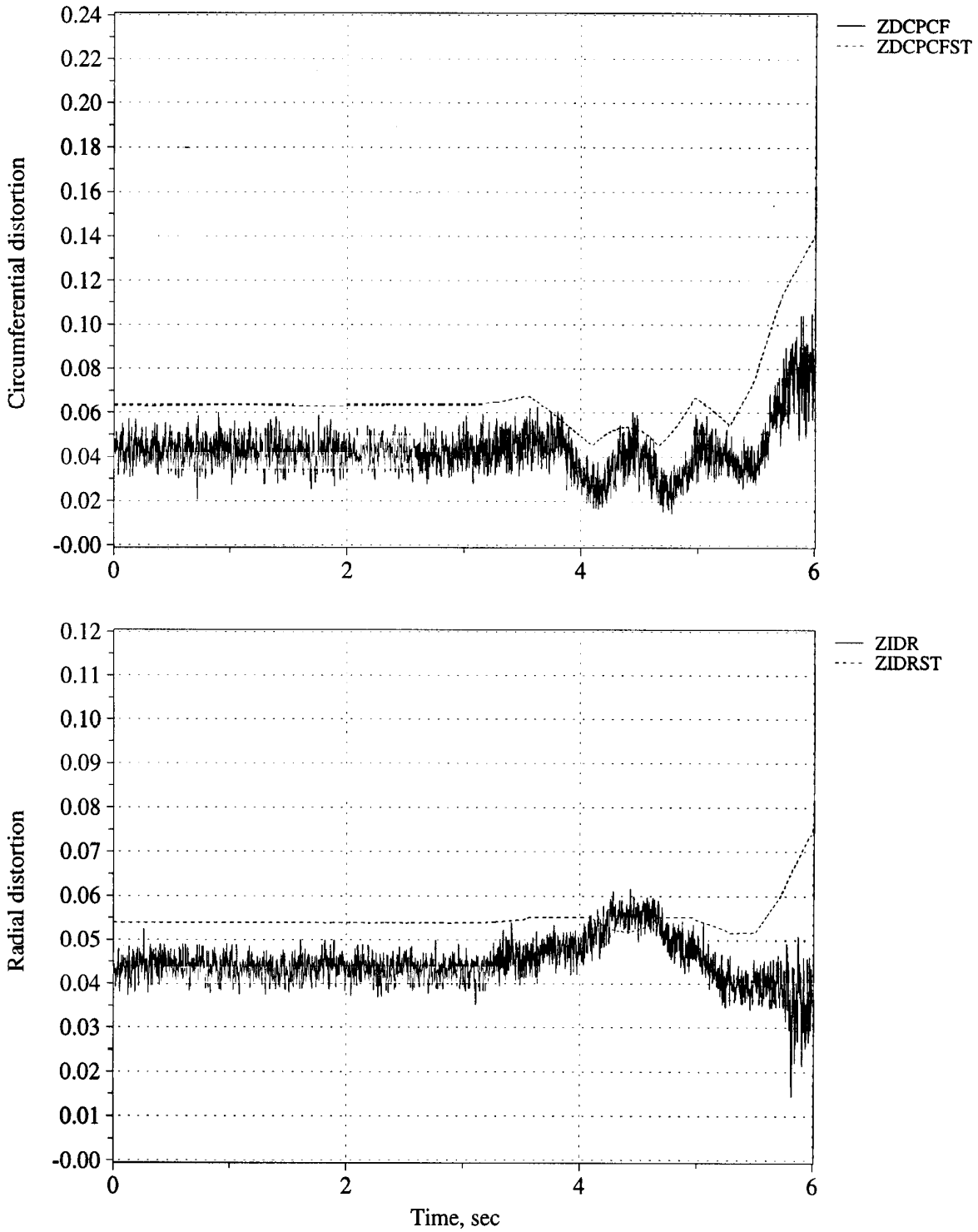

Figure C68. Time history of peak inlet dynamic circumferential and radial distortion (measured and estimated) - Flight 230, Test point 17b.

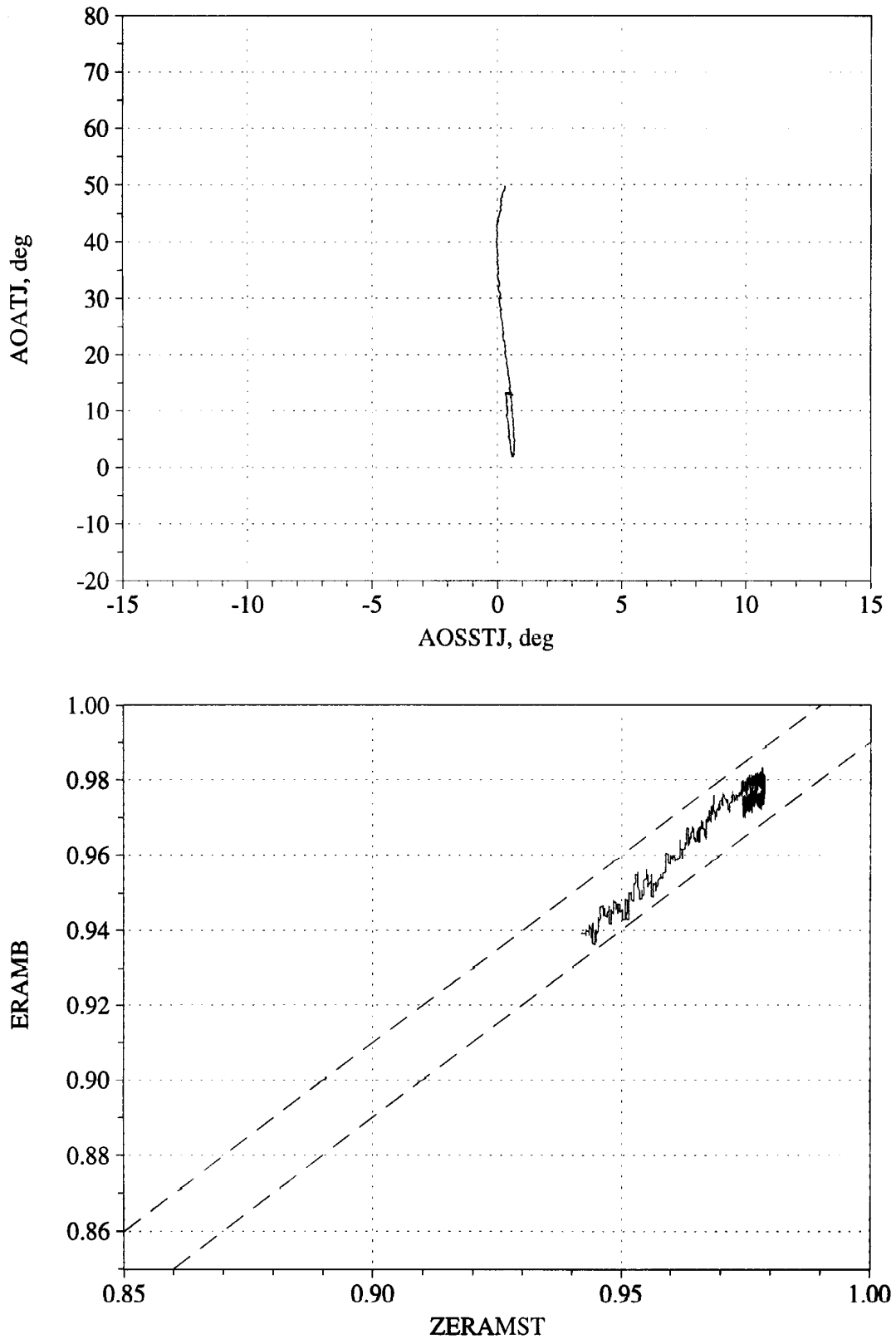

Figure C69. Angle of attack/angle of sideslip trajectory during maneuver; and measured versus estimated recovery - Flight 230, Test point 17b.

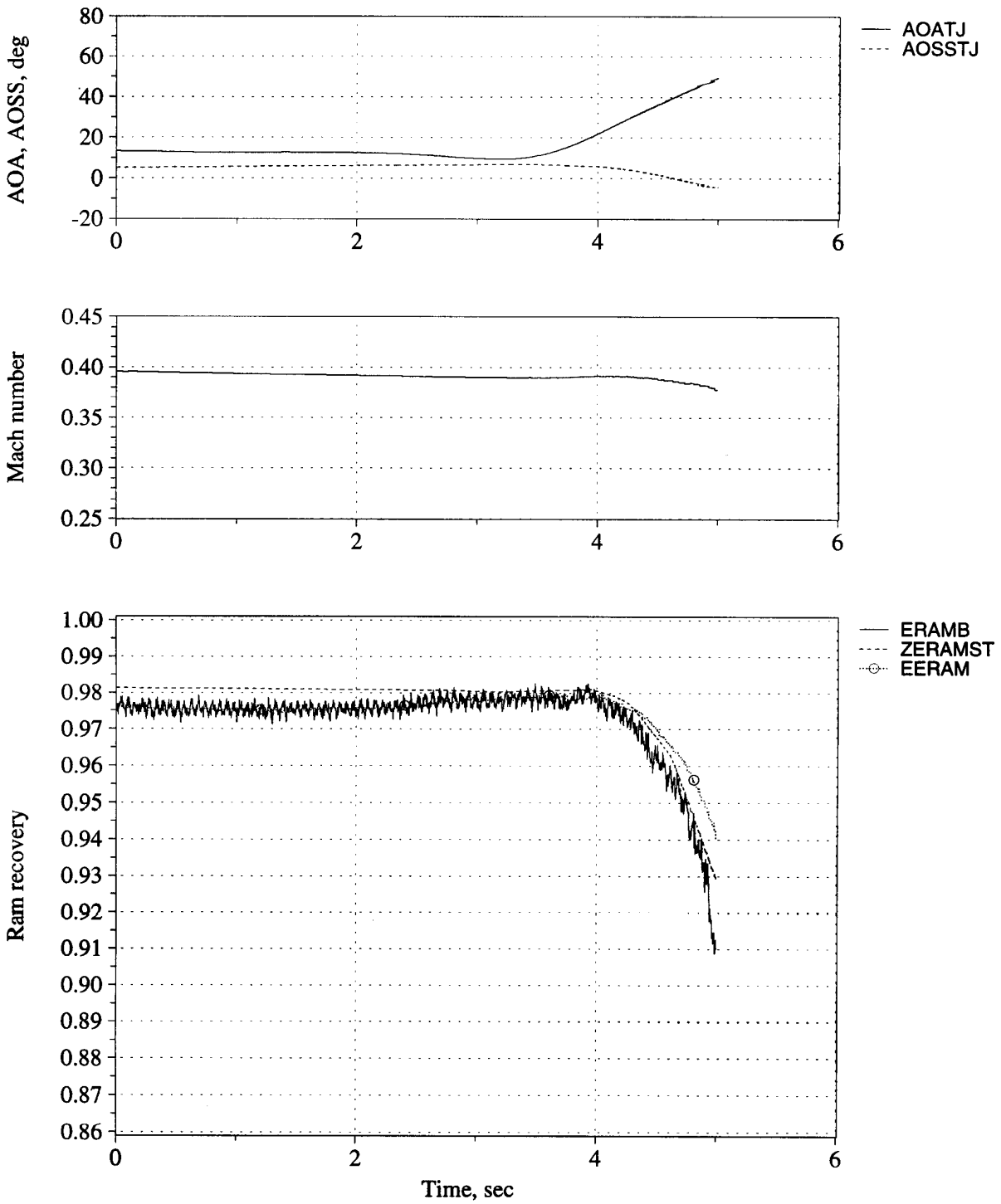

Figure C70. Time history of angle of attack, angle of sideslip, Mach number, and inlet recovery (measured and estimated) - Flight 242, Test point 20b.

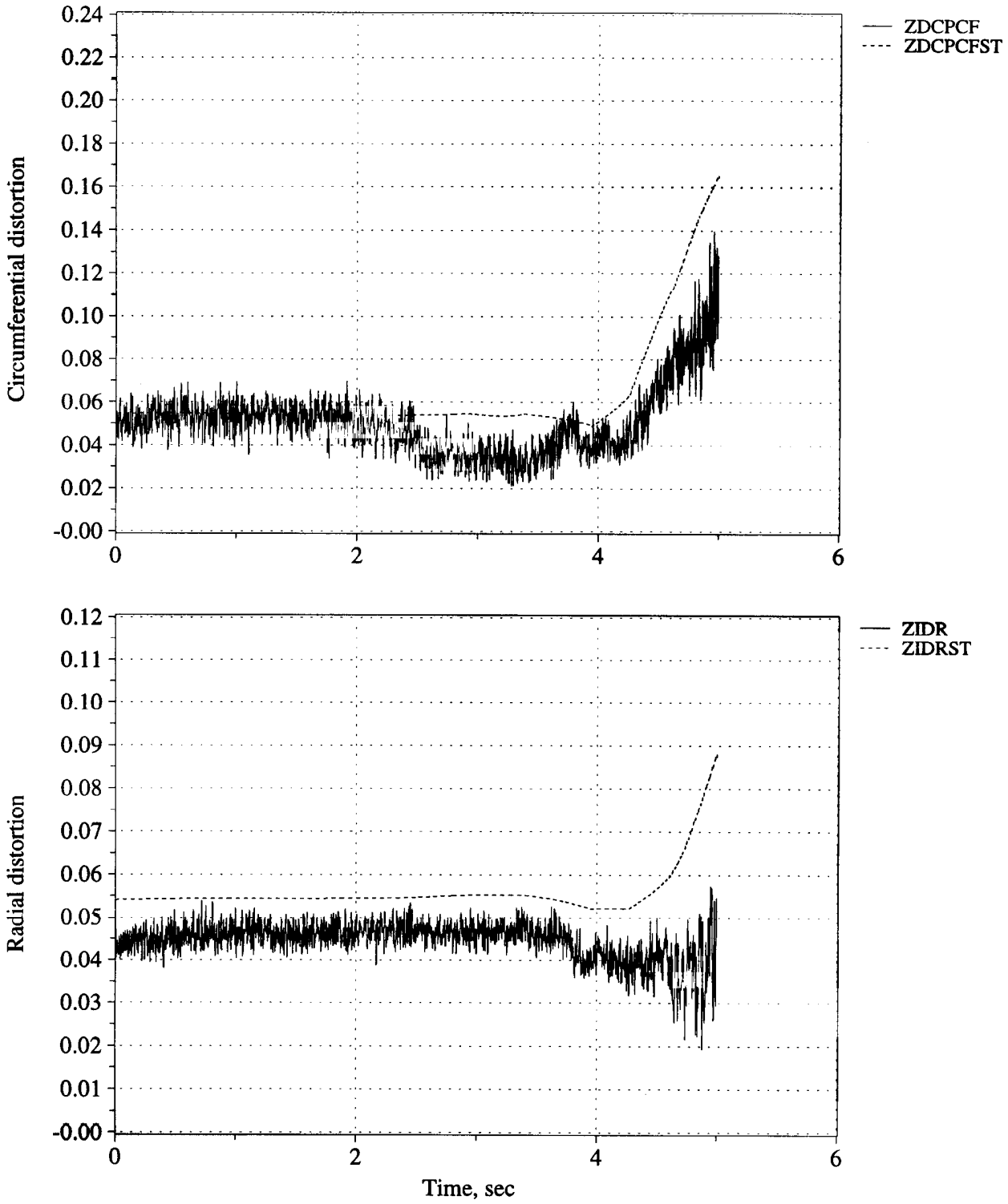

Figure C71. Time history of peak inlet dynamic circumferential and radial distortion (measured and estimated) - Flight 242, Test point 20b.

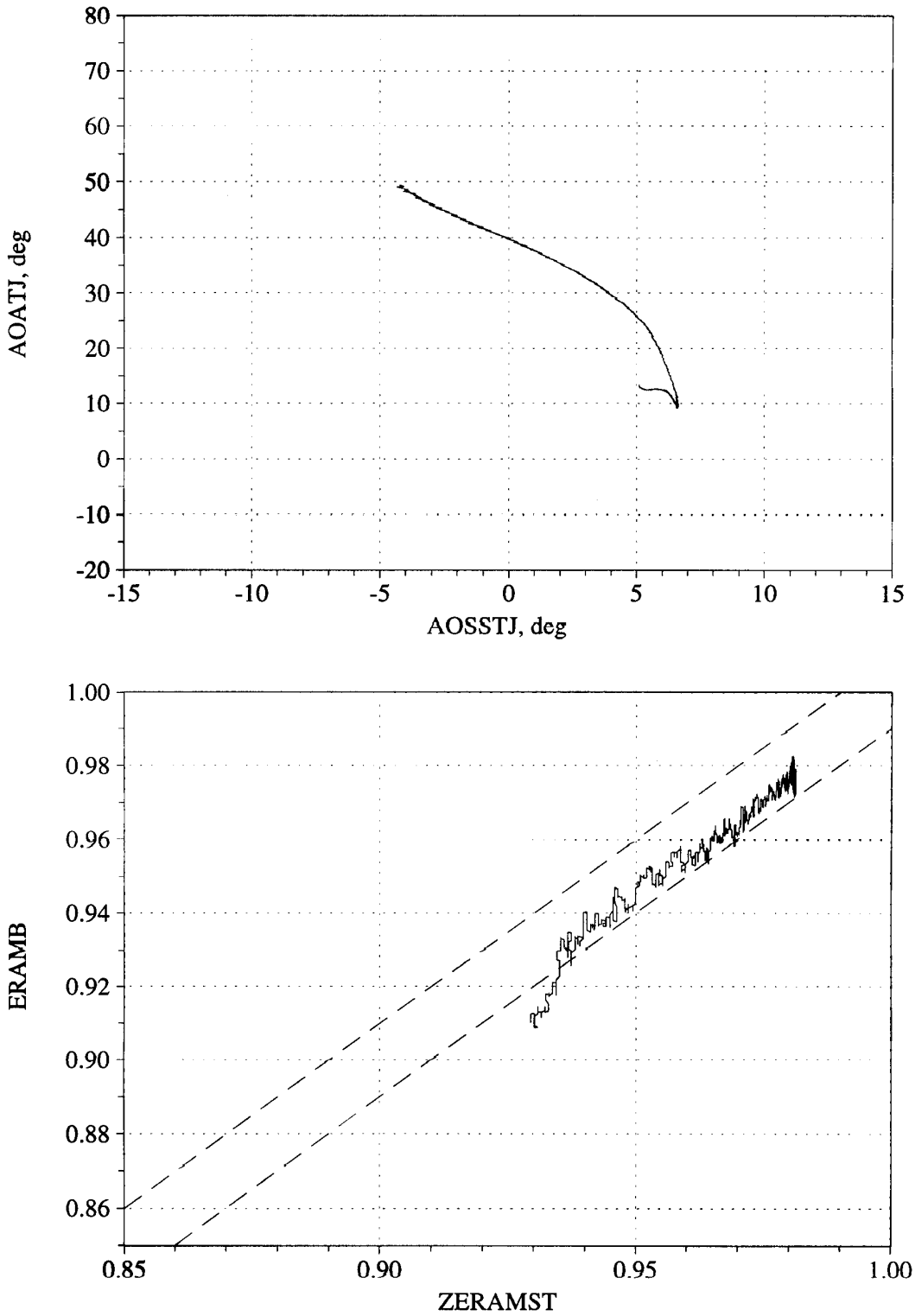

Figure C72. Angle of attack/angle of sideslip trajectory during maneuver; and measured versus estimated recovery - Flight 242, Test point 20b.

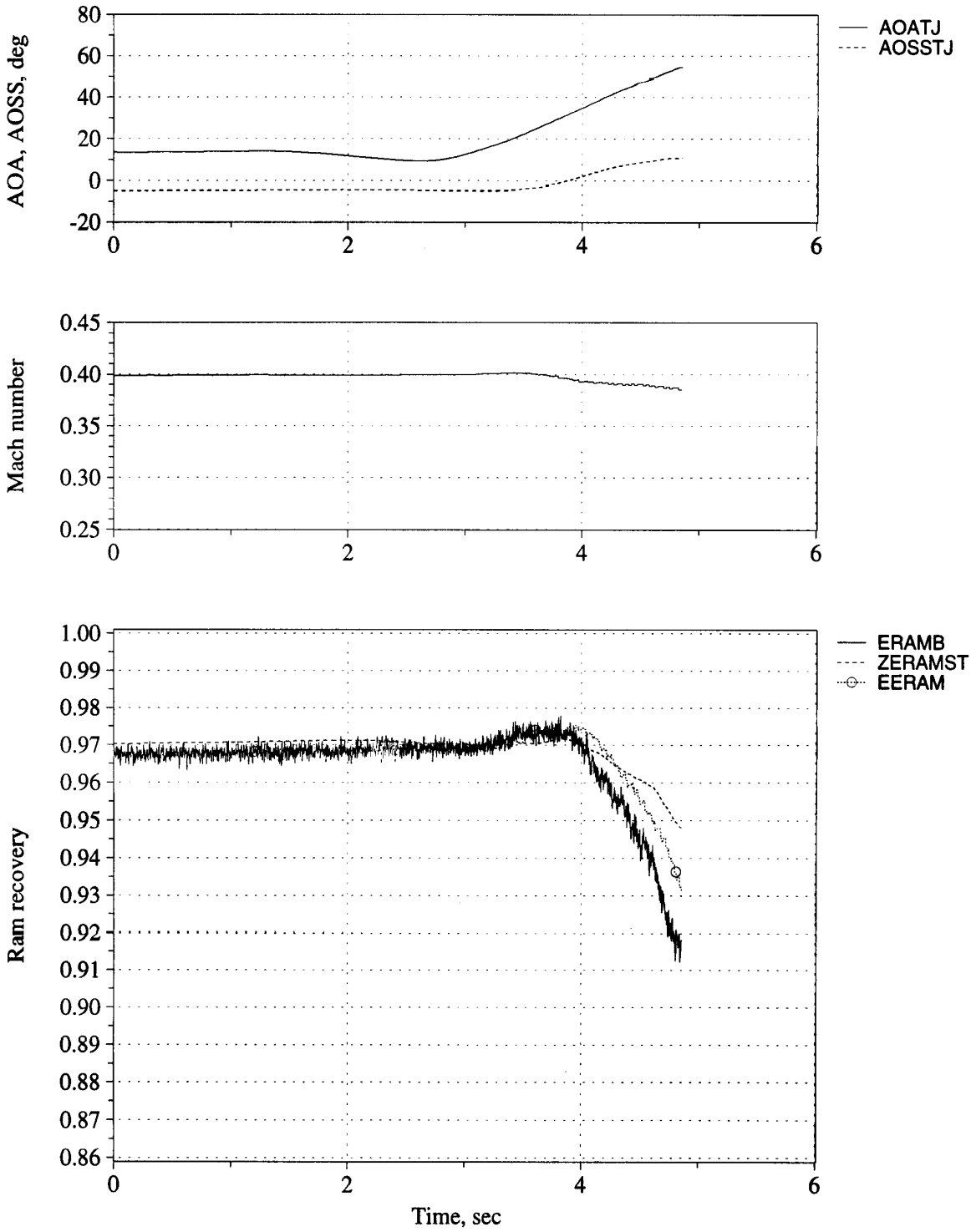

Figure C73. Time history of angle of attack, angle of sideslip, Mach number, and inlet recovery (measured and estimated) - Flight 242, Test point 20c.

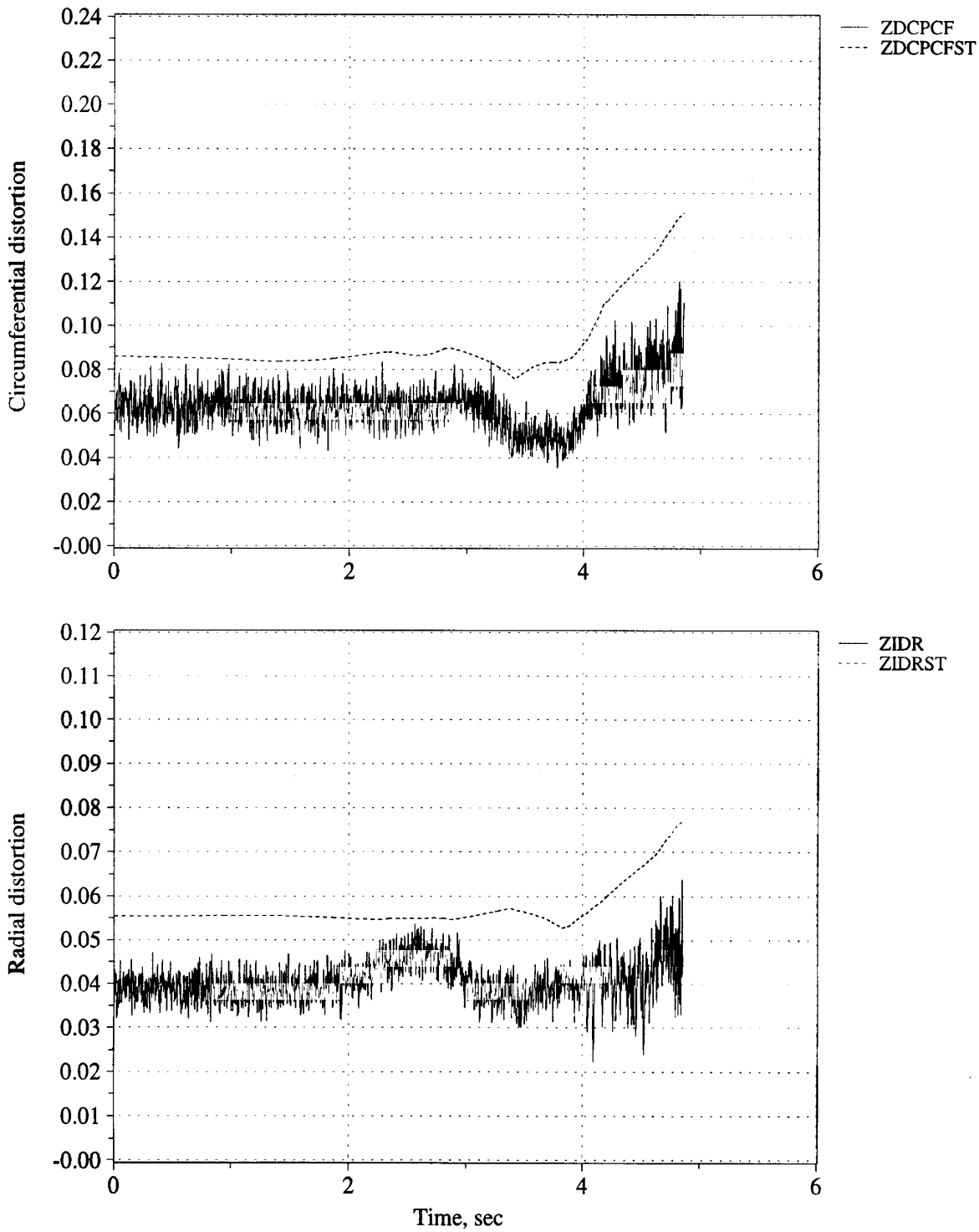

Figure C74. Time history of peak inlet dynamic circumferential and radial distortion (measured and estimated) - Flight 242, Test point 20c.

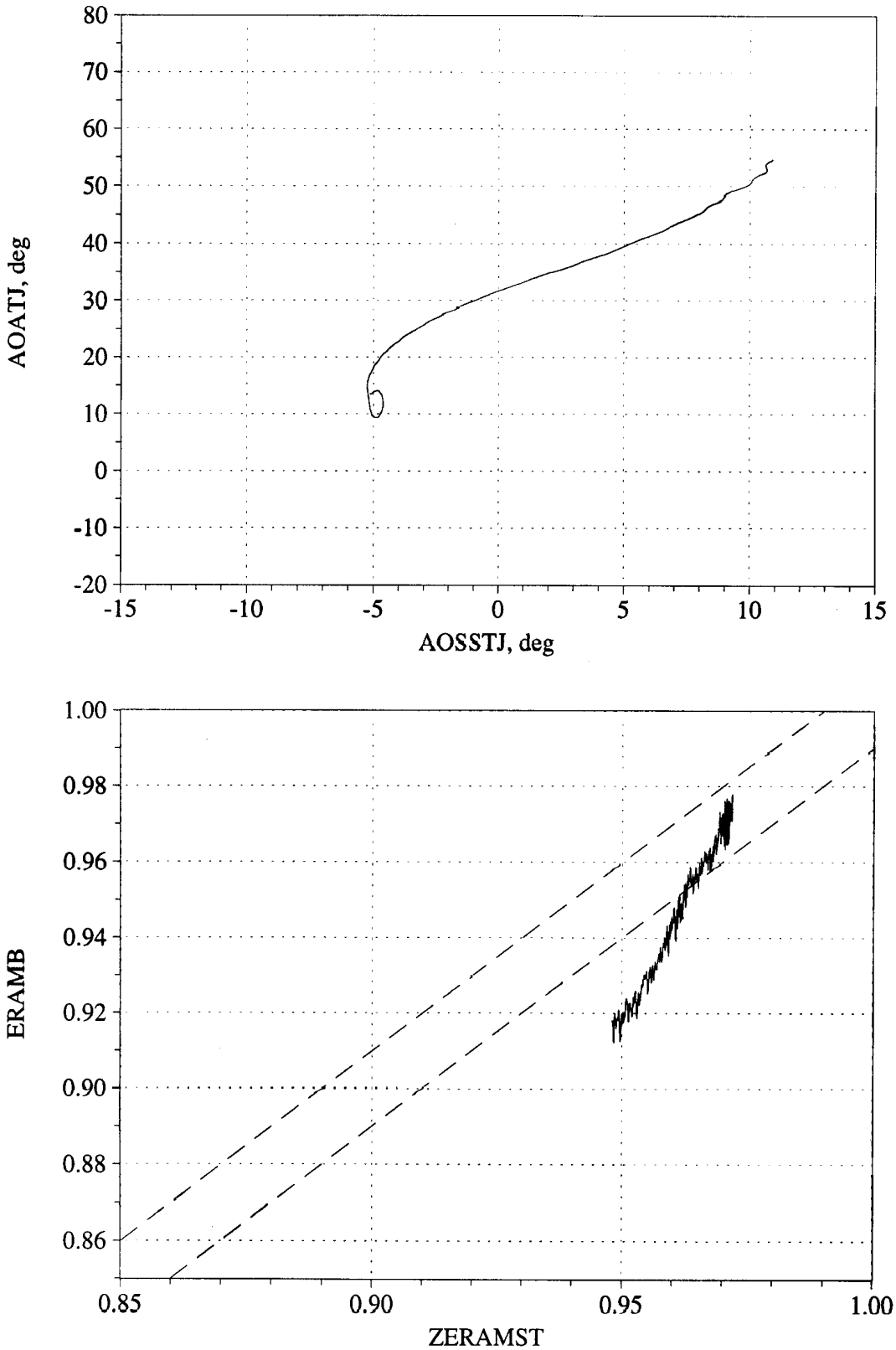

Figure C75. Angle of attack/angle of sideslip trajectory during maneuver; and measured versus estimated recovery - Flight 242, Test point 20c.

REPORT DOCUMENTATION PAGE

Form Approved
OMB No. 0704-0188

Public reporting burden for this collection of information is estimated to average 1 hour per response, including the time for reviewing instructions, searching existing data sources, gathering and maintaining the data needed, and completing and reviewing the collection of information. Send comments regarding this burden estimate or any other aspect of this collection of information, including suggestions for reducing this burden, to Washington Headquarters Services, Directorate for Information Operations and Reports, 1215 Jefferson Davis Highway, Suite 1204, Arlington, VA 22202-4302, and to the Office of Management and Budget, Paperwork Reduction Project (0704-0188), Washington, DC 20503.

1. AGENCY USE ONLY (Leave blank)

2. REPORT DATE
October 1999

3. REPORT TYPE AND DATES COVERED
Technical Memorandum

4. TITLE AND SUBTITLE
Inlet Flow Characteristics During Rapid Maneuvers for an F/A-18A Aircraft

5. FUNDING NUMBERS
WU 505-68-30-NAS3-26617

6. AUTHOR(S)
William G. Steenken, John G. Williams, and Kevin R. Walsh

7. PERFORMING ORGANIZATION NAME(S) AND ADDRESS(ES)
NASA Dryden Flight Research Center
P.O. Box 273
Edwards, California 93523-0273

8. PERFORMING ORGANIZATION REPORT NUMBER
H-2371

9. SPONSORING/MONITORING AGENCY NAME(S) AND ADDRESS(ES)
National Aeronautics and Space Administration
Washington, DC 20546-0001

10. SPONSORING/MONITORING AGENCY REPORT NUMBER
NASA/TM-1999-206587

11. SUPPLEMENTARY NOTES
W. G. Steenken and J. G. Williams, GE Aircraft Engines, Cincinnati, Ohio, and K. R. Walsh, Dryden Flight Research Center, Edwards, California. NASA Contract NAS3-26617.

12a. DISTRIBUTION/AVAILABILITY STATEMENT
Unclassified—Unlimited
Subject Category 07

12b. DISTRIBUTION CODE

13. ABSTRACT (Maximum 200 words)
The F404-GE-400 engine powered F/A-18A High Alpha Research Vehicle (HARV) was used to examine the characteristics of inlet airflow during rapid aircraft maneuvers. A study of the degree of similarity between inlet data obtained during rapid aircraft maneuvers and inlet data obtained at steady aerodynamic attitudes was conducted at the maximum engine airflow of approximately 145 lbm/sec using a computer model that was generated from inlet data obtained during steady aerodynamic maneuvers. Results show that rapid-maneuver inlet recoveries agreed very well with the recoveries obtained at equivalent stabilized angle-of-attack conditions. The peak dynamic circumferential distortion values obtained during rapid maneuvers agreed within 0.01 units of distortion over the 10 - 38 degree angle of attack range with the values obtained during steady aerodynamic maneuvers while similar agreement was found for the peak dynamic radial distortion values up to 29 degrees angle-of-attack. Exceedences of the rapid-maneuver peak dynamic circumferential distortion values relative to the peak distortion model values at steady attitudes occurred only at low or negative angles of attack and were inconsequential from an engine-stability assessment point of view. The results of this study validate the current industry practice of testing at steady aerodynamic conditions to characterize inlet recovery and peak dynamic distortion levels.

14. SUBJECT TERMS
Aircraft rapid maneuvers, F-18 aircraft, F/A-18A, High angle of attack, Inlet distortion, Inlet-engine compatibility

15. NUMBER OF PAGES
221

16. PRICE CODE
A10

17. SECURITY CLASSIFICATION OF REPORT
Unclassified

18. SECURITY CLASSIFICATION OF THIS PAGE
Unclassified

19. SECURITY CLASSIFICATION OF ABSTRACT
Unclassified

20. LIMITATION OF ABSTRACT
Unlimited